

The X-Ray Source Population of Nearby Spiral Galaxies

Dissertation submitted to the
Department of Physics of the
Ludwig-Maximilians-Universität München

by

Stefan Immler

from Nabburg

Munich, February 21, 2000

The X-Ray Source Population of Nearby Spiral Galaxies

Dissertation submitted to the
Department of Physics of the
Ludwig-Maximilians-Universität München

by

Stefan Immler

from Nabburg

Munich, February 21, 2000

1. Examiner: Prof. Dr. Joachim Trümper
2. Examiner: Prof. Dr. Rolf-Peter Kudritzki
Date of oral exam: August 1, 2000

“Together let us explore the stars . . . ”

John F. Kennedy
(Inaugural Address)

ZUSAMMENFASSUNG

*“Wahre Dein Recht auf des Weltalls Höhn!
Nicht haftend am Niedern
Sinke vom Staube beschwert dumpf in des Acheron Flut!
Nein, vielmehr zum Himmel empor!
Dort suche die Heimat!”*

Giordano Bruno

Im Rahmen dieser Arbeit wird ein umfassender Einblick in die Quellkomponenten von nahen Spiralgalaxien im Röntgenbereich gegeben. Schwerpunkt ist dabei Röntgenemission der nahen Galaxien M31, M51, M83, M100 und M101 auf Grundlage von Beobachtungen mit den HRI und PSPC Instrumenten an Bord des Satelliten ROSAT (‘Röntgensatellit’; Kapitel 1.). Ein wichtiger Teil der ausgewerteten Daten wurde vom Autor als ‘principal investigator’ (PI) zur Beobachtung vorgeschlagen, einschließlich einer ‘last light’ Beobachtung mit dem ROSAT PSPC wenige Tage bevor der Satellit endgültig nach mehr als acht Jahren erfolgreicher Beobachtung abgeschaltet wurde. Der Großteil der Daten stammt von Beobachtungsvorschlägen von Wolfgang Pietsch, Betreuer dieser Arbeit, und aus dem Datenarchiv des MPE. Beobachtungen aus anderen Wellenlängenbereichen (z.B. Radio- und optische Beobachtungen) ergänzen die ROSAT Daten.

Die Beobachtungen wurden dazu verwendet, die diskrete Population von Röntgenquellen in Galaxien zu untersuchen und Fragestellungen bezüglich des Beitrages von diskreten Quellen zur gesamten Abstrahlung der Galaxien im Röntgenbereich zu lösen (Kapitel 2.). Ausführliche Zeitvariabilitätsuntersuchungen wurden für jede einzelne Röntgenquelle durchgeführt und Langzeitveränderlichkeit durch Vergleich mit früheren Beobachtungen von Röntgenmissionen getestet. Radio und optische Beobachtungen wurden herangezogen, um entdeckte Röntgenquellen zu identifizieren (Kapitel 3.1.). Eine neue Methode wurde zum Nachweis von Röntgenquellen in Gebieten erhöhter diffuser Röntgenstrahlung entwickelt (z.B. in Kernregionen; Kapitel 3.2.). Durch die Anwendung auf virtuelle Beobachtungen unserer Nachbargalaxie M31 (690 kpc) im Abstand von M51 (7.7 Mpc) und Vergleich mit hochauflösenden Beobachtungen von M31 wurde die Methode erfolgreich getestet.

Etwa die Hälfte aller in den Galaxien nachgewiesenen Röntgenquellen sind massen-akkretierende Röntgendoppelsternsysteme, die damit die größte Quellpopulation repräsentieren (Kapitel 4.3. und 4.4.). Zusätzlich wurden mehrere röntgenhelle HII Regionen in den Spiralarmen der Galaxien nachgewiesen (Kapitel 4.4.1.).

Eine Anzahl ungewöhnlich heller Röntgenquellen (‘superluminous X-ray sources’, SLSs) wurde in den Galaxien M51 (10 SLSs), M83 (8), M100 (6) und M101 (5) entdeckt (Kapitel 4.4.3.). Interessanterweise ist jeder dieser SLSs während der HRI Beobachtungen variabel und ausschließlich in den äußeren Spiralarmen in großen HII Komplexen angesiedelt, was auf die Entstehung massiver Sterne hindeutet. In M83 beispielsweise wurde eine variable (Faktor $\gtrsim 2$) super-Eddington Röntgenquelle ($3.8 \times 10^{39} \text{ erg s}^{-1}$) gefunden, die mit einem schwachen, optisch ausgedehnten Objekt zusammenfällt. Aufgrund der spektralen Indizes Optisch-zu-Röntgen $\alpha_{\text{OX}} = 1$ und Radio-zu-Optisch $\alpha_{\text{RO}} < 0$ ist es unwahrscheinlich, daß die Quelle eine Hintergrundgalaxie, AGN oder Quasar darstellt. Stattdessen repräsentiert sie höchstwahrscheinlich ein massives ($\sim 30 M_{\odot}$) akkretierendes Schwarzes Loch in einer kompakten HII Region oder einem Kugelsternhaufen in M83. Ähnliche breitbandige Eigenschaften

wurden für SLSs in den Galaxien M51 und M101 beobachtet. Die PSPC Spektren der Quellen ergeben ein bestangepaßtes thermisches Bremsstrahlung Spektrum mit einer Temperatur von ~ 2 keV.

Zusätzlich wurde eine Anzahl röntgenheller ($\gtrsim 10^{38}$ erg s $^{-1}$) und zuvor unbekannter Supernovaüberreste ('supernova remnants', SNRs) in den Galaxien M51, M83 and M101 entdeckt, die in ausgedehnten H α Emissionskomplexen lokalisiert sind und mit kompakten 6 cm und 20 cm Radioquellen zusammenfallen (Kapitel 4.4.2.). Kürzlich wurden Hinweise auf die Existenz von zwei röntgenhellen Hypernovaüberresten in der Galaxie M101 bekannt, die breitbandige Eigenschaften haben, die denen der SNRs ähnlich sind, die in M51 und M83 entdeckt wurden. Hinsichtlich ihrer Leuchtkräfte (3.0 und 1.2×10^{38} erg s $^{-1}$), spektraler Parameter (0.3 keV für einen bestangepaßtes thermisches Plasma) und Emissionslinienverhältnissen [SiII]/H α von 0.51 und 0.76 sind die Kandidaten von Hypernovaüberresten in M101 den SNR Kandidaten in M83 frappierend ähnlich. Es ist daher denkbar, daß eine weitere Anzahl von andauernd leuchtenden Röntgenquellen in nahen Galaxien die Überreste von energetischen Hypernova Explosionen sind.

Eines der wichtigsten Resultate ist die Entdeckung von Röntgenstrahlung der Typ II Supernova SN 1979C in M100 mit einer Leuchtkraft von 1×10^{39} erg s $^{-1}$ 16 Jahre nach Ausbruch (Kapitel 5.3.). Nachbeobachtungen mit ROSAT, einschließlich einer ROSAT 'last-light' PSPC Beobachtung, ergaben, daß die Emission relativ weich (0.5 keV) zu diesem spätem Zeitpunkt nach der Explosion ist. Ebenso konnte festgestellt werden, daß der starke Abfall der Röntgenhelligkeit $L_x \propto t^{-4}$ verschieden ist vom langsamen Abfall der Radiohelligkeit ($S_\lambda \propto t^{-0.7}$ für $\lambda = 2, 6$ und 20 cm). Hinweise für einen Anstieg der Emission ~ 4000 Tage nach Ausbruch der SN im Radiobereich wurde im Röntgenbereich nicht beobachtet. Mittels der gemessenen Leuchtkraft konnte die Massenverlustrate des Vorgängersterns zu 1×10^{-4} M $_\odot$ yr $^{-1}$ bestimmt werden. Ebenso wurde abgeschätzt, daß die maximal erreichte (0.1 – 2.4 keV Band) Röntgenleuchtkraft der SN 1979C im Bereich 5 – 8×10^{40} erg s $^{-1}$ lag. Der im Nachhinein ebenso bestimmte Zeitpunkt zum Einsetzen der Röntgenemission lag zwischen 2000 und 2500 Tagen nach Ausbruch.

Ein weiteres bedeutendes Ergebnis ist die Entdeckung einer Röntgenquelle mit einer Leuchtkraft von 1.6×10^{38} erg s $^{-1}$ an der Position der SN 1994I in M51 79–85 Tage nach der Explosion (Kapitel 5.2.). Dies ist der erste starke Hinweis für den Nachweis von Röntgenstrahlung einer Typ I SN. Unter der Annahme, daß die Emission von schock-angeregtem Gas stammt, das vom Vorgängerstern durch nicht-konservativem Massentransfer an einem Begleitstern abgegeben wurde, wird eine konstante Gasdichte von $\rho = 2 \times 10^5$ cm $^{-3}$ $v_{16}^{2/3}$ und eine Gesamtmasse leuchtendes Gases von $\dot{M} = 1 \times 10^{-3}$ M $_\odot$ innerhalb einer Kugelschale mit Radius 1.2×10^{16} cm abgeschätzt. Falls die Strahlung vom schock-angeregten Wind des Vorgängersterns stammt, der durch die nach Aussen gehende Schockfront erhitzt wird, wird eine Massenverlustrate vor Ausbruch der SN von $\dot{M} = 3.6 \times 10^{-6}$ M $_\odot$ yr $^{-1}$ abgeleitet.

Ebenso wurde in einer ultra-tiefen ROSAT HRI Beobachtung von M101 zwei Röntgenquellen an den Positionen der Typ II SNe 1951H and 1970G nachgewiesen (Kapitel 5.1.). Für die HRI Leuchtkraft der SN 1970 25 Jahre nach Ausbruch (4.5×10^{37} erg s $^{-1}$) wird die Massenverlustrate zu $\dot{M} = 2.0 \times 10^{-5}$ M $_\odot$ yr $^{-1}$ bestimmt. Dies ist identisch mit der Massenverlustrate, die aus Radiodaten abgeleitet wurde. Für SN 1951H wird die Massenverlustrate aus der HRI Leuchtkraft (2.0×10^{38} erg s $^{-1}$) 45 Jahre nach Ausbruch zu $\dot{M} = 5.5 \times 10^{-5}$ M $_\odot$ yr $^{-1}$ bestimmt. Das PSPC Spektrum der Röntgenquelle zeigt, daß die Emission relativ weich (0.5 keV) und unabsorbiert ist ($N_H = 4 \times 10^{20}$ cm $^{-2}$).

Die ausgedehnte Röntgenstrahlung innerhalb der Kernregionen der Galaxien kann fast vollständig für M51 (95%) und M100 (96%) in Punktquellen aufgelöst werden (Kapitel 6.). Insgesamt beträgt der Anteil von Punktquellen $\sim 1/3$ zur Gesamtemission der Galaxien. Die restliche Emission wird von großen Mengen heißen Gases innerhalb der Scheiben und in den Halos der Galaxien und von unaufgelösten Punktquellen erzeugt. Für M83 beträgt der Anteil von heißem Gas und unaufgelösten Punktquellen zur Emission innerhalb der Kernregion 45%. Analog tragen Punktquellen ca. die Hälfte zur Gesamtstrahlung der Galaxie im Röntgenbereich bei.

Unter Ausschluß bekannter Vordergrund- und Hintergrundobjekte wurden die Leuchtkraftvertei-

lungen der Quellen in den Galaxien verglichen (Kapitel 4.5.). Interessanterweise wurde festgestellt, daß alle Galaxien, unabhängig von deren morphologischen Typ, eine ähnliche Leuchtkraftverteilungsfunktion besitzen, die am Besten durch ein Potenzgesetz $N(> L_x) = N_0 L_x^{-\alpha}$ mit Exponenten ~ 1 beschrieben wird. Sowohl die Anzahl superheller Röntgenquellen mit Leuchtkräften über dem Eddington Limit für einen $1.4 M_\odot$ akkretierenden Neutronenstern ($L_x > 1.3 \times 10^{38} \text{ erg s}^{-1}$) als auch die gesamte Röntgenleuchtkraft scheinen dabei mit der Sternentstehungsrate der Galaxien korreliert zu sein.

SYNOPSIS

*“Maintain your rights for the universe’s heights!
Lest, sinking to the depths,
Assailed, you drown in Acheron’s black waters!
Rather go soaring, probing nature’s lairs!”*

Giordano Bruno

Within the scope of this work, a comprehensive insight into the X-ray source components of nearby spiral galaxies is given. Emphasis will be put on the X-ray emission from the nearby galaxies M31, M51, M83, M100 and M101, based on observations with the HRI and PSPC instruments onboard ROSAT (‘Röntgensatellit’; Sec. 1.). An important fraction of the data analyzed was proposed by the author as principal investigator (PI), including a ROSAT ‘last light’ PSPC observation just days before the ROSAT satellite was finally turned off after more than eight years of successful operation. Most of the data are from proposals submitted by Wolfgang Pietsch, supervisor of this thesis, and from the MPE data archive. Observations obtained in other wavelength regimes (e.g. radio, optical) were used to complement the ROSAT analysis.

The observations were utilized to study the discrete X-ray source population in the galaxies and attack questions as to the contribution of discrete sources to the total X-ray output of the galaxies (Sec. 2.). Detailed timing analysis was performed for each individual X-ray source and the long-term variability was tested by comparison with previous X-ray observations from past X-ray missions. Radio and optical observations were used to identify detected X-ray sources (Sec. 3.1.). A new source detection technique (‘image subtraction technique’) was developed to detect sources in regions of enhanced diffuse X-ray emission (e.g. the bulge regions; Sec. 3.2.). The method was successfully tested by applying it to a virtual observations of one of our neighbour galaxies M31 (690 kpc) at a distance of M51 (7.7 Mpc) and comparing the results to the high-resolution observations of M31.

Almost half of all X-ray sources detected inside the galaxies are mass-accreting X-ray binaries, representing the largest X-ray source population (Sec. 4.3. and 4.4.). In addition to X-ray binaries, many X-ray luminous HII regions are found in the spiral arms of the galaxies (Sec. 4.4.1.).

A number of exceptionally bright X-ray sources (‘superluminous X-ray sources’, SLSs) are detected inside the galaxies M51 (10 SLSs), M83 (8), M100 (6) and M101 (5; Sec. 4.4.3.). It is interesting to note that each of the SLSs is variable during the HRI period of observation and that they are located exclusively in the outer part of the spiral arms, coincident with giant HII complexes, indicating massive star origins. In M83, for example, a variable (factor $\gtrsim 2$), super-Eddington ($3.8 \times 10^{39} \text{ erg s}^{-1}$) X-ray source is found to coincide with a faint, extended optical counterpart. Based on the spectral indices optical-to-X-ray $\alpha_{\text{OX}} = 1$ and radio-to-optical $\alpha_{\text{RO}} < 0$, the source is unlikely to be a background galaxy, AGN or quasar and most likely represents a massive ($\sim 30 M_{\odot}$) accreting black hole binary, located in a compact HII region or in a globular cluster in M83. Similar broadband properties are observed for SLSs located in M51 and M101. The PSPC spectrum of the sources gives a best fit thermal bremsstrahlung spectrum with a source temperature of $\sim 2 \text{ keV}$.

Also, a number of X-ray luminous ($\gtrsim 10^{38} \text{ erg s}^{-1}$), previously unknown supernova remnant (SNR) candidates were discovered in M51, M83 and M101, located in extended H α emission complexes and coinciding with compact 6 cm and 20 cm radio sources (Sec. 4.4.2.). Recently, evidence for the

presence of two X-ray luminous hypernova remnants in the galaxy M101 was presented, with broadband properties similar to the SNR candidates discovered in M51 and M83. In terms of luminosities (3.0 and $1.2 \times 10^{38} \text{ erg s}^{-1}$), spectral parameters (0.3 keV best thermal plasma fit) and $[\text{SiII}]/\text{H}\alpha$ emission line ratios of 0.51 and 0.76 , respectively, the hypernova remnant candidates in M101 are strikingly similar to the SNR candidates in M83. It is hence conceivable that a number of persistent X-ray sources in nearby galaxies are the relics from energetic hypernova explosions.

One of the most important results was the discovery of X-ray emission from the type II supernova SN 1979C in M100, 16 years after the explosion, with a luminosity of $1 \times 10^{39} \text{ erg s}^{-1}$ (Sec. 5.3.). Follow-up observations with ROSAT, including a ROSAT ‘last-light’ PSPC observation, showed that the emission is rather soft (0.5 keV) at this late stage and that the steep X-ray rate of decline of $L_x \propto t^{-4}$ is in contrast to the observed slow radio rate of decline ($S_\lambda \propto t^{-0.7}$ with $\lambda = 2, 6$ and 20 cm). Indications for an *increase* in the emission of the SN beyond ~ 4000 days after the outburst in the radio regime are not observed in the X-ray band. By using the inferred luminosities, the mass-loss rate of the progenitor could be determined to be $1 \times 10^{-4} M_\odot \text{ yr}^{-1}$. Also, by using a mean X-ray rate of decline of t^{-4} over the last ~ 19 years, the maximum attained ($0.1\text{--}2.4 \text{ keV}$ band) luminosity of SN 1979C could be determined to be in the range $5\text{--}8 \times 10^{40} \text{ erg s}^{-1}$ for a predicted turn-on phase between day 2000 and 2500 after the outburst.

Another important result is the detection of an X-ray source with a $0.1\text{--}2.4 \text{ keV}$ band luminosity of $1.6 \times 10^{38} \text{ erg s}^{-1}$, coinciding with the position of SN 1994I in M51, 79–85 days after the explosion (Sec. 5.2.). This is the first strong evidence for the detection of X-ray emission from a type I SN. Assuming the emission arises from shocked circumstellar gas, deposited by the progenitor through non-conservative mass-transfer to a companion, a constant gas density of $\rho = 2 \times 10^5 \text{ cm}^{-3} v_{16500}^{2/3}$ and a total mass of X-ray luminous gas of $M = 1 \times 10^{-3} M_\odot$ inside a sphere of radius $1.2 \times 10^{16} \text{ cm}$ is estimated. If the emission arises from the shocked stellar wind of the progenitor, heated by the outgoing shock wave, a mass-loss rate prior to the outburst of $\dot{M} = 3.6 \times 10^{-6} M_\odot \text{ yr}^{-1}$ is derived.

Also, based on ultra-deep ROSAT HRI observations of M101, X-ray sources are detected at the positions of both the type II SNe 1951H and 1970G (Sec. 5.1.). Using the HRI luminosity observed for SN 1970G 25 years after the outburst ($4.5 \times 10^{37} \text{ erg s}^{-1}$), a pre-outburst mass-loss rate of $\dot{M} = 2.0 \times 10^{-5} M_\odot \text{ yr}^{-1}$ is derived. This is the same mass-loss rate as inferred from radio data. The mass-loss rate of the progenitor of SN 1951H inferred from the HRI luminosity ($2.0 \times 10^{38} \text{ erg s}^{-1}$) 45 years after the outburst is $\dot{M} = 5.5 \times 10^{-5} M_\odot \text{ yr}^{-1}$. The PSPC spectrum of the X-ray source shows that the emission is rather soft (0.5 keV) and relatively unabsorbed ($N_H = 4 \times 10^{20} \text{ cm}^{-2}$).

The extended X-ray emission within the bulge regions can almost entirely be resolved into point sources for the galaxies M51 (95%) and M100 (96%; Sec. 6.). The overall contribution of point sources to the total emission of the galaxies is $\sim 1/3$, the rest being due to large amounts of hot gas from within the disk and the halo and to unresolved point-sources. For M83, the amount of residual X-ray emission within the bulge from either hot gas and unresolved point sources is 45%. Similarly, point sources account for half of the total X-ray emission of the galaxy.

Excluding known interlopers (i.e. foreground and background objects), the luminosity distributions of sources within the galaxies were compared (Sec. 4.5.). Interestingly, it was found that all galaxies, regardless of their morphological type, have similar source luminosity functions, being best described by a power-law $N(> L_x) = N_0 L_x^{-\alpha}$ with exponent ~ 1 . Both the number of superluminous X-ray sources with luminosities exceeding the Eddington limit of a $1.4 M_\odot$ accreting neutron star ($L_x > 1.3 \times 10^{38} \text{ erg s}^{-1}$) and the total X-ray luminosity, however, appear to be correlated with the star forming rate of the galaxy.

Contents

Zusammenfassung	iii
Synopsis	vii
Contents	x
1. Introduction	1
1.1. Aim of the Thesis	1
1.2. Röntgenstrahlung from the Universe	3
1.3. The ROSAT X-Ray Satellite	6
2. X-Ray Sources in Spiral Galaxies	9
2.1. Active Galactic Nuclei	13
2.2. X-ray Binaries	15
2.3. Supernovae	17
2.3.1. Type I Supernovae	17
2.3.2. Type II Supernovae	18
2.3.3. Supernova Remnants	19
2.3.4. γ -Ray Bursts and Hypernova Remnants	22
2.4. Hot Interstellar Medium	23
2.5. The Distribution of X-Ray Sources in the Bulge and Disk	24
3. Analysis Methods of ROSAT Observations of Galaxies	27
3.1. The Study of Point Sources	27
3.1.1. Detection of Point Sources	29
3.1.2. Spectral Emission Models	29
3.1.3. Timing Analysis of Point Sources	30
3.1.4. Analysis of a ROSAT PSPC ‘Last Light’ Observation	31
3.2. The Image Subtraction Technique	31
3.2.1. Principles of the Method	31
4. The X-Ray Source Population of Nearby Spiral Galaxies	33
4.1. Properties of the Analyzed Galaxies	33
4.2. General X-Ray Morphology of the Galaxies	36
4.3. Point Sources in M31	39
4.3.1. Bulge vs. Disk Population	41
4.3.2. Point Sources in a ‘Virtual’ M31 Observation at Larger Distance	47
4.4. Point Sources in Nearby Galaxies	50
4.4.1. HII Regions	56
4.4.2. Supernova Remnants	58
4.4.3. Superluminous X-Ray Sources	61
4.5. Luminosity Distribution of Point Sources in Nearby Galaxies	66

5. X-Ray Emission from Supernovae	71
5.1. X-Ray Emission from Supernovae 1970G and 1951H in M101	75
5.2. Evidence for X-Ray Emission from the Type Ic Supernova 1994I in M51	79
5.3. Discovery of X-Ray Emission from Supernova 1979C in M100	84
6. The Bulge Regions of Nearby Spiral Galaxies	91
7. Conclusions and Outlook	103
A. Source Lists	107
B. Source Identifications	115
C. Lightcurves	123
D. Colour Plates	129
E. Advance Publications	131
List of Figures	134
List of Tables	135
List of Boxes	137
Glossary	139
Bibliography	143
Acknowledgements	149
Curriculum Vitæ	151

1. INTRODUCTION

*“I’m astounded by people who want to ‘know’ the universe
when it’s hard enough to find your way around Chinatown.”*

Woody Allen

1.1. AIM OF THE THESIS

The aim of this project is to provide a comprehensive and deep insight into the high energetical astrophysical processes taking place within nearby spiral galaxies. Emphasis are the X-ray emission from the galaxies M31, M51, M83, M100 and M101, observed with the instruments onboard ROSAT. Based on deep ROSAT HRI and PSPC observations of the galaxies and on comparison to previous X-ray observations and data obtained in other wavelength bands, the following questions are addressed:

- ⇒ How big is the total output of nearby spiral galaxies in the (0.1–2.4 keV) X-ray band?
- ⇒ What fraction of the integrated X-ray emission is due to discrete X-ray sources?
(e.g. X-ray binaries, supernovae, supernova remnants, HII regions, etc.)
- ⇒ What are the physical properties of the discrete X-ray sources?
(e.g. luminosities, spectral type, temperature, variability, etc.)
- ⇒ Is there a difference in the X-ray source population for the galactic disk and bulge regions?
- ⇒ How much residual emission can be attributed to hot gas within the galactic disks and halos?
- ⇒ How large is the contribution of discrete X-ray sources to the extended bulge emission?
- ⇒ Is the residual extended bulge emission due to truly diffuse hot gas or unresolved point-sources?
- ⇒ What is the nature of superluminous X-ray sources (SLSs) found within the galaxies?
- ⇒ Are SLSs due to spatially unresolved X-ray sources or due to single, massive accreting objects?
- ⇒ How many of the detected X-ray sources are due to young supernovae and supernova remnants?
- ⇒ What are the physical properties of the supernova ejecta and the progenitors?
(e.g. temperature and density of the ejecta, mass-loss rates of the progenitors, etc.)
- ⇒ How do X-ray emitting supernovae evolve in time?
- ⇒ Is there a difference in the X-ray source luminosity functions for galaxies of different types?

In order to attack the above questions, source lists of X-ray sources detected within the galaxies are created. The short-term and long-term variability of the X-ray sources is studied by timing analysis of the individual ROSAT HRI observations and by comparison with previous X-ray observations. Where spectral information is available from the ROSAT PSPC, spectral parameters of the sources are derived (e.g. spectral type, temperature, absorption, etc.). All results are discussed and compared with already published data from previous X-ray observations.

The structure of the thesis is as follows: In Sec. 1., the history of X-ray astronomy will be briefly outlined and major discoveries and important results of past X-ray missions is presented (Sec. 1.2.). As most of the analyzed data presented in this work were obtained with ROSAT, the principles of the X-ray telescope and the detectors onboard ROSAT are described in Sec. 1.3. Key issues of our current understand regarding the X-ray emission from galaxies are explained in Sec. 2. Both the emission mechanism giving rise to X-rays and different source classes responsible for the X-ray emission are described. A detailed explanation of the analysis methods applied to the ROSAT data is given in Sec. 3. Within this section, the source detection strategies, timing analysis and a new method for the detection of discrete, variable X-ray sources within regions of enhanced diffuse emission are explained. Both the general X-ray morphology of the analyzed galaxies and the individual properties of detected X-ray sources found within the galaxies are studied in detail in Sec. 4. The discoveries of new X-ray emitting supernovae are presented in Sec. 5., together with an in-depths analysis of the results. The bulge regions of the nearby galaxies are subject to a thorough study in Sec. 6., being followed in Sec. 7. by a compilation of the most important results of this thesis and a brief outlook into the future of X-ray astronomy.

1.2. RÖNTGENSTRAHLUNG FROM THE UNIVERSE

Astronomical observations are performed by recording the electromagnetic radiation travelling from space to the Earth. The energy distribution of the radiation ranges from short gamma rays to long radio waves. The optical band, perceived by the human eye, represents only a minor fraction of the entire energy band (cf. Fig. 1.2.). The sensitivity of the human eye to radiation from the relatively small optical band is due only to the fact that only radiation from this band is transmitted by the Earth's atmosphere and can be used by the human eye to get information on the environment. Astrophysical processes, however, give also rise to characteristic radiation in different wavelength bands. Many important astronomical discoveries resulted from observations performed at wavelengths not visible to our eye. Examples of some of these observations are the discovery of the cosmic microwave background radiation (one of the most convincing evidence for the existence of the Big Bang), the discovery of pulsars through radio observations (proving theories postulating the existence of ultra-compact objects), the existence of large amounts of warm interstellar matter visible in the infrared or the identification of Galactic objects as close, mass-exchanging binary systems, observed in the X-ray band.

Whereas observations in the radio, microwave and infrared bands primarily give information on the cold universe, X-ray observations are mostly obtained from matter at high temperature. Characteristic X-rays in the range from 0.1 to 100 keV¹ are produced by gas heated to high temperature (millions of degree), high-energy particles with interaction with magnetic fields (synchrotron radiation) or photons (inverse Compton radiation). Hence, observations in the X-ray band are a particularly good diagnostical tool to study the high-energetic state of matter in the universe, e.g. mass-accretion onto a compact object like a neutron star or black hole, supernova explosions or hot gas heated to high temperatures within galaxies and clusters of galaxies.

Since the Earth's atmosphere is not transparent to X-rays (cf. Fig. 1.2.), all observations in this band must be performed with detectors above the Earth's atmosphere. Despite astronomy being one of the oldest science of mankind in general, X-ray astronomy in particular only became possible with the advent of rockets that could aloft detectors above the absorbing atmosphere. Early attempts with balloon techniques in the 1920s, placing detectors to an altitude of some dozen kilometres above most of the Earth's hydrogen, resulted in the first detection of energetic cosmic rays. However, the origin of this high-energetic radiation remained unclear and was disputed for many years due to the poor spatial resolution of the detectors. Improved follow-up balloon-borne experiments (most important of which were the photographic plates and Geiger-Müller counter experiments by Bruno B. Rossi (*1905, †1993) in the 1930s) revealed that most of the cosmic rays are produced in the Sun's corona and are reprocessed in the outer parts of the Earth's atmosphere. The high temperature of the solar corona (millions of degree) was also found to be the site where X-ray emission, recorded by balloon experiments in 1940s, is produced. However, other than the Sun, no cosmic X-ray source was detected with ballooning experiments till the 1960s. It was the development of rockets that finally pushed the door open to study the *invisible universe*.

One of the most important pioneers in the development of sounding rockets was undisputively Hermann Oberth (*1894, †1989; for his biography, cf. Barth 1991; Freeman 1993; Rauschenbach 1994). While still at high-school and later as a student, Oberth started with his theoretical work on two-stage liquid-fuel cosmic rockets that could overcome Earth's gravity and travel into space. As a physics school teacher and without funding, Oberth started with experiments proving his theories that the exhaust velocity of the combustion products from a rocket engine, consisting of either liquid oxygen and hydrogen or a mixture of alcohol and oxygen, made it possible to enter space. Oberth gradually developed into the world's prime expert in designing and building two-stage rockets that could climb to an altitude of some hundred kilometres above the ground and orbit around the Earth.

¹ In high-energy astrophysics, photon energies and temperatures are usually given in units of 'electron volts' (eV) or 'kilo electron volts' (keV). $E[\text{keV}] = k_B T[\text{K}]$. 1 keV hence corresponds to a temperature 1.16×10^7 K

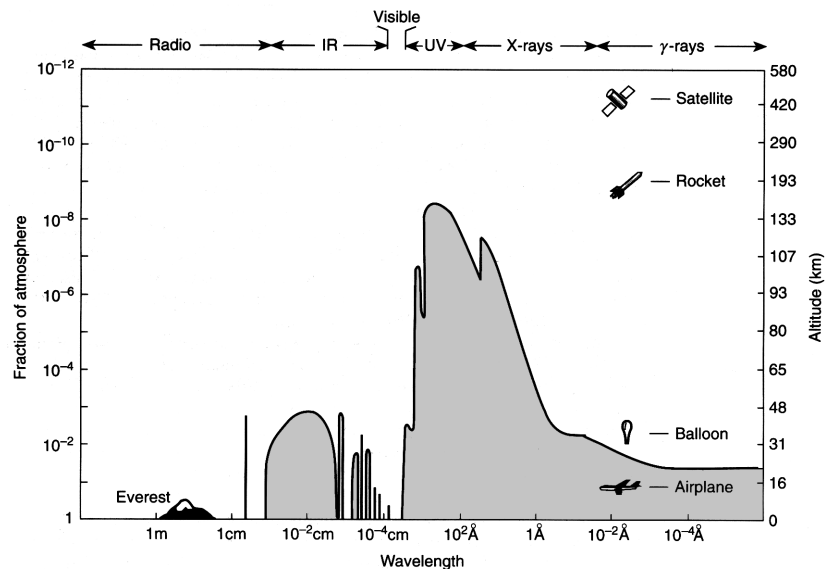


FIGURE 1.1. Transmission of electromagnetic radiation by the Earth's atmosphere. The solid line shows the altitude by which half the radiation from space has been absorbed (adopted from Charles & Seward 1995).

He compiled his detailed theoretical work on the construction of two versions of liquid fuel rockets into a book of 92 pages and submitted it as Ph.D. thesis to the Department of Astronomy at the University of Heidelberg in 1921. The thesis, however, was rejected by the astronomer Max Wolff, being considered as too speculative. In 1923, Oberth nonetheless published his book entitled '*Die Rakete zu den Planetenräumen*' ('The Rocket into Interplanetary Space') on his own expense after another discouraging phase of finding a publisher (Oberth 1923).

Detailed construction plans of two liquid fuel rocket models are presented, supplemented by numerous chapters about energetically best-suited trajectories for putting rockets into orbit, onboard navigation systems, biological effects of space travel on humans (including space-sickness), possible malfunctions of the rocket during the ascent, etc. Interestingly, already in this historically unprecedented and surprisingly detailed description of designing rockets – at a time when mankind had just entered the age of general aviation – Oberth speculates about the purpose of rockets and possible scientific payloads in the closing remarks of his book. Here, he already preempts a field of science, the space-borne and high-energy astronomy, that will be born more than three decades later (Oberth 1923):

Mit dem eben beschriebenen Apparat (= Rakete) lassen sich zunächst folgende Versuche und Beobachtungen ausführen: ...

c) Im Ätherraum können Fernrohre von jeder Größe benutzt werden, da die Sterne nicht flimmern. ...

d) Da der Himmel vollkommen dunkel ist, genügt ein Abblenden der Sonnenscheibe, um die Sonnennähe nach Belieben zu beobachten.

With the apparatus just described (= rocket), the following experiments and observations can just be conducted: ...

c) Over the air, telescopes of any aperture can be used because the stars do not twinkle. ...

d) Since the sky is completely dark, screening the Sun's disk is sufficient to observe the Sun's environment at will.

e) Gewisse Untersuchungen über strahlende Energie sind auf der Erde nicht möglich, da die Atmosphäre kurzwellige Lichtstrahlen verschluckt.

...

Gerade diese könnten leicht ... zu den interessantesten und weittragenden physikalisch-chemischen Entdeckungen führen.

f) Wir können feststellen, wie groß die strahlende Energie ist, die aus verschiedenen Gegenden des Himmels kommt. ... Es ist nicht ausgeschlossen, daß dabei z.T. ganz neuartige Erscheinungen (z.B. im Verhalten der Elektronen usw.) eintreten. Mindestens wäre es der Mühe wert, diesen Versuch zu machen.

e) Certain studies about the radiating energy are not possible from the earth because the atmosphere absorbs short-wave light rays.

...

Exactly those that might easily lead ... to the most far-reaching physical-chemical discoveries.

f) We can find out how much radiating energy is coming from different regions in the sky. ... It cannot be excluded that some new phenomena appear (e.g. about the behaviour of electrons etc.). It would at least be worth the effort to conduct these experiments.

First attempts with rocket-borne X-ray detectors were made in the US in 1946 using German A4 rockets (better known as V-2 rockets), developed by Oberth himself and his pupil Wernherr von Braun. Just weeks after the end of World War II, 300 box-cars were filled with V-2 rocket parts captured from Germany and sent to the White Sands Proving Ground to the US, together with the rockets scientists that had built and operated the rockets in Germany (however, much to his disappointment, Oberth was not selected to join this group). Using rocket-born Geiger-Müller counters in 1949, Herbert Friedman and collaborators succeeded in proving that the atmospheric X-rays recorded with earlier balloon experiments are of solar origin. However, despite numerous efforts, no other X-ray source apart from the Sun was detected.

The first discovery of an X-ray emitting extra-solar object by Giacconi et al. (1962) marks the actual birth of X-ray astronomy. The X-ray emitting object, named 'Sco X-1' denoting the first X-ray source in the constellation Scorpio, was later identified as a mass-accreting neutron star. Since this early discovery, mass-exchanging binary system have been identified as common high-energetic and high-luminosity phenomena in galaxies. Ever since, the rapid development of this young field has established X-ray astronomy as an indispensable part of multi-wavelength astronomy to study energetic astrophysical events not visible in other wavelength regimes.

Whereas the sensitivity of rocket-born X-ray detectors was very limited due to the short observation period based on the ballistic flight of the rockets (typically lasting for ~ 5 minutes) and the limited payload masses of a few kilograms only, dedicated X-ray satellites with sensitive imaging X-ray telescopes led to a subsequent breakthrough in the field of X-ray astronomy. The first X-ray satellite UHURU (US, 12 Dec 1970 – March 1973, energy range: 2–20 keV) was the first in a series of 'Small Astronomical Satellites' ('SAS-1', launched from the San Marco platform in Kenya and given the Swahili name for 'freedom' to mark the seventh anniversary of Kenya's independence). UHURU led to the detection of 339 X-ray sources while performing an all-sky survey. Highlights of this mission were the discovery of X-ray emission from hot gas filling clusters of galaxies and galactic pulsars emitting X-rays by accreting matter from an evolved companion star. Next followed a series of similar satellites in terms of scientific payloads: ANS ('Astronomische Nederlandse Satelliet', Dutch/US, 30 August 1974 – 14 June 1977, energy range: 0.1–30 keV), Ariel V (UK, 15 October 1974 – 14 March 1980, energy range: 0.3–40 keV), a series of OSO-satellites ('Orbiting Solar Observatories', US) designed to study the UV-, X-ray and cosmic ray emission from the Sun, Copernicus ('Orbiting Astronomical Observatory', OAO-3, US/UK, 21 August 1972 – late 1980, energy range: 0.5–10 keV) and the first of the 'High Energy Astronomical Observatories', HEAO-1 (US, 12 August 1977 – 9 January 1979, energy range: 0.2 keV–10 MeV). The second in this series, HEAO-2 (later renamed the 'EINSTEIN observatory', 12 November 1978 – April 1981, energy range: 0.2–4.5 keV), set a new

milestone by using instruments more sensitive and better in resolution by a factor of $\sim 1\,000$ compared to its predecessors. Major results from the successful EINSTEIN observatory were the discovery of pervasive X-ray emission from stars of all types and establishing supernova remnants (SNRs) as an important class of X-ray objects. Also, normal galaxies were unveiled to be an interesting new class of X-ray emitting objects with more than 200 EINSTEIN observations of galaxies. With the European EXOSAT observatory (European X-Ray Observatory Satellite, launched in 1983), the variability of strong X-ray sources could be continuously monitored for a period of four days, given the high eccentricity of the satellite's orbit. Due to the many interesting new astrophysical aspects disclosed by these X-ray missions and their limited capabilities on the other hand, the need for more powerful facilities arose. Although the EINSTEIN observatory reached a sensitivity and angular resolution far exceeding that of other X-ray missions, its observations only covered less than 1% of the entire sky. The wish for an all-sky survey with similar or better sensitivity and angular resolution, extending to photon energies below 1 keV, finally resulted in the proposal of a new X-ray mission, the German ROSAT X-Ray Satellite.

1.3. THE ROSAT X-RAY SATELLITE

The requirements for this new space-borne X-ray observatory, proposed by Joachim Trümper to the German Ministry of Science in 1975, were very ambitious and, from a technological point-of-view, extremely challenging: putting an X-ray satellite into an orbit of ~ 500 km altitude that is capable of an imaging all-sky survey in the soft (0.1–2.4 keV) X-ray band, while being significantly more sensitive than all X-ray missions before. As the proposed mission grew both in terms of mass, costs and complexity, partners from allied countries joined the ROSAT project in the 1980s. While astronomers from Leicester University, UK, contributed an ultraviolet camera (Wide Field Camera), piggyback mounted onto the satellite, the NASA agency supported the mission by building a modified version of the High Resolution Imager already used for the EINSTEIN mission. Also, NASA was to supply the launch vehicle (at that time a space shuttle was anticipated) in exchange for a large fraction of observation time. The joint German/UK/US effort, led by the Max-Planck-Institut für extraterrestrische Physik/Garching, was finally realized in the '*Röntgensatellit*' ROSAT (Trümper 1983), named in honour of Wilhelm Conrad Röntgen (*1845, †1923 in Munich), who won the Nobel Prize in Physics in 1901 for the discovery of a new kind of rays he denoted X-rays (in German: '*Röntgenstrahlung*'). After the Challenger disaster, ROSAT was extensively modified for a rocket launch and successfully put into an orbit of 580 km altitude with a Delta II rocket on June 1, 1990.

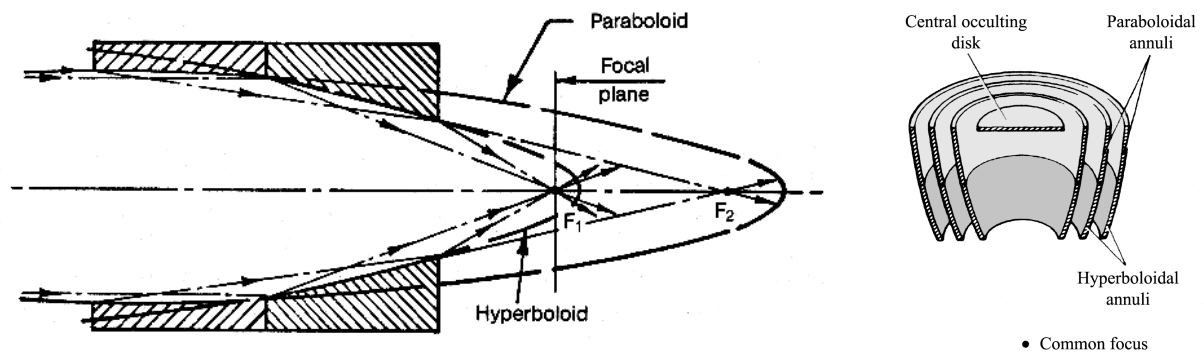


FIGURE 1.2. Schematic representation of a Wolter I X-ray telescope (left-hand panel; drawing by H. Wolter, reproduced from Karttunen et al. 1993) and a section through a nested grazing incident X-ray telescope with three mirror modules (right-hand panel; reproduced from Kitchin 1998).

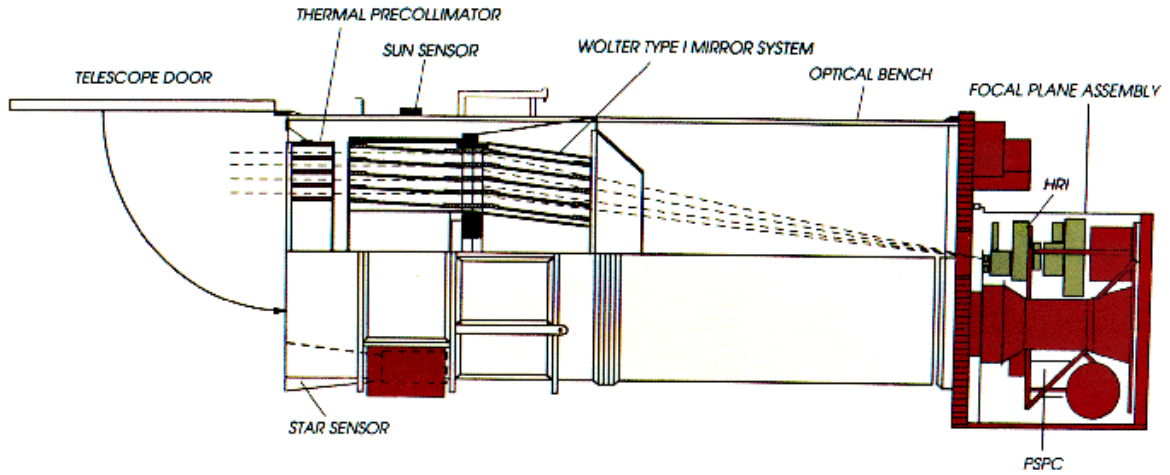


FIGURE 1.3. Schematic representation of the ROSAT X-ray telescope and the detector unit.

The ‘heart’ of the ROSAT satellite is a Wolter type I telescope with 0.84 m aperture, a focal length of 2.4 m, a geometrical collecting area of 1.14 m^2 and a maximum surface roughness of $< 5 \text{ \AA}^2$ (for a detailed technical description of the X-ray telescope, cf. Aschenbach 1988). The telescope is an assembly of four nested confocal mirror shells made of Zerodur, each of which is composed of one parabolic and one hyperbolic mirror segment. If X-rays meet the mirror almost parallel to its surface, they are reflected (‘grazing reflection’) and can be focused by a high-quality surface with a surface roughness small compared to the wavelength of the radiation. A parabolic mirror segment can hence be used as an X-ray telescope. In practise, parabolic mirrors show large aberration errors (‘coma’), which can be minimized by using a second, confocal hyperbolic mirror segment. This assembly is called a ‘Wolter I telescope’, originally proposed by H. Wolter for imaging X-ray microscopes (Wolter 1952). In order to increase the collecting area of the X-ray telescope, a number of mirror cones can be ‘nested’, i.e. one put inside the other. A schematic representation of a Wolter I X-ray telescope is given in Fig. 1.2.

Onboard ROSAT, two different detector units are mounted on a turret behind the mirror assembly and can be placed into the focus of the telescope: a High Resolution Imager (HRI) with $38'$ field-of-view and an angular resolution of $\sim 4''$, and two Position Sensitive Proportional Counters (PSPCs) with 2° field-of-view, an angular resolution of $\sim 25''$ and an energy resolution of 43% at 0.93 keV. A schematic representation of the ROSAT X-ray telescope and the detector units is given in Fig. 1.3, an illustration of the final flight configuration is given in Fig. 1.4.

The PSPC detectors represent multi-wire proportional counters, operated in a gas-flooded pressure chamber filled with 65% argon, 15% methane and 20% xenon (for a detailed technical description of the PSPC detectors, cf. Pfeiffermann et al. 1988). The entrance window is a 1μ thin polypropylene foil, mechanically supported by a rib structure. The energy resolution of the PSPC is defined by

$$\frac{\Delta E}{E} = \frac{0.43}{\sqrt{\frac{E[\text{keV}]}{0.93}}} . \quad (1.1)$$

With the XRT+PSPC configuration, spectral *and* spatial characteristics of X-ray sources can be studied in the 0.1–2.4 keV ROSAT band. During the ROSAT all-sky-survey, performed with the PSPC during the first half year (1990/91) of the ROSAT mission, the entire sky was mapped with a sensitivity of ~ 100 times better than with previous missions. Altogether, more than 150 000 X-ray sources were recorded, increasing the total number of known X-ray sources in the universe by

² $1 \text{ \AA} (\text{\AA ngstr\o m}) = 10^{-10} \text{ m}$

more than two orders of magnitude compared to all previous X-ray observatories. In $\sim 9\,000$ pointed observations, dedicated to selected targets during the following years of the ROSAT mission, spectral, spatial and timing characteristics of some 80 000 X-ray objects were studied in detail, resulting in more than 3 000 scientific publications.

The HRI instrument is comprised of two cascaded, z-stacked micro-channel plates (MCPs) based on the photo-effect with secondary electron multiplying and a crossed-grid signal readout system (for a detailed technical description of the HRI, cf. David et al. 1995). The XRT+HRI configuration reaches an angular resolution of $\lesssim 5''$, similar to the EINSTEIN mission, however, with a sensitivity a factor 3–4 better compared to the EINSTEIN HRI. Contrary to the PSPC, the HRI has no intrinsic energy resolution, its bandpass being cut-off at lower energies by the UV/ion filter and at high energies by the reflectivity of the XRT mirror. The gain on the detector is controlled by the voltage setting and the pulse height of the readout signal is converted to (un-calibrated) raw channels 0–15. Because the ROSAT HRI is a purely electronical device, the lifetime is not limited by the consumption of gas as in the case of the PSPC.

Although ROSAT was designed and built to achieve a lifetime of approximately two years, it continued to successfully operate for more than eight years. After the loss of the last star tracker, a chain of accidents regarding the operation of the satellite led to an irreversible damage of the HRI. The guest observer programme was hence to be terminated and a ‘last light’ campaign was initiated in December 1998. During the last days of ROSAT, the PSPC detector was activated again, not in operation for four years. With the XRT+PSPC configuration, valuable data could be obtained from targets of high scientific interest, e.g. comet C/1998 U5, GB 1428+421 (a radio-loud quasar), Nova LMC 1995, S 520 (a cluster of galaxies), the Active Galactic Nuclei 1ES 1927+654 and 1H 0707-495, the recently discovered supernova remnant G 266.3-1.2 and the supernovae SN 1987A (the ‘first light’ target of ROSAT) and SN 1979C, proposed by the author and collaborators (discussed in Sec. 5. and Sec. 5.3.). ROSAT was finally turned off on February 12, 1999, making it the most successful X-ray mission ever operated and leaving behind an enormous data archive utilized by $\sim 4\,000$ scientists from 26 countries to date.

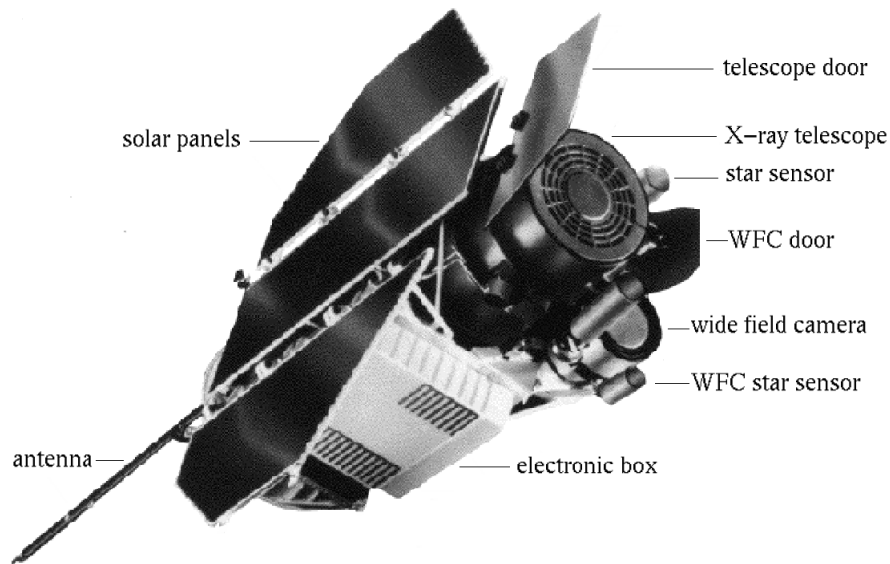


FIGURE 1.4. Illustration of the ROSAT flight configuration.

2. X-RAY SOURCES IN SPIRAL GALAXIES

*“The sun was shining on the sea,
Shining with all his might:
He did his very best to make
The billows smooth and bright –
And this was odd because it was
The middle of the night.”*

Lewis Carroll

Prior to the launch of the EINSTEIN mission, only four galaxies had been detected in X-rays: our Galaxy, and the local group galaxies M31, the Small Magellanic Cloud (SMC) and the Large Magellanic Cloud (LMC; see Helfand 1984 and references therein). The EINSTEIN observatory gave a wealth of information on the X-ray emission from normal galaxies with observations of ~ 500 galaxies. About half the observed galaxies (238) were found to be sites where significant X-ray emission is produced (see Fabbiano, Kim & Trinchieri 1992 and Kim, Fabbiano & Trinchieri 1992 for the EINSTEIN catalogue and spectra of galaxies). With its high sensitivity and angular resolution, combined with the spectral capabilities, the X-ray properties of the galaxies could be studied in detail. Normal galaxies of all morphological types showed to be extended X-ray sources with luminosities in the EINSTEIN 0.1–4.5 keV band in the range 10^{38} – 10^{42} erg s $^{-1}$. Although the X-ray band is a relatively small part of the electromagnetic spectrum and the X-ray output of the galaxies represents only a small fraction of the broadband output (cf. Fig. 1.2.), X-ray observations proved to be essential and uniquely suited to studying astrophysical processes elusive in other wavelength regimes. As will be explained in detail in the following sections, astrophysical processes giving rise to X-rays are related to the high-energetic phenomena associated with end-points of the stellar evolution (e.g. supernova explosions and remnants and accretion from compact objects such as white dwarfs, neutron stars and black holes) and the hot phase of the interstellar medium. Stars of all classes were also found to be X-ray emitters, albeit at a low level ($\lesssim 10^{33}$ erg s $^{-1}$). The X-ray to optical ratios measured in spiral galaxies, however, are significantly larger than those expected from a normal stellar population and the average X-ray spectra of galaxies are harder than that of stellar emission. Hence, as opposed to the optical, where the overall emission of a galaxy is dominated by stars, contributions from normal stars to the overall X-ray emission from galaxies is relatively small ($\lesssim 15\%$ for our Galaxy; Watson 1990).

Highlights of the EINSTEIN mission were the discovery of ‘plumes’ of hot gas ejected from the nuclei of starburst galaxies (e.g. M82, NGC 253, NGC 3628) and hot gaseous X-ray halos surrounding ellipticals and spirals. In most cases, a bright extended X-ray source was found at the center of the galaxy. Given the spatial resolution of the EINSTEIN observatory, the nuclear X-ray sources could only be spatially resolved in some very nearby local group galaxies (e.g. M31). Whereas the bright nuclear X-ray emission could be attributed to active galactic nuclei (AGN) in many systems, some galaxies also showed X-ray emission from starburst activity confined to the nucleus (e.g. the Galactic center region, M51, M82, M83, NGC 253, NGC 3628, NGC 6946 and IC 342). The spectra of these nuclear regions could be best described by the presence of a young stellar population and a shock-heated interstellar medium (soft emission) and a component from an X-ray binary population (hard emission). This issue

¹ 1 erg $\hat{=}$ 10^{-7} joule

is further discussed in Sec. 6. Also, a large number of individual X-ray sources was detected within the disks of nearby galaxies, dominated by X-ray binaries. About $\frac{1}{4}$ of the discrete sources could be attributed to X-ray emitting supernova remnants for the SMC (discussed in Sec. 2.3.3.), some of which contain a central pulsar left behind from the supernova explosion. Enigmatic super-Eddington sources were found to be associated with a number of nearby galaxies. Given the high luminosities (10^{38-39} erg s $^{-1}$), exceeding the Eddington limit for a $1M_{\odot}^2$ accreting object, their nature is still a matter of debate. New light will be shed on these ultra-luminous objects in Sec. 4.4.3., while the X-ray source population is discussed in more detail in Sec. 4. The overall luminosities of the galaxies (10^{38-42} erg s $^{-1}$) are linearly correlated with their emission in the optical B-band, linking the X-ray emission to the star formation rate (for a comprehensive review of EINSTEIN results on spirals, cf., e.g. Fabbiano 1989 and 1990).

During the ~ 8 year life-span of the ROSAT satellite, some 950 pointed X-ray observations were dedicated to normal galaxies (let alone an even higher number of pointings devoted to AGN). Not surprising, the galaxy studied in most detail was the neighbouring ‘Andromeda galaxy’ M31, which was covered by deep ROSAT PSPC (200 ks observation time) and HRI surveys (800 ks, corresponding to more than one week of continuous observation). An optical image of M31 and the same area as seen in X-rays with the ROSAT HRI is given in Figs. 2.1 and 2.2.

The enormous amount and high quality of the ROSAT data on galaxies led to a significantly deeper understanding of all aspects related to the X-ray emission from normal galaxies and the X-ray sources found therein. The PSPC spectra of some nearby spirals (e.g. NGC 253, NGC 3079, NGC 3628, NGC 4631) allowed us to assess different spectral components in the gaseous halos. The halos were found to consist of at least two components, i.e. a rather soft (0.2–0.4 keV) and a harder (0.7–0.9 keV) phase of the ISM, with indications of a third component at a very low temperature (e.g. NGC 4631 with ~ 0.05 keV; cf., e.g. Dahlem, Weaver & Heckman 1998; Vogler & Pietsch 1996). The element abundance of the hot diffuse gas was found to be compatible with near-solar metallicities. The wealth of data showed that the complex halo ISM was chemically processed through stellar evolution, implying that the constituents of the disk ISM take part in outflows via winds. One of the most important ROSAT findings was to establish young supernovae as a new class of X-ray emitting objects. With ROSAT, the interaction processes of type II supernova shock waves with the ambient circumstellar medium could be studied in detail. This work will significantly add to the study of the X-ray interaction region from type II supernovae (see Sec. 5.1. and 5.3.). The stringent ROSAT upper limits for type I supernovae were used to demonstrate the lack of dense circumstellar matter. Again, this work will shed new light on the X-ray production of type I supernovae and on physical parameters of the ambient ISM (see Sec. 5.2.). The most extensively studied galaxy in the X-ray regime is the local group spiral M31 (distance 690 kpc). With ROSAT PSPC and HRI observations, the whole extent of the galaxy was covered with a homogeneous mosaic-like pattern of pointings totalling in more than 200 ks exposure for each region of the galaxy (Primini, Forman & Jones 1993; Supper et al. 1997). More than 500 X-ray sources were found in the galaxy down to a limiting luminosity of some 10^{35} erg s $^{-1}$. The luminosity distribution of all X-ray sources found in the galaxy follows a power-law, identical with the distribution of sources associated with globular clusters. This was interpreted as being indicative of most of the sources being due to low-mass X-ray binaries (LMXB). Because the published PSPC data could not spatially resolve the bulge region of M31, the analysis of the high-resolution HRI data presented in Sec. 4.3. will give further information as to the luminosity distribution of bulge and disk sources in M31. Earlier claims based on EINSTEIN data that the globular cluster distribution function significantly differs from that of our Galaxy, albeit being of the same morphological type Sb, could be ruled out with the ROSAT data (Supper et al. 1997). Both in M31 and the Magellanic Clouds sources with an exceptionally soft X-ray spectrum with $kT < 1$ keV were discovered with ROSAT. Contrary to accreting binaries, which release energy from gravitational

² $1M_{\odot}$ (solar mass) = 1.989×10^{30} kg

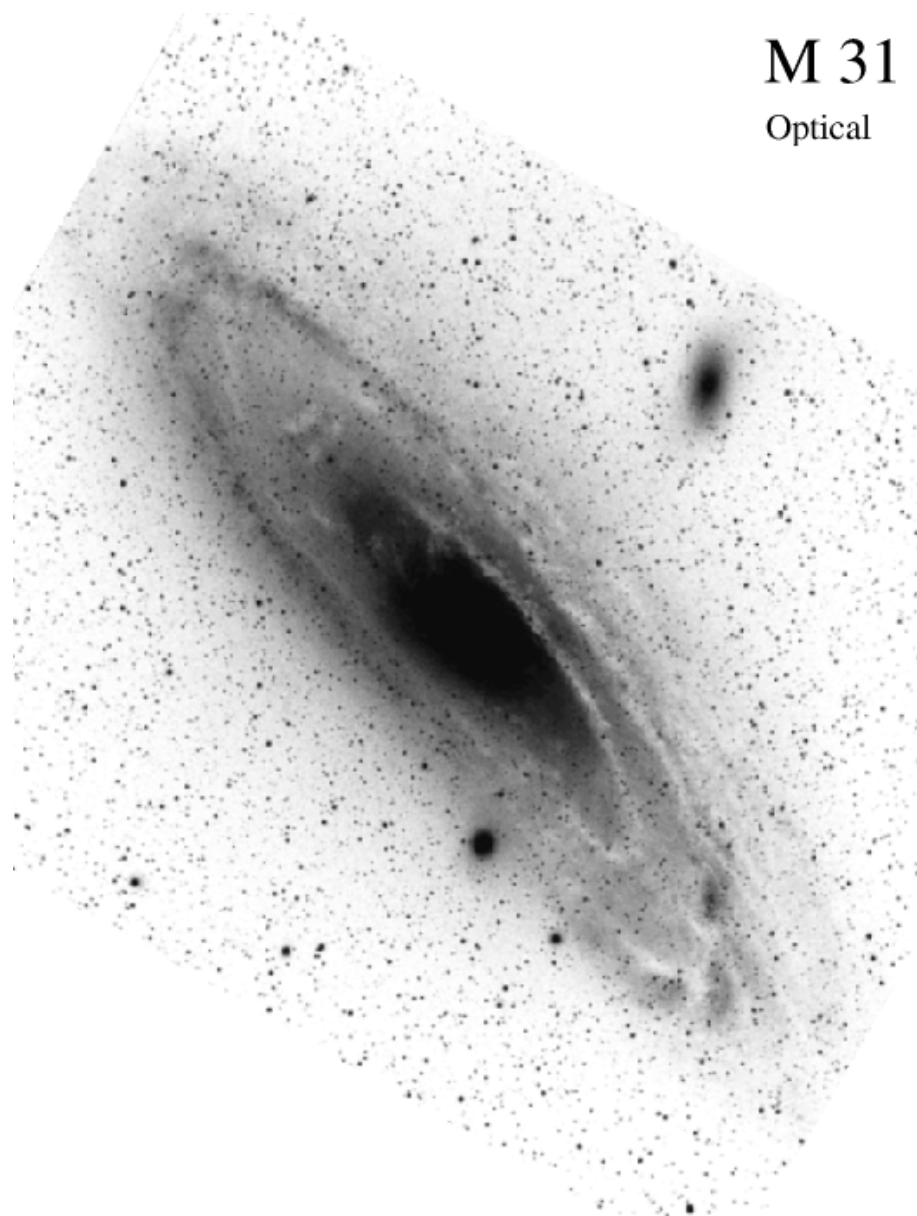


FIGURE 2.1. Optical image of the 'Andromeda galaxy' M31 in negative representation (from the Astronomy Digital Image Library/ADIL).

potential of accreted material, these 'supersoft X-ray sources' (SSS) were found to be white dwarfs with a steady nuclear burning on their surface due to a sufficiently high and steady accretion rate from a companion star (cf., e.g. Greiner, Hasinger & Kahabka 1991).

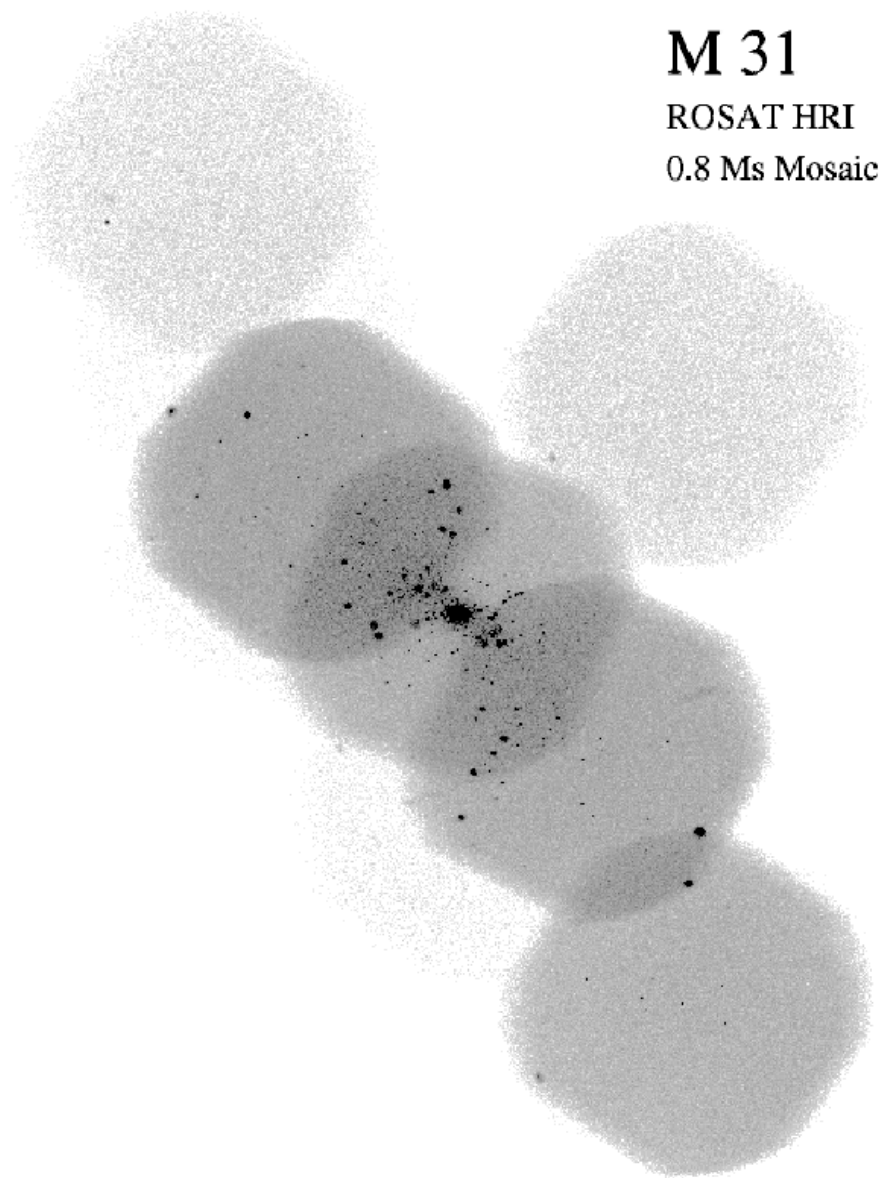


FIGURE 2.2. ROSAT HRI image of the 'Andromeda galaxy' M31. The composite image represents the deepest X-ray observation of a galaxy ever performed, with a total exposure times of 0.8 Msec (corresponding to more than one week of continuous observation). The pixel size of the image is $10''$. Same scale as Fig. 2.1.

2.1. ACTIVE GALACTIC NUCLEI

This thesis concentrates on *normal* spiral galaxies. In normal spirals, the absence of a bright active nucleus is characteristic. The broadband luminosities are hence not dominated by a bright nucleus typical for a variety of AGN classes. However, since a large fraction of normal spirals also host mildly active AGN, the concept of active galactic nuclei will be briefly introduced.

The term ‘AGN’ is generally used for many sub-sets of AGN classes, e.g. Seyfert galaxies (Sy 1 and Sy 2), quasars or QSOs (quasi-stellar objects), Narrow/Broad Line Radio Galaxies (NLRG/BLRG), LINERS (Low Ionization Nuclear Emission Regions), Fanaroff-Riley radio galaxies (FR I and FR II), BL Lac objects (Broad-Line Emission Galaxies), etc. They all have in common that the emission is predominantly produced in a rather small region, extending to only a few light years, at the position of the nucleus of the galaxy (hence the term ‘active galactic *nucleus*’). In the X-ray domain, AGN have luminosities ranging from 10^{39} to 10^{46} erg s $^{-1}$, whereas normal galaxies attain maximum X-ray luminosities of some 10^{41} erg s $^{-1}$. In some cases, huge amplitude variations in the X-ray flux (factors 10–80) on timescales of days were observed. (e.g. the Sy 1 galaxy NGC 5905; Komossa & Bade 1999)

From a phenomenological point of view, AGN are generally classified as ‘radio-loud’ ($f_{5\text{GHz}}/f_B \geq 10$, representing 15%–20% of all optically-selected AGN) and ‘radio-quiet’, and are further sub-classified based on their emission line strengths and widths (broad/narrow line radio galaxies etc.) The diversity of observed AGN properties, however, just seems to be different facets of one underlying basic phenomenon: the existence of a massive black hole (10^6 – 10^9 M_\odot) at the center of the galaxy, which energetically dominates the nucleus. Due to the high mass of the black hole at the nucleus and the high density of matter in the nuclear regions, matter is accreted onto the black hole. Typical accretion rates are 1–100 M_\odot yr $^{-1}$. The angular momentum of the infalling material leads to the formation of a flattened accretion disk. The accretion disk is heated by viscous friction, magnetic fields and turbulence. Observed high bolometric luminosities can be explained by conversion of gravitational energy of matter into non-thermal radiation. Non-thermal processes are synchrotron emission from energetic electrons and inverse Compton radiation (collision between low-energy photons and relativistic electrons). The non-thermal emission gives rise to the characteristic power-law spectrum observed in the X-ray band with a photon index of $\Gamma = 1$ –2. Also, an excess of X-ray emission at low photon energies below 0.4 keV with respect to the overall power-law spectrum (‘soft X-ray excess’), extending to the blue band in the optical (‘blue bump’), can be explained by a superposition of the black body spectra of regions at different temperatures within the accretion disk. Contrary, normal galaxies show thermal X-ray spectra for their nuclear regions due to thermal bremsstrahlung from hot gas. The central black hole is further surrounded by a thick and dusty torus (or warped disk), sometimes obscuring a direct view onto the nucleus. Broad emission lines (BLR) are produced in clouds located 2 – 20×10^{16} cm above the disk. Narrow line emission regions are observed from clouds much further away from the nucleus (10^{18} – 10^{20} cm). The hot corona may be the site where hard X-ray continuum emission is produced. Relativistic radio-jets emanating from the nucleus have been detected on scales from 10^{17} to 10^{24} cm, a factor of 10 larger than the largest galaxies. Depending on the direction of the line-of-sight with respect to the orientation of the disk, torus and the jet, AGN with different properties are observed. All different AGN classes, however, can be explained by one unified AGN model (cf. Urry & Padovani 1995).

It is difficult and, to some extent, arbitrary to distinguish between normal and active galaxies, since many galaxies are believed to host a black hole at the position of their kinetical center. If a normal galaxy hosts a mildly active nucleus, i.e. a black hole with a rather small accretion rate, a galaxy at a transition between normal and active is observed. From the sample of galaxies presented in this work, only M51 (classified as LINER or Sy 2.5 galaxy) represents such a galaxy. Whereas the galaxies have overall properties typical of normal galaxies, their nuclei show some broadband activity and their X-ray spectra are best described by a power-law. This activity will be subject to further discussion and comparison to other normal spirals in Sec. 6.

BOX 1. X-RAY EMISSION FROM ACCRETION

The most effective process for liberating large amounts of radiation is accretion. A compact object of mass M_* and radius R_* accreting material at a rate $\dot{M} = dM/dt$ will release its gravitational energy, E_{acc} , almost entirely in the form of radiation with luminosity, L :

$$L = E_{\text{acc}} = \frac{GM_*\dot{M}}{R_*}, \quad (2.1)$$

where G is the gravitational constant ($G = 6.68 \times 10^{-11} \text{ m}^3 \text{ s}^{-2} \text{ kg}^{-1}$). For a compact object of $1M_\odot$, a small amount of accreted material of $10^{-8} M_\odot \text{ yr}^{-1}$ is sufficient to produce a luminosity of $10^{38} \text{ erg s}^{-1}$, typical for the brightest X-ray emitting objects within our Galaxy. The effectivity in releasing radiation from accretion is determined by the ‘compactness’ of the object, expressed by the term $(M/R)_*$. At a given compactness, the liberated radiation only depends on the rate of accretion, \dot{M} . Since the equation above according to Einstein’s formula $E = mc^2$ can be expressed as

$$L = E_{\text{acc}} = \eta \dot{M}c^2, \quad (2.2)$$

with $\eta = G (M/R)_* c^{-2}$ being its effectivity. The effectivity η for compact objects is 0.1 for neutron stars, 0.06–0.42 for black holes and 0.001 for white dwarfs, whereas the efficiency of transforming energy from thermonuclear fusion of hydrogen to helium into radiation is ~ 0.0007 .

2.2. X-RAY BINARIES

The first object other than the Sun discovered in X-rays was Sco X-1 (Giacconi et al. 1962; see Sec. 1.2.). By the time of the discovery in the 1960s, no X-ray emission process was known capable of producing such a high X-ray flux. Also, optical identification of Sco X-1 turned-out to be very difficult since the optical counterpart was found to be a faint (~ 14 th magnitude) star in a rather crowded region of the sky. With subsequent rocket-born X-ray detectors and during the first few months of the UHURU mission, a number of these enigmatic X-ray sources were detected. The regular pulsations observed from SMC X-1 and Cen X-3 with the UHURU satellite, together with periodic eclipses revealed that the X-ray sources are due to rapidly spinning compact objects in a binary system. Since a white dwarf could not survive the centrifugal forces associated with the observed rapid spin periods (e.g. 0.7 sec for SMC X-1 and 1.2 sec for Her X-1; Lucke et al. 1976, Tananbaum et al. 1972), the compact object could only be either a neutron star or a black hole. Since these objects were exclusively X-ray selected with their optical counterparts difficult to detect, these mass-accreting objects was given the name '*X-ray binaries*' (for an extensive review of the multiwavelength properties of X-ray binaries, cf., e.g. Lewin, van Paradijs & van der Heuvel 1995).

The large amount of X-rays produced in X-ray binaries is due to conversion of gravitational energy from accreted matter into radiation by a mass-exchange from a companion star onto the compact object. The basic source of energy is hence gravity (cf. Box. 1). Mass-transfer from the companion onto the compact object occurs when the evolved companion fills its Roche lobe and mass can flow through the Lagrange point L_1 . The infalling matter will form a rotating accretion disk around the compact object due to its angular momentum. From the accretion disk, the matter gradually spirals in onto the compact object and X-rays are produced. Alternatively, in a binary system containing a compact object and a massive star with a strong stellar wind, material can be accreted directly from the stellar wind. The emission properties are determined by a few parameters, i.e. the mass of the central object, the accretion rate, the strength and geometry of the magnetic field (in the case of a neutron star or a white dwarf) and the geometry of the accretion flow (disk vs. wind accretion). Dependent on the mass of the companion, X-ray binaries are classified as *low mass X-ray binaries* (LMXBs; $M < 1 M_\odot$) or *high mass X-ray binaries* (HMXBs; $M > 10 M_\odot$). In an LMXB system, the companion is evolved and later than type A, or even a white dwarf. Since late type stars do not have strong winds, the accretion onto the compact object can only occur via Roche lobe overflow. In an HMXB system, the companion is a young ($< 10^7$ yrs) O or B star. Since OB stars have significant winds with mass-loss rates between $10^{-6} - 10^{-10} M_\odot \text{ yr}^{-1}$, a neutron star or black hole in a close orbit can capture a large fraction of the wind. The accretion of the wind onto the compact object powers the X-ray emission. Mass-accretion can also occur in HMXBs via Roche lobe overflow, however, due to the high mass of the companion, the accretion flow will be rather unstable. In case the accreting object is a neutron star with a strong magnetic field, the accreted matter will funnel onto the magnetic poles of the neutron star. If the rotation axis and the direction of the magnetic field are misaligned, X-ray pulsations can be observed if the beamed emission from the magnetic poles rotates through the line-of-sight of the observer.

Some X-ray binaries are also observed to be *transient*, i.e. they flare-up in a rather short period (\sim hours to days) and disappear again some weeks after. Probably all transients are recurrent, i.e. they exhibit repeated outbursts. The intervals between quasi-periodic or irregular outbursts can range as far as from less than a month up to tens of years or more. At the peak of the outburst, X-ray luminosities are typically $10^{37} - 10^{38} \text{ erg s}^{-1}$, but can be as high as $10^{39} \text{ erg s}^{-1}$ in some cases. Transient X-ray sources appear to be associated with either LMXBs (late-type companions), having rather soft X-ray spectra, or HMXBs showing rather hard spectra. The optical counterparts of LMXB transients are typically $\sim 10^2$ times brighter near transient maximum than in quiescence, which facilitates the search for them. Optical brightening during outburst is absent or mild for most HMXB transients. The outburst of the source itself is due to a sudden rise in the accretion rate. However, the mechanism responsible for the change of mass accretion rate is still a matter of debate (e.g. rapid mass-loss of the

donor, thermal or tidal disk instabilities, irradiation-induced instabilities, etc.). Despite X-ray binaries being the most luminous isolated X-ray sources in general, the Eddington limit poses an upper limit to the X-ray luminosity of $1.4 \times 10^{38} \left(\frac{M_\star}{M_\odot}\right) \text{ erg s}^{-1}$ for steady accretion. This is because with increasing luminosity, the radiation pressure limits the accretion rate of matter falling onto the compact object (cf. Box 2).

It should be noted that from low-quality X-ray data alone, it is very difficult to determine whether an X-ray binary is an LMXB or HMXB system. An unambiguous classification can only be made if their optical counterparts, orbital and spin periods and/or X-ray spectra are well known.

BOX 2. THE EDDINGTON LIMIT

Scattering of radiation exerts a pressure on the scattered material. Despite this ‘radiation pressure’ being a very small effect, it plays an important role in the emission of compact accreting objects. Every photon absorbed or scattered by an accreted ion accelerates the ion. The radiation acceleration on the infalling material can be expressed by

$$g_{\text{rad}} = \frac{1}{c} \int_0^\infty \underbrace{(\kappa_\nu + \sigma_\nu)}_{k_\nu} \times \pi f_\nu d\nu, \quad (2.3)$$

where k_ν is the effective cross-section of the ion. For light elements, the opacity of the accreted material is dominated by the Thomson cross-section for electrons $\sigma_T = (8\pi/3)r_e^2 = 6.65 \times 10^{-25} \text{ cm}^2$. Since the absorption cross-section can be even higher for heavier elements and additional acceleration processes like photo-ionization might occur (observed as absorption edges in the spectra), the Thomson cross-section represents a lower limit only. Since the cross-section for Thomson scattering is independent of the photon energy, the radiation acceleration can be re-written as

$$g_{\text{rad}} = \frac{\sigma_T}{c} \int_0^\infty \pi f_\nu d\nu = \frac{\sigma_T}{c} \pi f = \frac{\sigma_T}{c} \sigma T_{\text{eff}}^4 \quad (2.4)$$

by applying the Stephan Boltzmann law $F^+ = 4\pi f = \sigma T_{\text{eff}}^4$ with σ being the radiation constant ($\sigma = \frac{2\pi^5 k^4}{15c^2 h^3} = 5.67 \times 10^{-5} \text{ erg s}^{-1} \text{ cm}^{-2} \text{ K}^{-4}$). For accreting objects with steady emission, the radiation acceleration must balance the gravitational acceleration:

$$g_{\text{grav}} = \frac{GM_\star}{R_\star^2} \gtrsim g_{\text{rad}} \approx \frac{\sigma_T}{c} \sigma T_{\text{eff}}^4 \quad (2.5)$$

The maximum luminosity a steadily accreting object can attain is hence

$$L_E = 4\pi R_\star^2 \times \sigma T_{\text{eff}}^4 \quad (2.6)$$

It is called the Eddington luminosity and can be re-arranged as

$$L_E = \frac{GM_\star 4\pi c}{\sigma_T} = \frac{GM_\odot 4\pi c}{\sigma_T} \left(\frac{M_\star}{M_\odot}\right) = 1.4 \times 10^{38} \left(\frac{M_\star}{M_\odot}\right) \text{ erg s}^{-1}. \quad (2.7)$$

A neutron star of mass $1.4 M_\odot$ can hence not produce a *steady* luminosity greater than $2 \times 10^{38} \text{ erg s}^{-1}$. If the accretion, however, is non-spherical or beaming effects and jet-formation occur, accreting magnetized neutron stars and massive black holes can attain luminosities above the Eddington limit. Some of these observed ‘Super-Eddington’ or superluminous X-ray sources (SLSs) will be discussed in Sec. 4.4.3.

2.3. SUPERNOVAE

Apart from the Big Bang, the disintegration of massive stars into supernova (hereafter: SN) explosions are the energetically most violent short-lived phenomena in the universe. During the supernova explosion, the gravitational binding energy of the entire star is released within a few seconds, liberating a few 10^{52} erg s^{-1} . The largest fraction of the binding energy is transported into space by neutrinos ($\sim 99\%$) and the ejected shell ($\sim 1\%$), whereas radiation released during the SN explosion only accounts for $\sim 0.01\%$ of the total liberated energy. Nonetheless, SNe are spectacular events in the optical band, sometimes brighter than an entire galaxy over periods of weeks. Since heavy elements are synthesised during the explosion, the expanding shell plays an important role in the chemical evolution of the universe. In fact, all heavy elements (e.g. silicon and iron) on Earth and in our own body were produced during consecutive SN explosions and spread into the interstellar medium, from which planets and stars formed. Also, SNe are vital in the formation of stars and planets, since the expanding SN blast wave can trigger the collapse of nearby molecular clouds into dense clumps of matter. During collapse of a molecular cloud, gravitational potential energy is released and transformed into thermal energy of the gas into radiation. After the end of the dynamical collapse, the gas has reached a temperature of 10^5 K and the gas is completely ionized. A protostar has formed that will evolve on the thermal timescale and most of its mass will be radiative. At that time, the central temperature will be large enough for thermonuclear fusion to set in and a new star is born that will shine for several million years till it eventually explodes again as SN, if massive enough.

2.3.1. TYPE I SUPERNOVAE

Based on their optical spectra, SNe are classified into two distinct classes: type I and type II. The former is further subdivided into classes Ia, Ib and Ic, all of which have in common as to show no hydrogen emission lines in their spectra.

- Type Ia SNe are the result of the deflagration or detonation of a white dwarf, located in a binary system. When the secondary star (companion) has filled its Roche lobe, mass transfer onto the surface of the white dwarf will occur, leading to an accumulation of matter on the surface of the white dwarf. If the white dwarf exceeds the Chandrasekar mass, the temperature and pressure of the underlying hydrogen layer will reach the thermonuclear ignition point. The white dwarf will be disrupted by either deflagration (subsonic speed of the ignition front outward through the layers of the white dwarfs) or detonation (supersonic speed of the ignition front). Since the white dwarf is disrupted completely, no stellar remnant is created.

- Type Ib SN originate from the core collapse of a massive star at the end of its evolution, when the hydrogen and helium fuel is exhausted. The lack of burning material leads to a sudden halt of the thermonuclear reactor at the core of the star, causing a sudden implosion of the outer layers due to the lack of radiation pressure from photons emitted during thermonuclear burning. The subsequent gravitational collapse of the massive star produces a sudden increase of both temperature and pressure at the core, leading to the final ignition of heavier elements from material of the outer shells falling into the core. This explosion is energetical enough as to almost completely disrupt the massive star, producing the outgoing supersonic SN shock front and leaving behind a neutron star, often observed at the center of old supernova remnants (SNRs).

- The progenitor of type Ic SNe is located in a close binary system and loses its outer envelopes, leaving a bare C+O star, which explodes when its iron core collapses. Three evolutionary paths were suggested by Nomoto et al. (1994):

- A: The binary system consists of two stars of masses $M_1 \approx (11-16) M_\odot$ and $M_2 \approx (1-4) M_\odot$. Highly non-conservative mass-transfer $1 \rightarrow 2$ leads to the formation of a *common envelope*. The subsequent spiral-in of matter will form either one merged star or two stars with a helium star of $M_1 \approx (2.2-4) M_\odot$ and a main-sequence star with $M_2 \approx (1-4) M_\odot$, circling in a closer orbit. A second non-conservative mass-transfer $1 \rightarrow 2$ leads to the formation of a bare C+O star,

which loses its outer helium envelope to star 2, and a low-mass main-sequence companion. At the iron core collapse, the SN of type Ic is formed.

- B: In path B, a massive star $M_1 > 11 M_\odot$ collapses, leaving behind a neutron star. The mass-transfer prior to this is *conservative* due to the relative small mass ratio. Star 2 hence becomes massive ($> 11 M_\odot$) and fills its Roche lobe. Mass-transfer from 2 \rightarrow 1 leads to the formation of a compact star $M_1 \approx 1.4 M_\odot$ and a helium star $M_2 \approx (2.2-4) M_\odot$, circling in a close orbit. The helium star (2) expands and again fills its Roche lobe, undergoing a *non-conservative mass-transfer* and leaving a C+O star (2) and a neutron star.
- C: In path C, star 1 has an initial mass of $M_1 \approx (6-11) M_\odot$ and evolves to become a C+O or O-Ne-Mg white dwarf. Due to almost similar masses, the mass-transfer is conservative. The evolution is identical to path B, except that star 1 will eventually become a white dwarf instead of a neutron star.

The resultant C+O star formed through one of the proposed paths will finally explode as a type Ic SN due to photodisintegration of Fe, and a strong shock wave is generated.

The proposed models should account for the presence of circumstellar matter expected to form from a remnant of a helium-rich common envelope as well as from stellar wind material from the C+O star. Hot plasma from the collision between the ejecta and circumstellar matter is formed. The plasma should be rich in heavy elements, mostly C+O, which may effect X-ray emission and cooling properties. Thermal X-ray emission is expected from the hot gas in the interaction region (cf. Chevalier 1984a). It should be noted, however, that due to the small amount of circumstellar material, only weak X-ray emission is expected from type I SNe. As of today, *no* X-ray emitting type I SNe had been detected, despite numerous attempts. In Sec. 5.2., however, the first evidence for X-ray emission from a type Ic supernova (SN 1994I in M51) will be presented.

2.3.2. TYPE II SUPERNOVAE

Type II SNe show hydrogen emission lines in their optical spectra. The SNe are formed during the core collapse of massive stars and the subsequent ejection of the envelopes. The core collapse itself starts when the hydrogen and helium fuel at the core of a massive star is exhausted. Due to a lack of radiation pressure from the thermonuclear burning at the core, overlaying layers can fall onto the core, heating the core as gravitational energy is converted into thermal energy. The rise in temperature and pressure initiates a prompt thermonuclear burning of hydrogen and helium from outer layers and heavy material produced during the whole lifespan of the massive star. As a result, the shell is ejected into space and the collapsed core is expected to leave a compact remnant (white dwarf or neutron star). Because massive stars emit strong stellar winds during the phase of steady thermonuclear burning, the type II SNe are expected to be surrounded by dense circumstellar material. ‘Prompt’ X-ray emission is produced as a high-temperature flash associated with the SN shock wave breaking through the stellar surface. ‘Late’ X-ray emission ($\gtrsim 100$ days) is produced when either the hot expanding shell becomes optically thin to X-rays or when the outgoing wave runs into the circumstellar material, deposited by the progenitor star prior to the explosion. This interaction produces a fast shock wave in the circumstellar wind and a reverse shock wave into the outer supernova ejecta. The shocked region is the site for high-energy emission and particles with observational signatures of radio, late-time optical, ultraviolet, and, most importantly, thermal X-ray emission. For a smooth, spherically symmetric supernova and circumstellar medium, the interaction region can be calculated in detail. For a circumstellar medium with an r^{-2} density profile and typical supernova parameters, two characteristic emission regions are produced. The forward shock wave in the circumstellar wind at $\sim 10^4 \text{ km s}^{-1}$ produces gas with $T \sim 10^9 \text{ K}$. The reverse shock wave in the supernova ejecta at $\sim 10^3 \text{ km s}^{-1}$ produces gas with $T \sim 10^7 \text{ K}$. The reverse shock is formed where the freely expanding supernova ejecta catch up with the decelerating interaction region. The gas at the reverse shock front is denser

and typically dominates the luminosity. At early times the reverse shock front is radiative and a dense, cool ($T < 10^4$ K) shell can build up downstream from the radiating region (Chevalier & Fransson 1994). The dense shell can absorb X-rays from the reverse shock region and reprocess them to lower energies.

This scenario was supported by observations of SN 1993J with ROSAT (Zimmermann et al. 1994a, 1996a,b) and with ASCA (Kohmura et al. 1994). The early X-ray spectrum was hard, with $T \sim 10^9$ K. At day ~ 200 , a softer component with $T \sim 10^7$ K dominated. The emergence of the softer spectrum could be attributed to the decreased absorption by a cool shell (Fransson, Lundqvist & Chevalier 1996). The other X-ray supernovae have not been well observed at such early times. Where spectral information is available, it is compatible with emission from the reverse shock front. However, there is another possibility for this component. Type IIn supernovae, some of which are especially X-ray luminous, have narrow lines in their optical spectra (Filippenko 1997). These lines are likely to be formed by radiative shock fronts moving into circumstellar clumps. For clumps of the appropriate density, the softer X-ray emission can be produced by ‘forward’ shock fronts moving into the clumps (Chugai 1993). The main shock front passes around the clumps at high velocity. There is a clear difference between these possibilities for the X-ray emission. The reverse shock gas would be characterized by velocities $\sim 10^4$ km s $^{-1}$ and the shocked clump gas by velocities $\sim 10^3$ km s $^{-1}$. Houck et al. (1998) attempted to determine the line widths in X-ray spectra of SN 1986J, but failed to distinguish between the possibilities with the available ASCA observations.

The interaction of a type II SN with circumstellar gas hence gives radiation predominantly in the X-ray range. Analysis of this emission can yield the amount of the pre-supernova mass loss rate as well as the density and velocity profile including element abundances of the supernova ejecta. X-ray observations of SNe are therefore an important diagnostic tool to probe the interaction of the outgoing shock wave with the circumstellar material.

2.3.3. SUPERNOVA REMNANTS

No information is available on the X-ray emission from supernova remnants at an intermediate age between a few dozen and some hundred years. However, more than 100 remnants within our Galaxy are known from the ROSAT all-sky-survey, with ages ranging from several hundred to ten thousands of years (for a review of Galactic SNR, cf. Aschenbach 1996). In the LMC local group galaxy, an additional ~ 30 X-ray emitting SNRs were discovered (cf., e.g. Williams et al. 1997, 1999b, 1999c). Since X-ray luminosities of SNRs typically vary between 10^{35} and 10^{37} erg s $^{-1}$, they are at or just below the detection threshold for observations of more distant galaxies and difficult to detect.

The evolution of a SNR can be best described in terms of three phases: the first phase in the evolution of a SNR is a *free expansion* of the SN ejecta into the ambient ISM. If the total ejected mass is $1M_{\odot}$, the initial velocity $15\,000$ km s $^{-1}$ and the density of the surrounding medium 0.3 atoms cm $^{-3}$, parameters typical for SNRs and the ambient ISM, the shock wave can expand freely for ~ 200 years, until the swept-up material reaches a mass similar to the ejecta. X-ray and radio emission are produced by shock-heated material at temperature 10^7 – 10^8 K. In due evolution, the propagating shock slows down and the remnant enters the phase of *adiabatic expansion*. During this phase, the mass of the swept-up material is comparable to the mass of the initial shock front and the remnant adiabatically cools as it sweeps up the cold ISM. This phase is known as the ‘blast wave’ or ‘Sedov-Taylor phase’. While the material behind the shock continues to cool and electrons start to combine with carbon and oxygen atoms, most of the internal energy is radiated away. This phase of evolution, lasting $\sim 10^5$ years, is hence called the *radiative phase*. As the X-ray morphology of most SNR in the adiabatic and radiative phase is very patchy, its spectrum being mostly thermal, the observations favour models of evaporating clouds from within the SNR shell.

In general, the X-ray emission from SNRs is generated by different mechanisms: Most of the observed emission is thermal line emission from the forward and reverse shock. These SNRs appear as

shell-like remnants, with some limb brightening and hot spots within the interaction region. Thermal bremsstrahlung spectra are observed from radiative cooling of hot material from behind the shock (irregular or center-filled SNR). Non-thermal X-ray emission is produced by synchrotron emission associated with the shock interaction, as the shock accelerates relativistic electrons while compressing magnetic fields. If SN explosions are not spherically symmetric due to instabilities excited by the explosion shock wave through the interior of the progenitor, blobs of matter are formed during the collapse which are expelled in the subsequent SN explosion. These explosion fragments have been observed from the Vela SNR (Aschenbach, Egger & Trümper 1995). In some cases (e.g. for the Crab Nebula), a significant contribution to the overall SNR emission may also arise from the pulsar's synchrotron radiation.

Characteristic X-ray spectra for different X-ray emission mechanisms are presented in Box 3. The dominant astrophysical mechanism for the production of X-rays are mainly black body radiation, synchrotron radiation from relativistic electrons and thermal emission from hot gas. Each individual process gives rise to a characteristic X-ray spectrum, illustrated in Figs. 2.3 and 2.4.

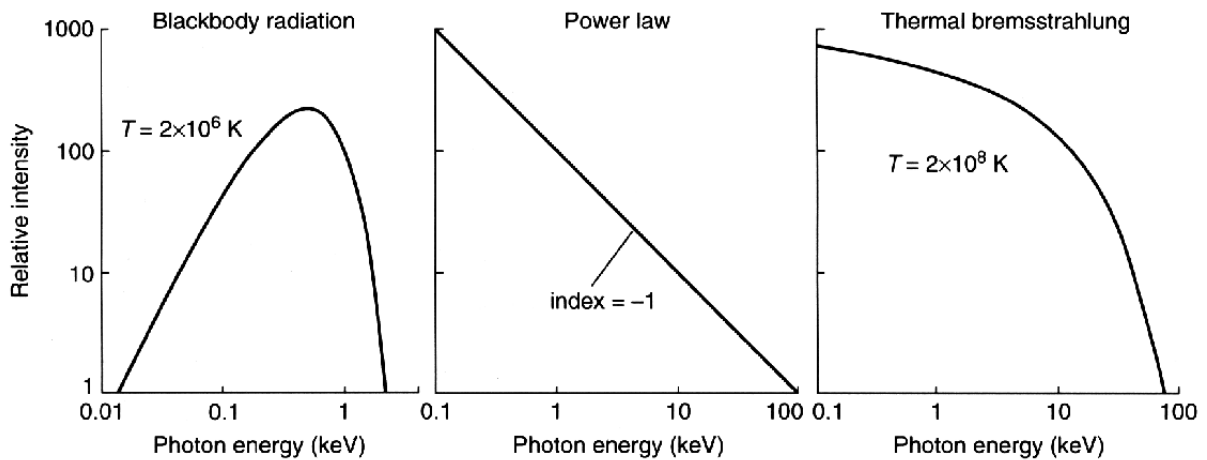


FIGURE 2.3. Characteristic spectral forms for a black body spectrum at a temperature of $T = 2 \times 10^6 \text{ K}$ (left-hand panel), a power-law spectrum with photon index 1 from synchrotron radiation (middle panel) and a thermal bremsstrahlung spectrum (right-hand panel) for a thermal plasma with a temperature of $T = 2 \times 10^8 \text{ K}$ (illustration from Charles & Seward 1995).

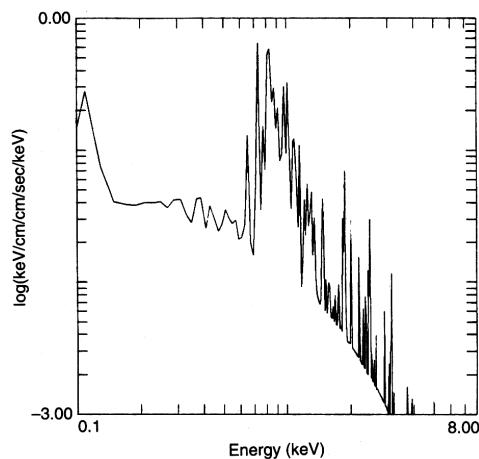


FIGURE 2.4. Simulated 'Raymond & Smith' spectrum from a thin, hot gas at a temperature of $T = 10^7 \text{ K}$. Emission lines from oxygen, iron and other heavy elements are superposed onto a thermal bremsstrahlung continuum (illustration from Charles & Seward 1995).

BOX 3. X-RAY EMISSION MECHANISM

- **Black Body Radiation:** (Fig. 2.3, left-hand panel)

An object that neither reflects nor scatters incident radiation but absorbs and re-emits the radiation completely is defined as a black body. Despite the definition being rather idealistic, many astrophysical objects almost perfectly resemble black bodies. The energy distribution of a black body is only dependent on its temperature, T , and completely independent of its shape, material or internal structure. The intensity of radiation from a black body at given temperature T at energy E is described by

$$I(E, T) = 2 \times E^3 \frac{1}{h^2 c^2 (e^{E/kT} - 1)}, \quad (2.8)$$

where h is the Planck constant (6.63×10^{-34} J s), c the speed of light ($\sim 3 \times 10^8$ m s $^{-1}$) and k the Boltzmann constant (1.38×10^{-23} J K $^{-1}$). Typical black body emitters are young neutron stars (e.g. at the center of SNRs) which are expected to have a hot surface.

- **Synchrotron Radiation:** (Fig. 2.3, middle panel)

Charged particles moving through a magnetic field will be accelerated by the magnetic field perpendicular to their instantaneous direction of motion. Due to the acceleration, the charged particles emit radiation, called ‘synchrotron radiation’. Electron synchrotron radiation is the most dominant emission mechanism due to the low mass of the electrons. In an astrophysical setting with electrons with a power-law energy spectrum, the superposition of radiation from the entire electron ensemble is also characterized by a power-law spectrum

$$I(E) = A E^{-\Gamma} \quad \text{or} \quad I(\nu) = A \nu^{-\alpha}, \quad (2.9)$$

where Γ and $\alpha = \Gamma - 1$ are the photon and energy indices, respectively, A being a constant. As Γ or α increase, the spectrum becomes ‘softer’. Typical astrophysical processes for the production of synchrotron radiation are SNe or SNR with relativistic electrons moving in strong magnetic fields within shocked fronts associated with the circumstellar interaction region. Another example is the synchrotron emission produced from relativistic jets emanating from compact objects like the central objects within AGN.

- **Thermal Emission from Hot Gas:** (Fig. 2.3, right-hand panel, and Fig. 2.4)

The emission process most frequently encountered in this work is thermal emission from hot gas. Electrons in thermal equilibrium have a well-determined velocity distribution (‘Maxwell distribution’). If an electron passes close to a positive ion, the electric force cause the electron to change its trajectory and subsequently emit radiation (‘bremsstrahlung’). The higher the temperature of an electron, the higher its velocity and subsequently the higher the energy of its bremsstrahlung radiation will be. Thermal bremsstrahlung radiation is characterized by a spectral distribution of the form

$$I(E, T) = A G(E, T) Z^2 n_e n_i (kT)^{-1/2} e^{E/kT}, \quad (2.10)$$

where $G(E, T)$ is the Gaunt factor, Z the charge of the ions and n_e and n_i are the electron and ion densities, respectively. If line emission from excited ions of heavier elements due to collisions with electrons is taken into account, the thermal bremsstrahlung continuum emission is superposed by emission lines. For thermal plasma with characteristic parameters like abundance, temperature and density, the emission line strengths can be calculated in detail. Such spectra can be simulated based on thermal plasma codes. An example is the ‘Raymond & Smith’ spectrum, illustrated in Fig. 2.4. Thermal plasma spectra from hot gas are observed in various emission regions within galaxies, e.g. galactic halos, SNRs, HII regions or accretion of material onto a compact object.

2.3.4. γ -RAY BURSTS AND HYPERNOVA REMNANTS

A number of intriguing short-lived γ -ray sources (rise within $\lesssim 5$ sec, remaining at maximum for ~ 5 sec and steadily decaying within ~ 25 sec) and X-ray afterglows were observed to happen both at the same time and place in space, giving evidence that γ -ray bursts (GRB) and supernova explosions are linked.

The best studied GRB event is GRB090425. It was detected with the Wide Field Cameras and the Gamma Ray Burst Monitor onboard BeppoSAX and with the Burst and Transient Source Experiment (BATSE) onboard the Compton Gamma Ray Observatory on April 25, 1998 (Pian et al. 1999). Within the GRB error box ($8'$ radius) and within one day after the GRB event, an X-ray source was recorded, coincident with the type I SN 1998bw in the galaxy ESO 184-G82 ($z = 0.0085$, corresponding to 38 Mpc for a Hubble constant of $65 \text{ km s}^{-1} \text{ Mpc}^{-1}$). The BeppoSAX MECS observation of SN 1998bw was the first detection of hard X-ray emission from a type I SN, with a (2–10 keV band) luminosity of $5 \times 10^{40} \text{ erg s}^{-1}$. In the radio regime, SN 1998bw was exceptionally bright (50 mJy at 6 cm; Kulkarni et al. 1998). It was spectroscopically classified as type Ic supernova, due to its lack of hydrogen and helium emission and SiII absorption features. Only SN 1994I (to be discussed in detail in Sec. 5.2.) and SN 1997ef showed similar spectra, their lightcurves being best described by core-collapse induced explosions of a C+O star. The optical spectra of SN 1998bw and the optical and radio lightcurves could only be well reproduced by an extremely energetic explosion of a massive star mainly composed of carbon and oxygen and required that the gas emitting radio and X-ray emission be expanding relativistically (Iwamoto et al. 1998; Galama et al. 1999; Kulkarni 1999). Its kinetic energy released ($2\text{--}5 \times 10^{52} \text{ erg s}^{-1}$; Pian et al. 1999) is more than an order of magnitude higher than that of previously observed SNe. In the extreme case of GRB990123, the inferred isotropic energy release ($> 3 \times 10^{53} \text{ erg s}^{-1}$) even exceeds the rest-mass of a neutron star (Kulkarni et al. 1999).

Stellar implosion that triggers a SN generally stops when the core of the star has collapsed into a dense neutron star. A shock wave subsequently blows off the outer layers of the star during a burst of neutrinos from the core. Contrary to supernovae, the progenitor for hypernovae is believed to be so massive ($> 25 M_{\odot}$) that the collapse would not stop at the production of a neutron star but would continue to the formation of a black hole (cf., e.g. Paczyński 1998; Fryer & Woosley 1998). The primary difference between supernovae and hypernovae therefore lies in the mass and the speed and in the optical depth of the ejecta. For SNe, high optical depths and non-relativistic speeds $\leq 0.2c$ ³ are typical, whereas the optical depths for hypernovae are low due to relatively small amounts of ejected mass ($M_{\text{ej}} \sim 10^{-5} M_{\odot}$, i.e. 5–6 orders of magnitude smaller than for SNe) and the ejecta are moving at relativistic speeds. These differences account for the effective high-energy emission of hypernovae with respect to the lower efficiency and energy emission for SNe. Also, although the same amount of energy is released by both objects during the same time span ($\sim 10^{53} \text{ erg s}^{-1}$ within seconds), 99% of the total energy of SNe is carried away by neutrinos. Most of the remaining 1% is converted into kinetic energy during adiabatic expansion due to the high optical depth. At typical interstellar particle densities ($< 10 \text{ cm}^{-3}$), a mere 10^{-4} of the total liberated energy is converted into electromagnetic emission during the early months, the rest being radiated into space by the heated plasma over the following 10^6 years (cf. e.g. Kulkarni et al. 1999).

Despite hypernova explosions being less numerous than supernovae, their relics might be detectable by X-ray observatories due to their interaction with the ambient ISM. Although hypernova remnants are difficult to distinguish from supershells and OB associations, their expected distinct signatures such as the emission line indicator [SiII]/H α , large shock velocities and strong soft X-ray emission, give rise to the hope that they might be identified in nearby spiral galaxies. First evidence for the detection of two X-ray luminous hypernova remnants was recently presented based on deep ROSAT HRI observations of M101 (Wang 1999; see also Wang, Immler & Pietsch 1999). Two further hypernova remnant candidates in M83 will be presented and discussed in Sec. 4.4.2.

³ c (speed of light) = $3.00 \times 10^8 \text{ m s}^{-1}$

2.4. HOT INTERSTELLAR MEDIUM

The X-ray sources described above can be attributed to the *discrete* source population as they represent individual objects, their energy being radiated within a spatially confined region in space. Given the spatial resolution of the current orbiting observatories and the distance of the objects, they appear point-like. As opposed to the discrete X-ray sources, a hot phase of the interstellar medium (hereafter: ISM) exists that can cover large areas both within the galactic disk and outside in the halo of a galaxy. This hot ISM appears extended and can be spatially resolved by orbiting X-ray instruments.

From the theory side of astrophysics, a hot phase of the ISM was postulated long before sensitive X-ray observatories were available (e.g. Spitzer 1956; Shapiro & Field 1976; McKee & Ostriker 1977). The models were based on the idea that massive winds from young stars and multiple SN explosions liberating a few 10^{52} erg s^{-1} will subsequently heat the gas and dust which is overabundant in the dense spiral arms of galaxies. The shock fronts of stellar winds and propagating SN blast waves within star formation regions can create shell-like structures and ‘bubbles’ in the ISM with radii of a few dozen pc and heat the ISM to temperatures of a few 10^6 K (e.g. Weaver et al. 1977). If energetically enough, shock fronts from multiple SN explosions and winds of some hundred O and B stars can form larger structures in space like supershells or superbubbles with diameters of some hundred pc. In this scenario, consecutive SN explosions hitting the wall or propagating through dense clumps of matter within an already created bubble can heat the ISM to some 10^{6-7} K. Hot gas at this temperature gives off radiation predominantly in the X-ray band. If these expanding shells break out of the galactic disk, they can transport hot gas into the halo of galaxies while forming ‘galactic winds’, feeding the halo with hot gas via ‘galactic chimneys’ or ‘fountains’ (cf. e.g. Normal & Ikeuchi 1989). Because the formation rate of superbubbles ($\sim 7 \times 10^{-5}$ yr $^{-1}$) is large compared to their lifetime (10^7 yr), the halo is continuously fed by hot ISM. Since the outflowing material cools radiatively while leaving the galactic disk due to a lack of heating processes outside the disk, it will fall onto the disk again.

X-ray emitting superbubbles have been detected in a number of nearby galaxies. However, detailed studies of the X-ray emission from various shell-type emission structures in the LMC have demonstrated that they account only for a small fraction of the total observed luminosity of the galaxy since they reach maximum luminosities of some 10^{37} erg s^{-1} (Chu & Mac Low 1990; Trümper et al. 1991; Wang & Helfand 1991; Bomans, Dennerl & Kürster 1994; Chu et al. 1995a; Magnier et al. 1996). At the distance of the analyzed galaxies here, they would be at or just above the detection threshold.

First evidence for hot gaseous halos surrounding galaxies became available with sensitive EINSTEIN observations of the starburst galaxies M82 (Watson, Stanger & Griffiths 1984), NGC 4631 (Fabbiano & Trinchieri 1987) and NGC 253 (Fabbiano 1988b). Almost one third of the observed X-ray emission of the galaxies (2×10^{39} erg s^{-1}) could be attributed to hot gas at a temperature of some 10^6 K and a density of $\sim 1 \times 10^{-3}$ cm $^{-3}$, containing a mass of some 10^7 M_{\odot} . With ROSAT, a large number of edge-on galaxies was observed to be surrounded by X-ray emitting, gaseous halos (cf. e.g. NGC 891: Bregman & Pildis 1994; NGC 4258: Pietsch et al. 1994; NGC 4565: Vogler, Pietsch & Kahabka 1996; NGC 4631: Wang et al., 1995, Vogler & Pietsch 1996; NGC 4559: Vogler, Pietsch & Bertoldi 1997; NGC 3079: Pietsch, Trinchieri & Vogler 1998; see also Dahlem, Weaver & Heckman 1998 for NGC 253, NGC 3079, NGC 3628, NGC 4631 and NGC 4666). For face-on galaxies it is difficult to decide whether observed diffuse emission covering large fractions of the galaxies D_{25} radii has its origin in hot ISM contained within the disk or the halo since the halo is projected onto the galactic plane. Also, it should be kept in mind that the integrated emission from discrete sources below the detection threshold and sources which are closer together than the spatial resolution of the instrument can mimic diffuse emission in face-on galaxies. In an attempt to attack source confusion, a new detection method was applied to the data of the sampled galaxies in order to resolve discrete sources in the extended bulge regions of the galaxies (see Sec. 3.2.). Here, the integrated emission of various components (X-ray binaries, nuclear X-ray sources and hot gas both from within the disk and possibly from the halo) leads to bright, extended bulge regions. The fraction of truly diffuse emission from hot gas to the overall bulge emission will be examined for several galaxies in detail in Sec. 6.

2.5. THE DISTRIBUTION OF X-RAY SOURCES IN THE BULGE AND DISK

Very little information is available on the spatial distribution of X-ray sources within our Galaxy. This is in part due to our position in the Galactic plane, the high obscuration towards the nucleus of our Galaxy and the inhomogeneities in the absorption column in different regions of the sky. External galaxies offer a better understanding of the spatial distribution since the sources are not effected by distance uncertainties and large line-of-sight absorption and it is relatively easy to associate sources with different galactic components (e.g. disk, spiral arms and bulge). Nonetheless, due to the proximity of Galactic sources, their X-ray properties can be studied in detail and compared to the properties of individual sources found in more distant galaxies. In this section, the current knowledge of the spatial distribution of X-ray emitting objects within our and nearby galaxies will be briefly summarized.

Within the spiral arms of a galaxy, bright, many variable X-ray sources are observed. The sources are believed to be associated with young Population I sources, i.e. massive accreting binaries. This picture is further strengthened by the presence of superluminous X-ray sources, which are almost exclusively located in the outer spiral arms and are in most cases embedded in HII regions, indicative of a young stellar population and high-mass X-ray binary (HMXB) formation. Also, X-ray emitting HII regions and SNR are present in the spiral arms, tracing star formation.

In globular clusters, low-mass X-ray binaries (LMXBs) dominate the X-ray output. EINSTEIN IPC and ROSAT PSPC observations of M31 showed that the average spectrum of bulge sources resembles that of Galactic and globular cluster LMXBs (Fabbiano, Trinchieri & van Speybroeck 1987; Supper et al. 1997). This was confirmed with spectral observations from GINGA (Makishima et al. 1989). A ROSAT PSPC survey of M31 (Supper et al. 1997) further demonstrated that the luminosity distribution of globular cluster sources can be represented by a single power-law with index 0.63. Against earlier reports, comparison of the PSPC X-ray luminosity distribution of globular cluster sources in M31 with globular clusters in our Galaxy showed that both come from the same parent population. Also, the luminosity of these sources is in the range of that of Galactic LMXBs. Based on timing analysis of ROSAT HRI data and comparison to the EINSTEIN source catalog of M31, Primini, Forman & Jones (1993) concluded that the fraction of variable sources within ~ 7.5 of the nucleus is $\sim 42\%$, confirming that a large fraction of sources within M31 are indeed X-ray binaries.

Furthermore, the entire EINSTEIN data set of M31 with 108 individual sources was used to study the luminosity distribution of X-ray sources within the bulge, the inner and outer bulge and the disk (Trinchieri & Fabbiano 1991). From the analysis it became evident that there is no significant luminosity gradient for the X-ray sources in M31 and that the luminosity distribution of sources in the bulge and in the disk are not different – contrary to earlier claims. Fig. 2.5. gives the luminosity distribution of EINSTEIN HRI sources found within and without a $5'$ radius (a and c) and in the inner and outer bulge (b and d). A KS-test performed on the data gives a possibility of $\sim 70\%$ that the distributions are draw from the same parent population.

However, it is interesting to note that in the disk of M31, the luminous sources with $L_x > 10^{38} \text{ erg s}^{-1}$ found in the disks of many other systems, are obviously missing. In M81, for example (also a type Sb galaxy as is M31 and our Galaxy), all sources are at or above the luminosity of the brightest sources detected in M31 (Fabbiano 1988a). If the sources are not clumps of a collection of fainter sources, there is a clear excess of luminous X-ray sources compared to M31. In Sec. 4.3.1. and 4.5., this question will be addressed again and solutions will be offered as to this obvious discrepancy in the source populations.

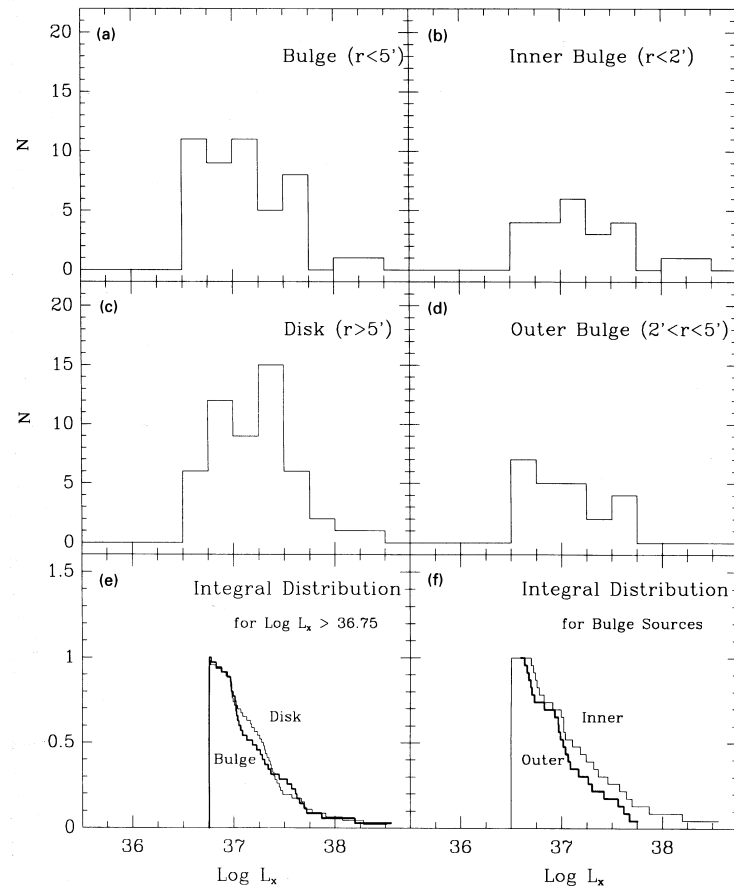


FIGURE 2.5. Luminosity distribution of EINSTEIN HRI sources in the disk (c), bulge (a) and in the inner (b) and outer (d) bulge of M31. Comparison of the integral distributions of disk (e) and bulge (f) sources shows the distributions being drawn from the same parent population (Trinchieri & Fabbiano 1991).

3. ANALYSIS METHODS OF ROSAT OBSERVATIONS OF GALAXIES

*“You know my method, Watson.
It is founded on the observance of trifles.”*

Sir Arthur Conan Doyle

After an observation has been successfully carried out with ROSAT, the attitude is reconstructed at GSOC and a standard software analysis is performed on the data at MPE (SASS; Voges et al. 1992). The processed data are written on magnetic tapes and sent to the scientist who originally proposed the observation and later put into a data archive. These data files contain all relevant information of the observation, e.g. the position of each detected photon on the sky, the energy of the photon (for PSPC observations) and its time of arrival. Also, data related to the orientation and status of the satellite and the detectors onboard ROSAT are given ('housekeeping data'), together with information regarding the attitude solution of the satellite.

Data used in this work were primarily analyzed using the EXSAS (Extended Scientific Analysis System; Zimmermann et al. 1994b) software package. EXSAS has been specifically written to evaluate ROSAT data and represents an extension of the MIDAS software package (Munich Data Analysis System), developed at ESO. The following sections describe some of the most relevant analysis procedures applied to the HRI data. The evaluation of PSPC data is mostly described in the relevant sections where the results are presented, since PSPC observations were only primarily used to supplement the HRI data. Also, where EINSTEIN data are presented, the results are preceded by a brief explanation of the relevant data analysis.

3.1. THE STUDY OF POINT SOURCES

At the distances of the observed galaxies and given the angular resolution of the ROSAT instruments, most X-ray emitting objects inside the galaxies appear 'point-like', i.e. are not extended in the ROSAT images and are compatible with the instrument's point-spread-function (PSF). Whereas the XRT+HRI point-spread-function is $\sim 5''$ (FWHM) for an on-axis point source with an energy of 1 keV, the XRT+PSPC PSF is roughly $25''$. Each ROSAT observation is the sum of individual observation blocks (OBs), which represent separated ROSAT pointings. The attitude error of these observation intervals is $6''$ – $7''$, defined by the error in the positioning of the satellite. In order to correct for these 'boresight' errors, the centroids of point sources visible in every single OB are determined and each of the different OBs are aligned with respect to the first (cf. Fig. 3.1, which gives an image of eight co-added point sources in M51 before and after boresight correction). Typically, an improvement of the PSF to $\lesssim 5''$ is achieved by applying the boresight-correction. To test the resulting attitude solution, the positions of point-like X-ray sources are compared with those of possible optical counterparts, suggested by the APM finding charts (Irwin et al. 1994). Corrections of expected attitude errors related to the 400 s phase of the telescope wobble could not be applied since none of the sources in the analyzed fields was bright enough.

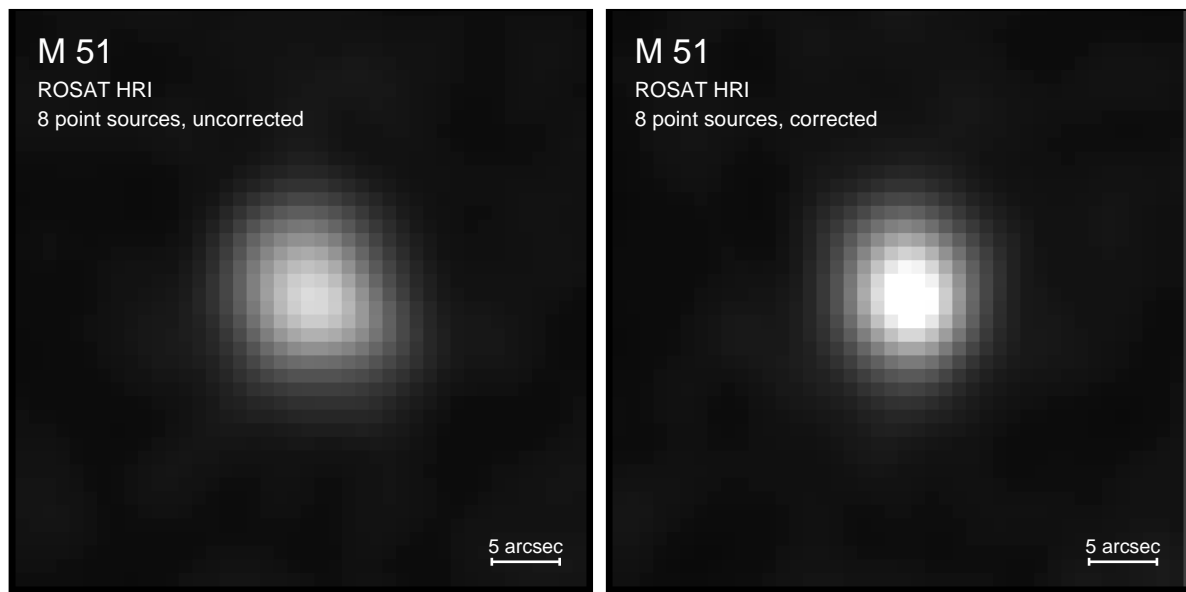


FIGURE 3.1. ROSAT HRI X-ray image of eight co-added point sources in M51 before (left-hand panel) and after boresight correction (right-hand panel).

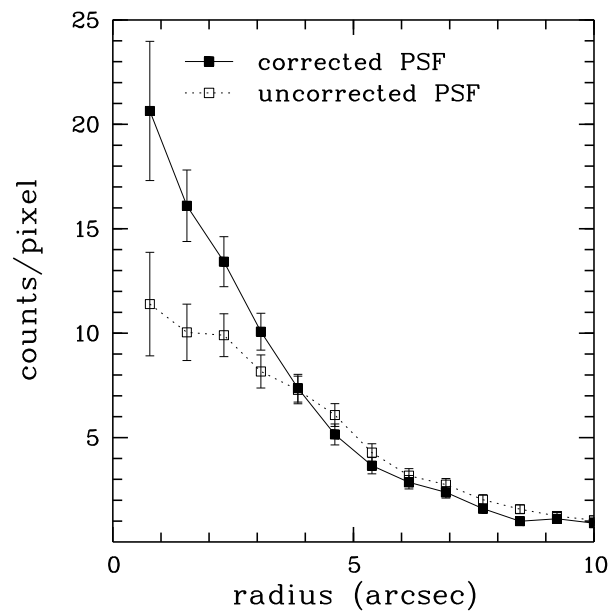


FIGURE 3.2. Radial surface brightness profile of the eight co-added HRI point sources in M51. The dotted lines gives the surface brightness profile before and the solid line after boresight correction, with radially binning of $1''.75$.

3.1.1. DETECTION OF POINT SOURCES

The boresight-corrected photon event tables were used to search for point sources in the full detector field-of-view for each observation. In order to reduce the background contamination due to UV emission and cosmic rays, only counts within the HRI raw channels 2–8 were used. For each individual observation, the HRI voltage setting was examined by constructing HRI ‘raw spectra’ of bright emission regions (e.g. the bulge regions of the galaxies), to ensure that the selection of the channels was appropriate.

Source detection was performed on HRI images following a procedure conducting local (sliding-box) and map detections, as well as final maximum likelihood and upper limit analysis of individual sources. Both local and map detections were based on HRI images with a binsize equal to $2''5$ (5×5 image pixels). Vignetting-effected outer parts of the detector were masked out and not further used. A local detect algorithm was applied to the image and sources with a significance exceeding 3σ (likelihood $L > 6$, see below) were used to create a smooth background map by excluding them from the image and interpolating across the holes with a bi-cubic spline fit. The background map hence represents a model of the radiation background of the observation. Next, the smooth background map was used to search for extended emission features by applying a map detect algorithm, using the same detection threshold of 3σ . Both local and map detect source lists were used as input for the final maximum likelihood analyses. This algorithm computes the likelihood that a detected source is real and does not represent a local enhancement due to photon statistics. The maximum likelihood L can be converted into Gaussian probabilities P according to the relation:

$$P = 1 - e^{-L} . \quad (3.1)$$

A likelihood of $L = 6$ corresponds to a Gaussian significance of 3σ and a probability of $P = 99.73\%$. An on-source detection aperture of $2 \times$ the 90% power-encircled radius of the HRI PSF was chosen to extract source net counts. The PSF is a function of off-axis angle. For the HRI, the count extraction radius ranges from $9''$ on-axis to $44''$ at $17'$ off-axis angle. Sources with a likelihood of $L > 8$ ($> 3.6\sigma$ Gaussian significance) were finally accepted after visual inspection and compiled in source lists, which are given in Appendix A.

3.1.2. SPECTRAL EMISSION MODELS

Count rates can be converted in source fluxes by assuming a spectral model for the source and taking the Galactic absorption into account (cf. Tab. 4.1):

$$f_x \left[\frac{\text{erg}}{\text{cm}^2 \text{ s}} \right] = \text{rate} \left[\frac{\text{cts}}{\text{s}} \right] \times \underbrace{\frac{1}{\text{ECF} \left[\frac{\text{cm}^2 \text{ cts}}{\text{erg}} \right]}}_{\text{conversion factor}} . \quad (3.2)$$

For a variety of spectral models and a vast range of source temperatures, the energy conversion factor, ECF, can be computed from calibration files. Assuming a cosmic X-ray source at a distance d (in units of parsecs¹) radiates isotropically into all directions in the sky, source fluxes, f_x , can be converted into source luminosities, L_x :

$$L_x = f_x \times 4\pi d^2 . \quad (3.3)$$

HRI energy conversion factors for 0.3 keV thin thermal plasma codes (RASM; Raymond & Smith 1977) and 1 keV and 5 keV thermal bremsstrahlung spectra (THBR) are given in Tab. 3.1 for sources inside the analyzed galaxies. Fluxes and luminosities for a count rate of $10^{-4} \text{ cts s}^{-1}$ are also given for the assumed spectra and distances of the targets (David et al. 1995).

¹ 1 parsec (pc) corresponds to a distance of $3.085 \times 10^{18} \text{ cm}$ or 3.26 light years

TABLE 3.1. ROSAT HRI Energy Conversion Factors

Galaxy	spectrum (keV)	ECF (cm ² cts erg ⁻¹)	rate (cts s ⁻¹)	f_{x} (erg cm ⁻² s ⁻¹)	L_{x} (erg s ⁻¹)	
M31	0.3 RASM	1.94×10^{10}	$\Rightarrow 10^{-4}$	$\hat{=}$	5.2×10^{-15}	2.9×10^{35}
	0.5 THBR	1.15×10^{10}	$\Rightarrow 10^{-4}$	$\hat{=}$	8.7×10^{-15}	4.8×10^{35}
	1.0 THBR	1.52×10^{10}	$\Rightarrow 10^{-4}$	$\hat{=}$	6.6×10^{-15}	3.7×10^{35}
	5.0 THBR	1.75×10^{10}	$\Rightarrow 10^{-4}$	$\hat{=}$	5.7×10^{-15}	3.2×10^{35}
M51	0.3 RASM	2.92×10^{10}	$\Rightarrow 10^{-4}$	$\hat{=}$	3.4×10^{-15}	2.4×10^{37}
	0.5 THBR	2.17×10^{10}	$\Rightarrow 10^{-4}$	$\hat{=}$	4.6×10^{-15}	3.2×10^{37}
	1.0 THBR	2.48×10^{10}	$\Rightarrow 10^{-4}$	$\hat{=}$	4.0×10^{-15}	2.8×10^{37}
	5.0 THBR	2.43×10^{10}	$\Rightarrow 10^{-4}$	$\hat{=}$	4.1×10^{-15}	2.9×10^{37}
M83	0.3 RASM	2.28×10^{10}	$\Rightarrow 10^{-4}$	$\hat{=}$	4.4×10^{-15}	4.2×10^{37}
	0.5 THBR	1.45×10^{10}	$\Rightarrow 10^{-4}$	$\hat{=}$	6.9×10^{-15}	6.5×10^{37}
	1.0 THBR	1.82×10^{10}	$\Rightarrow 10^{-4}$	$\hat{=}$	5.5×10^{-15}	5.2×10^{37}
	5.0 THBR	1.99×10^{10}	$\Rightarrow 10^{-4}$	$\hat{=}$	5.5×10^{-15}	5.2×10^{37}
M100	0.3 RASM	2.56×10^{10}	$\Rightarrow 10^{-4}$	$\hat{=}$	3.9×10^{-15}	1.4×10^{38}
	0.5 THBR	1.80×10^{10}	$\Rightarrow 10^{-4}$	$\hat{=}$	5.6×10^{-15}	2.0×10^{38}
	1.0 THBR	2.11×10^{10}	$\Rightarrow 10^{-4}$	$\hat{=}$	4.7×10^{-15}	1.7×10^{38}
	5.0 THBR	2.18×10^{10}	$\Rightarrow 10^{-4}$	$\hat{=}$	4.6×10^{-15}	1.6×10^{38}
M101	0.3 RASM	2.94×10^{10}	$\Rightarrow 10^{-4}$	$\hat{=}$	3.4×10^{-15}	2.3×10^{37}
	0.5 THBR	2.27×10^{10}	$\Rightarrow 10^{-4}$	$\hat{=}$	4.4×10^{-15}	3.0×10^{37}
	1.0 THBR	2.51×10^{10}	$\Rightarrow 10^{-4}$	$\hat{=}$	4.0×10^{-15}	2.7×10^{37}
	5.0 THBR	2.45×10^{10}	$\Rightarrow 10^{-4}$	$\hat{=}$	4.1×10^{-15}	2.7×10^{37}

3.1.3. TIMING ANALYSIS OF POINT SOURCES

The HRI data also allow for time variability analysis on various timescales. To achieve reasonable counting statistics, lightcurves were binned in ~ 10 ks exposure intervals. The time-dependent background was determined by normalizing the total background map of the HRI image according to the total source-removed HRI count rate in each exposure interval. Background subtracted source counts were extracted within $1.5 \times$ the 90% error radii around the fixed source positions. The variability of each HRI source in the tables of Appendix A was tested using the likelihood ratio statistic. Assuming a source is constant, its count rate

$$\bar{r} = \frac{\sum_{i=1}^n N_i}{\sum_{i=1}^n t_i} \quad (3.4)$$

should be equal in each (i) of the used (n) observation blocks (N : net counts, t : integration time). The likelihood ratio, Λ , tests this hypothesis. It is defined as:

$$\Lambda = 2 \times \sum_{i=1}^n n_i \cdot \ln\left(\frac{r_i}{\bar{r}}\right) . \quad (3.5)$$

If the hypothesis of no variability is true, the likelihood ratio has a χ^2 distribution with d.o.f. = $(n-1)$ degrees of freedom. The reduced χ_r^2 value is defined as:

$$\chi_r^2 = \frac{1}{n-1} \sum_{i=1}^n \frac{(r_i - \bar{r})^2}{\sigma_i^2} , \quad (3.6)$$

where r_i is the net count in observation block i of a total of n observation blocks. σ_i is the Gaussian error and \bar{r} is the mean count rate of the complete observation. The χ_r^2 values can be converted into Gaussian probabilities, P , of the source being variable.

For sources with significant variability, light curves are plotted in Appendix C, together with the likelihood ratio, Λ , the Gaussian probability, P , and the significance of the source being variable.

To enhance the long-term timing capability, HRI source fluxes were compared with PSPC fluxes and, where available, with EINSTEIN HRI and IPC fluxes. The conversion between the ROSAT HRI and PSPC count rates was assumed to be ~ 3 . However, for very soft sources or sources with little absorption (e.g. un-absorbed foreground stars), the conversion factor can be significantly higher ($\lesssim 8$). The conversion factor for sources with strong absorption could be as low as ~ 2.5 .

3.1.4. ANALYSIS OF A ROSAT PSPC ‘LAST LIGHT’ OBSERVATION

During the ROSAT ‘last light’ campaign in Dec. 1998, a 10 ks observation of M100/SN 1979C was accumulated with the PSPC. Because the ROSAT PSPC was not in operation for four years, special care was taken as to the performance of the PSPC detector. During the last days of ROSAT, a few targets of special scientific interest were observed with the PSPC. A large hole of reduced gain is apparent in the detector in all ‘last light’ observations. Since the parts of the detector in which the gain hole is located grew in time and could not be calibrated, the location of the gain hole was determined in the M100/SN 1979C PSPC observation by constructing an image in the hard band of 0.7–2.4 keV in detector coordinates. Fortunately, the border of the gain hole was $\sim 10'$ south of SN 1979C and did not hinder the analysis X-rays from the galaxy and the SN. Next, housekeeping data were analyzed to check for possible contaminations of the observation by high particle and instrumental background. Correlation of ‘accepted photon events’ (count rate in the full PSPC field-of-view, EE_AEXE) with the ‘master veto rate’ (rejected event rate due to anti-coincidence, EE_MV) showed no clear correlation. The accepted photons are hence not affected by high background. Also, the missing correlation of accepted events with the oxygen column in the Earth’s outer atmosphere, housekeeping parameter N_O, demonstrated that scattered solar X-ray photons did not effect the observation. Periods with low, however non-vanishing master veto ($< 5 \text{ cts s}^{-1}$) and accepted count rate ($< 1 \text{ cts s}^{-1}$) were excluded as this might indicate a malfunction of the detector during these periods. Flickering of count rates in any of the event rates was also not observed. Results of the PSPC ‘last light’ observations will be presented in Sec. 5.3.

3.2. THE IMAGE SUBTRACTION TECHNIQUE

In order to search for variable X-ray sources within regions of extended diffuse emission, a new analysis method was applied to the data, the ‘image subtraction technique’.

3.2.1. PRINCIPLES OF THE METHOD

To perform the ‘image subtraction technique’ on ROSAT observations, individual HRI observations were subdivided into observation blocks of ~ 10 – 12 ks integration time. Special care was taken that the observation blocks only contain OBIs, consisting of a relatively small number (< 7) of consecutive satellite orbits. High resolution X-ray images with a binsize $1''$ were constructed for each observation block and a Gaussian filter, corresponding to the on-axis HRI PSF ($4''.7$ FWHM), was applied to the images. The smoothing is essential to suppress photon statistics effects, which might mimic faint X-ray sources and produce artefacts. However, with the applied filter corresponding to the on-axis PSF, no spatial information is lost. The images were divided by their respective observation times in order to obtain ‘smoothed count rate images’ (i.e. images with pixels in units of cts s^{-1}). Similarly, a high resolution count rate image of the complete observation of the galaxy was created. Each count rate image was subtracted from the count rate image of the complete observation. The resulting images (‘diff-images’) show variable X-ray sources only, their X-ray photon flux being enhanced or reduced compared to their mean photon flux over the complete observation. Emission regions with constant X-ray photon flux (e.g. non-variable point sources or diffuse emission from hot gas within the extended bulge or spiral arms) are subtracted from the images and are no longer visible. In order to derive the amount of variable emission from sources, the absolute values of the ‘diff-images’ were computed, the

resulting images containing positive count rates only. A local detect algorithm was applied to these images to search for variable point sources with variabilities exceeding a Gaussian significance of 3σ . The background of the sources was determined locally, i.e. at the spline-interpolated source positions from background maps in which the sources are removed to a radius of $2.5\times$ the HRI PSF.

By nature, galactic sources found with this analysis method may either be variable X-ray binaries or young SNe. By comparison with quasi-simultaneous observations in other wavelength regimes, SNe should be identified in these nearby galaxies.

In order to illustrate the variable X-ray emission within the bulge regions of the sampled galaxies, we added the absolute ‘diff-images’ (with positive count rates only) of the bulge region to a single image.

The ‘image subtraction technique’ is very sensitive to variable X-ray sources, as the resulting image background consists only of background *fluctuations* (e.g. photon statistics, instrumental background) since regions of constant X-ray emission are subtracted. The background level for the subtracted images (‘diff-images’) for M83, for example, is 3×10^{-3} cts s⁻¹ arcmin⁻² for each of the four observation blocks. This converts to a 3σ detection limit of 2×10^{-4} cts s⁻¹ for a point source detection cell of radius $2\times$ the HRI PSF, corresponding to a (0.1–2.4 keV band) flux of $f_x \sim 1 \times 10^{-14}$ erg cm⁻² s⁻¹ and a luminosity of $L_x \sim 1 \times 10^{38}$ erg s⁻¹. The applied method therefore reaches a 3σ point source detection limit similar to the standard source detection algorithm described in Sec. 3., even in regions of enhanced extended diffuse emission, in which the standard source detection algorithm is significantly degraded. The method described here is thus especially well suited to search for variable X-ray sources in regions of enhanced diffuse X-ray emission, e.g. the bulge region of galaxies.

4. THE X-RAY SOURCE POPULATION OF NEARBY SPIRAL GALAXIES

*“If the Sun and Moon should doubt,
They’d immediately go out.”*

William Blake

4.1. PROPERTIES OF THE ANALYZED GALAXIES

The first systematic study of galaxies was performed by Edwin Hubble (★1889, †1953) at the Mt. Wilson 2.5m telescope in the 1920s. He also established a precise distance measurement of the nearby Andromeda Galaxy (M31) and started to classify galaxies based on their optical morphology. Prior to Hubble, only vague ideas about the nature of galaxies were available. Even today, some of these ideas, like Immanuel Kant’s (★1724, †1804) denotation of galaxies as ‘island worlds’ (in German: ‘*Inselwelten*’) in 1755, still remain visible in terms like ‘Andromeda nebula’ or the ‘Magellanic Clouds’. In reality, these ‘nebulae’ are extragalactic objects, representing large concentrations of matter in space, primarily consisting of stars, dust and gas.

Based on optical observations, Hubble drew the conclusion that galaxies can be classified into four basic categories: *ellipticals*, *spirals*, *barred spirals* and *irregulars*. A schematic representation of this ‘Hubble sequence’ of galaxies is given in Fig. 4.1. According to this classification, *ellipticals* are flattened galaxies without obvious spiral structure. Ellipticals mainly consist of population II stars, i.e. relatively old metal-poor stars, and contain only a little fraction of gas and dust. Diameters typically vary between 1 and 150 kpc. In the Hubble sequence, sometimes also called the ‘tuning fork diagram’, ellipticals are denoted by E0 – E7, the number referring to the oblateness of the galaxy. It is defined as the ratio between the major and minor axis, a and b , $10 \times \frac{a-b}{a}$. *Lenticulars* (or S0 galaxies) are located at the position in the Hubble diagram where the Hubble fork divides. They represent a transition between ellipticals and spirals, already showing a bright nucleus, however, still having no pronounced spiral pattern typical of spirals. *Spirals* can be separated into two distinct groups: normal spiral galaxies Sa – Sb – Sc, and barred spirals SBa – SBb – SBc. The letters ‘S’ denote spiral, ‘B’ barred and the letters a, b and c refer to the opening angle of the spiral arms (a: $\sim 10^\circ$, b: $\sim 15^\circ$, c: $\sim 20^\circ$). Barred spirals contain a central bar from which the spiral arms emerge. In this denotation, our Galaxy (the Milky Way) is classified as Sbc, intermediate between Sb and Sc. As opposed to ellipticals, spirals contain large amounts of gas and stars of both population I and II. Population I stars, i.e. young, a few 10^6 years old, stars, are generally concentrated within the galactic plane and are orbiting the center of the galaxy in almost circular orbits. They contain relatively large amounts of heavy elements (2–4%). Population II (i.e. up to 15 Gy old) stars are found both in the galactic plane and the halo and are metal-poor (0.001%). The orbits of population II stars can be very eccentric with high velocities up to 300 km s^{-1} . The halo itself contains only little interstellar medium. Galaxies that do not show a pronounced pattern like spiral arms, oblateness or a bright nucleus, are usually denoted as *irregulars* (Irr). They contain even larger amounts of gas than spirals and sometimes have luminous star-formation regions. Irregulars are sometimes subdivided into Irr I and Irr II classes. The

Irr I galaxies represent a mere continuation of the Hubble diagram beyond Sc galaxies, whereas Irr II galaxies appear as dusty, irregular small ellipticals.

At the time the Hubble diagram was introduced, it was commonly believed that the sequence of galaxies represents an evolution of galaxies in time. Hence, the terms ‘early type galaxies’ for Sa, ‘intermediate’ for Sb and ‘late galaxies’ for Sc galaxies arose. This denotation is still found in the literature. It should be stressed, however, that the Hubble sequence is not related to ages or evolutionary stages of galaxies from E0 – Sc/Irr.

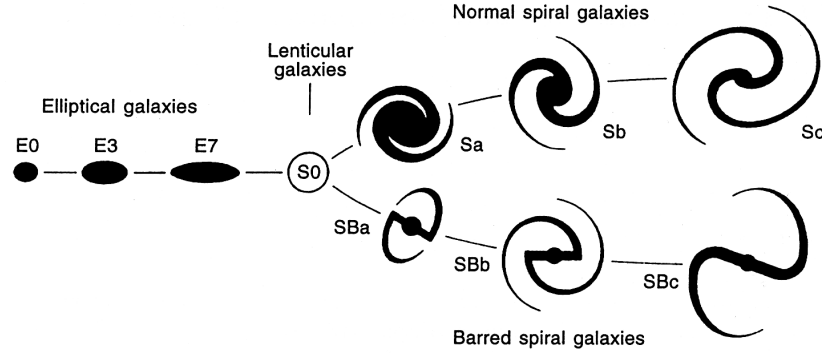


FIGURE 4.1. The ‘Hubble sequence’ of galaxies.

Subject to this study are only spirals of type Sb – Sc. Only one galaxy of the analyzed sample, M83, is a barred spiral of type SBc. The optical appearance of the galaxies nonetheless varies significantly, due to the orientation of the line-of-sight with respect to the galactic disks (inclination). Whereas M101 is seen almost ‘face-on’ (line-of-sight 17° inclined to the disk), M31 has a large inclination of $i = 77^\circ$. Spirals usually show a morphology consisting of a bright, compact nucleus (the galaxy’s dynamical center), an extended spherically symmetric bulge region exceeding the galactic plane’s height, spiral arms with sometimes luminous concentrations of star-forming regions, and a spherically symmetric halo mainly consisting of gas. The spiral arm pattern is only clearly visible in galaxies that are seen ‘face-on’. In this case, however, the halo is projected onto the galactic plane and observations of hot gas covering a large fractions of the galaxy’s diameter cannot disentangle gas within the disk from gas contained in the halo. For ‘edge-on’ galaxies (line-of-sight parallel to the disk), the halo emission can be clearly resolved from the galactic disk. However, emission components inside the galactic plane are difficult to disentangle due to projection effects. It should also be kept in mind that in addition to orientation effects and the distance of a galaxy that govern the resolution of different emission regions, galaxies, albeit of same type, can vary drastically in size (factor ≤ 100). Fig. 4.2 illustrates the two extreme cases of orientation for a Sbc galaxy, seen ‘edge-on’ and ‘face-on’. General parameters of the galaxies analyzed in this work are briefly summarized in Tab. 4.1.

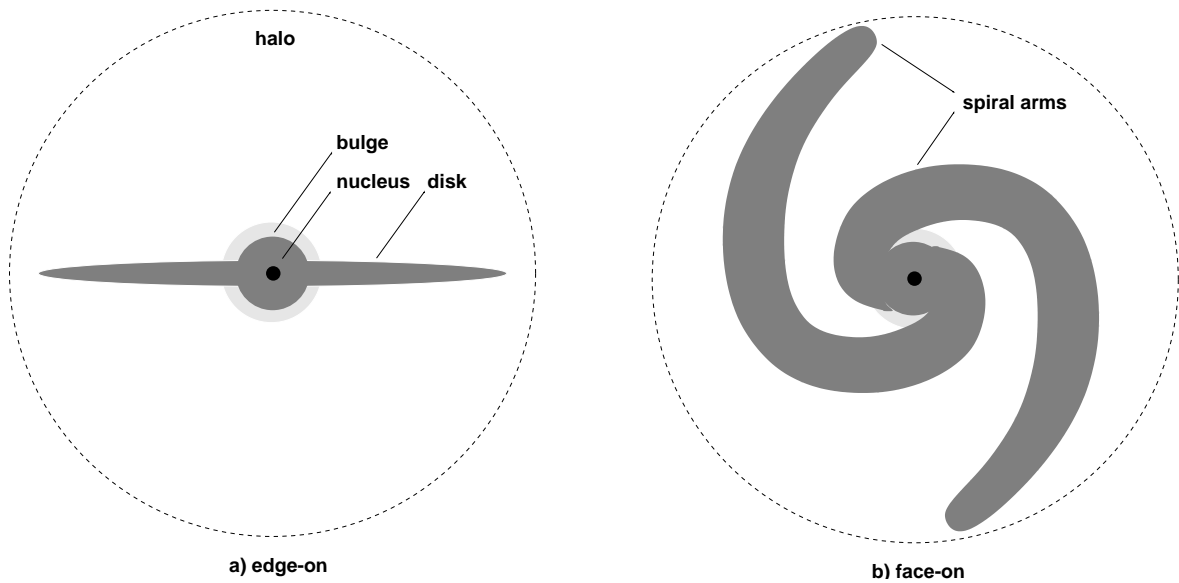


FIGURE 4.2. Schematic representation of a spiral galaxy, seen edge-on (a) and face-on (b).

TABLE 4.1. General Parameters of the Galaxies

TABLE 1.1: General Parameters of the Galaxies									
Galaxy		type	d	$1' \hat{=}$	i	D_{25}	$N_{\rm H}$	R.A. ²⁰⁰⁰	Dec. ²⁰⁰⁰
			(Mpc)	(kpc)	($^{\circ}$)	($'$)	(cm $^{-2}$)	(h m s)	($^{\circ}$ ' ")
(1)	(2)	(3)	(4)	(5)	(6)	(7)	(8)	(9)	(10)
M31	NGC 224	Sb	0.69	0.2	77	178.0	7.0×10^{20}	00 42 43.2	+41 16 12.0
M51	NGC 5194	Sc	7.7	2.2	20	11.0	1.3×10^{20}	13 29 52.7	+47 12 00.0
M83	NGC 5236	SBc	8.9	2.6	24	11.2	4.0×10^{20}	13 37 00.3	−29 51 51.3
M100	NGC 4321	Sbc	17.1	5.0	27	6.9	2.3×10^{20}	12 22 55.2	+15 49 12.0
M101	NGC 5457	Sc	7.5	2.2	17	26.9	1.1×10^{20}	14 03 16.0	+54 20 37.4

- (1) Messier number
- (2) New General Catalog number
- (3) Classification according to de Vaucouleurs (1991)
- (4) Distance (Tully 1988)
- (5) Conversion of radian measure into projected distances
- (6) Inclination of the galaxy's disk towards the line-of-sight
- (7) Diameter of the 25^m per arcsec² isophote of the galaxy in the blue band
- (8) Galactic hydrogen column density in the viewing direction
- (9) Right Ascension of the center of the galaxy for equinox 2000
- (10) Declination of the center of the galaxy for equinox 2000

4.2. GENERAL X-RAY MORPHOLOGY OF THE GALAXIES

Deep ROSAT HRI observations of the galaxies M31 (171 ks), M51 (68 ks), M83 (48 ks), M100 (68 ks) and M101 (229 ks) and PSPC observations of M51 (24 ks), M83 (25 ks), M100 (10 ks) and M101 (35 ks) were analyzed. Individual HRI and PSPC observations are summarized in Tab. 4.2. The HRI images of the galaxies show bright X-ray point sources and prominent X-ray emission from the bulge and from the disk of the galaxies (Figs. 4.4, 4.13, 4.14, 4.15 and 4.16). To further investigate the diffuse emission component within the galaxies, time intervals with a high particle background were rejected and X-ray maps were constructed by applying the ‘adaptive filtering technique’ (cf. Ehle, Pietsch & Beck 1995). Photons were binned into an image of $8''$ pixel size and pixels of amplitude n were smoothed with a Gaussian of $\text{FWHM} = 137 \times e^{0.35(1-n)}$. For M100, the image was created with a pixel size of $6''5$. Pixels with an amplitude larger than 8 remained un-smoothed to ensure that bright point sources were not smeared out into background regions. The adaptively filtered images show that large fractions of the D_{25} ellipses of the galaxies M51, M83 and M100 are filled with diffuse X-ray emission (Figs. 4.3). ‘Real colour’ ROSAT PSPC images of M51, M83 and M101 are given in Fig. 7.7 in Appendix D. The colour plates are composites of red, green and blue images from the PSPC soft (0.11–0.41 keV), hard1 (0.52–0.90 keV) and hard2 (0.91–2.01 keV) bands. The optical sizes of the galaxies are indicated by dashed D_{25} ellipses. 3σ contour lines for the emission in the soft band are drawn in order to illustrate the extent of diffuse X-ray emission in each galaxy.

The images show that the X-ray emission can be decomposed roughly into three emission components: (a) point sources, (b) extended X-ray emission from the bulge region of the galaxies and (c) further extended, patchy X-ray emission filling large fractions of the D_{25} ellipses of the galaxies. The point source emission component will be discussed in the following sections in more detail.

Radially binned surface brightness profiles of the galaxies from unfiltered low-background images with radial binning of $20''$ centred on the peak of the X-ray emission were constructed. To estimate the amount of spatially unresolved, diffuse emission within the D_{25} ellipses of the galaxies, point sources were excluded with cut radii of twice the FWHM of the HRI PSF. Source-free regions, well outside the D_{25} ellipses, were used to determine the mean background levels. The residual count rates inside the D_{25} ellipses of the galaxies were calculated after subtraction of the mean background rates. Assuming the residual diffuse X-ray emission to have spectra of a hot (3×10^6 K), low-density plasma with cosmic abundances (cf., e.g. Raymond & Smith 1977), fluxes and luminosities were calculated, taking galactic absorption into account. The results are compiled in Tab. 4.3.

In M51 (NGC 5194), the entire optical extent of the galaxy is filled with bright diffuse emission, even in regions where no optical emission is visible (e.g. in the space between M51 and its companion NGC 5195). Its contribution to the overall X-ray emission of the galaxy (5.0×10^{40} erg s $^{-1}$) is 75%. Similarly in the south-western spiral arm of M83 (see below), a local enhancement can be discerned from the overall X-ray emission of the galaxy in its north-eastern spiral arm. Since this local enhancement in the spiral arm of M51 close to its interacting companion NGC 5195 coincides with strong radio, CO and H α emission, this is highly suggestive of the detection of gas flowing into the halo of the galaxy, heated by the star-forming activity.

The M83 images show that approximately 60% of the D_{25} ellipse is filled with diffuse X-ray emission. While the ridges of diffuse X-ray emission are broadened in the adaptively filtered image, a spiral arm structure of high surface brightness diffuse emission is still discernable. After subtracting point sources from an un-filtered image of binsize $5''$, a count rate of 6.8×10^{-2} cts s $^{-1}$ remains within the inner $0.6 \times D_{25}$ ellipse of M83. According to Ehle et al. (1998), the diffuse emission component of M83 can be described by a two temperature plasma, composed of a rather soft (2×10^6 K \cong 0.2 keV) X-ray emitting plasma from the halo and an internally absorbed, hotter gas (6×10^6 K \cong 0.5 keV) from within the disk. w3PIMMS¹ calculations show that the HRI is more sensitive to a 0.5 keV thermal plasma spectrum (conversion factor between PSPC and HRI count rates 2.5) than to a 0.2 keV plasma

¹ w3PIMMS is a web version of the ‘Portable Interactive Multi-Mission Simulator’, developed at HEASARC

spectrum (conversion factor 3.1, taking Galactic absorption into account). We therefore assume that our observed diffuse emission arises from the hotter component, i.e. a thin thermal plasma with a temperature of 0.5 keV. For this component, we derive a luminosity of $L_x = 2.0 \times 10^{40} \text{ erg s}^{-1}$. The integrated luminosity of the point sources detected within the galaxy is also $2.0 \times 10^{40} \text{ erg s}^{-1}$ (cf. Sec. 4.4.). Half of the total emission of the galaxy ($4.1 \times 10^{40} \text{ erg s}^{-1}$) can therefore be separated into point sources, whereas in the PSPC observation detected point sources (excluding P6 and P13) contribute only 9% to the total luminosity (Ehle et al. 1998). As will be shown in Sec. 6., the diffuse emission within the bulge of M83 also accounts for half of the total bulge emission.

Also, bright extended X-ray emission in the south-western spiral arm can be discerned from point sources and from the overall diffuse emission of M83. The extended X-ray emission region coincides with strong radio and $H\alpha$ emission. Fitting a two-component spectrum to the PSPC data gives evidence for the detection of a soft (0.26 keV) component, absorbed by the Galactic foreground only, and a component at a higher temperature (0.95 keV) with additional intrinsic absorption. Whereas the temperature of the soft component found for the south-western spiral (0.26 keV) is similar to the soft component found for the overall diffuse emission of M83 (0.2 keV; Ehle et al. 1998), the temperature of the internally absorbed hotter component is slightly higher (0.95 keV) than that observed for the overall diffuse emission (0.5 keV; Ehle et al. 1998). This can be explained by the presence of unresolved X-ray binaries located within the star-formation region of the spiral arm. The two-temperature plasma is indicative of gas flowing into the halo of the galaxy (cooler, un-absorbed component) and hot gas heated by the star-forming activity in the south-western spiral arm of M83, which is highly obscured due to its location inside the disk of M83.

Diffuse emission is visible over almost the entire optical extent of M100 and contributes 64% ($3.5 \times 10^{40} \text{ erg s}^{-1}$) to the total luminosity of M100 inside the D_{25} ellipse ($5.5 \times 10^{40} \text{ erg s}^{-1}$, cf. Tab. 4.3). It can be seen that the X-ray luminosity of the diffuse emission in M100 is similar to that of M51, M83, M101 and NGC 1566, though these galaxies' diffuse components attain significantly higher luminosities when compared to edge-on galaxies, a fact partly due to the geometry of the line of sight, with a minimum absorption in the galactic disks. The unresolved emission, however, is more confined to the inner spiral arms of M100, similar to NGC 1566. The diffuse X-ray emission covers the same area for which Sakamoto et al. (1995) report the detection of strong CO emission. This might be suggestive of a star-formation driven outflow into the galactic halo via galactic fountains (Norman & Ikeuchi 1989), similar to M51 and M83.

In addition to the detected sources, there are large amounts of low-surface brightness X-ray emission associated with M101. After excluding individual sources, the excess of the diffuse X-ray emission within the D_{25} ellipse of M101 is estimated to be $8.9 \times 10^{39} \text{ erg s}^{-1}$ (32% of the total X-ray emission of M101). It is further found that the diffuse X-ray emission is strongly correlated with HII regions in M101. Thus as in the LMC (Wang & Helfand 1991), it is expected that the X-ray emission is dominated by hot gas heated by a combination of supernova blast waves and stellar winds from massive stars in star-formation regions.

Evidence for a diffuse X-ray emission component extending to large radii has been found in published PSPC data of the galaxies, too (M51: luminosity of the diffuse component in the ROSAT band $1.5 \times 10^{40} \text{ erg s}^{-1}$, Ehle, Pietsch & Beck 1995; M83: $3.6 \times 10^{40} \text{ erg s}^{-1}$, Ehle et al. 1998; M101: $3.6 \times 10^{39} \text{ erg s}^{-1}$ in the $\frac{3}{4}$ keV and 1.5 keV band and $10^{40} - 10^{41} \text{ erg s}^{-1}$ in the $\frac{1}{4}$ keV band, Snowden & Pietsch 1995; cf. also NGC 1566: $1.4 \times 10^{40} \text{ erg s}^{-1}$, Ehle et al. 1996). The diffuse component in these galaxies is thought to originate from a hot ($\sim 10^6 \text{ K}$) gaseous halo above the galactic plane. Regions confined inside the disk are unlikely to account for the emission since the required filling factors are very large and the required low temperatures contradict the measured values. The anti-correlation of the X-ray emitting regions and the polarised radio emission in the inner spiral arms of M51 and M83 is probably indicative of outflowing material from the galactic disk into the halo, driven by an enhanced star formation rate.

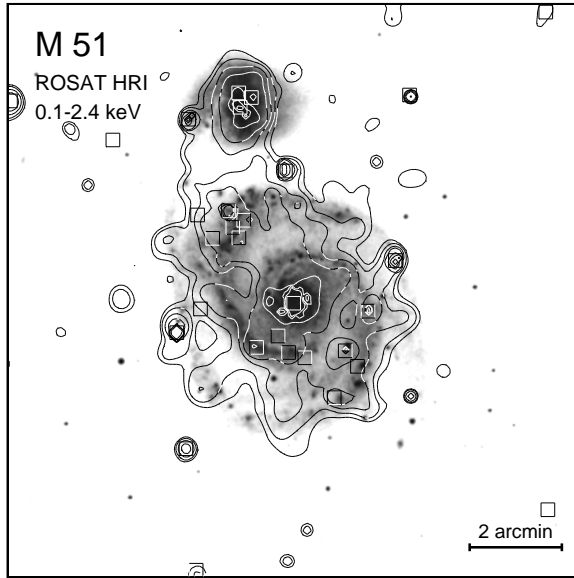


FIGURE 4.3. (a) Contour map of the ROSAT HRI image of M51 (0.1–2.4 keV), smoothed with an adaptive filter ($\text{FWHM} \leq 170''$) and superposed on a digitized optical POSS plate. Contour levels are at 3, 4, 6, 9, 25, 50 and 150σ above the background of $1.2 \times 10^{-2} \text{ cts s}^{-1} \text{ arcmin}^{-2}$. 1σ corresponds to $1.2 \times 10^{-3} \text{ cts s}^{-1} \text{ arcmin}^{-2}$. HRI sources are enclosed by boxes.

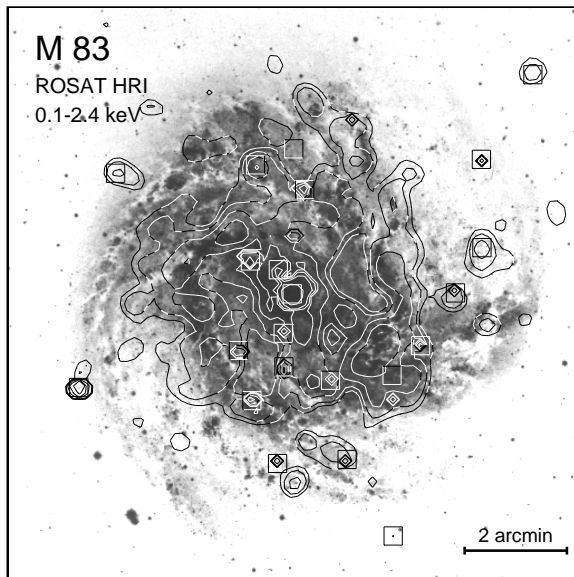


FIGURE 4.3. (b) Contour map of the ROSAT HRI image of M83 (0.1–2.4 keV), smoothed with an adaptive filter ($\text{FWHM} \leq 170''$) and superposed on a deep optical image from the Anglo Australian Telescope (kindly provided by David Malin). Contour levels are at 3, 4, 6, 9, 25, 50 and 150σ above the background of $2.3 \times 10^{-2} \text{ cts s}^{-1} \text{ arcmin}^{-2}$. 1σ corresponds to $3.6 \times 10^{-3} \text{ cts s}^{-1} \text{ arcmin}^{-2}$. HRI sources are enclosed by boxes.

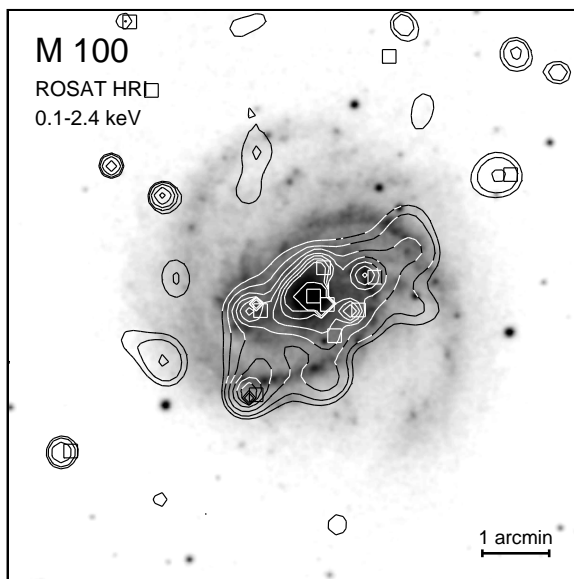


FIGURE 4.3. (c) Contour map of the ROSAT HRI image of M100 (0.1–2.4 keV), smoothed with an adaptive filter ($\text{FWHM} \leq 137''$) and superposed on a digitized optical POSS plate. Contour levels are at 3, 4, 6, 9, 13, 18, 24 and 35σ above the background of $1.8 \times 10^{-2} \text{ cts s}^{-1} \text{ arcmin}^{-2}$. 1σ corresponds to $1.1 \times 10^{-3} \text{ cts s}^{-1} \text{ arcmin}^{-2}$. HRI sources are enclosed by boxes.

TABLE 4.2. ROSAT Observations of Nearby Galaxies

Target	detector	obs.	obs. date	obs. time	total
M31	HRI	1	25/07/90 – 28/07/90	30.8 ks	
	HRI	2	07/07/94 – 08/07/94	18.8 ks	
	HRI	3	21/07/94 – 22/07/94	27.0 ks	
	HRI	4	17/07/95 – 07/08/95	9.1 ks	
	HRI	5	02/01/96 – 07/01/96	85.5 ks	171.2 ks
M51	PSPC	1	28/11/91 – 13/12/91	24.3 ks	24.3 ks
	HRI	2	07/12/91 – 10/01/92	8.5 ks	
	HRI	3	22/05/92 – 05/06/92	8.8 ks	
	HRI	4	22/05/94 – 23/05/94	9.4 ks	
	HRI	5	18/06/94 – 24/06/94	36.6 ks	
	HRI	6	26/12/97 – 30/12/97	5.0 ks	68.3 ks
M83	PSPC	1	28/01/92 – 11/01/93	25.2 ks	25.2 ks
	HRI	2	20/01/93 – 22/01/93	23.5 ks	
	HRI	3	30/07/94 – 03/08/94	24.2 ks	47.7 ks
M100	HRI	1	05/06/95 – 28/06/95	42.8 ks	
	HRI	2	18/12/97 – 04/01/98	25.0 ks	67.8 ks
	PSPC	3	08/12/98 – 14/12/98	10.0 ks	10.0 ks
M101	PSPC	1	08/06/91 – 09/06/91	34.5 ks	34.5 ks
	HRI	2	09/01/92 – 11/01/92	18.6 ks	
	HRI	3	10/12/92 – 14/12/92	32.6 ks	
	HRI	4	14/05/96 – 09/06/96	108.8 ks	
	HRI	5	21/11/96 – 23/11/96	68.9 ks	228.9 ks

4.3. POINT SOURCES IN M31

The deep ROSAT HRI pointings centred on the nucleus of M31 were used to compile an X-ray source catalogue with unprecedented sensitivity (down to some 10^{35} erg s $^{-1}$) and spatial resolution (down to ~ 15 pc for an on-axis resolution of the XRT+HRI configuration of $5''.0$ FWHM). Fig. 4.4 (upper panel) gives a contour representation of a $30' \times 30'$ region centred on the M31 nucleus. The enlarged region (Fig. 4.4 lower panel) gives the inner $4' \times 4'$ (800 pc \times 800 pc) bulge region of M31. Detected HRI sources are marked on the right sides of the panels. Interestingly, the position of the nucleus, coinciding with the HRI source H63, does not correspond to the peak X-ray emission of M31 (H47). This aspect will be further discussed in Sec. 4.3.1.

Within the $34' \times 34'$ HRI field-of-view, 128 X-ray sources are detected (cf. Tab. 7.1). Four of them represent foreground stars (cf. Tab. 7.7; H12, H37, H100, H121), three are associated with SNRs (H86, H118, H123). 21 X-ray sources are within globular clusters in M31, representing $\sim 17\%$ of all X-ray sources associated with M31. The sources detected within M31 have (0.1–2.4 keV band) X-ray luminosities ranging from 4×10^{35} erg s $^{-1}$ (H44) to 1.4×10^{38} erg s $^{-1}$ (H47) for an assumed thermal bremsstrahlung spectrum with $kT = 5$ keV, a line-of-sight attenuation of $N_H = 7 \times 10^{20}$ cm $^{-2}$ and a distance of 690 kpc. 50 HRI sources correspond to sources compiled in the ROSAT PSPC (Supper et al. 1997) and EINSTEIN HRI M31 source lists (Fabbiano, Trinchieri & van Speybroeck 1987). Timing analysis and comparison of the HRI X-ray luminosities with the luminosities obtained from previous X-ray observations shows that $\sim 50\%$ of all X-ray sources within M31 are variable with a significance exceeding 3σ .

Fitting a power-law to the X-ray source luminosity distribution of the form $N(> L) = N_0 L_x^{-\alpha}$ gives an index of 0.50 for all sources found within M31. A flattening of the luminosity function below $\sim 10^{37}$ erg s $^{-1}$ as proposed by Primini, Forman & Jones (1993) based on a fraction of the HRI data presented here, is confirmed. The luminosity distribution of X-ray sources found within M31 is given

TABLE 4.3. Count Rates, Fluxes and Luminosities of the Emission Components in the Galaxies

Emission component	count rate (10^{-3} cts s^{-1})	f_x^* (10^{-13} erg cm^{-2} s^{-1})	L_x^* (10^{39} erg s^{-1})	fraction (%)
M31:				
Total Galaxy [§]	2 200.0	505.0	2.9	100
Total bulge emission (< 1 kpc)	265.0	186.7	1.04	100
Point source at nucleus	9.2	6.0	0.03	2
Point sources within bulge (< 1 kpc) ...	124.8	70.7	0.41	39
Variable emission from point sources ...	13.2	7.5	0.04	4
Diffuse emission within bulge (< 1 kpc) [§]	117.8	102.5	0.57	55
M51:				
Total Galaxy	160.0	72.7	49.9	100
Point sources	43.7	19.2	12.7	25
Diffuse emission within D_{25}^\dagger	116.3	53.5	37.2	75
Total bulge emission (< 1 kpc)	27.8	11.4	8.1	100
Point source at nucleus [‡]	12.4	5.0	3.6	44
Variable emission from point sources ...	14.2	5.8	4.1	51
Diffuse emission within bulge (< 1 kpc) [§]	1.2	0.6	0.4	5
M83:				
Total Galaxy	108.7	43.9	40.5	100
Point sources	40.7	22.4	20.1	50
Diffuse emission within $0.60 \times D_{25}^\dagger$	68.0	21.5	20.4	50
Total bulge emission (< 1 kpc)	26.5	10.9	10.4	100
Point source at nucleus [¶]	8.4	4.6	4.4	42
Variable emission from point sources ...	2.6	1.4	1.3	13
Diffuse emission within bulge (< 1 kpc) [§]	15.5	4.9	4.7	45
M100:				
Total Galaxy	37.1	16.0	55.0	100
Point sources	9.3	4.0	14.0	25
Diffuse emission within D_{25}^\dagger	26.9	10.0	35.0	64
Total bulge emission (< 1 kpc)	7.1	2.9	9.9	100
Point source at nucleus	4.4	1.9	6.5	66
Other point source in bulge (H21)	2.4	0.9	3.0	30
Diffuse emission within bulge (< 1 kpc) [§]	0.3	0.1	0.4	4
M101:				
Total Galaxy	48.1	19.3	13.0	100
Point sources	32.9	13.5	8.9	68
Diffuse emission within D_{25}^\dagger	15.2	5.2	4.1	32
Total bulge emission (< 1 kpc)	0.79	0.23	0.21	100
Point source at nucleus	0.57	0.16	0.15	71
Diffuse emission within bulge (< 1 kpc) [§]	0.22	0.07	0.06	29

* Assumed spectral models: thermal bremsstrahlung ($T = 5$ keV) for point sources and thin thermal plasma ($T = 0.5$ keV) for diffuse emission components. The integrated fluxes and luminosities of the total galaxies and the total bulge regions have been calculated by using the different conversion factors for the different components

§ Since the analyzed HRI observations do not cover the entire M31 field, results from the PSPC survey are quoted for the total emission (Supper et al. 1997)

§ Partly due to unresolved point-sources (cf. Sec. 4.3.1.). A point-like source at the nucleus and the variable sources found with the ‘image subtraction technique’ were excluded, except the variable source corresponding to the nucleus

† Excluding point sources

‡ Derived from the radial intensity profile of eight co-added point-like X-ray sources, scaled to the nucleus

¶ Derived from the radial intensity profile of the point-like X-ray source H30, scaled to the nucleus

in Fig. 4.5. The luminosity function of X-ray sources within M31 will be further discussed in the next section.

4.3.1. BULGE VS. DISK POPULATION

The proximity of M31, combined with the high spatial resolution of the ROSAT HRI and the sensitivity of the survey allows a detailed comparison of the X-ray sources found within the bulge and disk of M31. Within the inner $1 \text{ kpc} \times 1 \text{ kpc}$ region centred on M31 (representing the bulge), 30 HRI sources are detected with (0.1–2.4 keV band) X-ray luminosities ranging from $1.1 \times 10^{36} \text{ erg s}^{-1}$ (H53 and H81) to $1.4 \times 10^{38} \text{ erg s}^{-1}$ (H47). 18 of the ROSAT HRI bulge sources coincide with EINSTEIN HRI sources. The range in luminosity for disk sources is $4 \times 10^{35} \text{ erg s}^{-1}$ (H44) to $3.8 \times 10^{37} \text{ erg s}^{-1}$ (H108).

TABLE 4.4. ROSAT HRI Luminosity Function of X-Ray Sources in in M31

Region	area (kpc^2)	no. of sources	no. of cases	constant N_0	index α
M31 total	167	127	24	17.82 ± 0.08	0.50 ± 0.02
M31 disk	166	98	24	16.07 ± 0.07	0.45 ± 0.02
M31 bulge	1	29	23	28.52 ± 0.16	0.75 ± 0.04
M31 inner bulge	0.25	18	22	26.09 ± 0.17	0.67 ± 0.05
M31 outer bulge	0.75	11	14	21.71 ± 0.10	0.57 ± 0.05

The cumulative luminosity distribution for bulge and disk sources is given in Fig. 4.5. Whereas the overall luminosity function of X-ray sources found within M31 is best fitted by a single power-law with index $\alpha = 0.50$, the distribution function for disk sources is apparently flatter ($\alpha = 0.45$) than that of bulge sources ($\alpha = 0.75$). The result is in clear contrast to the EINSTEIN HRI findings (Trinchieri & Fabbiano 1991). Based on deep EINSTEIN HRI observations of M31, Trinchieri & Fabbiano (1991) found that both the bulge and disk source distributions, as well as the inner and outer bulge source distributions are drawn from the same parent distribution (probability for a common parent distribution 70%; cf. Fig. 2.5.). However, since the ROSAT observations are significantly deeper than the EINSTEIN observations, the question to be addressed is whether this apparent difference in source luminosity functions is real. As can be seen from Fig. 4.5, the cut-off luminosity for bright sources is significantly higher for bulge sources. The situation becomes more clear if the luminosity function of inner and outer bulge sources is compared. Again, sources detected within the inner 0.5 kpc radius seem to have a steeper luminosity function ($\alpha = 0.67$; cf. Fig. 4.6 and Tab. 4.4) when compared to the luminosity distribution of outer bulge sources ($\alpha = 0.57$), extracted from an annulus of inner and outer radii of 0.5 kpc and 1.0 kpc respectively. As can be seen from the luminosity distribution given in Fig. 4.6, sources found within the inner bulge apparently have a higher cut-off luminosity ($2.5 \times 10^{36} \text{ erg s}^{-1}$) than that of outer bulge sources ($4.5 \times 10^{35} \text{ erg s}^{-1}$). Also, bright sources exceeding luminosities of $5 \times 10^{37} \text{ erg s}^{-1}$ seem to be exclusively located in the inner bulge region. As will be shown in the next Sec. 4.3.2. this apparent overpopulation of bright sources within the inner bulge is due to source confusion because of the increasing proximity of sources in the direction towards the nucleus. Also, the ‘image subtraction technique’ shows that some of the bright X-ray sources detected within the M31 bulge can be spatially resolved by applying the ‘image subtraction technique’ to the bulge region. The brightest X-ray source in M31 (H47; $1.4 \times 10^{38} \text{ erg s}^{-1}$), for example, can be resolved into three variable X-ray sources (D6/D7/D8). It therefore does not represent the brightest single X-ray source in M31. Also, H77 ($1 \times 10^{37} \text{ erg s}^{-1}$) is resolved into two point-like X-ray sources (D44/D46). It is therefore concluded that on the basis of the luminosity functions constructed for sources found within the disk, and the outer and inner bulge of M31, no

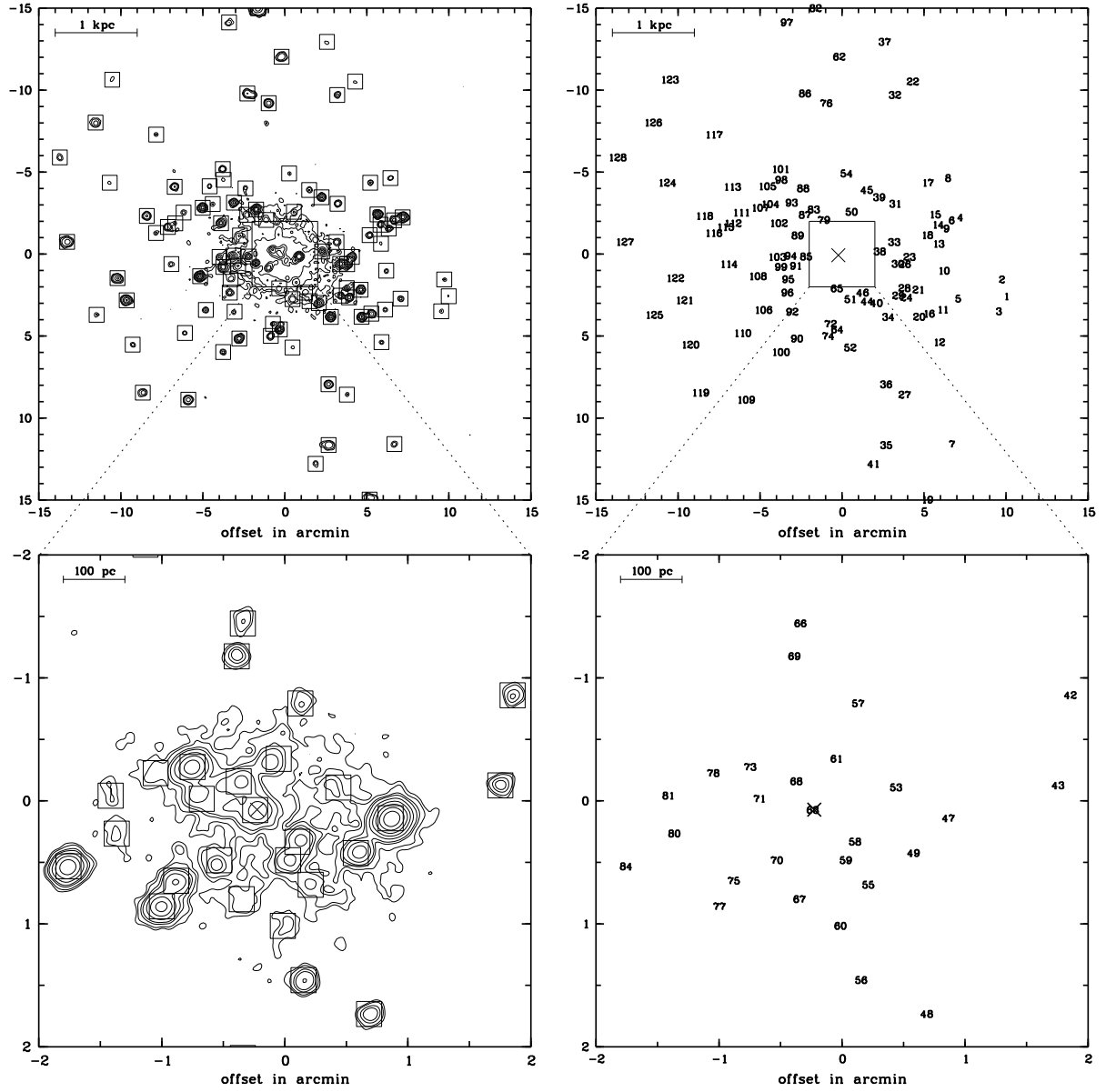


FIGURE 4.4. 0.1–2.4 keV band X-ray contours from the 171 ks HRI observation of M31. The upper left-hand panel gives the $6 \text{ kpc} \times 6 \text{ kpc}$ region centred on the nucleus of the galaxy, smoothed with a Gaussian of $12''$ (FWHM), the lower left panel the inner $0.8 \text{ kpc} \times 0.8 \text{ kpc}$ region around the nucleus of M31, smoothed with a Gaussian of $4''.7$ (FWHM). Contour levels are at $3, 5, 10, 30, 60, 120, 240$ and 480σ above the mean background rate (upper panel: $3.6 \times 10^{-2} \text{ cts s}^{-1} \text{ arcmin}^{-2}$, $1\sigma \cong 5.9 \times 10^{-3} \text{ cts s}^{-1} \text{ arcmin}^{-2}$, lower panel: $9.4 \times 10^{-3} \text{ cts s}^{-1} \text{ arcmin}^{-2}$, $1\sigma \cong 2.1 \times 10^{-3} \text{ cts s}^{-1} \text{ arcmin}^{-2}$). The right side of the panel indicates the location of HRI X-ray sources in M31 (cf. Tab. 7.1). The position of the nucleus is marked by a cross.

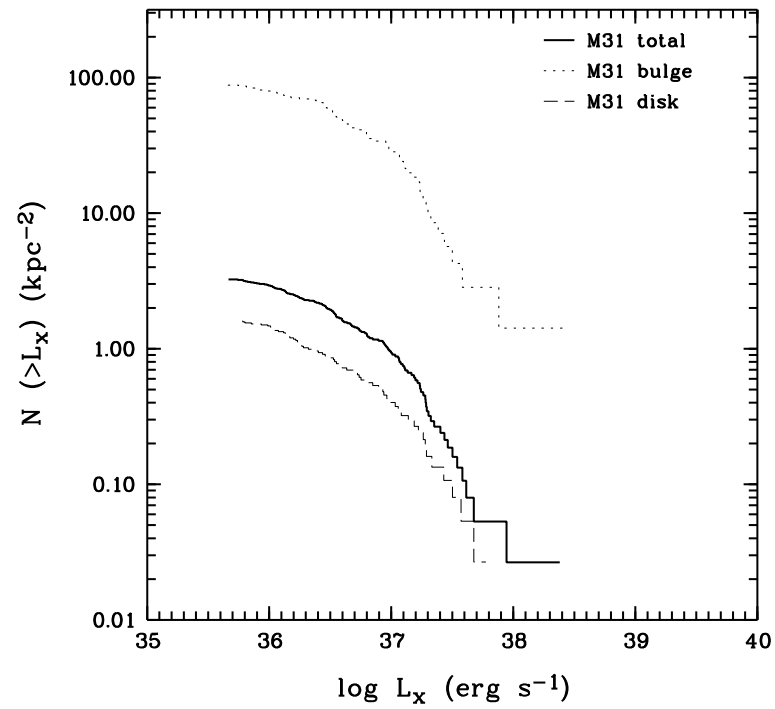


FIGURE 4.5. Luminosity distribution of ROSAT HRI X-ray sources in M31 for the bulge (dotted line), disk (dashed line) and for the total galaxy (solid line).

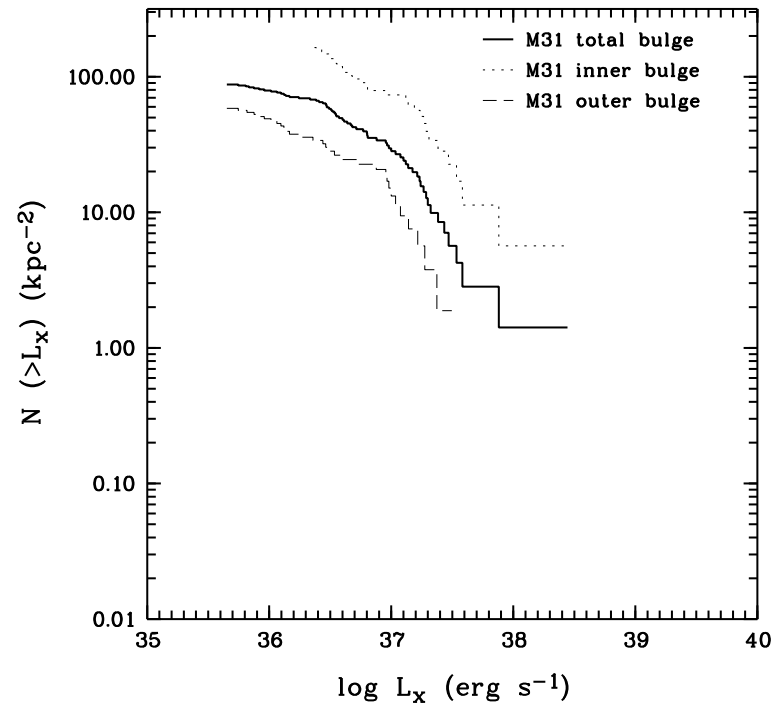


FIGURE 4.6. Luminosity distribution of ROSAT HRI X-ray sources within the total (solid line), inner bulge (dotted line) and outer bulge (dashed line) of M31.

significant difference in the power-law index is found. Hence, the results are compatible with the earlier EINSTEIN results that both the disk, outer and inner bulge sources belong to the same parent population. The source luminosity distribution within M31 is hence not a function of radius from the center of the galaxy.

Another result from the ‘image subtraction technique’ technique is that of the 30 HRI sources detected within the bulge of M31 (< 1 kpc), 29 coincide within $2\times$ the 90% confidence error radius of the X-ray positions with variable sources detected with the ‘image subtraction technique’ with significance of variability exceeding 3σ (cf. Figs. 4.7 and 4.8). Hence, $\sim 100\%$ of all sources detected within the inner 1 kpc radius are variable, indicating X-ray binary origin. Another 19 variable X-ray sources are detected within the bulge region with the ‘image subtraction technique’. Subtracting *all* the discrete X-ray sources detected within the M31 bulge region (sources denoted by ‘|’ in Tab. 7.7 plus the additional variable sources detected with the ‘image subtraction technique’) from the total bulge emission (1.0×10^{39} erg s $^{-1}$) gives residual emission from either hot gas and/or unresolved point sources with a luminosity of 5.7×10^{38} erg s $^{-1}$. This represents 55% of the total bulge emission of M31.

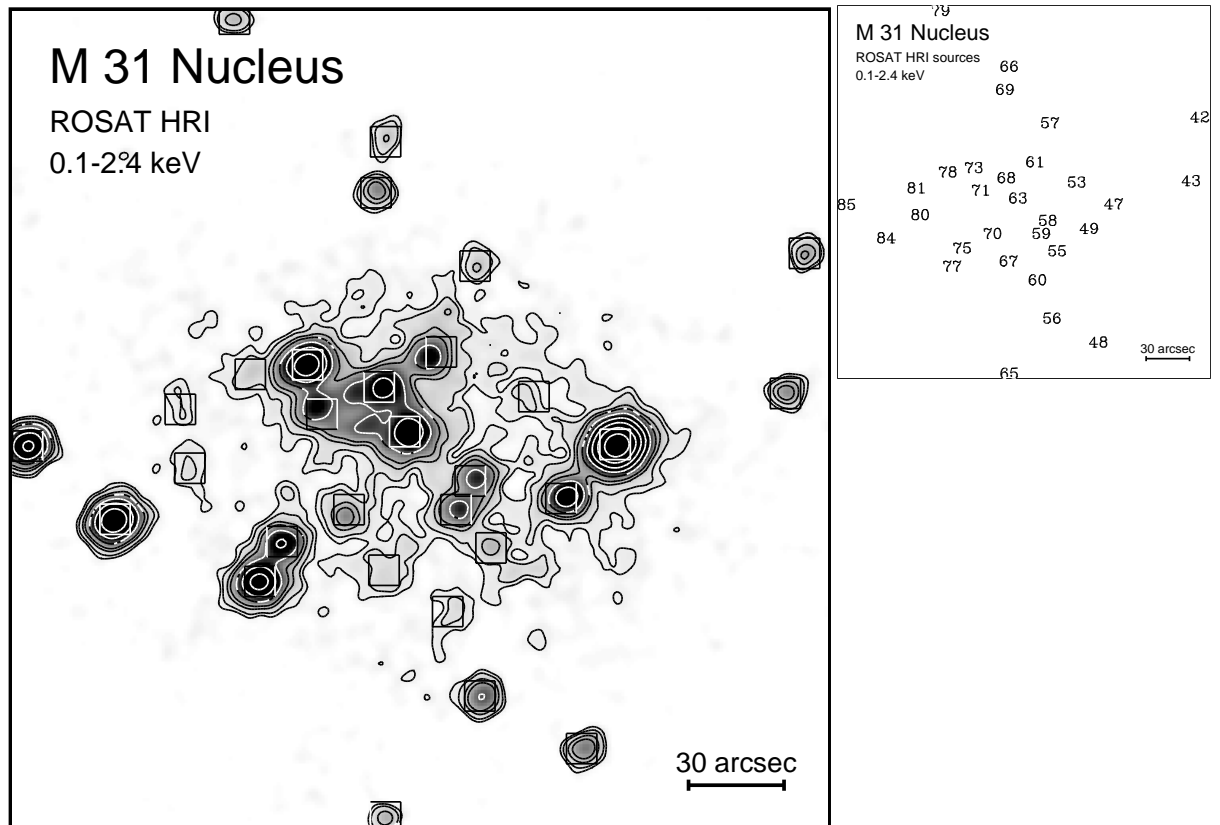


FIGURE 4.7. Contours of X-ray emission from the inner $1 \text{ kpc} \times 1 \text{ kpc}$ region of M31 in the ROSAT HRI band (0.1–2.4 keV), superposed on a linear grey-scale representation of the same image (left-hand panel). The image was constructed with a pixel size of $2''.5$ and smoothed with a Gaussian filter of $5''$ FWHM. Same contour levels as in Fig. 4.4. The right-hand panel gives the location of HRI X-ray sources.

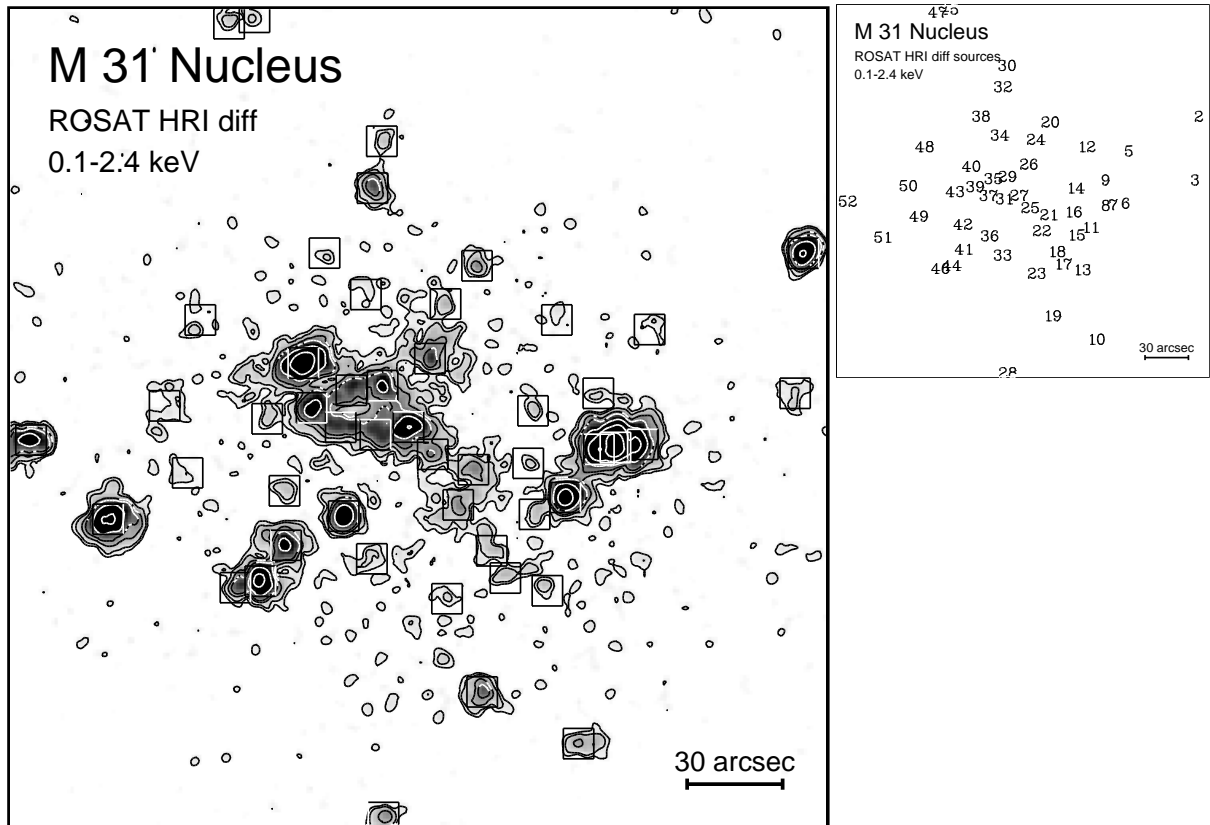


FIGURE 4.8. Contours of X-ray emission from the inner $1 \text{ kpc} \times 1 \text{ kpc}$ region of M31 in the ROSAT HRI band (0.1–2.4 keV) as result of the ‘image subtraction technique’, superposed on a linear grey-scale representation of the same image (left-hand panel). The image was constructed with a pixel size of $2''.5$ and smoothed with a Gaussian filter of $5''$ FWHM. Contour levels are at $3, 5, 10, 15, 30, 60, 120, 240$ and 500σ above the background of $6.3 \times 10^{-2} \text{ cts s}^{-1} \text{ arcmin}^{-2}$. 1σ corresponds to $1.3 \times 10^{-3} \text{ cts s}^{-1} \text{ arcmin}^{-2}$. The right-hand panel gives the location of variable HRI sources detected with the ‘image subtraction technique’. Same scale as Fig. 4.7.

4.3.2. POINT SOURCES IN A ‘VIRTUAL’ M31 OBSERVATION AT LARGER DISTANCE

Due to its proximity, M31 is the best-suited laboratory for probing the point source population in spiral galaxies. In order to further utilize the high-quality X-ray data obtained for M31 with the ROSAT HRI, the high-resolution data were compared to a ‘virtual’ observation of M31 at the distance of M51 (7.7 Mpc). In order to simulate an M31 observation at an assumed distance of M51, the pixel size of the actual M31 HRI observation was degraded by a factor of 11 (corresponding to the ratio of the M51 and M31 distances) to achieve the same pixel resolution as a high-resolution ROSAT HRI observation of M51. Furthermore, the photon statistics of the 117 ks M31 observation was reduced and artificial background noise added to the observation so as to exactly match the photon statistics of the 68 ks M51 observation. After having generated a virtual observation of M31 at the distance of M51, both the point source detection algorithm described in Sec. 3.1.1. and the ‘image subtraction technique’ were applied to the data. For the inner $3 \text{ kpc} \times 3 \text{ kpc}$ region centred on the nucleus of M31, 19 X-ray sources are detected with a likelihood exceeding $L = 8$, corresponding to 3.6σ Gaussian significance. With the ‘image subtraction technique’, 15 variable X-ray sources are detected within the same region. Fig. 4.11 (left panel) gives the variable X-ray emission of the inner $3 \text{ kpc} \times 3 \text{ kpc}$ M31 region at a virtual distance of M51. Variable X-ray sources detected with the ‘image subtraction technique’ are indicated on the right panel of Fig. 4.11, denoted with ‘D’ (‘difference’). A simulated M31 observation at a distance of M51 with $4''.7$ resolution (FWHM) is presented in Fig. 4.12 (left panel). Sources detected with a likelihood $L \geq 8$ are indicated on the right-hand panel, denoted by ‘S’ (‘simulated sources’).

Results obtained for the virtual M31 observation at the larger distance were compared with the actual high-resolution HRI observation of M31. Of the 19 sources detected with the source detection algorithm applied to the simulated observation of M31 at the distance of M51, 12 sources coincide with variable X-ray sources found with the ‘image subtraction technique’ within $2 \times$ the 90% confidence error radius of the X-ray positions. If the two source lists are compared to the actual high-resolution X-ray observation of M31 at 690 kpc, one notes that, except for one source found with the ‘image subtraction technique’ (D19), *all* the detected X-ray sources are indeed real X-ray sources. The percentage of false detections is less than 3% when both detection techniques are applied.

The source list containing 19 X-ray sources detected with a likelihood exceeding $L = 8$ was further used to compare the source luminosity distribution function of M31 at the distance of 7.7 Mpc with that of the actual distance of 690 kpc, also created with a likelihood threshold of $L = 8$. For comparison, both luminosity distributions are plotted in Fig. 4.9. Four major differences are noted:

1. The luminosity distribution function of M31 at larger distance of 7.7 Mpc is steeper with an index of $\alpha = 0.78$ when compared to $\alpha = 0.50$ for a distance of 690 kpc. As will be presented in Sec. 4.5., the power-law index of the M31 source luminosity function is very similar to that of more distant galaxies when shifted to the same distance.
2. The differences in power-law indices of the source luminosity functions for total, bulge and disk sources becomes even bigger when the photon statistics and resolution of the data is degraded. Whereas the M31 luminosity functions are best described by a power-law with indices $\alpha = 0.50$, 0.45 and 0.75 for total, disk and bulge sources using the full-resolution data obtained for a distance of 690 kpc (cf. Tab. 4.4), the indices change to $\alpha = 0.79$, 0.60 and 1.42 respectively, for the virtual M31 observation at a distance of 7.7 Mpc. The change in slope of the source luminosity functions is hence a function of the quality of the data (photon statistics, spatial resolution, etc.) and can be entirely understood by both source confusion and a degraded source detection threshold for lower-quality data. This argument is further subject to consideration in Sec. 4.5.
3. Due to the degraded detection threshold of the data when shifted to larger distance, sources at the lower end of the luminosity distribution are no longer detected.

4. At higher luminosities, previously undetected sources with apparent luminosities in the range $4 \times 10^{37} - 5 \times 10^{38} \text{ erg s}^{-1}$ are recorded. The sources are not real but are mimicked by source confusion. Each of the sources are still below or at the Eddington limit for a $1.4 M_{\odot}$ neutron star. Bright X-ray sources mimicked by source confusion hence do not explain the existence of variable superluminous X-ray sources (SLSs) detected in other galaxies with high attained luminosities up to $\sim 4 \times 10^{39} \text{ erg s}^{-1}$ (cf. Sec. 4.4.3.).

It should be stressed that all points mentioned above were also noticed for the inner bulge region of M31 at full resolution. It is hence concluded that the difference in source luminosity distribution functions when comparing disk, outer and inner bulge source is primarily an artefact generated by the higher level of diffuse X-ray emission within the bulge and also in part produced by source confusion. Also, in the inner bulge region, the source density is intrinsically significantly higher than in outer parts of the galaxy. Within a radius of $r < 1'$ centred on M31, for example, the X-ray source density is $0.12/\text{kpc}^2$, whereas in an annulus with $1' < r < 2'$ centred on M31, the source density for detected X-ray sources is $0.02/\text{kpc}^2$. Hence, source confusion is already expected to occur even at relatively high spatial resolution observations for the inner bulge regions of galaxies.

TABLE 4.5. ROSAT HRI Luminosity Function of X-Ray Sources in a virtual M31 observation at a distance of M51

Region	area (kpc^2)	no. of sources	no. of cases	constant N_0	index α
M31 total	167	38	20	28.04 ± 0.13	0.79 ± 0.05
M31 disk	166	18	20	20.86 ± 0.11	0.60 ± 0.04
M31 bulge	1	20	8	52.68 ± 0.22	1.42 ± 0.32

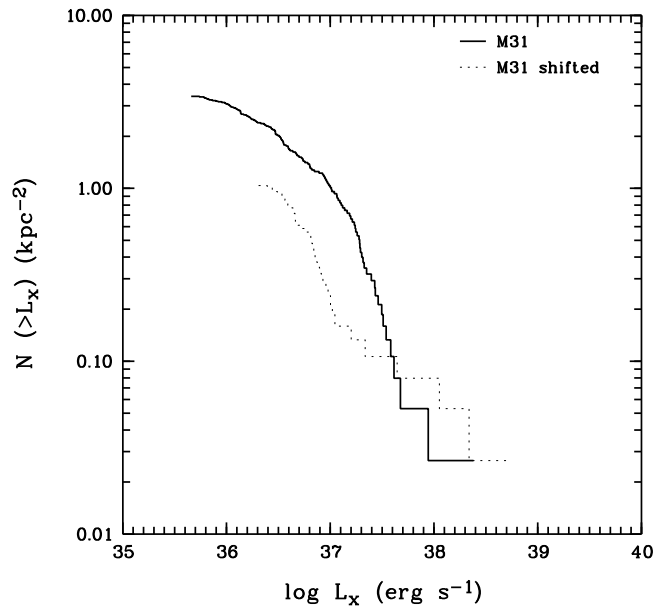


FIGURE 4.9. Luminosity distribution of ROSAT HRI X-ray sources in M31 (690 kpc) at a virtual distance of M51 (7.7 Mpc).

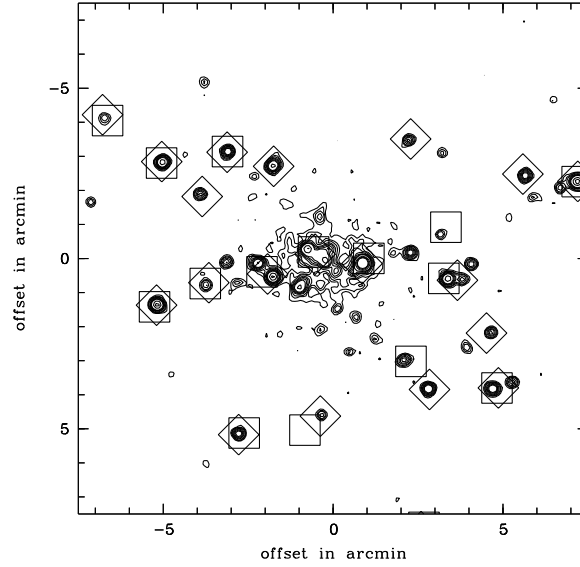


FIGURE 4.10. ROSAT HRI contour map of M31, smoothed with a Gaussian of $12''$ (FWHM). Diamonds give the positions of sources detected in the virtual observation of M31 at a distance of M51 (Fig. 4.12). Variable sources detected with the 'image subtraction technique' in the virtual observation are enclosed by boxes. The image illustrates the positional match of sources detected at a larger distance with X-ray sources seen in the high-resolution observation of M31.

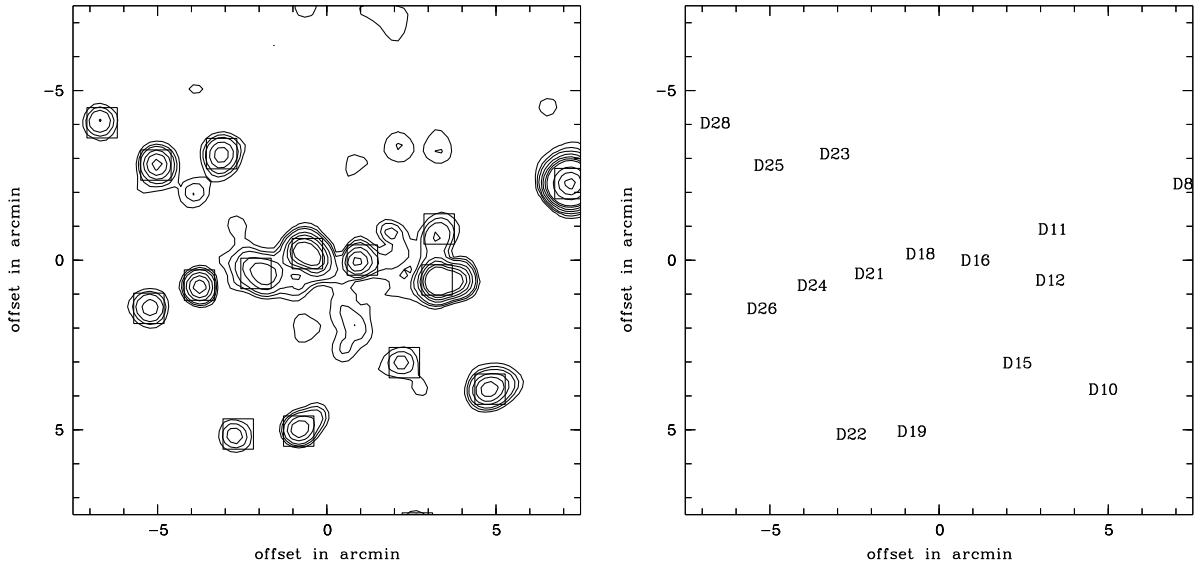


FIGURE 4.11. *Variable* X-ray emission from the M31 bulge region at a virtual distance of M51. The image is a result of the 'image subtraction technique' applied to the M31 HRI observation shifted to the distance of M51 (7.7 Mpc) for the inner $3 \times 3 \text{ kpc}^2$ region of the galaxy. Contour levels are at $3, 5, 7, 11, 15, 20, 25, 50, 75$ and 100σ above the background ($5.9 \times 10^{-2} \text{ cts s}^{-1} \text{ arcmin}^{-2}$. 1σ corresponds to $1.0 \times 10^{-3} \text{ cts s}^{-1} \text{ arcmin}^{-2}$). The right-hand panel gives the location of variable X-ray source that could be still detected with the 'image subtraction technique' with a Gaussian significance of $> 3.6\sigma$ ($L > 8$), if M31 was at the distance of M51.

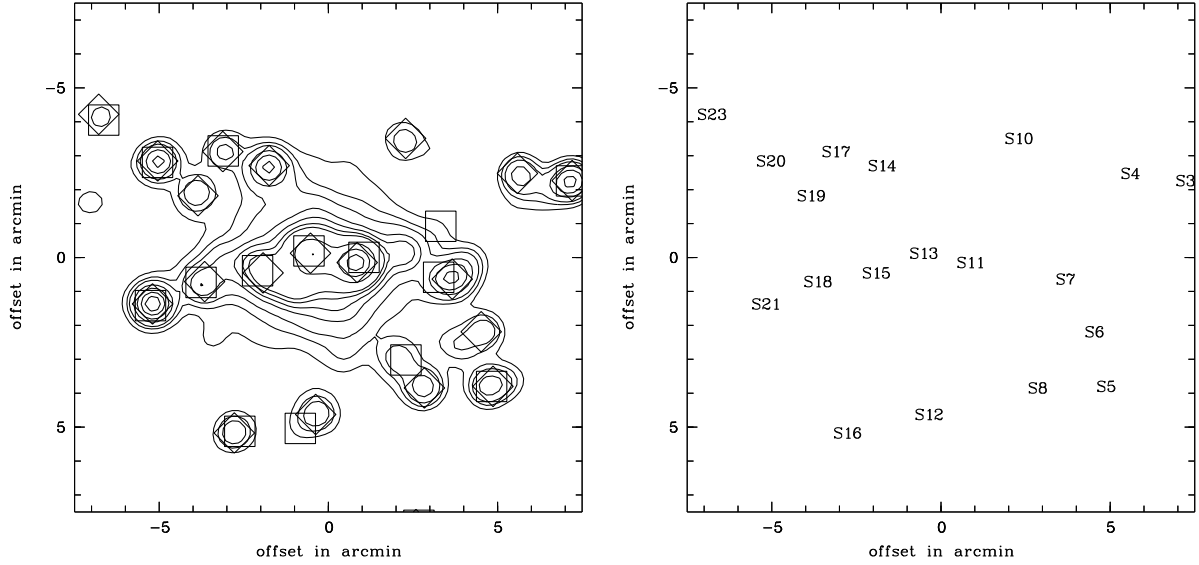


FIGURE 4.12. ROSAT HRI X-ray emission from the M31 bulge region at a virtual distance of M51. The image was constructed with a pixel size of $11''$ and smoothed with a Gaussian of $52''$ (FWHM) to attain the full point-spread-function of the HRI ($4''.7$ FWHM) if M31 was located at the distance of M51 (7.7 Mpc). The photon statistics of the observation was also reduced and random background noise added as to simulate an observation of M31 at a larger distance of 7.7 Mpc instead of 690 kpc. Contour levels and scale as in Fig. 4.11. The mean background level is 4.2×10^{-1} cts s^{-1} arcmin $^{-2}$, 1σ corresponds to 6.5×10^{-2} cts s^{-1} arcmin $^{-2}$. Diamonds mark sources detected with a Gaussian significance of $> 3.6\sigma$ ($L > 8$). The corresponding source numbers are given in the right-hand panel ('S' denotes 'shifted sources'). Positions of variable sources from Fig. 4.11 are enclosed by boxes.

4.4. POINT SOURCES IN NEARBY GALAXIES

Selecting point-like sources with a likelihood $L \geq 8$ (corresponding to 3.6σ Gaussian significance) leads to a detection of 51 X-ray sources in the $34' \times 34'$ ROSAT HRI field-of-view of M51, 37 sources in the field-of-view of M83, 33 sources in the field-of-view of M100, and 51 sources in the field-of-view of M101. The X-ray properties of the sources are summarised in Tables 7.1–7.5 in Appendix A: source number (col. 1, 'H' denotes HRI), right ascension and declination (col. 2, 3), 90% confidence error radius of the source position (col. 4, including $4''.0$ systematic error for the attitude solution), likelihood of existence (col. 5), net counts and error in the 0.1–2.4 keV ROSAT band (col. 6), count rates and error, corrected for vignetting and dead-time (col. 7), and fluxes in the ROSAT band (col. 8). Fluxes were computed assuming the corresponding galactic column densities in the galaxies line-of-sight (Dickey & Lockman 1990) and a 5 keV thermal bremsstrahlung spectrum. This is typical for point sources in normal galaxies derived from EINSTEIN observations (Fabbiano 1989). ROSAT results for point sources in normal galaxies show that they tend to have spectra of somewhat lower temperatures (~ 1 keV). Since the difference of the energy conversion factors for a 1 keV and a 5 keV thermal bremsstrahlung spectrum is less than $\sim 5\%$, a 5 keV thermal bremsstrahlung spectrum is assumed for all point sources.

Within the D_{25} ellipses of the galaxies, 24 (M51), 20 (M83), 8 (M100) and 37 X-ray sources (M101) are detected, respectively. Assuming the sources are associated with the galaxies and applying a 5 keV thermal bremsstrahlung spectrum and correcting for Galactic foreground absorption, their luminosity ranges are $L_x = (0.7\text{--}13.3) \times 10^{38}$ erg s^{-1} for M51, $(1.3\text{--}106.0) \times 10^{38}$ erg s^{-1} for M83, $(4.5\text{--}32.6) \times 10^{38}$ erg s^{-1} for M100 and $(0.4\text{--}19.0) \times 10^{38}$ erg s^{-1} for M101 (excluding the nuclei

of the galaxies which are discussed in Sec. 6.). Using the results of the ROSAT Medium Sensitivity Survey (Hasinger, Schmidt & Trümper 1991), the expected number of chance interlopers inside the D_{25} ellipses of the galaxies at the limiting fluxes are ~ 1 for M51 and M83, ~ 0.5 for M100 and ~ 8 for M101. To search for interlopers, all X-ray sources within the galaxies were cross-correlated with the SIMBAD, ROE and APM source catalogues (down to the ROE/APM limits of 21.5 mag for the DSS1 blue plates and 20.0 mag for the red plates; Irwin et al. 1994). A search radius of $2\times$ the 90% confidence error radius was adopted. $B - R$ colours of optical counterparts are quite discriminate: bright ($B \lesssim 20$) AGN essentially all have $B - R < 1$ (blue objects), while both galaxies and foreground normal stars typically have $B - R > 1$ (red objects). Bright ($R \lesssim 17$ mag) stellar (point-like) red objects are classified as Galactic stars, extended red objects as galaxies, and bright stellar objects with $B - R < 0.8$ as AGN. Although blue objects could also be white dwarfs in our Galaxy, the high expected optical brightness and the expected very soft X-ray spectral characteristics would identify them easily. For M101, 12 sources can be identified with either foreground or background objects (cf. Tab 7.12), whereas no interlopers are identified within the D_{25} ellipses of the other galaxies. The X-ray properties of individual sources are discussed in more detail in the following sections. Source luminosities and identifications with interlopers or objects assumed to be associated with the galaxies are summarized in Tabs. 7.9–7.12.

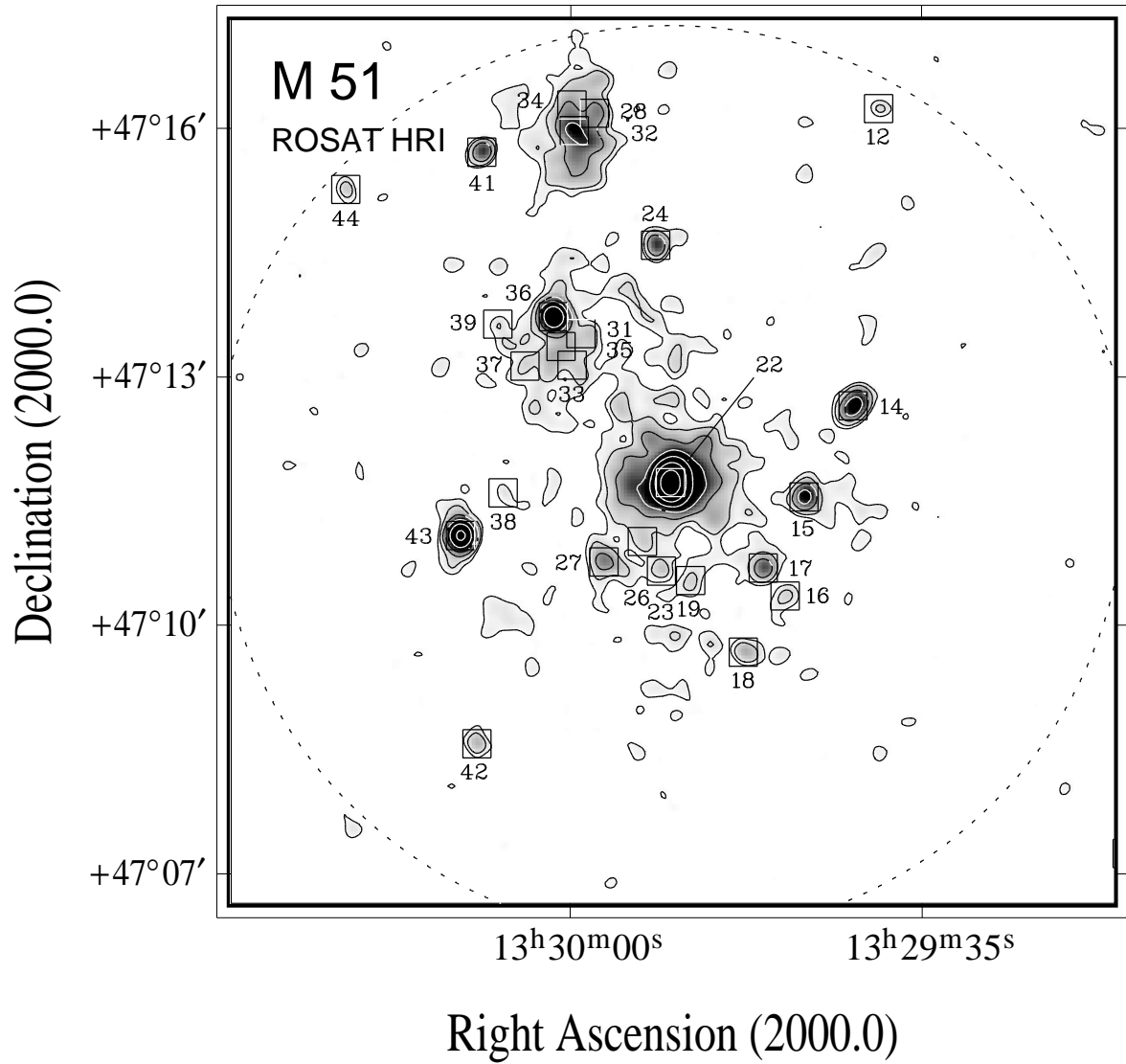


FIGURE 4.13. Contours of X-ray emission from M51 in the ROSAT HRI band (0.1–2.4 keV), superposed on a linear grey-scale representation of the same image. The image was constructed with a pixel size of $2''.5$ and smoothed with a Gaussian filter of $12''$ FWHM. X-ray contour levels are at $3, 5, 10, 20, 40, 80$ and 160σ above the mean background rate of $7.6 \times 10^{-3} \text{ cts s}^{-1} \text{ arcmin}^{-2}$. 1σ corresponds to $1.9 \times 10^{-3} \text{ cts s}^{-1} \text{ arcmin}^{-2}$. HRI sources are enclosed by boxes and enumerated according to the source list (Tab. 7.2). The D_{25} ellipse of the galaxy is indicated by the dotted line.

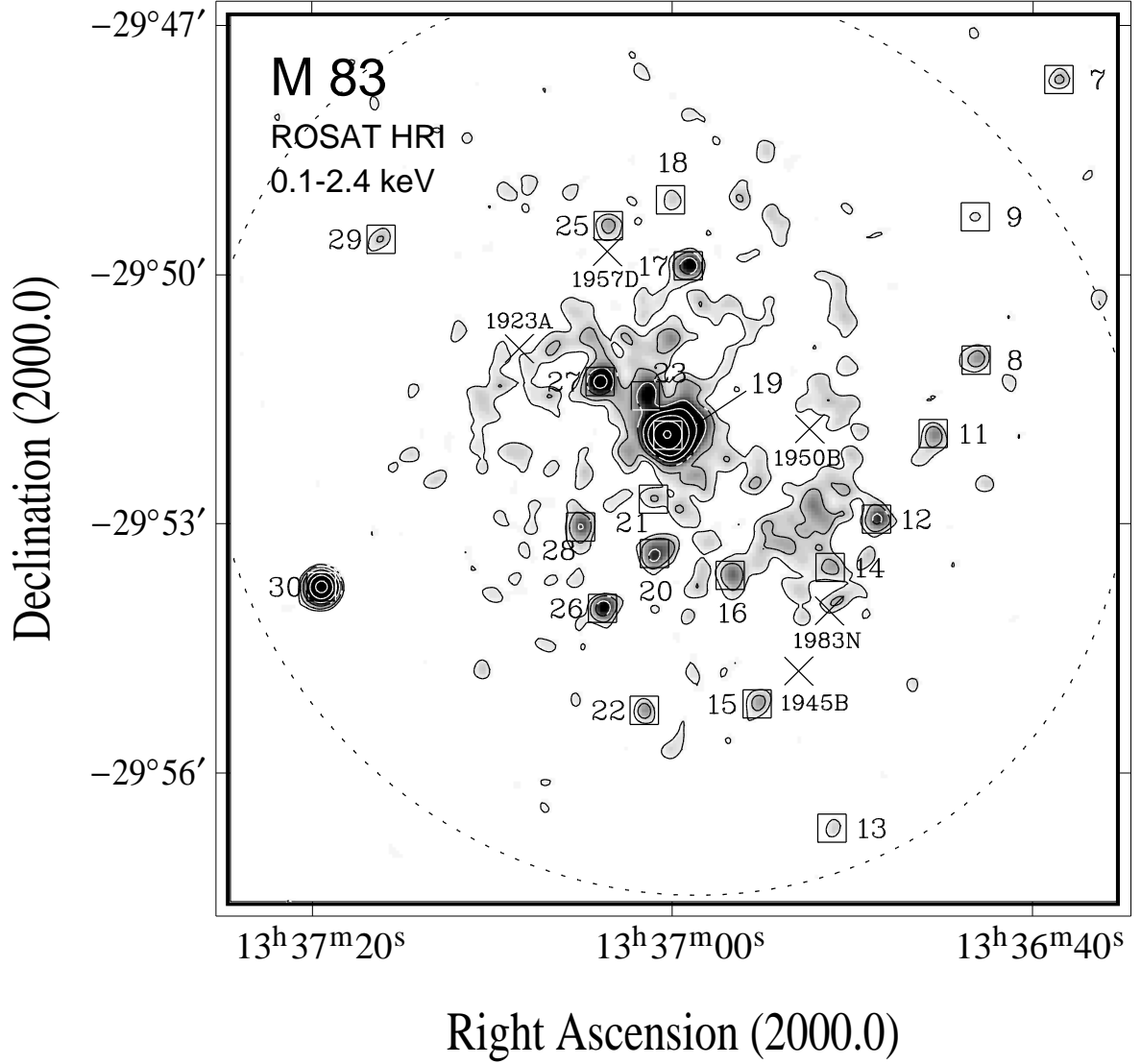


FIGURE 4.14. Contours of X-ray emission from M83 in the ROSAT HRI band (0.1–2.4 keV), superposed on a linear grey-scale representation of the same image. The image was constructed with a pixel size of $2''.5$ and smoothed with a Gaussian filter of $12''$ FWHM. X-ray contour levels are at $3, 5, 10, 20, 40, 80$ and 160σ above the mean background rate of $7.5 \times 10^{-3} \text{ cts s}^{-1} \text{ arcmin}^{-2}$. 1σ corresponds to $2.9 \times 10^{-3} \text{ cts s}^{-1} \text{ arcmin}^{-2}$. HRI sources are enclosed by boxes and enumerated according to the source list (Tab. 7.3). The positions of supernovae are marked with crosses and the D_{25} ellipse of the galaxy is indicated by the dotted line.

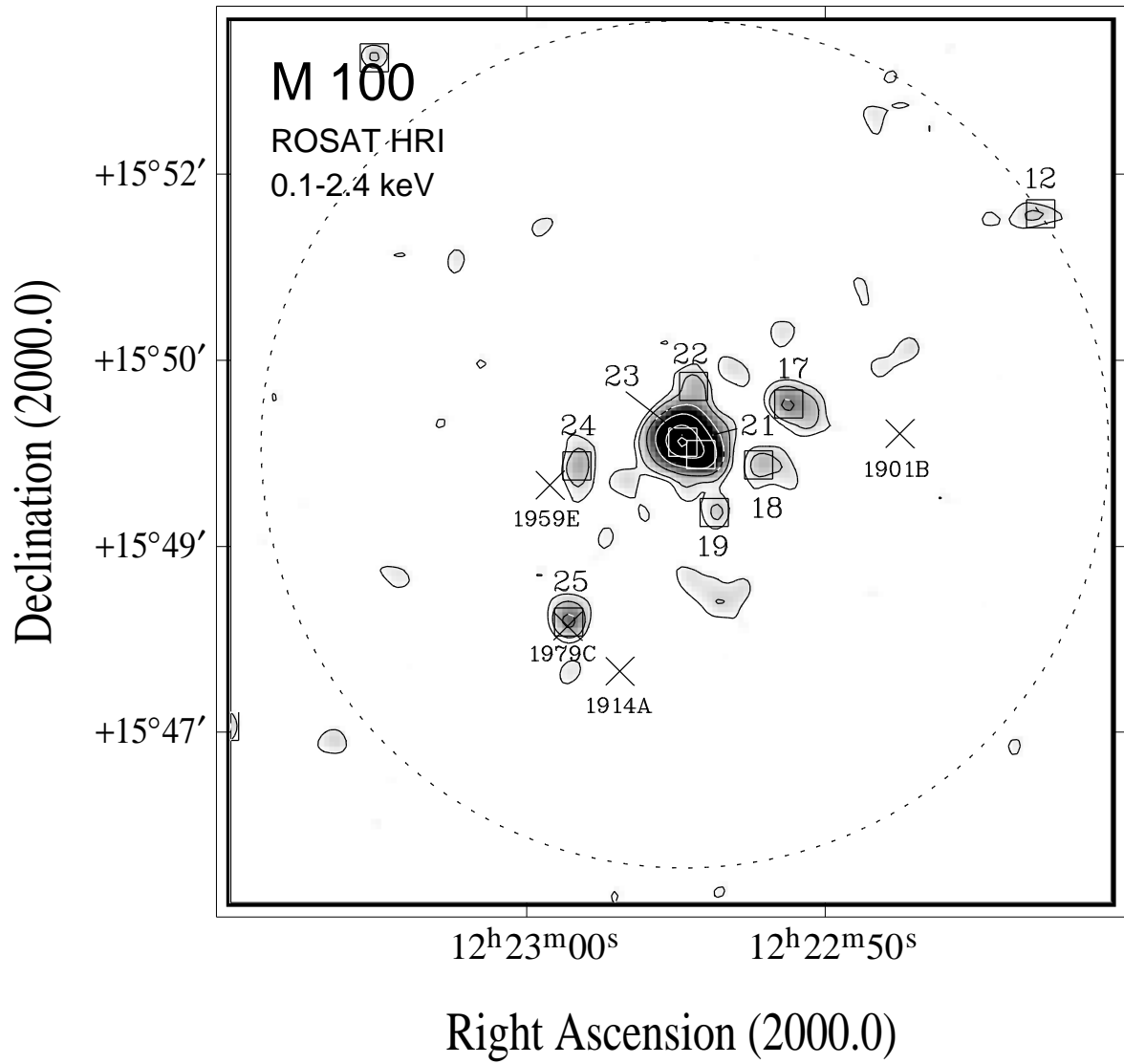


FIGURE 4.15. X-ray contour map of M100, superposed on an digitized Palomar Observatory Sky Survey plate. The lines give (0.1–2.4 keV) band X-ray contours from the 42.8 ks HRI observation, smoothed with a Gaussian of $12''$ (FWHM). Contour levels are at $3, 5, 10, 20$ and 40σ above the mean background rate (4.2×10^{-3} cts s^{-1} arcmin $^{-2}$, $1\sigma \cong 1.2 \times 10^{-3}$ cts s^{-1} arcmin $^{-2}$). HRI sources are enclosed by boxes and enumerated according to the source list (Tab. 7.4). The D_{25} ellipse of the galaxy is indicated by the dotted line.

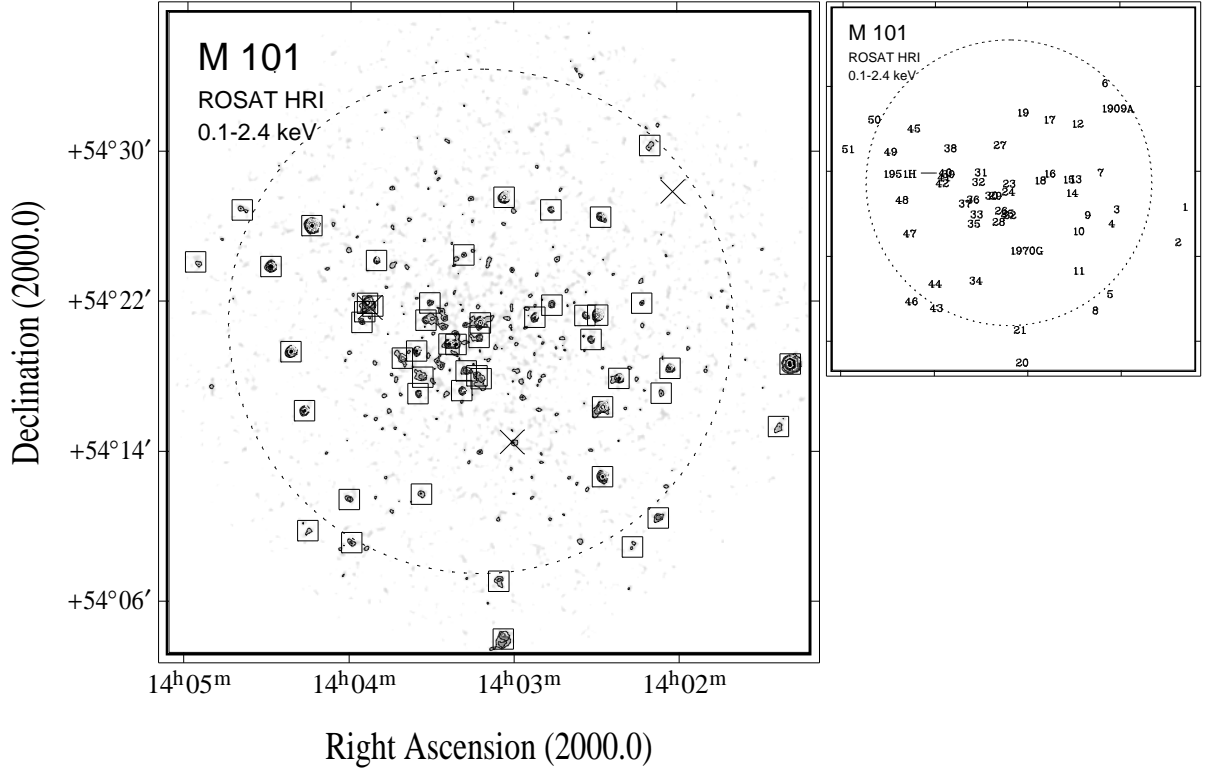


FIGURE 4.16. Contours of X-ray emission from M101 in the ROSAT HRI band (0.1–2.4 keV), superposed on a linear grey-scale representation of the same image (left-hand panel). The image was constructed with a pixel size of $5''$ and smoothed with a Gaussian filter of $12''$ FWHM. X-ray contour levels are at $3, 5, 10, 20, 40$ and 80σ above the mean background rate of 1.7×10^{-2} cts $\text{s}^{-1} \text{ arcmin}^{-2}$. 1σ corresponds to 1.9×10^{-3} cts $\text{s}^{-1} \text{ arcmin}^{-2}$. The positions of supernovae are marked with crosses and the D_{25} ellipse of the galaxy is indicated by the dotted line. The upper right-hand panel gives the location of HRI sources and SNe in M101 (Tab. 7.5).

4.4.1. HII REGIONS

TABLE 4.6. X-Ray Emitting HII Regions

Galaxy	Source	L_x ($10^{38} \text{ erg s}^{-1}$)	comment
M51	H14	5.1 ± 0.5	HII region, HI hole, variable
	H15	3.4 ± 0.4	HII region, HI hole, variable
	H16	0.9 ± 0.3	HII region, 6 cm radio source
	H18	1.0 ± 0.3	HII region, HI hole
	H19	1.0 ± 0.3	HII region, HI hole
	H23	0.8 ± 0.2	HII region
	H24	2.4 ± 0.3	HII region
	H26	0.8 ± 0.2	HII region
	H27	2.4 ± 0.4	HII region
	H35	2.5 ± 0.4	HII region
	H36	11.3 ± 4.9	HII region, variable
	H37	0.7 ± 0.2	HII region
	H43	13.3 ± 0.8	HII region, variable
M83	H21	1.4 ± 0.5	HII region
	H23	6.7 ± 1.1	SNR candidate, HII region 6 cm and 20 cm radio source
	H26	3.7 ± 0.8	SNR candidate, HII region 6 cm and 20 cm radio source
M100	H24	6.2 ± 1.8	HII region
M101	H37	1.1 ± 0.2	HII region, NGC 5461
	H40	2.2 ± 0.2	HII region, HI hole, NGC 5462, SN 1951H
	H49	3.5 ± 0.3	HII region, NGC 5471

Many individual X-ray sources in the galaxies coincide with optically luminous HII regions (cf. Tab. 4.6). A large fraction of them also coincides with HI holes or at least a local depression in the neutral hydrogen distribution, indicating energetic phenomena such as outflow of gas into the halo. However, variable sources found to coincide with HII regions clearly point towards the X-ray emission being due to X-ray binaries associated with the HII region, like H14, H15, H36 and H43 in M51, the latter being variable by a factor of > 5 on a timescale of just hours (cf. Fig. 7.3). Non-variable X-ray sources positionally associated with HII regions and/or HI holes are suggestive of a correlation of X-ray emission with star-formation regions. However, the inferred luminosities of $\gtrsim 10^{38} \text{ erg s}^{-1}$ for each individual candidate is rather high when compared to X-ray sources identified with hot gas within HII regions found in the LMC, which typically have some $\times 10^{37} \text{ erg s}^{-1}$ in the ROSAT band (cf., e.g. Wang & Helfand 1991; Bomans, Dennerl & Kürster 1994; Williams & Chu 1995). PSPC observations of nearby galaxies have shown that HII regions typically have soft ($\sim 0.5 \text{ keV}$) spectra in the ROSAT band. The low-temperature component found to be associated with truly diffuse hot gas inside giant HII complexes in M101 or in the Large Magellanic Cloud, for example, have temperatures of $0.26\text{--}0.60 \text{ keV}$ in the ROSAT band. Given the limited spatial resolution of the HRI at the distance of the galaxies and the absence of good spectral information, the possibility that the sources consist of multiple X-ray-emitting objects, such as unresolved emission from hot gas, young SNe, SNR and/or X-ray binaries, cannot be ruled out. Also, since some of the sources are associated with young SNe, SNR and BH candidates, discussed in the following sections, there is no clear evidence for the X-ray emission being solely due to hot gas from within, or outflow from, HII regions.

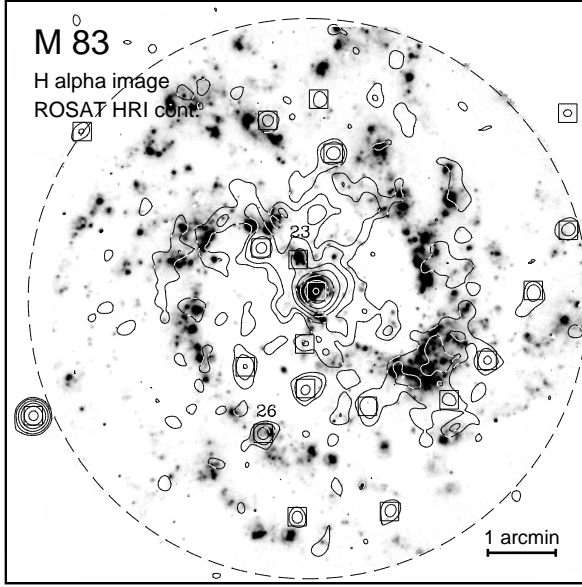


FIGURE 4.17. Overlay of HRI contours (12'' FWHM) on an H α map of M83 (kindly provided by Stuart Ryder). Contour levels are as in Fig. 4.14. SNR candidates are marked with the HRI source number. The dashed lines gives the H α image field-of-view.

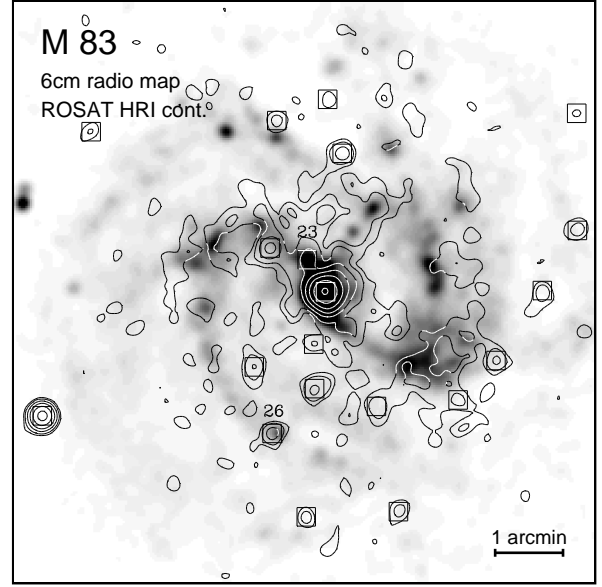


FIGURE 4.18. Overlay of HRI contours (12'' FWHM) on a 6 cm radio continuum map of M83 (Sukumar et al. 2000). Contour levels are as in Fig. 4.14 and the scale is as in Fig. 4.17. SNR candidates H23 and H26 are marked with the HRI source number.

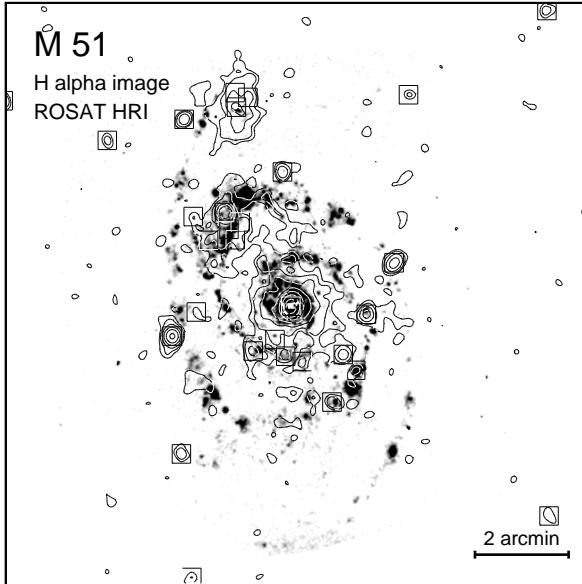


FIGURE 4.19. Overlay of HRI contours (12'' FWHM) on an H α map of M51 (van der Hulst et al. 1988). Contour levels are as in Fig. 4.13. HRI sources are enclosed by boxes.

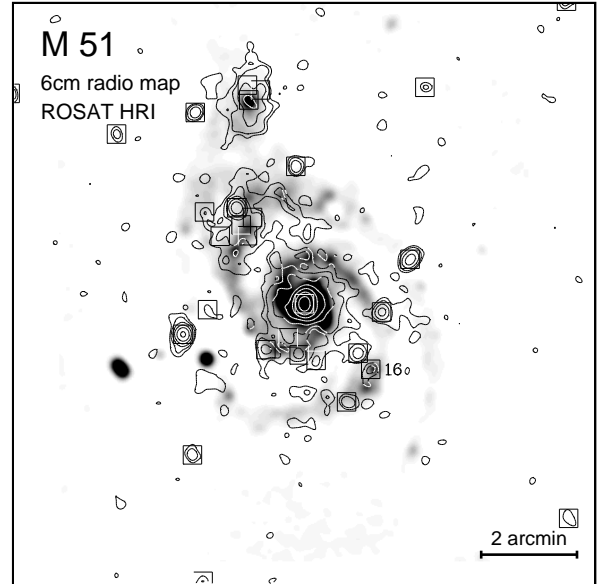


FIGURE 4.20. Overlay of HRI contours (12'' FWHM) on a 6 cm radio continuum map of M51. Contour levels are as in Fig. 4.13 and the scale is as in Fig. 4.19. The SNR candidate H16 is marked with its HRI source number.

4.4.2. SUPERNOVA REMNANTS

TABLE 4.7. X-Ray Emitting SNR Candidates

Galaxy	Source	L_x ($10^{38} \text{ erg s}^{-1}$)	comment
M31	H86	0.071 ± 0.004	6 cm radio source
	H118	0.063 ± 0.004	6 cm radio source
	H123	0.019 ± 0.004	6 cm radio source
M51	H16	0.9 ± 0.3	HII region, 6 cm radio source
M83	H23	6.7 ± 1.1	SNR candidate, HII region, 6 cm and 20 cm radio source
	H26	3.7 ± 0.8	HII region, 6 cm and 20 cm radio source
M101	H19	7.3 ± 0.3	6 cm and 20 cm radio source, variable
	H29	1.5 ± 0.2	6 cm and 20 cm radio source
	H30	1.3 ± 0.2	6 cm and 20 cm radio source
	H36	1.3 ± 0.2	6 cm and 20 cm radio source

To search for SNR candidates we correlated X-ray emission with $H\alpha$ and radio emission by superposing HRI X-ray contours on $H\alpha$ and radio maps of the galaxies.

In M83, two X-ray sources (H23 and H26) coincide with both compact radio sources and $H\alpha$ emission complexes within the north-eastern spiral arm. The sources are marked in Figs. 4.17 (red continuum-subtracted $H\alpha$ image, kindly provided by Stuart Ryder) and 4.18 (6 cm radio continuum map; Sukumar et al. 2000) according to the HRI source number (Tab. 7.3). The non-variable X-ray source H23 ($6.7 \times 10^{38} \text{ erg s}^{-1}$) coincides with a radio source and an HII region located just $\sim 30''$ north-east of the nucleus. Comparison with radio maps of Cowan et al. (1985, 1994) shows that the radio source is detected both at 6 cm and at 20 cm. However, since the source is not included in the source list of Cowan et al., we have no further information as to the radio properties of this source. More results are available on this region in the optical band, based on the emission line strengths reported by Dufour et al. (1980). Spectroscopic observations of the HII region coinciding with H23 (source I in Dufour et al. 1980) show an emission line ratio of $[\text{SII}]/\text{H}\beta = 0.21$. If this is scaled to the emission line intensity ratio $I(\text{H}\alpha)/I(\text{H}\beta) = 3.03$, as assumed by Dufour et al., a high emission line ratio of $[\text{SII}]/\text{H}\alpha = 0.63$ is derived. Since emission line nebulae with $[\text{SII}]/\text{H}\alpha \geq 0.45$ are usually identified with SNR (cf., e.g. Matonick & Fesen 1997), the result is indicative for the presence of a SNR at the position of H23. The detection of radio emission from this region further strengthens the assumption that the X-ray emission is due to a single luminous SNR or a collection thereof.

H26 also coincides with a giant HII region (source #120 in Rumstay & Kaufman 1983; $\log S_\alpha = -12.149$). However, the extent of the HII complex clearly exceeds that of the point-like X-ray source (cf. Fig. 4.17). The observed anti-coincidence of $H\alpha$ and $\text{H}\beta$ emission with HI emission (Tilanus & Allen 1993) supports the assumption of an X-ray luminous SNR, since the hydrogen is expected to be completely ionized at the position of SNRs. Unfortunately, no emission line ratio measurements are available from this region, leaving the SNR indicator $[\text{SII}]/\text{H}\alpha$ unknown.

The radio counterpart of H26 is listed as source 8 in Cowan, Roberts & Branch (1994). The radio source is detected at 6 cm and 20 cm and is described as a non-thermal radio source based on its flat radio spectrum. ($S_{6\text{cm}}$ and $S_{20\text{cm}} \sim 0.7 \text{ mJy}$). However, as Deutsch & Allen (1993) pointed out, intensive studies of the eastern spiral arm of M83 in the optical and radio regime have demonstrated that the emission in the neighbourhood of giant HII regions is predominantly non-thermal. The authors argue that the emission is mainly due to enhanced production of high-energy radiation (hard X-rays and cosmic rays) from historical supernovae. The observation of a bright CO emission complex coinciding with that region, excited by the enhanced production of high energetic cosmic rays from a SNR, points also towards the existence of an X-ray luminous SNR (Wiklind et al. 1990; Rand, Steven & Higdon 1999).

The HRI source H26 corresponds to the X-ray source P9 detected in the ROSAT PSPC observation.

Extracting photons from the position of P9 (120 net photons) and fitting spectral models to the data indicate a rather soft (0.3 keV) and highly absorbed spectrum ($N_{\text{H}} = 1.5 \times 10^{21} \text{ cm}^{-2}$) for the best fit thermal bremsstrahlung model ($\chi^2/\nu = 1.05$). A Raymond & Smith spectral fit gives the same temperature, whereas the absorption is a factor of 3 lower and its χ^2/ν value (3.13) worse. The PSPC luminosity of P9 ($7.5 \times 10^{38} \text{ erg s}^{-1}$) is slightly higher than the inferred HRI luminosity ($3.7 \times 10^{38} \text{ erg s}^{-1}$). Given the rather low temperature and the better response of the PSPC instrument in the soft band, the higher PSPC luminosity is consistent with the source being constant over several years.

The observed soft X-ray spectrum of H26 is typical of X-ray luminous SNRs. ROSAT and ASCA observations of the Galactic SNR RCW 103 (Gotthelf, Petre & Vasisht 1999) and the Honeycomb SNR in the LMC (Chu et al. 1995b), as well as the SNR complex N44 in the LMC (Magnier et al. 1996; Chu et al. 1993), N11L and N186 (Williams et al. 1999a) gave matching spectral parameters. However, most identified X-ray emitting SNRs to date have luminosities of the order of 10^{35} – $10^{37} \text{ erg s}^{-1}$ in the 0.1–2.4 keV band. H23 and H26 are significantly more luminous (6.7 and $3.7 \times 10^{38} \text{ erg s}^{-1}$, respectively, for a 0.3 keV thermal plasma spectrum).

The high luminosities may be explained by the cumulative emission of a high number of historical SNRs located at these positions. Alternatively, the sources might be energetic hypernovae remnants, which are expected to be an order of magnitude more luminous than SNRs. Recently, evidence for the presence of two X-ray luminous hypernova remnants in the galaxy M101 was presented, with luminosities similar to the SNR candidates reported in this paper (regions NGC 5471B and MF83 in M101; Wang 1999; see also Wang, Immler & Pietsch 1999). In terms of luminosity (3.0 and $1.2 \times 10^{38} \text{ erg s}^{-1}$), spectral parameters (0.3 keV best thermal plasma fit) and $[\text{SII}]/\text{H}\alpha$ emission line ratios of 0.51 and 0.76, respectively, the hypernova remnant candidates are strikingly similar to H23 and H26 (Wang 1999). The observed optical extent of the two remnants NGC 5471B and MF83 ($\geq 175 \text{ pc}$ and $\sim 86 \text{ pc}$, respectively) is below the resolving power of the HRI instrument ($\sim 200 \text{ pc}$) at the distance of M83.

However, as optical follow-up observations of the brightest known SNR found to date, SNR MF16 in NGC 6946, showed, there is no necessity for exotic objects like hypernova remnants to explain the high X-ray luminosities. With a (0.1–2.4 keV band) PSPC luminosity of $2.8 \times 10^{39} \text{ erg s}^{-1}$ (Schlegel 1994; Dunne, Gruendl & Chu 2000), SNR MF16 in NGC 6946 is ~ 1000 as luminous as the young Galactic remnant Cas A, ~ 3.5 times as luminous as the young SNR in NGC 4449 (Vogler & Pietsch 1999; Blair, Fesen & Schlegel 1997; Blair & Fesen 1994) and 4–8 times as luminous as M83 H23 and H26. It should be noted in passing, however, that HRI observations not discussed by Schlegel (1994) or Dunne, Gruendl & Chu (2000) clearly resolve the PSPC source into two point-like HRI sources. With a luminosity ratio of 15 : 1, the contribution of the second X-ray source to the PSPC luminosity of the SNR is negligible. Optical follow-up observations with the HST demonstrated that the X-ray luminous remnant can be attributed to a single SN explosion expanding into a dense shell of material. The multiple-loop morphology of the remnant is suggestive that the progenitor has shaped multiple shells of ambient material around the evolving star via main-sequence wind, supergiant wind and Wolf-Rayet wind (Dunne, Gruendl & Chu 2000). The detection of narrow emission lines with echelle spectroscopy confirmed the existence of such dense circumstellar material. The high nitrogen abundance and high $[\text{NII}]/\text{H}\alpha$ emission line ratio of ~ 1 also point towards the ambient matter being associated with nitrogen-rich Wolf-Rayet winds. If the remnant MF16 is assumed to be associated with a single SN explosion, Dunne, Gruendl & Chu (2000) derive an age of $\sim 25000 \text{ yrs}$ and determine the total released energy to be $\sim 3 \times 10^{50} \text{ erg s}^{-1}$. Hence, no exotic objects like hypernovae with a total energy output of $\sim 10^{53} \text{ erg s}^{-1}$, as in the case of the two hypernova remnant candidates in M101 (Wang 1999), are required.

The discussion above shows that without further knowledge, the luminous X-ray sources H23 and H26 in M83 may be due to hot gas, heated by either single or multiple supernova explosions. An energetic single hypernova explosion, however, cannot be ruled out.

Apart from the new SNR candidates in M83 presented above, four X-ray sources in M101 are positionally coincident with optically identified SNR, with luminosities ranging from 1.3 to $7.3 \times 10^{38} \text{ erg s}^{-1}$ (H19, H29, H30, H36; cf. Tab. 4.7). In M51, one X-ray source is associated with strong radio emission, suggestive of the X-ray source being due to a SNR (H16, $9 \times 10^{37} \text{ erg s}^{-1}$; cf. Tab. 4.7). In M31, four X-ray sources with (rather low) luminosities ranging from 1.9 to $7.1 \times 10^{36} \text{ erg s}^{-1}$ coincide positionally with identified SNRs. The number of identified X-ray emitting SNRs in nearby galaxies and their attained luminosities emphasize that SNRs are an important class of X-ray objects within spirals and contribute up to $\sim 10\%$ (e.g. in M101) to the overall X-ray emission of the galaxies.

4.4.3. SUPERLUMINOUS X-RAY SOURCES

TABLE 4.8. Superluminous X-Ray Sources

Galaxy	Source	L_x ($10^{38} \text{ erg s}^{-1}$)	comment
M51	H14	5.1 ± 0.5	HII region, H _I hole, variable
	H36	11.3 ± 4.9	HII region, variable
	H43	13.3 ± 0.8	HII region, variable
M83	H20	5.6 ± 1.0	HII region, 6 cm and 20 cm radio source
	H23	6.7 ± 1.1	
	H27	10.0 ± 1.1	
	H30	38.0 ± 2.1	faint optical counterpart, variable
M100	H17	13.4 ± 2.8	variable
	H21	32.6 ± 3.8	variable
	H24	6.2 ± 1.8	HII region, variable
	H25	11.0 ± 2.4	SN 1979C
M101	H13	7.9 ± 0.3	star, variable
	H19	7.3 ± 0.3	SNR, variable
	H45	19.0 ± 0.5	variable

Some persistent X-ray sources found within the D_{25} ellipses of the galaxies have luminosities exceeding the Eddington limit for a $1.4 M_{\odot}$ neutron star. Within this work, X-ray sources with luminosities in excess of $5 \times 10^{38} \text{ erg s}^{-1}$ are denoted ‘super-Eddington’ or ‘superluminous X-ray sources’ (SLSs). Detected SLSs are compiled in Tab. 4.8. The nature of these SLSs, which have also been reported in several additional galaxies, is still unclear. Possible explanations are massive black holes with high accretion rates, accreting magnetised neutron stars and collections of unresolved weaker point sources. If the sources are due to mass-accreting X-ray binaries, optical counterparts are only expected at the given large distances of the galaxies if they are located in globular clusters.

Within the D_{25} ellipse of M51, three sources (H14, H36, H43; cf. Tab. 4.8) have fluxes greater than $7.3 \times 10^{-14} \text{ erg cm}^{-2} \text{ s}^{-1}$ in the 0.1–2.4 keV band, clearly exceeding the Eddington limit for a $1.4 M_{\odot}$ accreting neutron star. It should be noted that within this work, a rather conservative, short distance is assumed (7.7 Mpc; de Vaucouleurs 1979) instead of the widely quoted 9.6 Mpc (Sandage & Tamman 1975), which would further increase the number of SLSs in M51.

All SLSs in M51 are variable during the HRI period of observation (cf. Tab. 4.8 and Figs. 7.1 and 7.2), as will be discussed in the following:

- H14 is variable by a factor of > 3.5 on long timescales (months). The likelihood ratio test performed on binned 10 ks time intervals gives a probability of $P = 99.9\%$ (3.6σ significance) for the source being variable. The luminosity of the EINSTEIN source corresponding to H14 (source C in Palumbo et al. 1985; $6.2 \times 10^{38} \text{ erg s}^{-1}$ corrected for a distance of 7.7 Mpc) and the ROSAT PSPC source (source R7 in Marston et al. 1985; $5.4 \times 10^{38} \text{ erg s}^{-1}$ corrected for a distance of 7.7 Mpc) are similar to the mean ROSAT HRI luminosity ($5.1 \times 10^{39} \text{ erg s}^{-1}$). Due to the observed high luminosity and variability, as well as to the absence of an optical counterpart, the source is categorized as a black hole candidate (BHC).

- H36 in M51 is also observed to be variable on long timescales (months), as the source is not detected in two of the 5 HRI observation blocks with similar integration times of ~ 10 ks each. Also, the EINSTEIN luminosity of the X-ray source (source C in Palumbo et al. 1985; $1.1 \times 10^{39} \text{ erg s}^{-1}$) is almost a factor of 2 lower than the mean luminosity inferred from the ROSAT HRI observations ($1.1 \times 10^{39} \text{ erg s}^{-1}$). Source H36 is located in a massive star formation region within the north-eastern spiral arm of M51. It coincides with a strong HII complex, as well as with a peak in the radio continuum emission. Since the source is variable, a number of individual, unresolved sources and/or hot gas associated with the star formation region cannot account for its high luminosity. It is hence quite plausible that the emission is due to a variable BHC associated with the star formation region.

◦ For H43, the timing analysis of the HRI data shows high variability on short timescales of just hours (factor ~ 5 ; probability of variability: $P = 100.0\%$, $> 8\sigma$ significance), indicative of the presence of an accreting binary. During the ROSAT PSPC observation, the corresponding source R3 (Marston et al. 1995) attained a luminosity almost a factor of 2 higher ($2.0 \times 10^{39} \text{ erg s}^{-1}$ corrected for a distance of 7.7 Mpc) than observed with the HRI ($1.3 \times 10^{39} \text{ erg s}^{-1}$). The source luminosity inferred from the EINSTEIN observation is slightly lower than the HRI luminosity (source B in Palumbo et al. 1985; $9.0 \times 10^{38} \text{ erg s}^{-1}$). Interestingly, the source appears to be extended in ROSAT HRI images (cf. Fig. 4.13), indicating that a fraction of the emission arises from hot gas associated with the HII complex coinciding with H43 (HII region S184 in Scowen 1992). The short-term variability and the high inferred luminosity are suggestive of the presence of a massive BH X-ray binary.

Of the 21 sources detected inside the D_{25} ellipse of M83, 4 sources (H20, H23, H27 and H30; cf. Tab. 4.8) have fluxes greater than $5.3 \times 10^{-14} \text{ erg cm}^{-2} \text{ s}^{-1}$ in the 0.1–2.4 keV band (Tab. 7.10). If associated with M83, and assuming a distance of 8.9 Mpc, each source has a luminosity of $\geq 5 \times 10^{38} \text{ erg s}^{-1}$. It should be noted, however, that distance estimates to M83 range rather significantly from 3.75 to 8.9 Mpc. At a distance of 3.75 Mpc, only H30 would still be super-Eddington ($6.7 \times 10^{38} \text{ erg s}^{-1}$). In the following, these sources will be discussed in more detail:

◦ A fraction of these super-Eddington sources might be interlopers (stars, AGN, quasars, etc.). Based on the results of the ROSAT Medium Sensitivity Survey (Hasinger, Schmidt & Trümper 1991), the expected number of chance interlopers inside the D_{25} ellipse of M83 at the limiting flux is 1.3. H20 might be such an interloper, since it is located between two spiral arms of the galaxy in a region of exceptionally low HI density. No optical counterpart, however, is visible in deep optical plates within the positional error of the X-ray source.

◦ H23 coincides with a compact 6 cm and 20 cm radio source and a bright $\text{H}\alpha$ emission region in the north-eastern spiral arm of M83. No variability is observed within the HRI observations. In Sec. 2.3.3., strong evidence was presented that this source is due to hot gas, heated by multiple SNRs or a hypernova remnant, based on its multi-wavelength characteristics. Since black hole candidates (BHCs) are also believed to be linked to star formation activity in the disk, H23 might also be a good BHC. However, with the limited spatial resolution of the HRI observations and given that H23 is not variable, we cannot rule out the possibility that this SLS is due to a collection of X-ray-emitting objects, such as unresolved emission from hot gas, young SNe, SNR and/or X-ray binaries. Such sources have been found also in other nearby spiral galaxies. Giant HII regions in M101, for example, have X-ray luminosities exceeding the Eddington limit for a single accreting object (Wang, Immler & Pietsch 1999). Both the X-ray morphology and spectral characteristics of the X-ray emitting HII regions in M101 suggest a multi-component superposition of X-ray sources.

◦ H27 is located close to a bright HII region within the north-eastern spiral arm of M83. This source is neither variable during the HRI observation nor on longer timescales, as comparison with the PSPC and Einstein HRI observations shows. As expected for a BHC, the source has no optical counterpart down to the APM magnitude limit. Hence, H27 might either be an accreting black hole or an interloper projected onto the galaxies disk.

◦ H30 is the brightest X-ray source in M83, apart from the nuclear X-ray source. It has a luminosity of $3.8 \times 10^{39} \text{ erg s}^{-1}$, clearly exceeding the Eddington limit for a $\sim 1.4 M_{\odot}$ accreting neutron star. Timing analysis shows that H30 is variable during the HRI period of observation by a factor of ~ 3 (cf. Fig. 7.4). The likelihood ratio test performed on binned 6 ks time intervals gives a probability of $P = 99.8\%$ (3.1σ significance) for the source being variable. The detections algorithm shows that the source is not extended.

H30 was also detected in the PSPC hard band (P19; Ehle et al. 1998). The (0.5–2.0 keV) hard band PSPC luminosity ($3.6 \times 10^{39} \text{ erg s}^{-1}$) is similar to the HRI luminosity, indicating no long-term variability.

Source H30 is the only source in M83 that was detected both by the EINSTEIN IPC and HRI (Trinchieri, Fabbiano & Palumbo 1985). Although the EINSTEIN (0.5–3.0 keV) HRI luminosity is

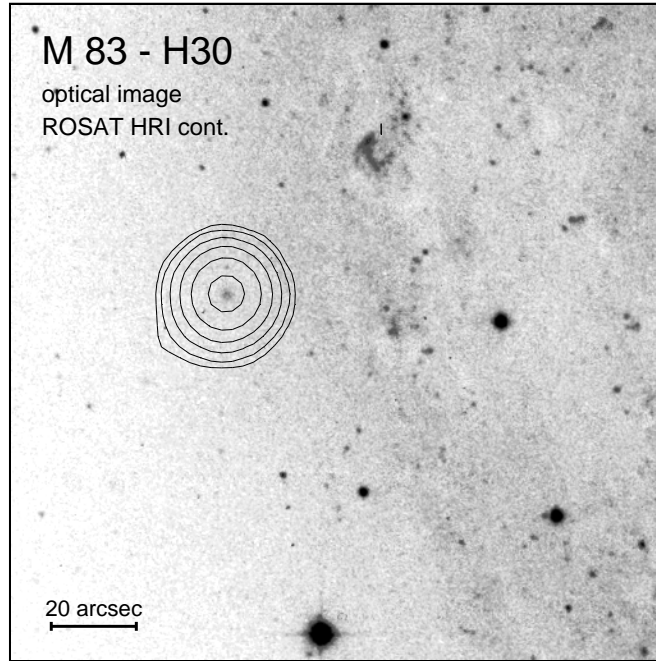


FIGURE 4.21. Overlay of HRI contours of the superluminous source H30 in M83 onto a deep AAO optical image (kindly provided by David Malin). Same contour levels as in Fig. 4.14.

slightly lower ($H2: 2.4 \times 10^{39} \text{ erg s}^{-1}$), it is still consistent with the EINSTEIN IPC ($I2: 3.9 \times 10^{39} \text{ erg s}^{-1}$) and ROSAT HRI luminosity, indicating no long-term variability. The IPC hardness ratio of 1.5 ± 0.4 , defined as the ratio of net counts in the (0.8–3.5 keV) band to those in the (0.2–0.8 keV) band, shows that the source is neither particularly soft nor highly absorbed.

To further investigate the nature of H30, we used the spectral capabilities of the PSPC. Given the point-like nature of H30, we extracted photons within an extraction circle of $30''$ diameter, containing a total of 428 photons. Background photons were extracted from an annulus with radius $30'' - 50''$, centred on the source position. The spectrum was binned into energy bands with signal-to-noise ratio of > 5 and thermal Bremsstrahlung (THBR), power-law (POWL) and thin thermal plasma models (RASM) were fitted to the data. All spectral models gave reasonable good fits with $\chi^2/\text{d.o.f.}$ values of the order of ~ 1 . Despite the good spectral fit ($\chi^2/11 = 1.11$), the RASM fitted to the data resulted in a total absorption similar to the Galactic foreground absorption only ($N_H = (4.04 \pm 1.60) \times 10^{20} \text{ cm}^{-2}$). The POWL fit resulted in an intrinsic absorption (after subtracting the Galactic column) of $N_H = (2.42 \pm 0.98) \times 10^{20} \text{ cm}^{-2}$ and a photon index of 1.09 ± 0.60 , rather typical of quasars. Its $\chi^2/\text{d.o.f.}$ value is slightly worse (1.22) than that of the THBR fit (1.07), which gives a temperature of $(2.30 \pm 1.30) \text{ keV}$, fixing the total absorbing column to the best fit value of $5.46 \times 10^{20} \text{ cm}^{-2}$. The PSPC spectrum of H30, its thermal bremsstrahlung fit and residuals are given in Fig. 4.22, together with the χ^2 contours. It can be seen from the χ^2 grid that H30 has a source temperature exceeding 1 keV at a 99.7% confidence level.

As already noted by Ehle et al. (1998), a diffuse faint optical object coincides with the position of the X-ray source. However, due to the large PSF of the PSPC ($\sim 25''$) and the positional error ($> 3''$), the match was not conclusive. We used the rather stringent HRI source position ($3''.5$ 90% confidence error radius) to confirm the identification. Inspection of the SERC ER/EJ Atlas at the European Southern Observatory revealed a faint extended source at the X-ray source position both visible in the blue (O) and red (E) plates. The offset between the X-ray source (R.A.²⁰⁰⁰ = $13^{\text{h}}29^{\text{m}}54^{\text{s}}.07$, Dec.²⁰⁰⁰ = $+47^{\circ}11'31''.5$) and the optical emission is $1''.6$, well below the error radius of the source

position ($3''.5$). The extended object has approximately the same magnitude in the blue and red band. An overlay of HRI contours onto a deep AAO image, kindly provided by David Malin, is given in Fig. 4.21. On the basis of the high-resolution three colour composite AAO image, it can be inferred that the optical counterpart of H30 has no marked colour or evident structure. It has roughly the same magnitude in the B, V and R band ($\sim 19^m$), typical for the optical emission of HII regions or globular clusters. No radio source is present at this position (cf. Fig. 4.21).

The source cannot be a foreground star, given the optical extent and that the X-ray-to-visual flux ratio $\log(f_x/f_v)$ is $+0.58$, whereas stars typically cover the range from -0.5 to -4.5 (using the definition $\log(f_x/f_v) = \log f_x + \frac{m_v}{2.5} + 5.37$ and results from the Einstein Extended Medium Survey; Maccacaro et al. 1988). All AGN essentially have $B - R < 1$ (blue objects), while the counterpart to H30 has no apparent colour. Also, the morphology is rather untypical of AGN, which usually have bright, compact nuclei. The chance probability of a background AGN at a given X-ray flux of $4.1 \times 10^{-13} \text{ erg cm}^{-2} \text{ s}^{-1}$ within the $34' \times 34'$ HRI field is $\sim 10^{-3}$ (calculated from the $\log N$ - $\log S$ distribution using results from the ROSAT Medium Sensitivity Survey; Hasinger, Schmidt & Trümper 1991). Alternatively, it might be a background galaxy. Again, the X-ray-to-visual flux ratio of $+0.58$ is different from galaxies, which cover the range from -0.5 to -2.0 (Maccacaro et al. 1988). Classes of X-ray emitting extragalactic objects for which no information on the distance is available were intensively studied in the past based on two-point spectral indices (e.g. Tananbaum et al. 1979; Stocke et al. 1991; Brinkmann et al. 1997). Diagnostic tools for classification include the two spectral indices α_{RO} and α_{OX} , defined as the radio-to-optical $\alpha_{\text{RO}} = \log(S_{\nu_{\text{opt}}}/S_{\nu_{\text{rad}}})/\log(\nu_{\text{rad}}/\nu_{\text{opt}})$ and optical-to-X-ray $\alpha_{\text{OX}} = -\log(S_{\nu_x}/S_{\nu_{\text{opt}}})/\log(\nu_x/\nu_{\text{opt}})$ ratios (Brinkmann et al. 1997). For H30, $\alpha_{\text{OX}} = 1$ and $\alpha_{\text{RO}} < 0$ are derived. The α_{OX} and α_{RO} diagrams were used to compare H30 with optically identified extragalactic objects from the Einstein Medium Sensitivity Survey (Stocke et al. 1991) and the ROSAT All-Sky Survey (Brinkmann et al. 1997). All radio-loud objects (BL Lac's, AGN, quasars) can be ruled out based on their large α_{RO} values of > 0.3 and the absence of radio emission for H30. Also, 'normal' galaxies and ellipticals essentially have α_{OX} values exceeding 1.5. Even the region in the α_{RO} - α_{OX} diagram covered by radio-quiet AGN and Seyferts ($\alpha_{\text{OX}} > 1.2$) is different from the spectral indices derived for H30.

Optical follow-up observations will help in clarifying the nature of this source. However, given the high X-ray luminosity, variability and temperature, as well as a positional match with a faint, extended optical source with no evident structure or colour at the edge of a spiral arm, H30 is most likely due to a luminous black hole, contained within a compact HII region or a globular cluster in M83.

In M100, three other HRI sources can be classified as SLS (H17, H21, H24; cf. Tab. 4.8), apart from the super-Eddington nuclear X-ray source (H23) and SN 1979C (H25), which will be discussed in Sec. 5.3. Within the HRI period of observation, none of the SLSs are variable. Source H21 is located $15''$ offset from the nucleus and might hence merely represent unresolved sources located in the bulge region of M100. H17 is also clearly extended (extent $12''.6$ FWHM) and might also be due to spatially unresolved X-ray sources. H24 coincides with a massive HII region (CF336; cf. Tab. 7.12).

Three HRI sources in the M101 field have fluxes greater than $7.4 \times 10^{-14} \text{ erg cm}^{-2} \text{ s}^{-1}$ ($\cong 5 \times 10^{38} \text{ erg s}^{-1}$) in the 0.1–2.4 keV band (H13, H19, H45; cf. Tab. 4.8). One of the sources (H13), projected in the outskirts of the galaxy, can be identified as an interloper (star, GSC 1275). The rest, however, most likely are SLSs within M101, clearly exceeding the expected number of chance interlopers of 0.5 inside the D_{25} ellipse of M101, based on the results of the ROSAT Medium Sensitivity Survey (Hasinger, Schmidt & Trümper 1991). Both H19 and H45 varied strongly during the HRI observations (cf. Fig. 7.5). As expected, none of the two sources has an optical counterpart to the APM magnitude limits. However, within its position uncertainty, H19 coincides with an unresolved optical emission line feature, which has been classified as SNR, although their physical relationship is not yet clear (Matonick & Fesen 1997). The hardness ratio values for the corresponding PSPC sources P13 (H19) and P28 (H45) ($\text{HR1} \gtrsim 0.8$; cf. Tab. 7.6 and Wang, Immler & Pietsch 1999)

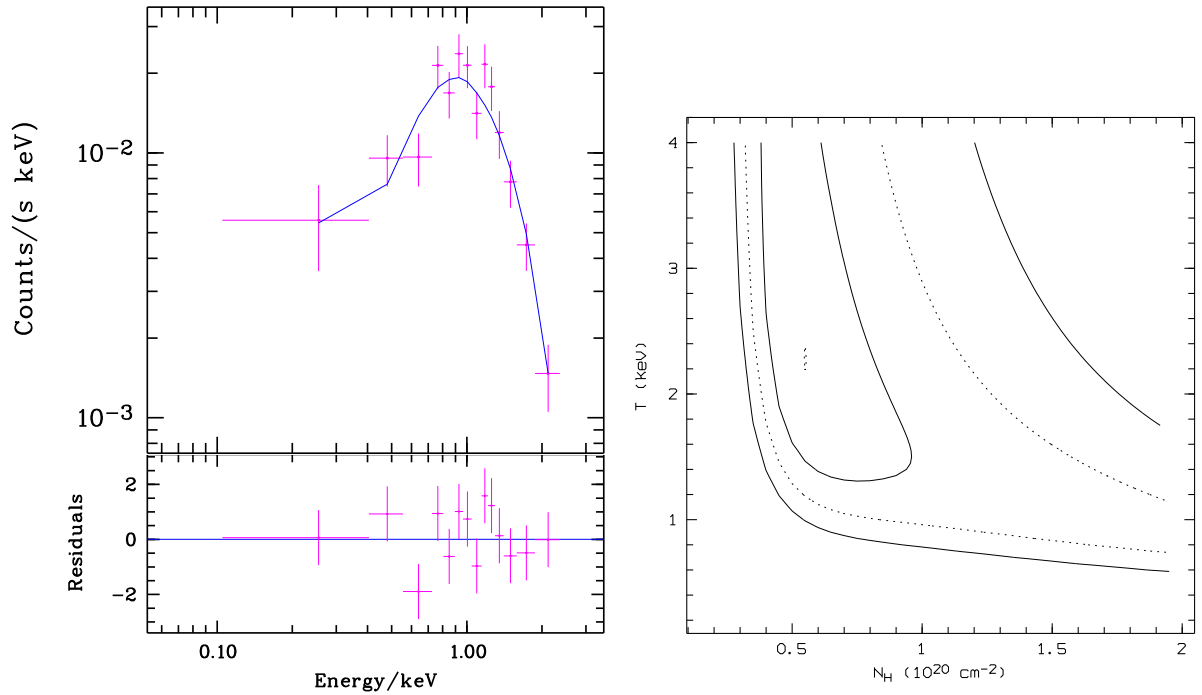


FIGURE 4.22. ROSAT PSPC spectrum of H30 in M83 in the 0.1–2.4 keV band (upper left-hand panel). A thermal bremsstrahlung spectrum is fitted to the data. The residuals to the observed spectrum are given in the lower left-hand panel. The right-hand panel gives χ^2 contours for the model fit spectrum (χ^2 minimum, followed by 68.3%, 96.5% and 99.7% levels of confidence).

indicate large X-ray absorptions along the lines of sight. Indeed, the positions of the sources are all projected well within two outer spiral arms of the galaxy. Therefore, the sources probably represent two BHCs or high-mass X-ray binaries.

Of the 33 ROSAT PSPC sources detected within the D_{25} ellipse of M101 (cf. Wang, Immler & Pietsch 1999 and Tab. 7.6), four sources, which may be classified as SLSs, are clearly resolved by the HRI: P8 into a point-like source (H10; which is still superluminous) and a diffuse component (NGC 5447), P19 into two separate sources of comparable fluxes (H29/H30; two SNR candidates MF54/MF57; cf. Matonick & Fesen 1997; Wang, Immler & Pietsch 1998; Wang 1999), P22 into apparently diffuse emission (H37; NGC 5461), and P25 into multiple components (H39/H40/H41; NGC 5462; SN 1951H; cf. Sec. 5.1. for a more detailed discussion). Thus at least a fraction of the emission of such sources, especially at low spatial resolution, arises in shock-heated hot gas associated with SNRs and/or giant HII complexes.

No SLS was detected in M31. However, source luminosities get apparently higher if M31 is virtually shifted to the distance of M51 (cf. Fig. 4.9). As explained in Sec. 4.3.2., this change in source flux is mimicked by source confusion. Each of the sources, however, are still below the Eddington limit. Therefore, source confusion cannot account for the high number of super-Eddington X-ray sources detected within the D_{25} ellipses of M51, M83, M100 and M101 with inferred luminosities as high as $\sim 4 \times 10^{39}$ erg s $^{-1}$. Also, the high variability observed for some of the SLSs argues against source confusion since a rather large number of unresolved ‘normal’ X-ray sources would be needed to account for the high observed luminosities (e.g. some 40 X-ray sources with luminosity of $\sim 10^{38}$ erg s $^{-1}$ to attain the high luminosity of the variable X-ray source H30 in M83).

It is interesting to notice that all SLSs found in nearby galaxies are located exclusively in outer spiral arms of the galaxies and are embedded in HII regions in most cases, indicating massive star origin. From the above discussion, we conclude that the ROSAT HRI observations result in the detection of many BHCs located within the spiral arms at large distances from the nuclei of the galaxies.

4.5. LUMINOSITY DISTRIBUTION OF POINT SOURCES IN NEARBY GALAXIES

Excluding known interlopers (i.e. foreground and background objects; cf. Tables 7.7, 7.9, 7.10, 7.11 and 7.12), the luminosity distributions of sources within the galaxies were compared. For normalization, the sizes covered by the galaxies (in units of kpc^2) were chosen. Each size was corrected for projection (cf. Tab. 4.1) in order to exclude observational effects and viewing geometries. As all galaxies presented here were analyzed in a coherent way, uncertainties regarding the source luminosity functions due to, e.g. different source detections thresholds, different background maps or different energy bands can be excluded. The comparison between the source luminosity distributions presented here hence represents one of the most coherent when compared to various attempts found in the literature. The luminosity functions for the galaxies are presented in Fig. 4.23 (also reproduced in Fig. 7.6 as colour plate in Appendix D).

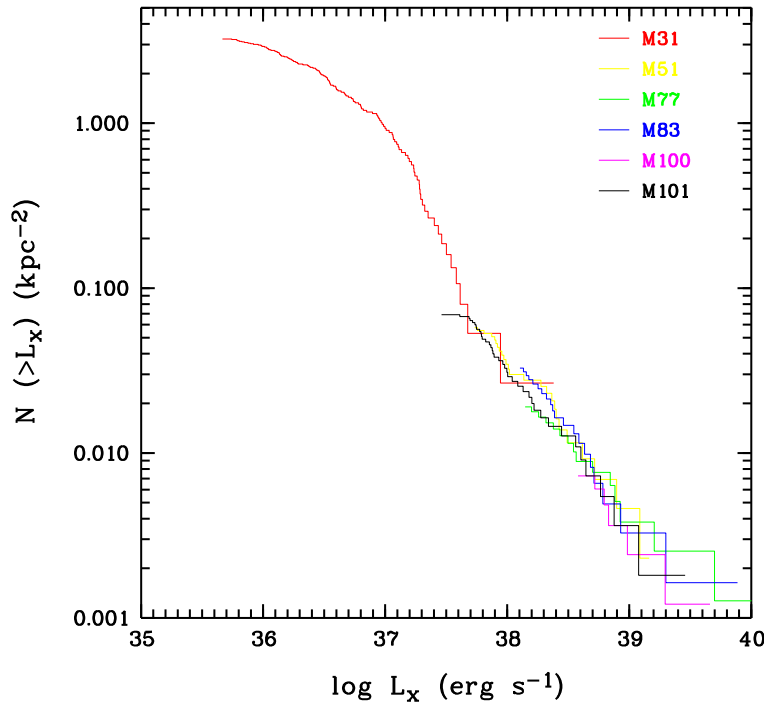


FIGURE 4.23. Luminosity distribution of ROSAT HRI X-ray sources inside the galaxies M31, M51, M83, M100 and M100 (see also colour plate Fig. 7.6 in Appendix D).

It was found that all galaxies, regardless of their morphological type, have similar source luminosity functions, being best described by a power-law $N(> L_x) = N_0 L_x^{-\alpha}$ with exponent ~ 1 . The best-fitted parameters for the power-law functions are compiled in Tab. 4.9: (1) galaxy, (2) area covered by the galaxy, (3) number of X-ray sources found inside the area covered by the galaxies (excluding known interlopers), (4) number of cases for the power-law fit (5) normalization constant N_0 and (6) power-law index α . Despite the rather vast range in distances (0.69–17 Mpc; cf. Tab. 4.1), inclination (17° – 77°), D_{25} diameters ($6'.9$ – $178'$) and morphological type (Sb–Sc), the range in power-law index α describing the steepness of the source luminosity function is quite small (0.75–1.32), excluding M31. The source luminosity functions themselves are almost identical apart from different low-luminosity cut-offs of the distributions, determined by the sensitivity of the surveys. Apart from M31, the high-luminosity cut-offs of the distributions are also similar and do not change the overall shape of the distributions. The close match between the source luminosity functions of the galaxies is still valid if the number of X-ray sources is normalized to the masses of the galaxies (in units of M_\odot). In Fig. 4.24,

the source luminosity distributions are plotted for a number of nearby galaxies and normalized to the neutral hydrogen mass of the galaxies. Again, all galaxies, regardless of their morphological type, seem to have similar source luminosity distributions.

Interesting to note is the cut-off of the M31 source luminosity distribution at a few $\times 10^{38}$ erg s $^{-1}$ in both source luminosity plots (Figs. 4.23 and 4.24), contrary to all other galaxies analyzed here. As was already discussed in Sec. 4.3., previously undetected sources with apparent luminosities in the range $4 \times 10^{37} - 5 \times 10^{38}$ erg s $^{-1}$ appear in M31 if the galaxy were located at a larger distance of 7.7 Mpc instead of 690 kpc, its overall luminosity distribution function being preserved. These apparently bright sources, however, are not real but are mimicked by source confusion and do not explain the existence of SLSs found in more distant galaxies, which attain high X-ray luminosities up to $\sim 4 \times 10^{39}$ erg s $^{-1}$ (cf. Sec. 4.4.3.). The absence of X-ray sources within M31 at luminosities above the Eddington limit can be understood as the number of superluminous X-ray sources seems to be correlated with the star-formation activity. The ratio between X-ray and blue luminosity was chosen as star-formation indicator. Since M31 shows no signs of star formation activity with a rather low blue luminosity, no SLSs are expected (cf. Tab. 4.10 and Fig. 4.25). The results for a number of nearby galaxies are listed in Tab. 4.9. Both the number of superluminous X-ray sources, with luminosities exceeding the Eddington limit of a $1.4 M_{\odot}$ accreting neutron star ($L_x \gtrsim 2 \times 10^{38}$ erg s $^{-1}$), and the total X-ray luminosity appear to be correlated with the star forming rate of the galaxy. This correlation is shown in Fig. 4.25.

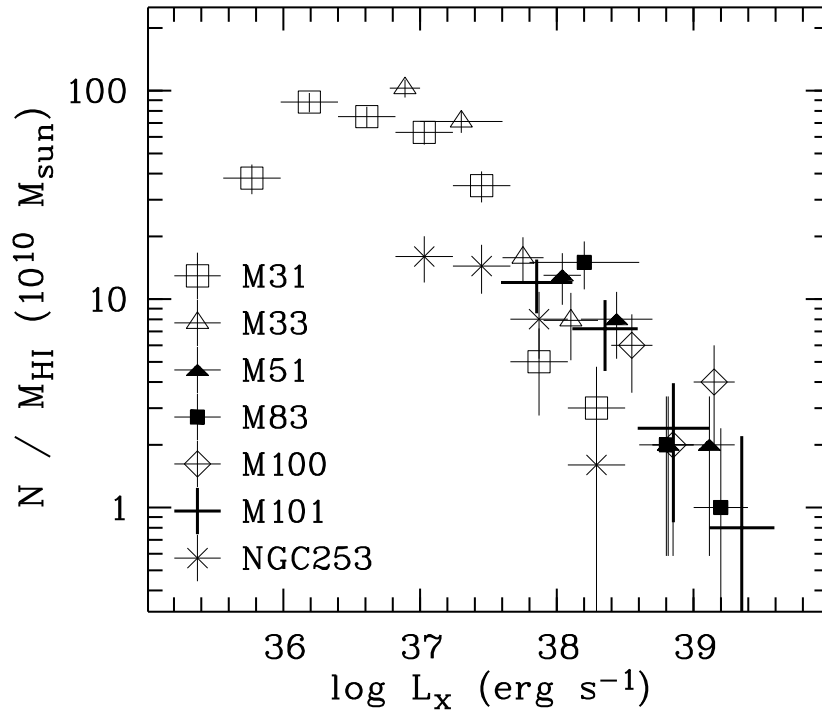


FIGURE 4.24. Comparison of the ROSAT HRI X-ray source luminosity distribution of nearby spirals, normalized to the neutral hydrogen masses of the galaxies. References: M33: Schulman & Bregman 1995; M31: this work; NGC 253: Read, Ponman & Strickland (1997); M101: this work, see also Wang, Immler & Pietsch (1999); M51: this work; M100: this work, see also Immler, Pietsch & Aschenbach (1998a); M83: this work, see also Immler et al. (1999).

TABLE 4.9. ROSAT HRI Luminosity Function of X-Ray Sources inside Galaxies

Galaxy	area (kpc ²)	no. of sources	no. of cases	constant N_0	index α
(1)	(2)	(3)	(4)	(5)	(6)
M31 total	167	127	24	17.82 ± 0.08	0.50 ± 0.02
M51	460	23	15	37.58 ± 0.12	1.02 ± 0.07
M83	666	30	11	49.28 ± 0.13	1.32 ± 0.11
M100	935	8	12	27.55 ± 0.07	0.75 ± 0.05
M101	2 750	53	16	44.47 ± 0.09	1.25 ± 0.05

TABLE 4.10. Selected Multiwavelength Properties of the Galaxies

Galaxy	d	type	$\log M_{\text{HI}}$ (M_{\odot})	$\log L_{\text{B}}$ (erg s^{-1})	$\log L_{\text{FIR}}$ (erg s^{-1})	L_{x} ($10^{40} \text{ erg s}^{-1}$)	$L_{\text{x}}/L_{\text{B}}$ (10^{-5})	N_{SLS}
(1)	(2)	(3)	(4)	(5)	(6)	(7)	(8)	(9)
M31	0.69	Sb	9.6	44.04	42.38	0.29	2.6	0
M33	0.72	Scd	9.1	43.20	42.23	0.08	5.0	0
NGC 253	2.6	Sc	9.8	43.78	43.50	0.8	13.3	1
M101	7.5	Sc	10.0	43.95	43.54	1.3	14.6	5
M100	17.1	Sbc	9.7	44.42	43.74	5.5	20.9	6
M83	8.9	Sc	10.0	44.17	44.17	4.1	27.7	8
M51	7.7	Sc	9.5	44.07	43.68	5.0	42.6	10

(1) Name of galaxy

(2) Tully (1988)

(3) Classification according to de Vaucouleurs (1991)

(4) Neutral hydrogen mass (Tully 1988)

(5) Blue luminosities (Tully 1988)

(6) Far infrared luminosities, calculated from the IRAS $60\mu\text{m}$ and $100\mu\text{m}$ fluxes, using the expression $L_{\text{FIR}} = 3.65 \times 10^5 (2.58 S_{60\mu\text{m}} + S_{100\mu\text{m}}) d^2 L_{\odot}$ (cf. Devereux & Eales 1989). IRAS fluxes are from Soifer, Boehmler & Neugebauer (1989) and Rice et al. (1988)

(7) Total 0.1–2.4 keV band X-ray luminosities. References:

M33: Schulman & Bregman 1995; Long et al. (1996)

M31: Supper et al. (1997) and this work

NGC 253: Read, Ponman & Strickland (1997)

M101: this work, see also Wang, Immler & Pietsch (1999)

M51: this work

M100: this work, see also Immler, Pietsch & Aschenbach (1998a)

M83: this work, see also Immler et al. (1999)

(8) Ratio of total X-ray to blue luminosity of the galaxy

(9) Number of superluminous sources (SLSs) with luminosities exceeding $2 \times 10^{38} \text{ erg s}^{-1}$

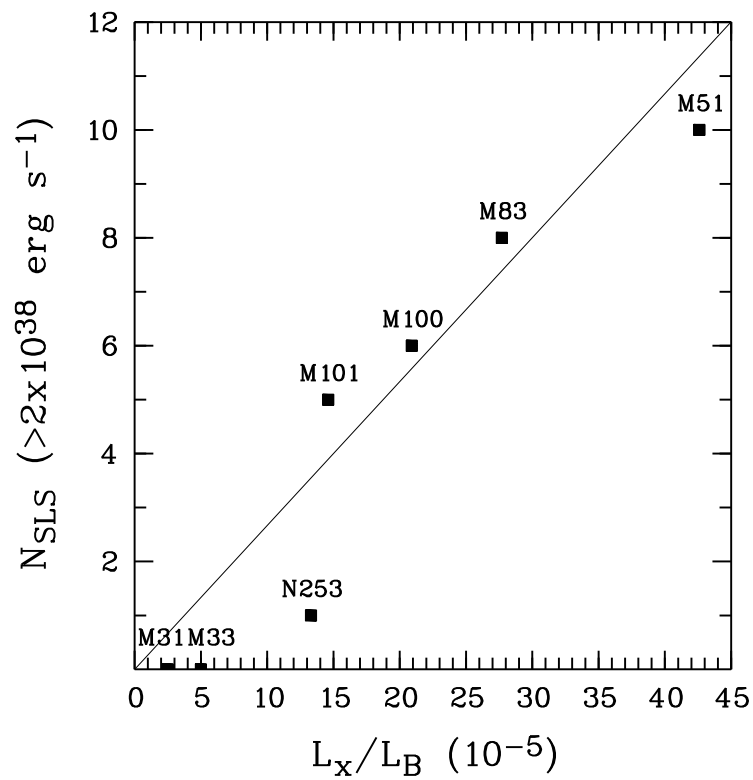


FIGURE 4.25. Number of superluminous sources (SLSs), with (0.1–2.4 keV band) X-ray luminosities exceeding $2 \times 10^{38} \text{ erg s}^{-1}$, vs. ratio between total X-ray and blue band luminosities of the galaxies.

5. X-RAY EMISSION FROM SUPERNOVAE

*“But he, with first a start and then a wink,
Said, ‘There’s another star gone out, I think!’ ”*

Lord Byron

An interesting aspect of studying nearby galaxies in the X-ray regime is to look for possible X-ray emission from supernovae (SNe) within the galaxies. Within the last two decades, a mere eleven SNe were observed to emit X-rays. The complete list of X-ray SNe is given in Tab. 5.1, including two detections resulting from this work, which will be discussed in detail in Sections 5.2. and 5.3. (see also Immler, Pietsch & Aschenbach 1998a, 1998b, 1998c). Two additional new detections will be reported and discussed in Sec. 5.1. (see also Immler & Pietsch 2000).

As described in Sec. 2.3., X-rays are produced from the interaction of the SN blast wave with the circumstellar medium, deposited either by non-conservative mass-loss in a binary system (in the case of type Ic SNe) or by the progenitor’s wind (type II SNe). Only SNe with a large amount of circumstellar matter are expected to produce significant X-ray emission. Stellar winds of massive stars blow large amounts of material into the ambient circumstellar medium. It is hence not surprising that all SNe discovered in the X-ray regime prior to this work are type II SNe, which are the natural endpoint in the stellar evolution of massive stars. Due to the limiting sensitivity of X-ray observatories prior to ROSAT, SNe were established as a new class of X-ray emitting object with this satellite. The most likely emission mechanism is thermal radiation from the collision of the high velocity SN gas with matter deposited by the progenitor star prior to the explosion either via massive stellar winds or non-conservative mass-transfer to a companion. The shocked interaction region is the site of radio, late-time optical, ultraviolet, and most importantly, X-ray emission. Comparison of all X-ray emitting SNe shows that there is an approximate proportionality between X-ray and radio emission over 5 orders of magnitude in X-ray luminosity, with X-ray to radio flux ratios f_x/f_r only in the narrow range 2–9 (excluding the only SN of type I detected in the X-ray regime, SN 1994I; cf. Tab. 5.1).

In the galaxy M83, an unusually high number of supernovae was recorded this century (SN 1923A, SN 1945B, SN 1950B, SN 1957D, SN 1968L, SN 1983N). The positions of these SNe are indicated in Fig. 4.14. Upper limits to the count rates were calculated within circles of radius $2.5\times$ the ROSAT HRI PSF at these SNe positions. The 3σ upper limits are listed in Tab. 5.2. Since SN 1968L is only $5''$ offset from the X-ray bright nucleus of M83, no stringent upper limits could be derived.

The luminosities of SN 1923A, SN 1945B, SN 1950B and SN 1957D are less than a few 10^{38} erg s $^{-1}$ for an assumed 1 keV thermal bremsstrahlung spectrum, indicating that the circumstellar matter, deposited by the progenitor star, was not dense enough to significantly produce X-ray emission during interaction with the expanding SN shell. According to the Chevalier mini-shell interaction model (explained in more detail in Sections 5.2. and 5.3.), the derived upper limits require mass-loss rates of $\dot{M} < 10^{-5} M_{\odot} \text{ yr}^{-1}$ (cf. Chevalier & Fransson 1994 and references therein). This is not surprising, since only powerful radio-SNe are found to have mass-loss rates exceeding some $10^{-5} M_{\odot} \text{ yr}^{-1}$ (cf., e.g. Weiler et al. 1986).

SN 1983N is the only SN in M83 that could be identified as a type I SN. Historically, it is the first type I SN from which radio emission was detected and is the best studied type I SN in the radio

TABLE 5.1. Complete List of X-Ray Supernovae

Supernova	type	galaxy	d (Mpc)	day after explosion	L_x^* 0.1–2.4 keV ($10^{38} \frac{\text{erg}}{\text{s}}$)	f_x^* 0.1–2.4 keV ($10^{-14} \frac{\text{erg}}{\text{cm}^2 \text{s}}$)	f_r^\S 6 cm (mJy)	f_x/f_r
SN 1978K	II _{L/P}	NGC 1313	4.5	4 400	92	380	60	6
SN 1979C	II _L	NGC 4321	17.1	5 900	14	3.9	2.5	2
SN 1980K	II _L	NGC 6946	5.1	35	0.6	1.8	0.2	9
SN 1986J	II _{pec}	NGC 891	9.6	3 300	140	119	30	4
SN 1987A [†]	II _P	LMC	0.05	—	0.003	40	14	3
SN 1988Z	II _{pec}	MCG+03-28-022	89	2 370	110	0.9	0.3	3
SN 1993J	II _{pec}	NGC 3031	3.6	6	7	50	23	2
SN 1994I	Ic	NGC 5194	7.7	79	1.6	2.3	8	0.3
SN 1994W	II _P	NGC 4027	10	1 180	80	67	—	—
SN 1995N	II _{pec}	MCG-2-38-017	24	440	275	40	5	8
SN 1999em	II _P	NGC 1637	7.8	4	1.0	2.0	—	—

* Maximum observed X-ray fluxes and luminosities.

References: in addition to the compilation of Schlegel (1995), the following publications have been used:

SN 1979C: Immler, Pietsch & Aschenbach (1998a, 1998c) and this work

SN 1987A: Hasinger et al. (1996)

SN 1988Z: Fabian & Terlevich (1996)

SN 1993J: Zimmermann et al. (1994, 1996a, 1996b)

SN 1994I: Immler, Pietsch & Aschenbach (1998b) and this work

SN 1994W: Schlegel (1999)

SN 1995N: Lewin, Zimmermann & Aschenbach (1996, 1997)

SN 1999em: Fox et al. (1999; 0.1–8.0 keV band Chandra ACIS-S results)

Also, unpublished results obtained by members of a SNe collaboration have been included. This refers to SN 1993J (Zimmermann et al. 1999), SN 1995N (Lewin et al. 1999, Fabian et al. 1999a), and SN 1988Z (Fabian et al. 1999b)

[§] The full set of radio data on SNe is available on <http://rsd-www.nrl.navy.mil/7214/weiler/sne-home.html>. For SN 1994W, no radio detection is reported. SN 1999em was detected at 3.6 cm with a flux density of 0.22 ± 0.04 mJy (Lacey et al. 1999)

[†] X-ray flux still rising

regime to date (Sramek, Panagia & Weiler 1984; Weiler et al. 1986). An X-ray source is found $5''.6$ offset from the radio position of the SN. Extracting photons within a circle of radius $2.5 \times$ the ROSAT HRI PSF at the SN position gives a count rate of $(2.3 \pm 1.1) \times 10^{-4}$ cts s⁻¹. Assuming the emission arises from the SN itself, a source flux and luminosity of $(1.3 \pm 0.6) \times 10^{-14}$ erg cm⁻² s⁻¹ and $(1.2 \pm 0.6) \times 10^{38}$ erg s⁻¹ are derived, respectively, applying a 1 keV thermal bremsstrahlung spectrum. According to the circumstellar interaction model (cf. Chevalier 1982a,b; 1984a,b; Chevalier & Fransson 1994; further explained in Box 4), using our observed luminosity at $t = 3\,800$ days and assuming a wind velocity of $v_w = 10$ km s⁻¹, a mass-loss rate of the progenitor of $\dot{M} = (2.1 \pm 0.5) \times 10^{-6} M_\odot \text{ yr}^{-1}$ is derived. This is typical of type I SNe, as inferred from radio observations (cf., e.g. SN 1983N, SN 1984L: $2 \times 10^{-6} M_\odot \text{ yr}^{-1}$, SN 1990B: $3 \times 10^{-6} M_\odot \text{ yr}^{-1}$, Weiler et al. 1993). No evidence for X-ray emission from a type I SN is reported as yet. The only stringent upper limit to the X-ray flux of a type Ia SNe found to date implies a mass-loss rates of $\dot{M} < (2 - 3) \times 10^{-6} M_\odot \text{ yr}^{-1}$ (SN 1992A; Schlegel & Petre 1993). Interestingly, long-term radio monitoring of SN 1983N resulted in the same mass-loss rate as is inferred by the detection of X-rays presented here ($2.0 \times 10^{-6} M_\odot \text{ yr}^{-1}$; Weiler et al. 1986, 1993).

TABLE 5.2. X-Ray Emission from the Positions of Supernovae in M83

Supernova	type	R.A. ^{2000§} (h m s)	Dec. ^{2000§} (° ' ")	count rate (10 ⁻⁴ $\frac{\text{cts}}{\text{s}}$)	f_x^* (10 ⁻¹⁴ $\frac{\text{erg}}{\text{cm}^2 \text{s}}$)	L_x^* (10 ³⁸ $\frac{\text{erg}}{\text{s}}$)
SN 1923A	II _P	13 37 09.24	-29 51 04.2	< 3.7	< 2.0	< 1.9
SN 1945B [†]	—	13 36 52.94	-29 54 46.3	< 0.5	< 0.3	< 0.3
SN 1950B	—	13 36 52.88	-29 51 55.7	< 2.6	< 1.4	< 1.4
SN 1957D	—	13 37 03.57	-29 49 40.7	< 0.8	< 0.4	< 0.4
SN 1968L [‡]	II _P	13 37 00.51	-29 51 59.0	—	—	—
SN 1983N	Ib	13 36 51.22	-29 54 01.7	2.3 ± 1.1	1.3 ± 0.6	1.2 ± 0.6

§ Positions are from NED at <http://nedwww.ipac.caltech.edu/>

* Fluxes and luminosities are computed applying a 1 keV thermal bremsstrahlung spectrum.

† Position from the Asiago Supernova Catalogue at <http://athena.pd.astro.it/~supern/>

‡ Since SN 1968 is only 5'' offset from the X-ray bright nucleus, no upper limits can be derived

TABLE 5.3. X-Ray Emission from the Positions of Supernovae in M100

Supernova	type	R.A. ^{2000§} (h m s)	Dec. ^{2000§} (° ' ")	count rate (10 ⁻⁴ $\frac{\text{cts}}{\text{s}}$)	f_x^* (10 ⁻¹⁵ $\frac{\text{erg}}{\text{cm}^2 \text{s}}$)	L_x^* (10 ³⁸ $\frac{\text{erg}}{\text{s}}$)
SN 1901B	I	12 22 47.48	+15 49 24.6	< 1.2	< 5.0	< 1.8
SN 1914A	I	12 22 56.85	+15 47 29.6	< 1.2	< 5.0	< 1.8
SN 1959E	I	12 22 59.20	+15 48 59.6	< 1.9	< 7.9	< 2.7
SN 1979C	II _L	12 22 58.62	+15 47 50.7		(see Sec. 5.3.)	

§ Positions are from NED at <http://nedwww.ipac.caltech.edu/>

* ROSAT HRI 3 σ upper limit within a radius of 2 \times the HRI PSF. Fluxes and luminosities are computed applying a 1 keV thermal bremsstrahlung spectrum

BOX 4. THE CIRCUMSTELLAR INTERACTION MODEL FOR SNe

As was discussed in Sec. 2.3., the interaction of a SN with circumstellar gas gives rise to radiation predominantly in the X-ray regime. The most likely emission mechanism is thermal radiation from the collision of the high velocity SN gas with matter deposited by the progenitor star prior to the explosion, either via massive stellar winds or non-conservative mass-transfer to a companion. The shocked interaction region is the site of radio, late-time optical, ultraviolet, and most importantly, X-ray emission. Hot gas at high temperature T of some 10^6 K inside a volume V gives off thermal radiation predominantly in the X-ray range while cooling. Its luminosity can be simply expressed in terms of the products of the electron and proton densities, n_e and n_p , inside a volume V multiplied by the cooling function $\Lambda(T, Z, E)$:

$$L = \int n_e n_p dV \times \Lambda(T, Z, E). \quad (5.1)$$

Since the ISM is mainly composed of light elements (e.g. hydrogen and helium), the luminosity of radiating hot gas inside a sphere ranging from radius R_0 to R is a function of mean density of the material and the cooling function $\Lambda(T, E)$:

$$L = \int_{R_0}^R \rho^2 dr \times \Lambda(T, E). \quad (5.2)$$

In the ROSAT (0.1–2.4 keV) band, the cooling function is proportional to $T^{-1/2}$ and can be calculated in detail (e.g. Raymond, Cox & Smith 1976; Raymond & Smith 1977; Cecil, Watson & dePree 1995 and references therein):

$$\Lambda(T) = 1.6 \times 10^{-22} \sqrt{\frac{T}{10^6 \text{ K}}} \text{ erg cm}^3 \text{ s}^{-1}. \quad (5.3)$$

Inside a sphere of radius R around a massive star, the density is given by

$$\rho = \frac{\dot{M}}{4\pi r^2 v_w} \quad (5.4)$$

and is determined by the mass-loss rate of the progenitor, \dot{M} , blown-off into the ambient ISM at a wind velocity v_w typically on the order of 10 km s^{-1} for massive stars. Equation (5.2) can hence be expressed as

$$L_x = \frac{\Lambda(T)}{4\pi^2} \frac{\dot{M}^2}{v_w} \times v_s^{-1} t^{-1} \quad (5.5)$$

in which the radius R of the X-ray emitting sphere is replaced by the product of the SN shock front velocity, v_s , and the time after the outburst, t . The equations can thus be re-written as

$$L_x = 1 \times 10^{40} A^2 (t/10 \text{ days})^{-1} \text{ erg s}^{-1}, \quad (5.6)$$

where A is a constant for typical SN parameters (Chevalier 1984a):

$$\dot{M}/v_w = 10^{-6} A (M_\odot \text{ yr}^{-1})/(\text{km s}^{-1}). \quad (5.7)$$

Setting $A = 1$, e.g., corresponds to a mass-loss rate of the progenitor of $10^{-5} M_\odot \text{ yr}^{-1}$ at $v_w = 10 \text{ km s}^{-1}$. Expressions (5.6) and (5.7) can hence be used to derive the mass-loss rate of the progenitor prior to the SN explosion by measuring the X-ray luminosity at a given time after the outburst. The description presented here for the interaction of a SN shock front with the ambient ISM is generally denoted the ‘mini-shell’ or ‘circumstellar interaction model’ and has been successfully applied to both the X-ray and radio evolution for a number of SNe (Chevalier 1984a).

5.1. X-RAY EMISSION FROM SUPERNOVAE 1970G AND 1951H IN M101

The ultra-deep HRI observation of M101 was used to look for possible X-ray emission from SNe known in this galaxy (SN 1909A, SN 1951H, SN 1970G). No X-ray source is found at the position of SN 1909A, the 3σ upper limit to its luminosity being $< 3.3 \times 10^{37} \text{ erg s}^{-1}$ (cf. Tab. 5.4). The SNe 1951H and 1970G, both type II, are located within giant HII regions inside the galaxy's spiral arms. Both HII regions (NGC 5455 and NGC 5462, respectively) are known to be strong X-ray emitters (cf., e.g. Williams & Chu 1995 and Snowden & Pietsch 1995). However, due to the limiting spatial resolution of the PSPC instrument and the limited photon statistics of the HRI observations analyzed prior to this work, it was difficult to decide whether the emission arises from hot gas within the HII regions or the SNe themselves. Also, the limiting photon statistics of the PSPC observation did not allow us to constrain the spectral characteristics of the X-ray sources as to shed light on the nature of the emission (Williams & Chu 1995).

Contours of the deep 229 ks HRI and the 35 ks PSPC observations of SN 1970G in the HII region NGC 5455 and SN 1951H in NGC 5462, overlaid onto $H\alpha$ observations (kindly provided by You-Hua Chu) are presented in Figs. 5.1. and 5.2. The images show that in both cases the peak of the X-ray emission coincides with the positions of the SNe (indicated by white crosses) within the HRI error radius. The offset of the HRI source H22 (90% confidence error radius: $5''.6$) from the position of SN 1970G is $5''.5$, the offset of H40 (90% confidence error radius: $4''.0$) from the position of SN 1951H is $4''.5$. For SN 1951H/NGC 5462, X-ray contour maps are also presented as overlays onto an HI observation (21 cm observation from the WSRT; Kamphuis, Sancisi & van der Hulst 1991) to illustrate that the X-ray emission does not coincide with possible outflow of hot gas from the HI hole ('superbubble') coinciding with that region (Fig. 5.3). Timing analysis shows that both X-ray sources are not variable. Extracting photons from the HRI positions of the X-ray sources gives count rates

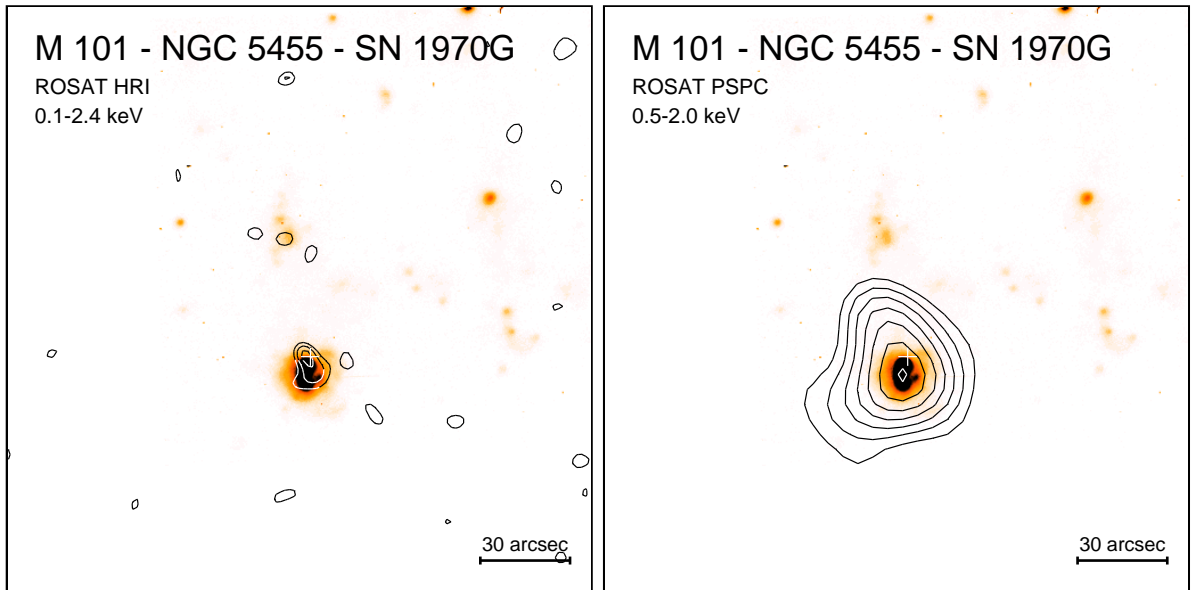


FIGURE 5.1. Contour map of X-ray emission from the position of SN 1970G in NGC 5455, superposed on an $H\alpha$ observation from the Kitt Peak 2.1m telescope. The left-hand panel gives X-ray contours in the (0.1–2.4 keV) ROSAT HRI band, smoothed with a Gaussian of $7''$ (FWHM). Contours are $3, 4, 5\sigma$ above the mean background rate of $4.9 \times 10^{-3} \text{ cts s}^{-1} \text{ arcmin}^{-2}$. 1σ corresponds to $8.2 \times 10^{-4} \text{ cts s}^{-1} \text{ arcmin}^{-2}$. The right-hand panel gives X-ray contours in the (0.5–2.0 keV) ROSAT PSPC band, smoothed with a Gaussian of $25''$ (FWHM). Contours are $3, 4, \dots, 9\sigma$ above the mean background rate of $4.2 \times 10^{-3} \text{ cts s}^{-1} \text{ arcmin}^{-2}$. 1σ corresponds to $1.2 \times 10^{-3} \text{ cts s}^{-1} \text{ arcmin}^{-2}$. The position of SN 1970G is marked with a cross.

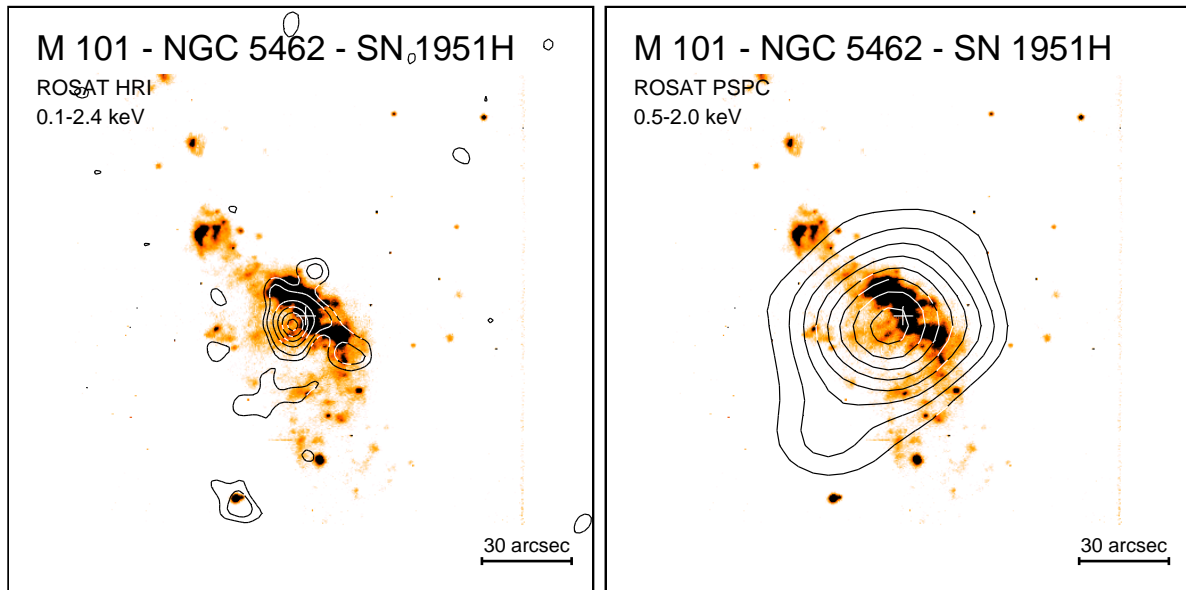


FIGURE 5.2. Contour map of X-ray emission from the position of SN 1951H in NGC 5462, superposed on an H α observation. Contours of the (0.1–2.4 keV) band HRI observation (left-hand panel) are 3, 5, 10, 15, 20, 25 σ above the background, contours of the (0.5–2.0 keV) band PSPC observation are 3, 5, 7...15 σ above the background (same levels as in Fig. 5.1.). The position of SN 1951H is marked with a cross.

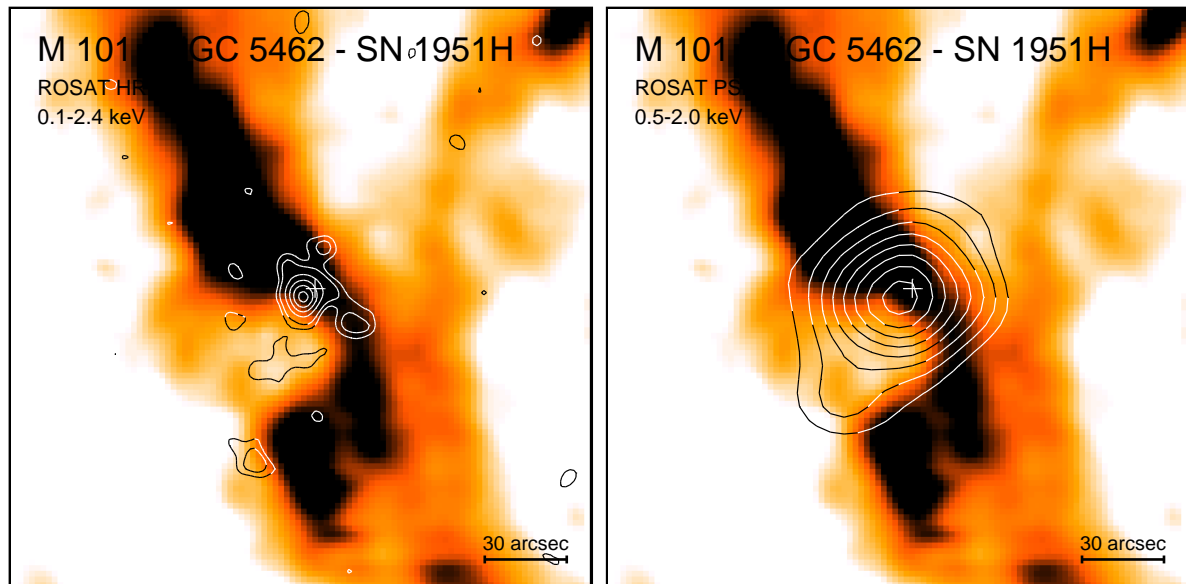


FIGURE 5.3. Overlay of X-ray contours onto an HI map of NGC 5462 (same levels as in Fig. 5.1.).

TABLE 5.4. X-Ray Emission from the Positions of Supernovae in M101

Supernova	type	R.A. ²⁰⁰⁰ (h m s)	Dec. ²⁰⁰⁰ (° ' ")	count rate (cts s ⁻¹)	f_x^* (erg cm ⁻² s ⁻¹)	L_x^* (erg s ⁻¹)
SN 1909A	II _{pec}	14 02 02.4	+54 27 53.5	$< 1.2 \times 10^{-4}$	$< 3.3 \times 10^{-15}$	$< 3.3 \times 10^{37}$
SN 1951H	II	14 03 53.9	+54 21 58.6	$(8.0 \pm 0.7) \times 10^{-4}$	$(2.4 \pm 0.7) \times 10^{-14}$	$(2.2 \pm 0.2) \times 10^{38}$
SN 1970G	II _L	14 03 00.6	+54 14 30.4	$(1.8 \pm 0.4) \times 10^{-4}$	$(5.0 \pm 1.0) \times 10^{-15}$	$(4.9 \pm 1.0) \times 10^{37}$

* 0.1–2.4 keV band fluxes and luminosities, applying a 0.5 keV thermal bremsstrahlung spectrum

of $(8.0 \pm 0.7) \times 10^{-4}$ cts s⁻¹ for H22 and $(8.0 \pm 0.7) \times 10^{-4}$ cts s⁻¹ for H40 (cf. Tab. 5.4). The count rates of the corresponding PSPC sources (P12 and P25) are a factor of ~ 7 and ~ 4 higher than the HRI rates, which may be explained by rather soft spectra. For P12, the counting statistic did not allow detailed spectral analysis, however, the hardness ratios of $HR1 = 1.00 \pm 0.14$ and $HR2 = -0.23 \pm 0.24$ indicate that the emission is relatively soft and strongly absorbed, typical for the late emission of SNe embedded in HII regions. Assuming the X-ray emission arises from SN 1970G, a mass-loss rate of the progenitor of $\dot{M} = 2.0 \times 10^{-5} M_{\odot} \text{ yr}^{-1}$ is derived for day 9100 after the outburst, applying the Chevalier interaction model, a source luminosity of 4.9×10^{37} erg s⁻¹ for an assumed a 0.5 keV thermal bremsstrahlung spectrum (justified below), and a stellar wind velocity of 10 km s⁻¹. 6 cm and 20 cm radio observations of the radio bright SN 1970G ($f_{6\text{cm}} = 21.5$ mJy) also gave a mass-loss rate of $2 \times 10^{-5} M_{\odot} \text{ yr}^{-1}$ (Weiler et al. 1993). For the PSPC source P25, coinciding with SN 1951H, the large number of photons (232 net counts) allowed more detailed spectral analysis. A spectrum was created by binning counts extracted from a circle with radius 45'' centred on the source position into energy channels with signal-to-noise ratios of > 5 and extracting background photons from an annulus of outer radius 90''. Whereas a RASM spectrum resulted in a poor χ^2/ν value of 4.68 for a best fit value of $T = 1$ keV, a THBR spectrum gave a good χ^2/ν of 0.13 for a best fit temperature of $T = (0.48 \pm 0.25)$ keV. Snowden & Pietsch (1995) have shown that the emission from hot gas within M101 is observed primarily at $\sim 1/4$ keV, substantially softer than the emission observed from the position of SN 1951H/NGC 5462. Where spectral information is available for other X-ray emitting SNe, the temperature derived from EINSTEIN IPC and ROSAT PSPC observations are essentially the same as the temperature inferred for the X-ray source coinciding with SN 1951H (SN 1978K: 0.5 keV THBR, SN 1980K: 0.4 keV THBR, Schlegel 1995; SN 1986J: 0.5 keV THBR, Bregman & Pildis 1992, SN 1987A: 0.5–0.7 keV for the late emission, Gorenstein, Hughes & Tucker 1994, Beuermann, Brandt & Pietsch 1994). The best fit N_H of $(4.0 \pm 1.7) \times 10^{20} \text{ cm}^{-2}$ (excluding Galactic absorption) does also point towards the X-ray source being embedded within the HII region. The PSPC spectrum and the χ^2 grid are given in Fig. 5.4.

Taking the spectral properties of the X-ray sources found to coincide with SNe 1951H and 1970G, their inferred luminosities, leading to mass-loss rates typical of type II SNe, their non-variability and their close positional match with the SNe, it is quite conceivable that the X-ray sources are in fact due to emission from the SNe itself. High-resolution observations from the recently launched Chandra observatory (0.5 FWHM resolution), with the potential of spatially resolving the emission components within the HII complexes, will help clarifying the origin of the X-rays.

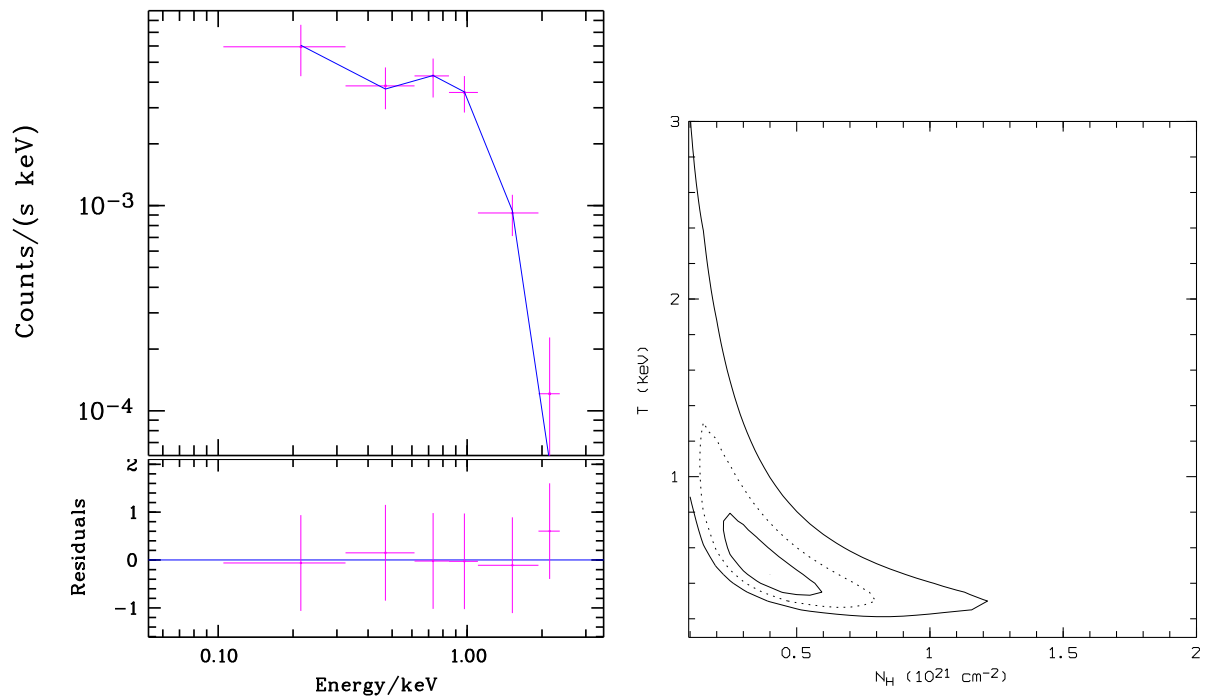


FIGURE 5.4. ROSAT PSPC spectrum of H22 in M101, coinciding with the position of SN 1951H and the HII region NGC 5462, in the (0.1–2.4 keV) band (upper left-hand panel). A thermal bremsstrahlung spectrum is fitted to the data. The residuals to the observed spectrum are given in the lower left-hand panel. The right-hand panel gives χ^2 contours for the model fit spectrum (χ^2 minimum, followed by 68.3%, 96.5% and 99.7% levels of confidence).

5.2. EVIDENCE FOR X-RAY EMISSION FROM THE TYPE IC SUPERNOVA 1994I IN M51

The ROSAT HRI X-ray observations of the galaxy M51 were analyzed to search for X-ray emission from the type Ic supernova 1994I. Observation periods are given in Tab. 5.5. Applying the image subtraction technique, described in Sec. 3.2., an X-ray point source is detected at the radio position of SN 1994I in the 6.4 ks observation (no. 4a) of M51.

The offset between the X-ray source and the radio position of SN 1994I (R.A.²⁰⁰⁰ = 13^h29^m54^s.07, Dec.²⁰⁰⁰ + 47°11'31".5; Morrison & Argyle 1994) is 1".2, well below the systematic error of the attitude solution (3".2). The source has a count rate excess of $(4.3 \pm 0.8) \times 10^{-4}$ cts s⁻¹ in the 6.4 ks observation interval, compared to the complete observation. To confirm the existence of the source, a source detection algorithm was applied to images of pixel size 1" for the observation blocks listed in Tab. 5.5. Within the inner 1' × 1' of the galaxy, two sources are detected in the observation blocks 4a and 4b, with a likelihood $L \geq 6$. While one source is located at the position of the optical nucleus of the galaxy, the other source coincides with the variable source found in the subtracted images at the position of SN 1994I. The source at the position of SN 1994I is detected with a likelihood of $L = 7.2$ (3.4 σ) in the 6.4 ks observation (no. 4a) and with a likelihood of $L = 6.3$ (3.1 σ) in the 29.9 ks observation (no. 4b). The corresponding net counts within an extraction circle of radius 5" are 7 ± 3 and 12 ± 5 , respectively. Analysis of the complete 36.3 ks observation (no. 4) gives a total of 19 ± 6 net counts. No source is found at the position of SN 1994I for the remaining epochs at a 3 σ confidence level, and 3 σ upper limits (99.7% confidence level) were calculated.

TABLE 5.5. ROSAT HRI Observation Intervals of SN 1994I

Obs. no.	time (ks)	date	day since outburst	
1	8.5	07/12/91 – 10/01/92	–798	
2	8.8	22/05/92 – 05/06/92	–679	
3	9.4	22/05/94 – 23/05/94	52	
4	36.3	18/06/94 – 24/06/94	79–85	
4	4a	6.4	18/06/94	79
	4b	29.9	19/06/94 – 24/06/94	80–85
5	5.0	26/12/97 – 30/12/97	1368	

Source photons from the position of SN 1994I and photons from the nuclear region of M51 appear predominantly in the HRI raw channels 1–8, the peak being located in channel 4 (cf. Fig. 5.5). The background, however, is distributed across all HRI raw channels 0–15 (instrumental background, UV emission, weak galactic and extragalactic sources, cosmic rays, etc.). This comparison indicates that the X-ray source detected at the position of SN 1994I does not represent a local enhancement in the radiation background.

Since SN 1994I is only $\sim 18''$ offset from the nucleus of M51, the contribution of emission from the extended bulge region to the emission of the source at the position of SN 1994I was estimated by constructing surface brightness profiles, centred on the X-ray peak emission of the galaxy. Three sectors were extracted, with radial binning of 1".75. The sectors extend to 35" radius from the nucleus, having a width of 5" at the distance of SN 1994I. The middle sector is centred on the position of the SN, and the two adjacent sectors have been co-added. The location of the sectors is shown in the inset of Fig. 5.6 for the 6.4 ks observation (no. 4a), together with the X-ray contours from the inner 1' × 1' nuclear region of M51. The contour levels are at 1, 1.5, 2, 3, 4, 5 and 6 in units of 1 count per detection cell (5.6×10^{-1} cts s⁻¹ arcmin⁻²). The position of the optical nucleus of M51 is at the origin of the sectors, while the radio position of the SN is indicated by a cross. Comparison of

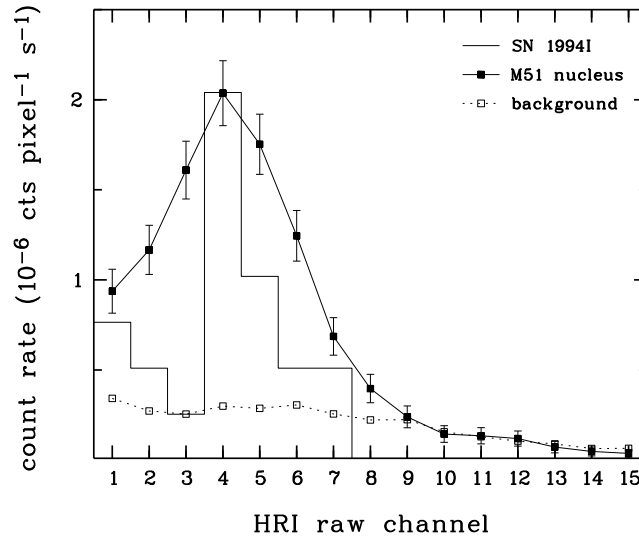


FIGURE 5.5. HRI raw spectrum of SN 1994I, the M51 nucleus and a large background region.

the surface brightness profiles of the sector containing SN 1994I (solid line, labelled ‘on’) and the two adjacent sectors to either side (dashed line, ‘off’), shows an excess of X-ray emission at the position of SN 1994I. The extended bulge emission component (‘off’) exceeds the PSF of the eight co-added point sources used for the boresight correction (dotted line, ‘PSF’). The extent of the bulge emission, however, can only be observed to a distance of $\sim 12''$ from the nucleus of the galaxy. Hence, the contribution of the bulge emission to the source flux at the position of SN 1994I is negligible.

TABLE 5.6. X-Ray Emission from the Position of SN 1994I

Obs. no.	net counts	rate ($10^{-4} \frac{\text{cts}}{\text{s}}$)	f_x ($10^{-14} \frac{\text{erg}}{\text{cm}^2 \text{ s}}$)	L_x ($10^{38} \frac{\text{erg}}{\text{s}}$)
1	—	< 7.1	< 3.0	< 2.1
2	—	< 3.6	< 1.6	< 1.1
3	—	< 3.1	< 1.3	< 0.9
4	19 ± 6	5.2 ± 1.7	2.3 ± 0.7	1.6 ± 0.5
4	4a 7 ± 3	10.9 ± 3.1	4.7 ± 1.3	3.3 ± 0.9
	4b 12 ± 5	4.0 ± 1.7	1.7 ± 0.7	1.2 ± 0.5
5	—	< 8.4	< 3.7	< 2.5

The (0.1–2.4 keV) flux and luminosity of the source at the position of SN 1994I over observation block 4 (i.e. between days 79–85 after the outburst) are $f_x = 2.3 \times 10^{-14} \text{ erg cm}^{-2} \text{ s}^{-1}$ and $L_x = 1.6 \times 10^{38} \text{ erg s}^{-1}$, respectively, assuming a 5 keV thermal bremsstrahlung spectrum, a galactic hydrogen column of $N_H = 1.3 \times 10^{20} \text{ cm}^{-2}$ (Dickey & Lockman 1990) and a distance of 7.7 Mpc (Tully 1988). Assumption of a 1 keV thermal bremsstrahlung spectrum increases the source flux and luminosity by $\sim 5\%$. Fluxes and luminosities for observation bins 4a and 4b are listed in Tab. 5.6, together with 3σ upper limits for the remaining epochs.

The chance probability of a background AGN, at the flux given above, being within $5''$ of the position of SN 1994I, is 3×10^{-5} (using the ROSAT Medium Sensitivity Survey; Hasinger, Schmidt & Trümper 1991). However, if we suppose that the seven variable sources detected with the ‘image subtraction technique’ are distributed randomly within the inner $1' \times 1'$ (excluding the source at the nucleus of the galaxy), we derive a probability of 15% that one such source accidentally falls within

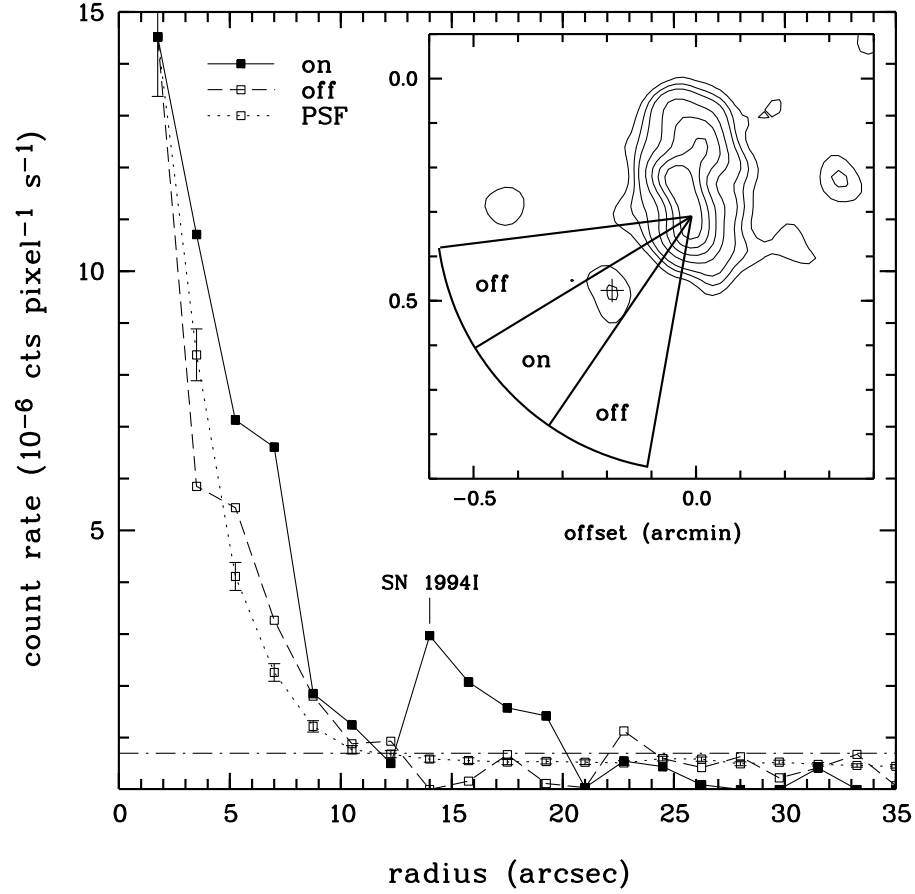


FIGURE 5.6. Radial surface brightness profile of the X-ray emission, centred on the nucleus of M51. Photons were extracted from three sectors in the 6.4 ks observation. The locations of the sectors are shown in the inset image, which gives a contour representation of the inner $1' \times 1'$ region X-ray emission from the 6.4 ks observation. The image was constructed with a pixel size of $1''$ and smoothed with a Gaussian filter of $4''.7$ FWHM. Contour levels are at 1, 1.5, 2, 3, 4, 5 and 6 in units of 1 count per detection cell (5.6×10^{-1} cts s $^{-1}$ arcmin $^{-2}$). The position of the optical nucleus of M51 is at the origin of the sectors, the radio position of the SN 1994I is indicated by a cross. The solid line shows the radially-binned surface brightness profile of the X-ray emission from the center sector, containing SN 1994I ('on'). The dashed line gives the mean surface brightness profile of the emission in the two outer sectors ('off'). The dotted line gives the surface brightness profile of eight co-added point sources. The mean background level of 7×10^{-7} cts pixel $^{-1}$ s $^{-1}$ is indicated by the dot-dashed horizontal line.

5'' of the position of the SN. It therefore should be stressed that we cannot be certain whether the X-ray source at the position of SN 1994I can be attributed to the supernova itself. The positional coincidence and the time correlation, however, are highly suggestive.

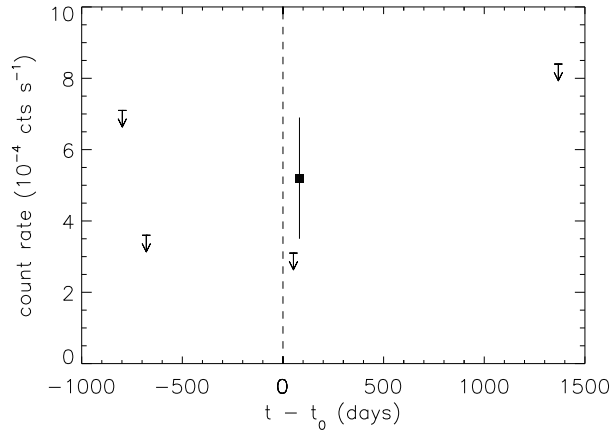


FIGURE 5.7. X-ray lightcurve of SN 1994I. The data points correspond to the five HRI observations (cf. Tab. 5.6), time is given in days relative to the outburst of the SN (March 31, 1994). Arrows represent upper limits at a 3σ confidence level, the count rate error for observation 4 corresponds to a $\pm 1\sigma$ statistical error.

Two models have been proposed for the progenitor of SN 1994I, one by Woosley, Langer & Weaver (1995) and another by Nomoto et al. (1994). In the model presented by Woosley et al., the progenitor was in a close binary system and lost its outer envelope both by mass-transfer to the companion and by a strong stellar wind, leaving a C+O star, which exploded when its iron core collapsed. According to the circumstellar interaction model (cf. Box 4), using our observed luminosity at $t = 82$ days (no. 4) and assuming a wind velocity of $v_w = 10 \text{ km s}^{-1}$, we derive a mass-loss rate of the progenitor of $\dot{M} = 3.6 \times 10^{-6} M_{\odot} \text{ yr}^{-1}$. This is typical of type I SNe, as inferred from radio observations (cf., e.g. SN 1983N, SN 1984L: $2 \times 10^{-6} M_{\odot} \text{ yr}^{-1}$, SN 1990B: $3 \times 10^{-6} M_{\odot} \text{ yr}^{-1}$, Weiler et al. 1993), whereas the mass-loss rate of type II SNe is more than an order of magnitude higher (cf., e.g. SN 1979C: $1 \times 10^{-4} M_{\odot} \text{ yr}^{-1}$, SN 1980K: $3 \times 10^{-5} M_{\odot} \text{ yr}^{-1}$, SN 1996J: $2 \times 10^{-4} M_{\odot} \text{ yr}^{-1}$, Weiler et al. 1993; SN 1988Z: $7 \times 10^{-5} M_{\odot} \text{ yr}^{-1}$, van Dyk et al. 1993). The only stringent upper limit to the X-ray flux of a type I SN (SN 1992A, type Ia) found to date implies a mass-loss rate of $\dot{M} < (2-3) \times 10^{-6} M_{\odot} \text{ yr}^{-1}$ (Schlegel & Petre 1993). However, as Chevalier (1998) pointed out, if synchrotron self-absorption is the dominant absorption mechanism, then it might not be possible to estimate the mass-loss rate using radio observations.

The second model, proposed by Nomoto et al. (1994), suggests that the progenitor of SN 1994I lost its envelope to the companion through two stages of non-conservative mass-transfer, which accounts for the presence of circumstellar matter. We can estimate the density and mass of the circumstellar matter by assuming that the observed X-ray emission on day 82 arises from the shocked circumstellar gas, heated by the outgoing wave. At this time, the SN ejecta had reached a distance of $r_{82} = 1.2 \times 10^{16} \text{ cm}$ for an expansion velocity of $v_s = 16\,500 \text{ km s}^{-1}$ (Filippenko et al. 1995), well outside the orbit of the binary ($\sim 10^{13} \text{ cm}$). For $L_x = \int \Gamma(T)(4\rho)^2 dV$ with a cooling function of $\Gamma(5 \text{ keV}) = 3 \times 10^{-23} \text{ erg cm}^3 \text{ s}^{-1}$ (Raymond et al. 1976), we derive a constant density of $\rho = 2 \times 10^5 \text{ cm}^{-3} v_{16\,500}^{2/3}$ (for a shell expansion velocity in units of $16\,500 \text{ km s}^{-1}$) and a total mass of deposited X-ray luminous gas of $M = 1 \times 10^{-3} M_{\odot}$ inside a sphere of radius $1.2 \times 10^{16} \text{ cm}$. On day 52, the expanding shell had reached a radius of $r_{52} = 7 \times 10^{15} \text{ cm}$. The expected L_x , normalized

to that on day 82, is $4.1 \times 10^{37} \text{ erg s}^{-1}$ with $\rho = 2 \times 10^5 \text{ cm}^{-3}$, which is not in conflict with the 3σ upper limit of $L_x < 9 \times 10^{37} \text{ erg s}^{-1}$ (cf. Lewin et al. 1994). On day 1368, another observation of SN 1994I provided a 3σ upper limit of $2.5 \times 10^{38} \text{ erg s}^{-1}$, which is much lower than expected for a constant velocity expansion into a constant density medium of $\rho = 2 \times 10^5 \text{ cm}^{-3}$. Clearly, the ambient density and/or the expansion speed are significantly lower at these later times and large distances.

5.3. DISCOVERY OF X-RAY EMISSION FROM SUPERNOVA 1979C IN M100

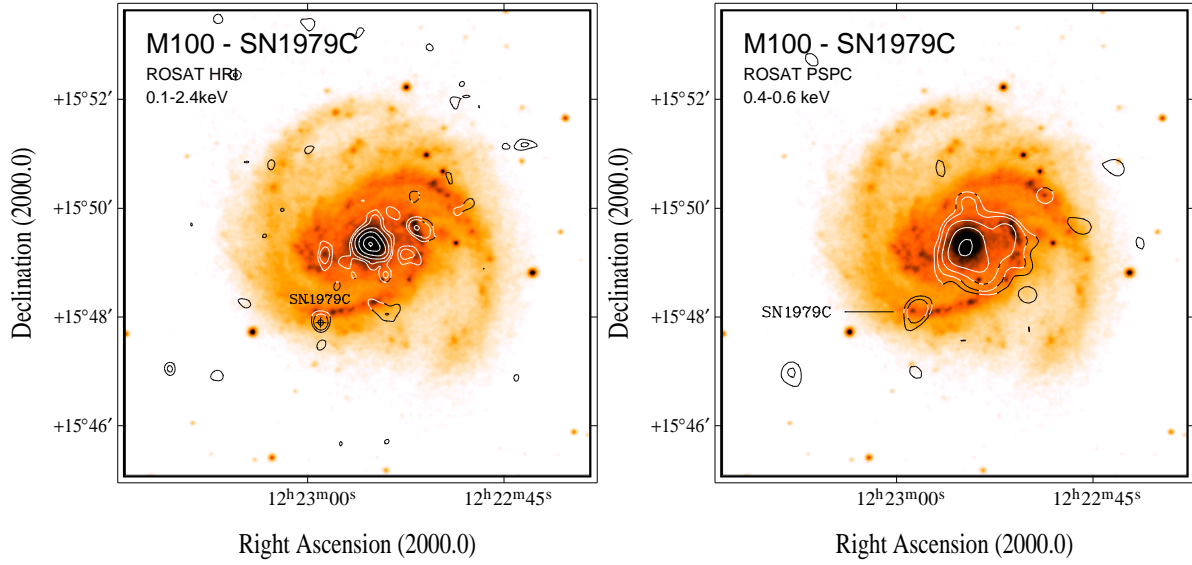


FIGURE 5.8. X-ray contour maps of M100 and SN 1979C, superposed on digitized Palomar Observatory Sky Survey plates. The left-hand panels gives (0.1–2.4 keV) band X-ray contours from the 42.8 ks HRI observation, smoothed with a Gaussian of $12''$ (FWHM), and the right panel from the (0.4–0.6 keV) band PSPC observation, smoothed with a Gaussian of $24''$ (FWHM). Contour levels are at $3, 5, 10, 20$ and 40σ above the mean background rate (HRI: 4.2×10^{-3} cts s^{-1} arcmin $^{-2}$, $1\sigma \cong 1.2 \times 10^{-3}$ cts s^{-1} arcmin $^{-2}$; PSPC: 1.2×10^{-3} cts s^{-1} arcmin $^{-2}$, $1\sigma \cong 8.6 \times 10^{-4}$ cts s^{-1} arcmin $^{-2}$).

SN 1979C was detected by the author and collaborators in a 43 ks ROSAT HRI observation with a luminosity of $L_x = 1.4 \times 10^{39}$ erg s^{-1} (for an assumed 0.5 keV thermal bremsstrahlung spectrum), 16.2 years after the explosion (Immler, Pietsch & Aschenbach 1998a, 1998c). To look for possible earlier X-ray emission from SN 1979C, archival EINSTEIN HRI data were re-analyzed. EINSTEIN IPC observations of M100 were not used because of their poor spatial resolution ($\sim 1'$). Three EINSTEIN HRI observations from June 7, 1979 (4 ks), December 10, 1979 (13 ks), and July 1–2, 1980 (24 ks), taken between days 64 and 454 after the explosion, were merged into a single observation. Inside the region where the individual observations overlap, the merged observation has a total integration time of 41 ks. A local source detection algorithm was applied to an $\sim 18' \times 18'$ image (where the three observations overlap) of $8''$ pixel size. Background corrected count rates were evaluated within circles of $18''$ radius (corresponding to the standard EINSTEIN HRI detection cell, Harris 1984) at the positions of both the EINSTEIN sources detected with a maximum likelihood $L \geq 8$, the ROSAT HRI sources, and the historical SNe. Six point-like X-ray sources are detected inside the D_{25} ellipse of M100 with EINSTEIN (0.1–4.5 keV) band luminosities in the range 1.1 – 5.1×10^{39} erg s^{-1} . However, no X-ray emission is observed from the position of SN 1979C. The 3σ upper limits to the count rates were converted to (0.1–4.5 keV) X-ray flux limits, assuming a 0.5 keV thermal bremsstrahlung spectrum (absorbed by a hydrogen column density of $N_H = 2.3 \times 10^{20}$ cm $^{-2}$) using W3PIMMS. The 3σ upper limit of the merged 41.3 ks EINSTEIN observation is 5.9×10^{39} erg s^{-1} . The upper limits for the individual EINSTEIN observations are 1.8×10^{40} erg s^{-1} (day 64), 7.6×10^{39} erg s^{-1} (day 239) and 6.9×10^{39} erg s^{-1} (day 454), respectively.

The upper limits to the luminosity for the early epochs (EINSTEIN HRI) and the measurement 16 years after (ROSAT HRI) do not differ much, allowing only a small long-term X-ray rate of decline. It has been proposed that X-rays from type II supernovae are created by the interaction of the supernova gas with the circumstellar medium, which is likely to be the wind blown by the progenitor star (Chevalier

1982a,b; 1984a,b; Chevalier & Fransson 1994). The circumstellar matter is heated by the outgoing shock wave associated with the explosion, the supernova gas is heated by the reverse shock wave and the entire matter is confined in a shell. This sometimes called 'mini-shell' model (cf. Box 4) has successfully been used to explain the radio emission from type II supernovae. The radial supernova gas profile is approximated by a power-law, $\rho_{\text{SN}} \sim r^{-n}$ and the density distribution of the circumstellar matter is $\rho_w \sim r^{-2}$. Both radio and X-ray luminosity depend on the shocked matter density, which is proportional to the mass loss rate \dot{M} of the progenitor star divided by the wind velocity v_w , assuming a constant v_w . The supernova shock front radius increases with time as t^m with $m = (n-3)/(n-2)$ (Chevalier & Fransson 1994). The change in radius with time is reflected in the radio and X-ray light curves, and Weiler et al. (1991) have used the 10 year radio light curve of SN 1979C to determine $\dot{M}/v_w = 12$, with \dot{M} in units of 10^{-5} solar masses per year, and v_w , measured in 10 km s^{-1} (see also Lundqvist & Fransson 1988). The index m has been determined to be very close to unity, which means that n is large, and the best fit to the radio light curve by Weiler et al. gives $n = 79$ with a lower limit of $n > 22$ (cf. Chevalier & Fransson 1994). We have used these values to determine the X-ray luminosity expected from the circumstellar interaction model, and it turns out that the ROSAT measurements give a luminosity at least a factor of 30 lower than the model predicts. Such an excess predicted by the model has already been noted for the early EINSTEIN upper limits by Chevalier & Fransson (1994). They have proposed that photoelectric absorption of the reverse shock X-rays by an outer cool shell could explain the discrepancy between model and data. However, photoelectric absorption is unlikely to happen at the time of the ROSAT measurements because of the expansion of the shell and the correspondingly low column density at this late stage after the outburst.

Applying the Chevalier mini-shell model to the luminosity of SN 1979C observed 16.2 years after the outburst (cf. Box 4), a mass-loss rate of the progenitor of $\dot{M} = 1.0 \times 10^{-4} M_{\odot} \text{ yr}^{-1}$ is derived. The same mass-loss rate was derived from radio observations of SN 1979C (Weiler et al. 1993). Monitoring of the radio emission over a period of more than 10 years (Weiler et al. 1991) resulted in the main results that the

- radio emission is due to non-thermal synchrotron process with an optically thin spectral index,
- absorption or optical depth, τ , is purely of a thermal, free-free nature in an ionized medium external to the emitting region with a radial density dependence $\rho \propto r^{-2}$ from a red supergiant wind of constant speed (10 km s^{-1}),
- observed flux density, S , and optical depth, τ , can be well described as function of SN age, $t - t_0$, to the power β and δ , respectively, after an explosion epoch t_0 :

$$S(\text{mJy}) = K_1 \left(\frac{t - t_0}{1 \text{ day}} \right)^{\beta} e^{-\tau}, \quad (5.8)$$

where

$$\tau = K_2 \left(\frac{t - t_0}{1 \text{ day}} \right)^{\delta} \quad (5.9)$$

(the factors K_1 and K_2 are scaling factors for the units of choice) and

- radio rate of decline is linear with $f_{\lambda} \propto t^{-0.7}$ for $\lambda = 2 \text{ cm}$, 6 cm and 20 cm .

Since both the radio and X-ray emission are considered to be linked to the interaction of the SN blast wave with the ambient circumstellar medium, similar results regarding the linear rate of decline of SN 1979C in the X-ray domain are expected. In order to observe the X-ray rate of decline, a ROSAT HRI follow-up observation of SN 1979C was proposed by the author and collaborators. The 25 ks observation from January 1998 gave a count rate of $(4.1 \pm 1.5) \times 10^{-4} \text{ cts s}^{-1}$ for day 6 800 after the outburst of SN 1979C. The best fit X-ray rate of decline to the two HRI observations, computed from regression analysis, is $L_x \propto t^{-3.7}$. The result is in clear contrast to the observed radio rate of

decline ($S_\lambda \propto t^{-0.7}$ with $\lambda = 2, 6$ and 20 cm; Weiler et al. 1991). Indications for an *increase* in the emission of the SN beyond ~ 4000 days after the outburst in the radio regime (cf. Fig. 5.10; Weiler et al. 1997; Montes et al. 2000) are not observed in the X-ray band.

In order to get more information on the declining X-ray flux and possible spectra characteristics, the ROSAT PSPC ‘last light’ campaign was used to apply for a PSPC observation of M100/SN 1979C. Between December 8 and 14, 1998, 10 ks of PSPC data were accumulated. Despite the significantly degraded attitude solution from $\sim 5''$ to $\sim 15''$ – $18''$, the strong X-ray emission of the host galaxy’s nucleus allowed us to determine coordinates within the ROSAT PSPC observation to within $\sim 10''$. In general, the performance of the PSPC observation turned out to be nominal and allowed a detailed analysis of the X-ray emission from SN 1979C.

Images in the broad (0.11–2.35 keV), soft (0.11–0.41 keV), hard (0.52–2.01 keV), hard1 (0.52–0.90 keV) and hard2 (0.91–2.01 keV) bands were created with binning of $5''$ and Gauss-filtered images with a smoothing of $24''$ (FWHM). Within the error of the PSPC positions ($\sim 15''$), an X-ray source is clearly visible at the position of SN 1979C in the hard1 band image. Photons were extracted with a ring of radius $25''$, centred on the position of SN 1979C. The background was taken from a large, source-free region of radius $0'.25$ north-east of the galaxy, since other X-ray sources are found within an annulus centred on the position of SN 1979C. A net rate of $(4.0 \pm 2.0) \times 10^{-4}$ cts s^{-1} is inferred for the X-ray source found at the position of SN 1979C. Photons from within the extraction circle were further binned into the PSPC channels in order to study the spectral distribution of the recorded photons. The resulting raw spectrum of SN 1979C is given in Fig. 5.3. As can be seen, photons are distributed within PSPC energy channels corresponding to photon energies of 0.4–0.6 keV with a peak at 0.5 keV. A Gauss-filtered PSPC image with $25''$ resolution (FWHM) was created in this band and superposed onto a digitized optical image of M100 to illustrate the positional match of the X-ray source with the position of SN 1979C. The image is given in Fig. 5.3.

On the basis of the analysis of the PSPC ‘last light’ observation, and despite the limited photon statistics, there is clear evidence that the X-ray emission of SN 1979C at this late stage after the outburst is rather soft. For conversion of count rates into fluxes and luminosities, a 0.5 keV thermal bremsstrahlung spectrum is hence assumed, similar to the late X-ray emission of SNe 1978K, 1980K, 1986J and 1987A (cf. Sec. 5.1.). The corresponding fluxes and luminosities for the ROSAT HRI and PSPC observations are compiled in Tab. 5.7.

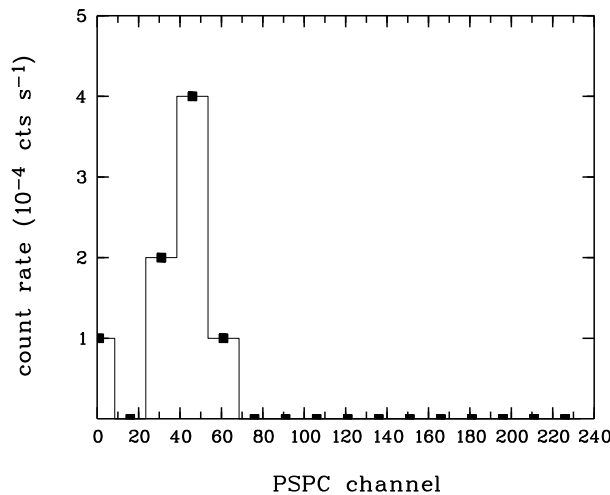


FIGURE 5.9. PSPC pulse height spectrum of photons recorded from the position of SN 1979C.

TABLE 5.7. X-Ray Emission from SN 1979C

Obs. No.	Obs. time	detector	date	day after outburst	Counts	Rate ($10^{-4} \frac{\text{cts}}{\text{s}}$)	f_x^* ($10^{-14} \frac{\text{erg}}{\text{cm}^2 \text{s}}$)	L_x^* ($10^{38} \frac{\text{erg}}{\text{s}}$)
1	4.0	EINSTEIN HRI	06/79	64	—	< 32.9	< 50	< 175
2	13.0	EINSTEIN HRI	12/79	239	—	< 17.0	< 21.7	< 76
3	24.0	EINSTEIN HRI	07/80	454	—	< 15.6	< 20.0	< 69
4	42.8	ROSAT HRI	06/95	5 900	29.5 ± 6.4	6.9 ± 1.5	3.9 ± 0.8	13.8 ± 3.0
5	25.0	ROSAT HRI	01/98	6 800	10.3 ± 3.7	4.1 ± 1.5	2.3 ± 0.8	8.2 ± 3.0
6	10.0	ROSAT PSPC	12/98	7 100	4.0 ± 2.0	4.0 ± 2.0	1.2 ± 0.6	4.2 ± 2.0

* 0.1–2.4 keV band fluxes and luminosities, applying a 0.5 keV thermal bremsstrahlung spectrum

The X-ray lightcurve of SN 1979C is given in Fig. 5.11 EINSTEIN 3σ upper limits based on three EINSTEIN HRI observations of integration time 4 ks, 13 ks and 24 ks, respectively, are plotted as arrows. ROSAT HRI data are marked with filled boxes, the ROSAT PSPC observation is indicated by an open square. The dotted lines give the model predictions according to equation 5.6 in the absence of free-free absorption, while the solid lines include free-free absorption by a circumstellar medium, i.e. by an absorbing material with density profile r^{-2} . The ROSAT data points are hence fitted with a modelled rate of decline of $L_x(\text{erg s}^{-1}) \propto \left(\frac{t-t_0}{1 \text{ day}}\right)^\beta e^{-\tau}$ with $\tau \propto \left(\frac{t-t_0}{1 \text{ day}}\right)^{-2}$. The $t^{-0.7}$ curve represents the rate of decline derived from 6 cm radio observations (Weiler 1986; 1991). The $L_x \propto t^{-3.7}$ curve gives the best fit X-ray rate of decline for the HRI observations only, whereas the $t^{-5.7}$ rate of decline represents the best fit X-ray rate of decline for all ROSAT observations (including PSPC). All models are normalized to the ROSAT data point corresponding to the discovery of X-ray emission from SN 1979C. If the X-ray rate of decline was constant over the last ~ 19 years, a predicted turn-on phase between day 2 000 and 2 500 with a maximum attained luminosity in the range $5\text{--}8 \times 10^{40} \text{ erg s}^{-1}$ is estimated for an assumed t^{-4} rate of decline. If the X-ray rate of decline prior to an assumed change in evolution beyond day ~ 4000 was identical to the observed radio rate of decline of $t^{-0.7}$, SN 1979C attained a maximum (0.1–2.4 keV band) luminosity of $5 \times 10^{39} \text{ erg s}^{-1}$ for a predicted turn-on phase on day 500 after the outburst.

It should be emphasized, however, that the predictions are severely hampered by the large statistical errors due to the limited number of recorded photons. In the near future, such predictions as to the maximum attained X-ray luminosity and the date of X-ray onset for SNe detected after their peak X-ray emission will be feasible with the large collecting power of the Chandra and XMM observatories. Such predictions can then be used to significantly improve the probability for detections of new X-ray SNe with TOO observations and to further revise the interaction models.

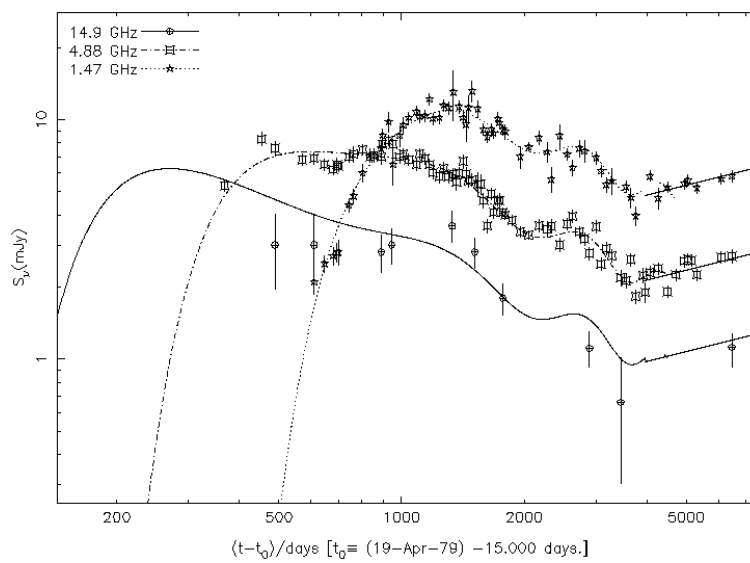


FIGURE 5.10. Radio lightcurve of SN 1979C at 2 cm (14.9 GHz, circles), 6 cm (4.88 GHz, squares) and 20 cm (1.47 GHz, stars). The lines are the best fitted $t^{-0.7}$ rates of decline including sinusoidal modulations (Weiler et al. 1997). Note the change in evolution after day ~ 4000 (year 1990; Montes et al. 2000).

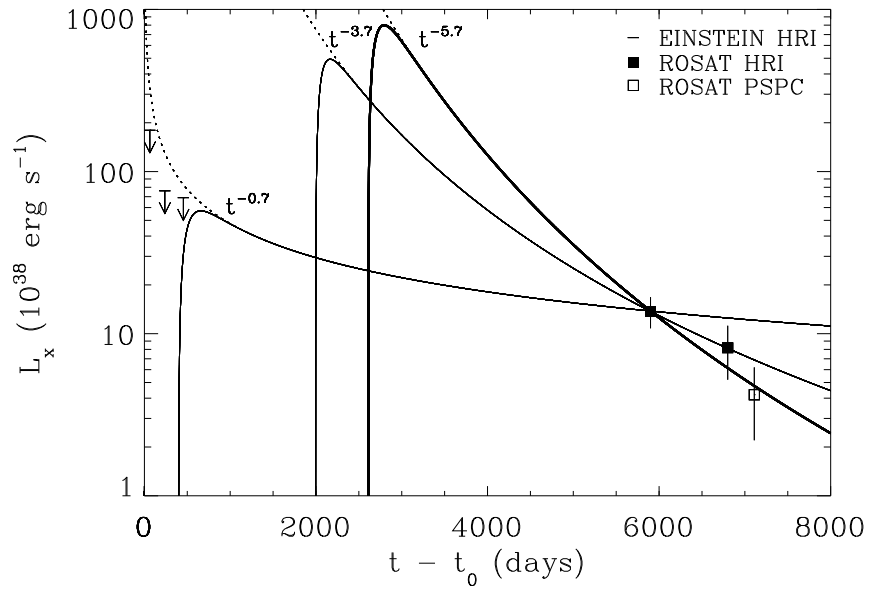


FIGURE 5.11. X-ray lightcurve of SN 1979C and evolutionary models for different rates of decline. EINSTEIN 3σ upper limits are marked with arrows, ROSAT HRI and PSPC luminosities are plotted with filled and open squares, respectively. The dotted lines give the model predictions in the absence of free-free absorption, while the solid lines include free-free absorption by a circumstellar medium. The $t^{-0.7}$ curve represents the rate of decline derived from 6 cm radio observations (Weiler 1986; 1991). The $L_x \propto t^{-3.7}$ curve gives the best fit X-ray rate of decline for the HRI observations only, whereas the $t^{-5.7}$ rate of decline represents the best fit X-ray rate of decline for all ROSAT observations (including PSPC). All models are normalized to the ROSAT data point corresponding to the discovery of X-ray emission from SN 1979C.

6. THE BULGE REGIONS OF NEARBY SPIRAL GALAXIES

*“Innumerable suns exist;
innumerable earths revolve around these suns in a manner
similar to the way the seven planets revolve around our sun.
Living beings inhabit these worlds.”*

Giordano Bruno

In this section, the bulge regions of the galaxies are examined in more detail. Questions will be addressed as to the activity of the nucleus and as to the contribution of discrete X-ray sources to the observed extended bulge emission of the galaxies. Count rates, fluxes and luminosities of the emission components within the bulge regions of the galaxies already have been compiled in Tab. 4.3.

The galaxy M83 shows prominent and extended bulge emission. HRI images of the central $\sim 2' \times 2'$ region of M83 are presented in Fig. 6.1. The left panel (Fig. 6.1a) shows a high-resolution image (constructed with a pixel size of $1''$ and smoothed with a Gaussian filter of $4''.7$ FWHM) with contours of the same image and detected X-ray point sources superposed. The point source candidate H19 at the position of the nucleus of M83 represents the brightest X-ray source in M83 ($L_x = 1.1 \times 10^{40}$ erg s $^{-1}$), while another bright source (H27, 1×10^{39} erg s $^{-1}$) is located $\sim 1'$ to the north-east. H19 is clearly extended (extent $11'' \pm 2''$ FWHM, likelihood of extent $L_{\text{ext}} = 991$), indicative of either the presence of diffuse X-ray emission in the bulge region, several unresolved point sources or the superposition of both emission components. Timing analysis shows that H19 is marginally variable (2.5σ significance, cf. Fig. 7.4).

In an attempt to disentangle the observed extended nuclear X-ray emission from X-ray point sources, the ‘image subtraction technique’ was applied to the data (cf. Sec. 3.2.). Four variable sources are detected within the inner < 1 kpc radius bulge region of M83 with variabilities exceeding 3σ significance (D1–D4; cf. Fig. 6.1b). They are compiled in Tab. 7.10, denoted with ‘D’ (‘difference’), referring to the fact that the X-ray emission at the source positions deviates significantly from the mean X-ray emission during the total period of observation. Luminosities were computed assuming a 5 keV thermal bremsstrahlung spectrum typical for X-ray binaries. It should be noted, however, that the luminosities given in Tab. 7.10 are the luminosities for the variable source emission, representing a lower limit to the absolute source luminosities. Source D1 (luminosity of the variable X-ray emission: 1.0×10^{39} erg s $^{-1}$) coincides with the position of the nuclear source H19, its offset ($1''.9$ south-west of H19) being significantly smaller than the systematic error of the attitude solution and the 90% confidence error radius of H19 ($3''.5$). Besides the nuclear X-ray source, three more sources are detected with the ‘image subtraction technique’ within the bulge region, with variabilities of 6.2×10^{38} erg s $^{-1}$ (D2), 3.7×10^{38} erg s $^{-1}$ (D3) and 3.5×10^{38} erg s $^{-1}$ (D4), respectively. The variability of these sources confirms the marginal variability found by the timing-analysis for the M83 central region.

Furthermore, a radial surface brightness profile was constructed, centred on the X-ray peak emission of the galaxy with a radial binning of $1''.25$ (cf. Fig. 6.2). The background subtracted count rate of the bulge region, computed from the integrated surface brightness profile with a radius $< 25''$ ($\hat{=}$ 1 kpc) from the nucleus, is 2.7×10^{-2} cts s $^{-1}$. As calibration measurements of the HRI showed (David et al.

1997), the PSF is the same for off-axis angles $< 5'$ ($\lesssim 5''$ FWHM). Hence, the radial surface brightness profile of the bright point-like X-ray source H30 (off-axis angle $4.5'$) was subtracted from the bulge region, scaled to the peak X-ray emission of the nucleus ($\times 0.9$, 8.4×10^{-3} cts s^{-1}). Also subtracting the variable emission from sources D2, D3 and D4 (total count rate 2.6×10^{-3} cts s^{-1}) gives a residual emission of 15.5×10^{-3} cts s^{-1} for the bulge region. Assuming the emission arises from truly diffuse, hot gas with a temperature of 0.5 keV, the corresponding luminosity is 4.7×10^{39} erg s^{-1} . This represents 45% of the total luminosity of the bulge region within 1 kpc radius from the nucleus.

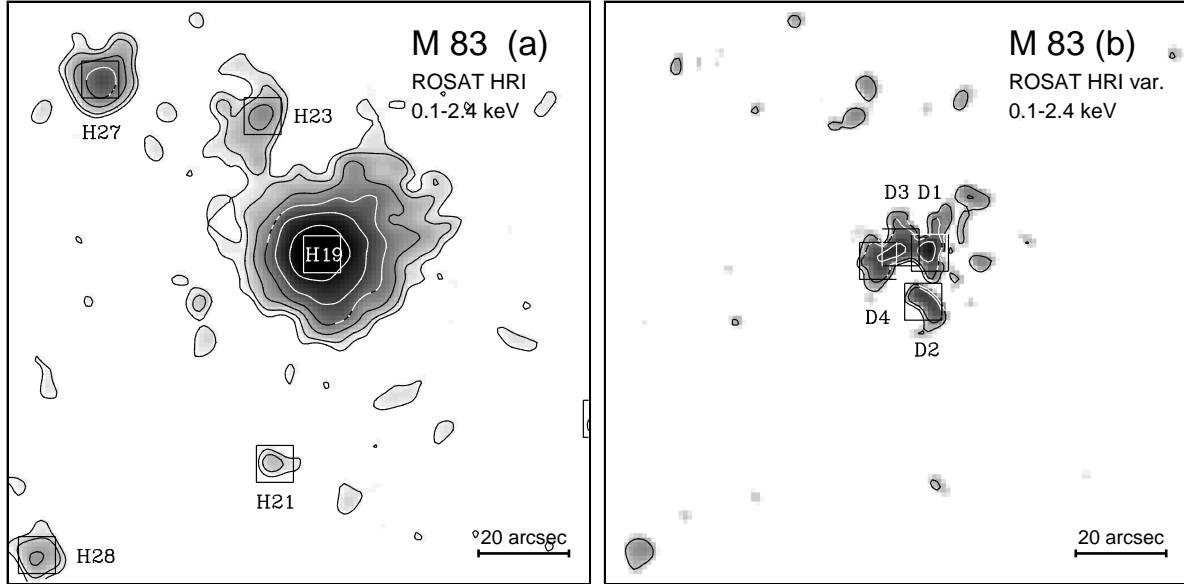


FIGURE 6.1. (a, left-hand panel) Contour representation of X-ray emission (HRI) from the inner region of M83, superposed on a logarithmic grey-scale representation of the same image. The image was constructed with a pixel size of $1''$ and smoothed with a Gaussian of $4.7''$ (FWHM). X-ray contour levels are at $3, 5, 10, 20, 40$ and 80σ above the mean background rate (6.5×10^{-3} cts s^{-1} arcmin $^{-2}$, $1\sigma \equiv 2.2 \times 10^{-3}$ cts s^{-1} arcmin $^{-2}$). HRI detected sources are marked with boxes. The right-hand panel (b) shows *variable* X-ray emission from the nuclear region, resulting from the 'image subtraction technique'. X-ray contour levels are at $3, 5, 10, 20$ and 30σ above the mean background rate (background and 1σ level: 1.5×10^{-2} cts s^{-1} arcmin $^{-2}$). Boxes give the positions of variable X-ray sources detected with a significance exceeding 3σ .

At the center of M101, a relatively weak X-ray source with a luminosity of 2.1×10^{38} erg s^{-1} is detected with the HRI (cf. Fig. 6.4). Timing analysis of the HRI observations and comparison with previous X-ray observations shows that the nuclear X-ray source is not variable on timescales of days – years. Comparison of the radial surface brightness profile of the M101 nuclear region with the modelled on-axis point-spread function demonstrates that the fit of the PSF to the profile is not acceptable ($\chi^2/\nu = 84.1/28$; cf. Fig. 6.5). Subtracting the PSF profile from the radial surface brightness profile of the M101 nucleus gives an excess of emission with luminosity 6×10^{37} erg s^{-1} . Also, the soft X-ray spectral characteristics of the PSPC source at the position of the nucleus (HR1 = 0.53 ± 0.19 , HR2 = 0.04 ± 0.16 for P23 in Wang, Immler & Pietsch 1999), combined with the extended HRI morphology, indicate that a large fraction of the X-ray emission from the nuclear region arises in diffuse hot gas which emits soft X-rays. Indication of extended bulge emission is also visible in the colour image of M101, given in Fig. 7.7.

To further explore the nature of the X-ray emission from the central region, the spectral data from both the PSPC (35 ks observation time) and ASCA GIS (20 ks) observations were studied. Data were extracted from the $R \leq 5'$ region and the background contribution was estimated from an annulus

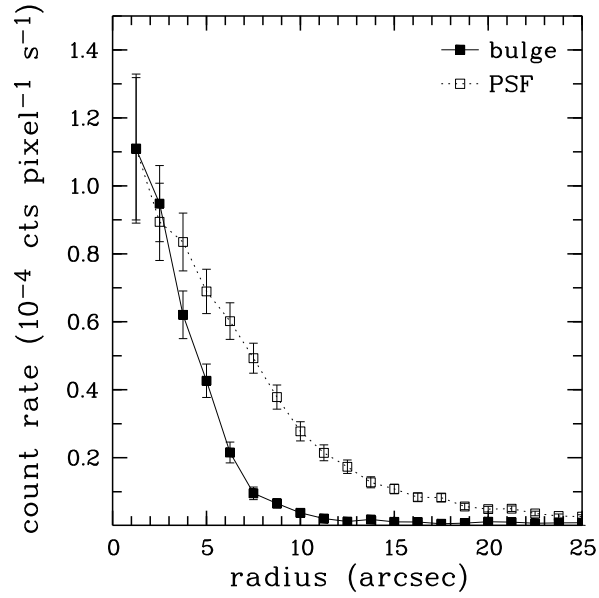


FIGURE 6.2. Radial surface brightness profiles of the X-ray emission from the M83 bulge region within a radius of $< 25''$ ($\cong 1$ kpc) from the nucleus (solid line) and from the point-like X-ray source H30 (dotted line), with radially binning of $1''.25$ each.

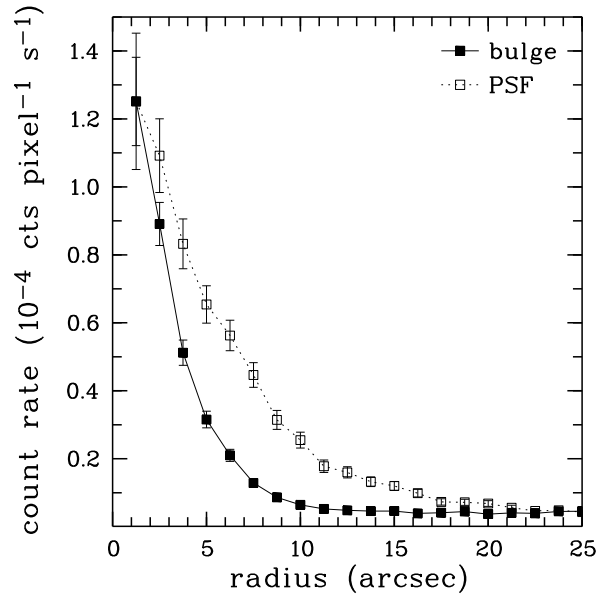


FIGURE 6.3. Radial surface brightness profiles of the X-ray emission from the M51 bulge region within a radius of $< 27''$ ($\cong 1$ kpc) from the nucleus (solid line) and from eight co-added point source (dotted line), with radially binning of $1''.25$ each.

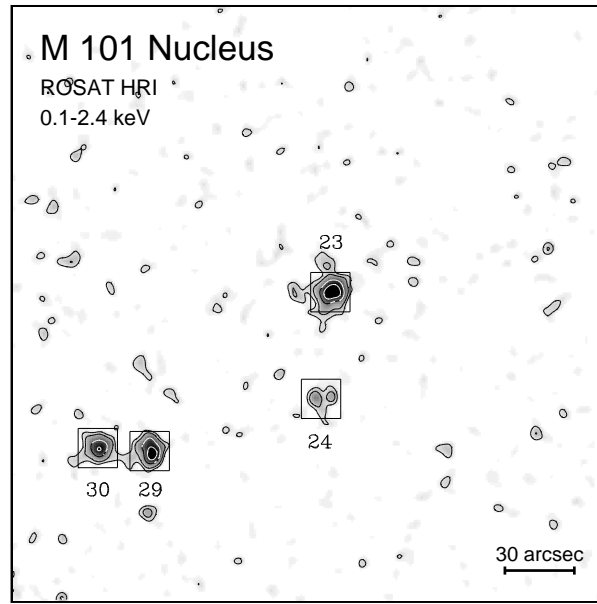


FIGURE 6.4. ROSAT HRI contours of the inner $4'3 \times 4'3$ region of M101, superposed on a greyscale representation of the same image. The image was constructed with a pixel size of $1''$ and smoothed with a Gaussian of $4''.7$ (FWHM). Numbers correspond to HRI source numbers, H23 representing the nucleus of M101. X-ray contours are 4.0×10^{-3} cts s^{-1} arcmin $^{-2}$, 1σ corresponds to 1.0×10^{-3} cts s^{-1} arcmin $^{-2}$.

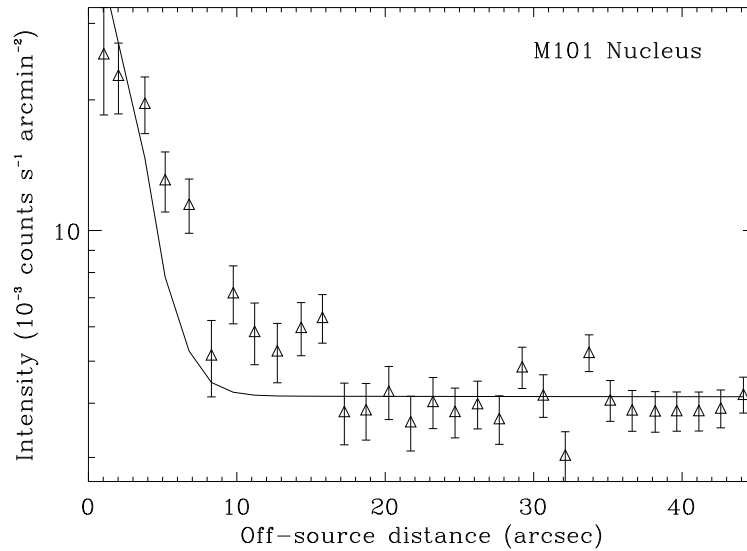


FIGURE 6.5. Radial surface brightness profile of the X-ray emission from the M101 bulge region within a radius of $< 45''$ ($\cong 1.65$ kpc) from the nucleus, with radially binning of $1''.5$ (data points), compared with the PSF of the instrument (solid line).

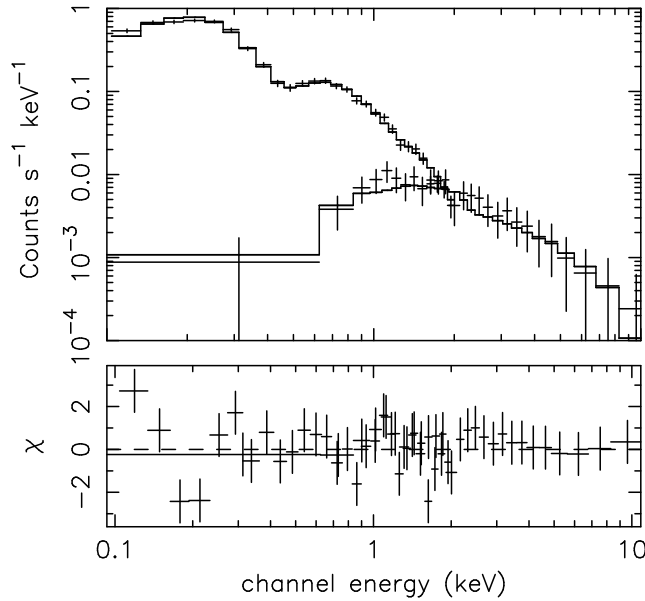


FIGURE 6.6. Combined ROSAT PSPC and ASCA GIS spectrum of the inner $\leq 5'$ region around the M101 nucleus. The best-fit two-temperature thermal plasma model with $T_{\text{low}} = 0.19$ keV and $T_{\text{high}} = 17$ keV is drawn as a histogram. The lower panel shows the residuals to the data.

of radius $12' - 15'$. Because of the limited spatial resolution of the data, sources were not removed. Satisfactory joint fits to the PSPC and GIS spectra were obtained (cf. Fig. 6.6), assuming two-component models: the first model is composed of two thermal plasma spectra with $T_{\text{low}} = 0.19$ keV and $T_{\text{high}} = 17$ keV with an absorption of $N_{\text{H}} = 2.6 \times 10^{19} \text{ cm}^{-2}$ ($\chi^2/\nu = 51.6/50$). The second model comprises a thermal plasma with $kT_{\text{low}} = 0.19$ keV and a power-law component with photon index 1.37, both being attenuated by a hydrogen column of $2.8 \times 10^{19} \text{ cm}^{-2}$ ($\chi^2/\nu = 51.6/50$). Both models give a 0.1–10 keV luminosity of $\sim 2.0 \times 10^{40} \text{ erg s}^{-1}$. The high temperature thermal plasma (or the power-law component) alone predicts an HRI count rate of $\sim 0.01 \text{ cts s}^{-1}$, or about twice the total detected source count rate in the region. It is hence reasonable to assume that this component arises in discrete sources such as X-ray binaries with highly absorbed and relatively hard X-ray spectra, which are not seen with ROSAT. The low-temperature component is likely dominated by truly diffuse hot gas. The characteristic temperature is even lower than that (0.26 – 0.60 keV) of diffuse hot gas observed in the Large Magellanic Cloud (Wang et al. 1991; Trümper et al. 1991; Snowden & Petre 1995). This is, at least partly, due to the high gas column density ($N_{\text{H}} \sim 6 \times 10^{20} \text{ cm}^{-2}$ in our Galaxy alone) toward the LMC; very soft ($\lesssim 0.3$ keV) X-rays are severely absorbed, which biases the detection towards gas at temperatures $\gtrsim 0.3$ keV in the Cloud. There might be an even cooler (a few times 10^5 K) gas component in M101. The best-fit N_{H} is considerably smaller than the expected Galactic column density. This is an indication for the presence of a very soft component in the spectral data (Wang et al. 1995), although the quality of the data used here is not good enough to quantify this spectral component.

In M51, a large fraction of the bulge emission can be resolved into variable point-like X-ray sources by applying the ‘image subtraction technique’. A high-resolution HRI map of the inner $1 \text{ kpc} \times 1 \text{ kpc}$ M51 bulge region is given in Fig. 6.7 (upper panel), together with a map of the variable X-ray emission resulting from the ‘image subtraction technique’ (Fig. 6.7 lower panel). In total, six variable X-ray sources are detected within the inner $1 \text{ kpc} \times 1 \text{ kpc}$ bulge region, totalling in $4.1 \times 10^{39} \text{ erg s}^{-1}$ of variable X-ray emission (excluding the source D5 coinciding with the nucleus of the galaxy). The radial surface brightness profile for the inner region X-ray emission illustrates that the extent of the

emission is not compatible with the radial surface brightness profile of the on-axis PSF, represented by eight co-added point sources (cf. Fig. 6.3). Subtracting the modelled PSF, scaled to the peak X-ray emission of the nucleus, and further excluding the variable X-ray sources detected with the ‘image subtraction technique’ gives a residual emission with a luminosity of $4 \times 10^{38} \text{ erg s}^{-1}$ for unresolved diffuse emission within the inner $< 1 \text{ kpc}$ M51 bulge region. This represents only 5% of the total bulge emission. The different emission components are compiled in Tab. 4.3.

For the inner M51 bulge region, high-quality 6 cm radio band and NII emission maps are available. The greyscale image Fig. 6.8 (Crane & van der Hulst 1992) illustrates the location of the nucleus of M51 (marked as ‘Nuc’), a southern extranuclear cloud (‘XNC’) and a northern ring of radio emission (‘Ring’). NII emission line contours are superposed on the radio map (Cecil 1988). The kinematic line of nodes is indicated with a dashed line. The nucleus and the XNC are linked by a jet-like feature, co-aligned with the kinematic axis of the galaxy (P.A. $\sim 166^\circ$). Kinematic studies have shown that the emission structures result from thermalization of the kinematic energy of a directed nuclear outflow along well-defined shock fronts in the ambient medium. Thus, the southern cloud and the northern ring are tracing outflowing material, inflated by the radio jet (Crane & van der Hulst 1992; Cecil 1988; Scoville et al. 1998; Grillmair et al. 1997).

It has been suggested that the physical conditions of the nuclear region with large amounts of hot, dense matter, are responsible for large productions of X-rays due to hot gas (Ehle, Pietsch & Beck 1995; Kohno et al. 1996). Due to the high-absorbing column along the direction to the nucleus, the low-level AGN itself is highly obscured in X-rays. Interestingly, the X-ray emission, as observed with the ROSAT HRI, seems to trace the outflowing structures (Fig. 6.9 left-hand and right-hand panels). However, after subtraction of a nuclear point source and the variable X-ray emission detected with the ‘image subtraction technique’, only a low level of X-ray emission is left which might be due to hot gas tracing the outflow structures ($\lesssim 4 \times 10^{38} \text{ erg s}^{-1}$ corresponding to 5% of the total bulge emission). The location of the variable, point-like X-ray sources (visible in the overlays of variable X-ray emission on 6 cm radio and NII emission; Fig. 6.10) within the regions of dense molecular gas outside the nucleus demonstrate that the extended X-ray emission structure is mostly mimicked by the presence of variable X-ray point sources.

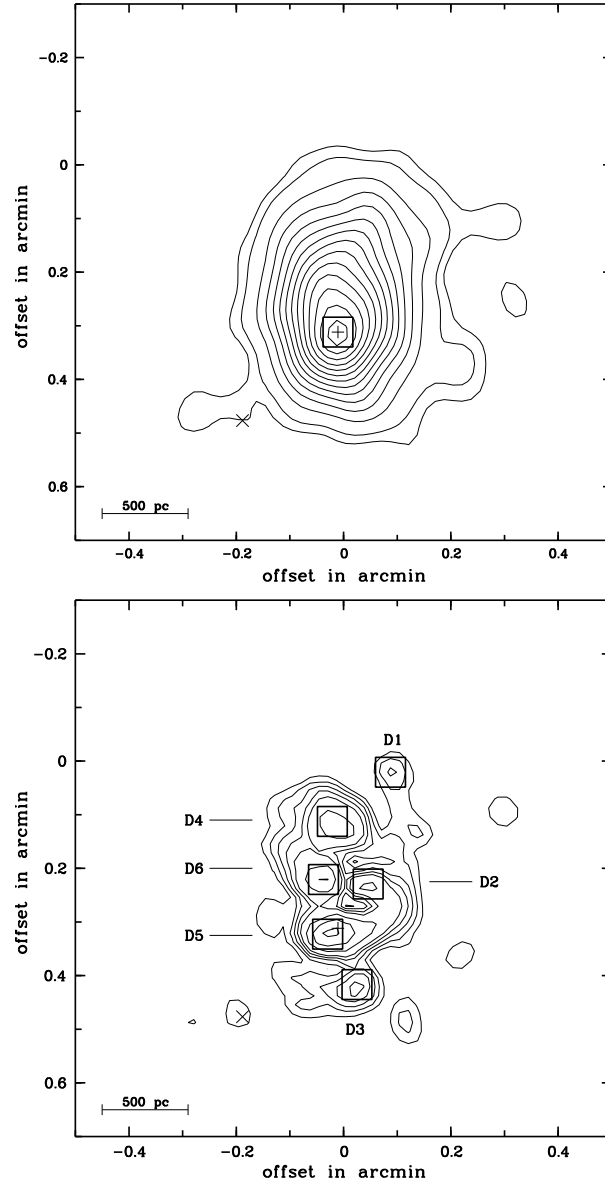


FIGURE 6.7. ROSAT HRI X-ray emission from the bulge region of M51. The upper panel gives X-ray contours from the inner $1' \times 1'$ ($2.2 \times 2.2 \text{ kpc}^2$) bulge region of M51 at the full spatial resolution of the HRI ($4''.7$ FWHM). The first contour level is at $3 \times 10^{-2} \text{ cts s}^{-1} \text{ arcmin}^{-2}$, the second contour level is at $4 \times 10^{-2} \text{ cts s}^{-1} \text{ arcmin}^{-2}$. Increments are at $2.5 \times 10^{-2} \text{ cts s}^{-1} \text{ arcmin}^{-2}$ for all consecutive levels. The plus marks the position of the optical nucleus of the galaxy, the cross indicates the position of SN 1994I. The box marks the position of the nuclear X-ray source (H22). The lower panel gives *variable* X-ray emission for the same region, resulting from the 'image subtraction technique'. Boxes give the positions of variable X-ray sources, detected with a significance exceeding 3.6σ ($L > 8$). Contour levels are at $3, 4, \dots, 13\sigma$ above the background ($3.3 \times 10^{-2} \text{ cts s}^{-1} \text{ arcmin}^{-2}$). 1σ corresponds to $3 \times 10^{-3} \text{ cts s}^{-1} \text{ arcmin}^{-2}$.

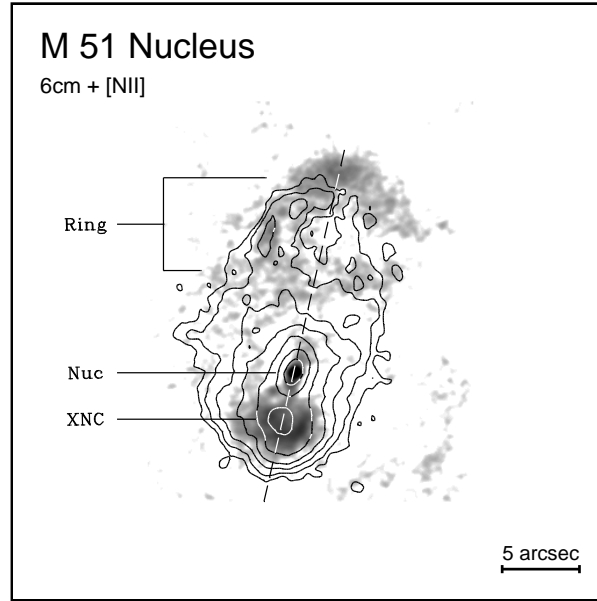


FIGURE 6.8. 6 cm radio band (greyscale representation) and NII emission (contours) from the bulge region of M51. The image gives the inner $0''.6 \times 0''.6$ of the M51 bulge region. The spatial resolution of the 6 cm radio continuum emission is $0''.55 \times 0''.45$. The greyscale dynamics ranges from 0 to $200 \mu\text{Jy/beam}$. Contours give the velocity-integrated [NII] emission at $\lambda = 6583 \text{ \AA}$. The lowest contour level is at $1.2 \times 10^{-16} \text{ erg s}^{-1} \text{ cm}^{-2}$, the highest contour level is at $3.3 \times 10^{-15} \text{ erg s}^{-1} \text{ cm}^{-2}$ (corrected for a distance of 7.7 Mpc). The compact nuclear source (Nuc), the northern radio ring ('Ring') and the southern extranuclear cloud are indicated. The dashed line gives the kinematic axis of the galaxy at a position angle of 166° P.A.

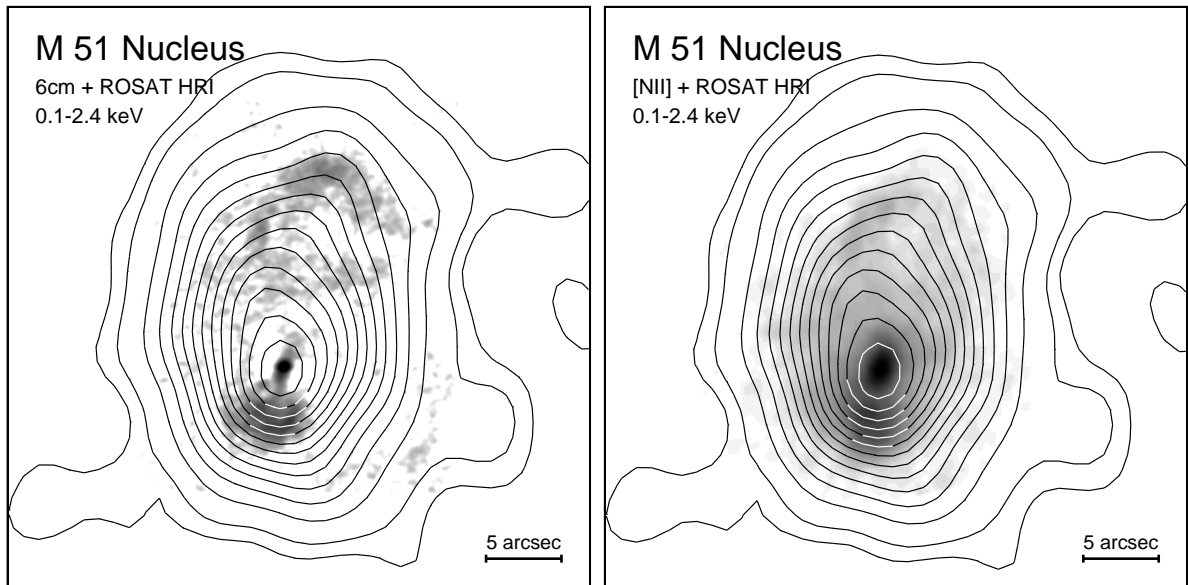


FIGURE 6.9. Contour map of the ROSAT HRI X-ray emission, superposed on a 6 cm radio map (left-hand panel) and [NII] emission (right-hand panel) of the M51 bulge region. Same scale as Fig. 6.8 and same X-ray contour levels as in the upper panel of Fig. 6.7.

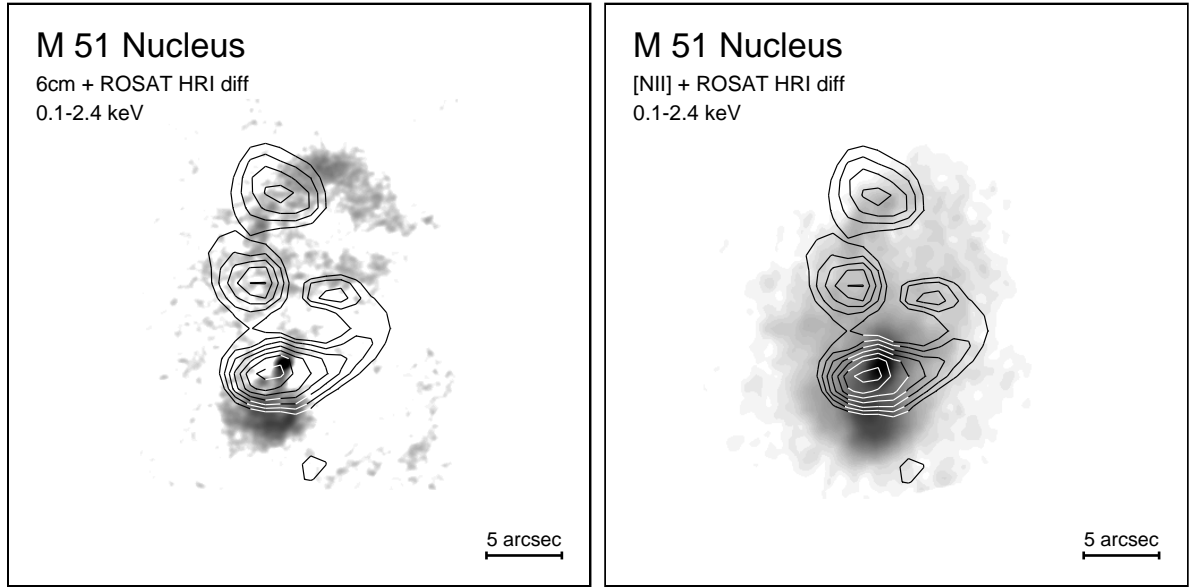


FIGURE 6.10. Contour map of the variable X-ray emission, resulting from the ‘image subtraction technique, superposed on a 6 cm radio map (left-hand panel) and [NII] emission (right-hand panel) of the M51 bulge region. Same scale as Fig. 6.8. X-ray contour levels are at 7, 8...13 σ above the background. Background and standard deviation as in the lower panel of Fig. 6.7. Same scale as Fig. 6.9.

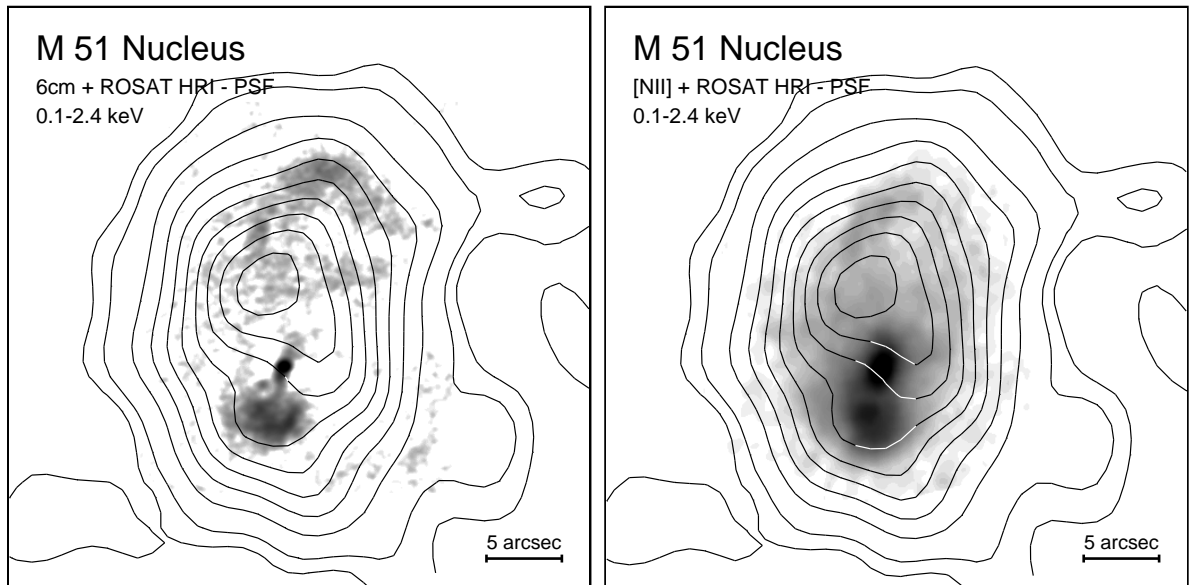


FIGURE 6.11. ROSAT HRI X-ray contours of the M51 bulge region, minus a modelled point-sources at the center of M51. The X-ray contours are superposed on 6 cm radio (left-hand panel) and [NII] emission (right-hand panel). From the 4''7 FWHM HRI X-ray data (cf. Fig. 6.7 upper panel), a modelled point-like X-ray source, constructed from co-adding eight point-like X-ray sources, was subtracted (Fig. 3.1), normalized to the peak X-ray emission of the nucleus.

This correlation of point-like X-ray sources with the extended molecular gas structures becomes also visible in a ROSAT HRI X-ray map, where a modelled X-ray point-source was subtracted from the position of the M51 nucleus (Fig. 6.11). After subtraction of a modelled point-like X-ray source, scaled to the peak X-ray emission, two X-ray sources emerge from the high-resolution X-ray map, coincident with the southern extranuclear cloud and the eastern part of the northern ring. Both sources coincide with peaks of the variable X-ray emission (D6 and south of the nucleus). The results are highly suggestive that the extended X-ray emission, apparently tracing the outflow structures from the M51 nucleus along the bi-directional jet, is due to X-ray binaries located in the molecular clouds north and south of the nucleus. If the map of variable X-ray emission is further compared to the HCN emission maps of the M51 bulge region (Fig. 6.12), it is noticed that the locations of the variable X-ray sources are coincident with peaks in the HCN emission. As the HCN emission regions are believed to be the rotating, dense molecular disk around the M51 nucleus, it is concluded that the variable X-ray sources coinciding with the rotating molecular ring are due to X-ray binary formation within the ionized gas around the nucleus. The detection of an iron K emission line at 6.4 keV from an obscured AGN at the center of M51 with ASCA (not visible with the ROSAT HRI) and large amounts of hard emission typical for LMXBs (Terashima et al. 1998) also support the assumption presented here that a large fraction of the total X-ray emission from the M51 bulge region is due to X-ray binaries. The contribution of variable X-ray sources detected with ROSAT to the total bulge emission is 51% (cf. Tab. 4.3). Approx. $\sim 44\%$ of the X-ray emission is due to an obscured AGN ($3.6 \times 10^{39} \text{ erg s}^{-1}$), while emission from truly diffuse hot gas contributes only $\sim 5\%$ ($4 \times 10^{38} \text{ erg s}^{-1}$) to the total bulge emission within $< 1 \text{ kpc}$ ($8.1 \times 10^{39} \text{ erg s}^{-1}$). The total X-ray output of the M51 bulge hence seems to be dominated by emission from X-ray binaries, which can be spatially resolved from the extended M51 bulge emission.

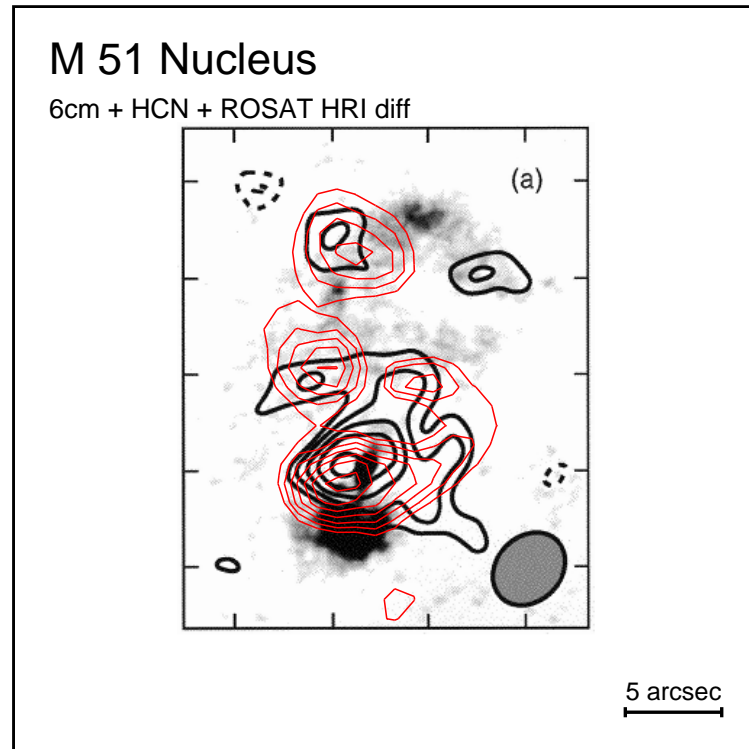


FIGURE 6.12. ROSAT HRI contours of variable X-ray emission, superposed on HCN and 6 cm radio emission from the M51 bulge region. The thin contour lines give variable X-ray emission resulting from the 'image subtraction technique'. Contour levels as in Fig. 6.10. Thick contour lines represent the velocity-integrated HCN emission ($V_{\text{LSR}} = 387 - 546 \text{ km s}^{-1}$). HCN contour levels are at $-3, -2, 2, 3, 4, 5, 6\sigma$, with $\sigma = 0.55 \text{ Jy beam}^{-1} \text{ km s}^{-1} = 5.5 \text{ km s}^{-1}$. The grey-scale image gives 6 cm radio emission (cf. Fig. 6.8). Same scale as Fig. 6.11.

7. CONCLUSIONS AND OUTLOOK

“Sic itur ad astra — Thus shall you go to the stars”

Virgil

Within the scope of this work it was demonstrated that X-ray observations of nearby galaxies provide a unique opportunity to obtain a deep insight in the highly energetic physical processes taking place in our universe. The ROSAT mission undoubtedly led to the most important discoveries and results regarding our understanding of the hot X-ray universe. It is anticipated that with new X-ray observations using the superior capabilities of the next generation X-ray missions Chandra (in operational orbit since July 1999) and XMM (successfully launched on December 10, 1999), our understanding of the physical processes giving rise to X-ray emission in nearby galaxies will be significantly expanded. Major results from this thesis and selected examples of anticipated new studies related to this work are:

◦ X-ray Source Populations:

Strong X-ray emission is observed from all analyzed galaxies, with total (0.1–2.4 keV band) luminosities in the range $1.3 \text{ (M101)} - 5.0 \times 10^{40} \text{ erg s}^{-1} \text{ (M51)}$. Within the D_{25} ellipses of the galaxies, 25 (M51), 21 (M83), 8 (M100) and 40 (M101) X-ray sources, respectively, are detected, with luminosities ranging over two orders of magnitude ($4 \times 10^{37} - 4 \times 10^{39} \text{ erg s}^{-1}$). The sources account for 25% (M51) – 68% (M83) of the total X-ray luminosities of the galaxies (excluding the nuclear X-ray sources). Using the high spatial resolution of the HRI instrument and applying a new technique to search for variable sources in the extended bulge regions, the contribution of discrete X-ray sources to the bulge regions is derived to be 42% (M83) – 71% (M101). The amount of unresolved diffuse emission to the total bulge emission ranges from $\sim 5\%$ (M51, M101) to $\sim 45\%$ (M83). Of all detected X-ray sources, X-ray binaries represent the largest source class ($\sim 50\%$). Up to 10% (M101) of the total X-ray emission of the galaxies can be attributed to identified SNR. There is no clear evidence for X-ray emission due to hot gas from within or outflow from HII regions.

◦ Superluminous X-ray Sources:

Within the D_{25} ellipses of the galaxies, a number of persistent X-ray sources is found with luminosities in excess of the Eddington limit for a $1.4 M_{\odot}$ neutron star (M51: 3, M83: 4, M100: 4, M101: 3). The nature of these superluminous X-ray sources, also observed in many other nearby galaxies, is still unclear. Possible explanations are massive black holes, accreting magnetised neutron stars and collections of unresolved weaker point sources. Although there is still no conclusive proof for the existence of black holes in galaxies, compelling evidence for the presence of off-nuclear black holes in the outer spiral arms of galaxies has been presented within this work. The evidence is based on the high persistent X-ray luminosities for each of the 12 detected sources ($5 \times 10^{38} - 4 \times 10^{39} \text{ erg s}^{-1}$), the variability found for 10 of these sources (e.g. factor of > 3.5 for M51/H14), the hard spectral characteristics (e.g. M83/H30), as well as their apparent correlation with HII regions in the outer spiral arms of the galaxies. It is hence concluded that at least a fraction of these SLSs are due to single, accreting black hole binaries. With the next generation X-ray missions XMM and Chandra, the high number of expected net counts for the luminous target sources will allow high resolution X-ray spectroscopy. X-ray line-diagnostics will allow us to determine the emission spectrum, source

temperature and absorption to an accuracy of only few per cent. In combination, monitoring of the short-term X-ray lightcurve during XMM and Chandra observations and the long-term lightcurve by comparison with previous X-ray observations, together with optical follow-up observations and spectroscopy of optical counterparts will help identifying these enigmatic objects.

◦ **Young Supernovae:**

Prior to this work, nine X-ray emitting SNe were detected. This work led to the discovery of three new X-ray emitting type II SNe (SN 1951H, SN 1970G and SN 1979C). Also, the first evidence for X-ray emission from a type I SN was presented (SN 1994I). From the X-ray observations, physical parameters of both the ejected SN shell and the ambient interstellar medium were derived. It could be shown that, while the progenitors of type II SNe have mass-loss rates of a few $\times 10^{-5} M_{\odot} \text{ yr}^{-1}$, the mass-loss rate of the type Ic SN 1994I is more than an order of magnitude lower ($\sim 10^{-6} M_{\odot} \text{ yr}^{-1}$). Assuming the emission from SN 1994I arises from shocked circumstellar gas, deposited by the progenitor through non-conservative mass-transfer to a companion, a constant gas density of $\rho = 2 \times 10^5 \text{ cm}^{-3} v_{16,500}^{2/3}$ and a total mass of X-ray luminous gas of $M = 1 \times 10^{-3} M_{\odot}$ inside a sphere of radius $1.2 \times 10^{16} \text{ cm}$ is estimated. Spectral analysis showed that the emission of the type II SNe is rather soft ($\sim 0.5 \text{ keV}$) at this late stage after the outburst.

It is expected that with an increasing number of X-ray observations of SNe, it will soon be possible to determine both the date of onset of X-ray emission as well as maximum attained luminosities, even in cases where the actual peak of X-ray emission was not observed. It is essential for a better understanding of the evolution of SNe to both collect high-quality X-ray data of young SNe and refine models as to the emission processes. Due to the high collecting power of the XMM and Chandra instruments and the excellent spectral capabilities, combined with the large energy band extending to 10 keV, it will be possible to distinguish between the characteristic X-ray emission of the forward shock producing gas at $T \sim 10^9 \text{ K}$ and the reverse shock wave in the SN ejecta with $\sim 10^{6-7} \text{ K}$. Also, by establishing long-term X-ray lightcurves, questions related to stellar evolution can be addressed. If the progenitor has undergone non-conservative mass-exchange with a companion, the density structure of the ISM is expected to be clumpy, which will give rise to a non-uniform X-ray rate of decline. X-ray spectroscopy will also clarify the clumpiness of the ambient matter, since the iron emission line width arising from clumps will be significantly narrower ($< 1000 \text{ km s}^{-1}$) than that of the reverse shock at an expansion velocity of $\sim 10000 \text{ km s}^{-1}$. Even physical parameters difficult to derive, such as the chemical composition of the ejecta can be addressed with X-ray line spectroscopy. Simulations show that with a short 10 ks Chandra observation of SN 1978K for example, a high-quality spectrum with ~ 10000 net counts would be recorded with the ACIS-I instrument, given the actual luminosity of the SN of $9 \times 10^{39} \text{ erg s}^{-1}$.

To date, each detection of a SN in the X-ray regime has been published and discussed purely on a case by case basis. A large fraction of the data (e.g. on the X-ray rate of decline) still needs thorough analysis and interpretation. As the number of known X-ray emitting SNe has been significantly expanded within this work and since powerful new X-ray missions are available to monitor the X-ray rate of decline, it can be started to compile all information available on the X-ray emission from young SNe. The combined results can be used in the context of the broadband emission in order to revise and improve models describing the interaction processes of SNe with their ambient interstellar medium.

◦ **Intermediate-Age SNRs:**

Another aspect closely related to the X-ray emission from young SNe is the search for X-ray emission from the missing intermediate-age SNR. In our own and in the Local Group SMC and LMC galaxies alone, some ~ 150 X-ray emitting SNR are known to date, with ages ranging from a few hundred years (e.g. Cas A: ~ 300 years) to many thousands of years (e.g. Vela, Cygnus Loop: 10 000–20 000 years). Interestingly, *no* X-ray emitting SNR at intermediate age between dozens to hundreds of years has yet been found. In terms of the evolutionary phases of a SNR, the lack of detections of interme-

diate SNR is unexplained and somewhat surprising. An expanding SN shell is expected to persistently produce X-rays over a long period starting from the CSM interaction some hundred days after the outburst till the Sedov-Taylor and radiative phases of the SNR some 10^5 years later. The lack of such SNRs cannot be entirely understood by SN explosions in low density bubbles producing fast winds. However, the detection of X-ray emission coinciding with the position of SN 1951H in M101 presented in this work might mark the advent of the detection of this class of X-ray emitting objects. Clearly, more sensitive and high-resolution X-ray follow-up observations with Chandra are needed. Given the high spatial resolution of Chandra ($\sim 0''.5$ FWHM on-axis), SNRs with a diameter of 100 pc will be spatially resolved up to a distance of the host galaxy of ~ 50 Mpc. It is expected that a large fraction of persistent X-ray sources in nearby galaxies are due to the missing intermediate-age SNRs. Coordinated radio and optical observations will be indispensable in identifying SNR candidates, e.g. by their emission line ratio indicators $[\text{SII}]/\text{H}\alpha$.

◦ Old Supernova and Hypernova Remnants:

Based on deep ROSAT HRI observations of M101, four previously unknown X-ray bright SNRs are discovered (H19, H29, H30, H36). The sources are optically well resolved and could be identified as SNRs based on their high emission line ratios $[\text{SII}]/\text{H}\alpha > 0.47$. Optical spectroscopy showed that two of the sources most likely represent relics from energetic hypernova explosions with inferred blast wave energies in excess of 10^{52} erg s^{-1} . Given their high X-ray luminosities of 1 and 3×10^{38} erg s^{-1} , respectively, they are one of the brightest SNRs detected as yet. Previously unknown SNR candidates are also discovered in M51 (H16) and M83 (H23, H26), each coinciding with both bright compact 6 cm and 20 cm radio sources and $\text{H}\alpha$ emission complexes located within the spiral arms of the galaxies. However, as the X-ray sources are not resolved with the ROSAT HRI and as we have no further information as to the radio properties of these sources, Chandra observations capable of spatially resolving the sources and radio follow-up observations are needed. In terms of X-ray luminosities ($\gtrsim 10^{38}$ erg s^{-1}), spectral parameters (0.3 keV best thermal plasma fit) and $[\text{SII}]/\text{H}\alpha$ emission line ratios (0.51–0.76), the hypernova remnant candidates in M101 are strikingly similar to the sources detected in M51 and M83 (e.g. $[\text{SII}]/\text{H}\alpha = 0.63$ for a SNR candidate in M83). Remnants from massive stellar explosions similar to the proposed hypernova remnant candidates in M101 might be an important population of persistent X-ray sources in galaxies with vast implications as to γ -ray bursts/X-ray afterglow events.

By focusing on observations obtained with the next generation X-ray missions with its superior spectral capabilities (XMM and Chandra) and spatial resolving power (Chandra), together with follow-up optical spectroscopy and a thorough re-analysis of selected archival X-ray observations, it is presumed that hypernova remnants might be established as a new class of X-ray emitting objects.

◦ X-Ray Source Luminosity Distributions:

By comparing the luminosity distributions of X-ray sources found within the galaxies, it was found that all galaxies, regardless of their morphological type, distance, inclination and sizes, have similar source luminosity functions, being best described by a power-law $N(> L_x) = N_0 L_x^{-\alpha}$ with exponent ~ 1 . The source luminosity functions only differ in the cut-off at low luminosities, determined by the sensitivity of the observations, and the cut-off at high luminosities. The different high-luminosity cut-offs, however, can be explained by the observed correlation of number of superluminous X-ray sources with star-formation rate of the galaxy. The absence of X-ray sources within M31 at luminosities above the Eddington limit can thus be understood as M31 shows no signs of star formation activity.

◦ Hot Interstellar Medium:

While X-ray emission from the hot interstellar medium was not a prime objective of this work, it is worth to mention that, whereas observations of our own Galaxy cannot give a global picture of the distribution of the hot interstellar medium, both face-on and edge-on galaxies offer a unique chance

to study the overall distribution of the hot galactic ISM. Based on the spectral information supplied by the XMM EPIC and the Chandra ACIS detectors, we will be able to separate the hot gas in the disk from that in the halo for face-on galaxies. For edge-on galaxies, we will determine the morphology, extent, mass and temperature of the halo component with unprecedented accuracy. Radio observation will supplement the X-ray data and allow us to estimate the contribution of hot gas to Faraday rotation. If significant, the combination of X-ray data and Faraday rotation data from the radio range will allow estimates of both the electron density and the filling factor of the hot gas. We will compare electron densities and temperatures in star-forming (active) and less active regions and address the questions whether the hot gas is confined in dense loops above the active regions, or if active regions are the foot-points of fast galactic winds with low density and low temperature. From the observations of the hot ISM in nearby and more distant galaxies, conclusions will be drawn on how large a fraction of the observed soft X-ray background is due to hot gas associated with the Galaxy.

The wealth of information extracted within this project from the analysis of X-ray observations of nearby galaxies has been published in a number of refereed articles (cf. Appendix E). Results were also used to successfully apply for a number of ROSAT and XMM observations both as PI and as Col. Observations proposed as Col for X-ray detections of previously undiscovered SNe with Chandra are also in preparation. The first in a series of Chandra observations of SNe (proposed as Col) already led to the detection of a new X-ray emitting supernova, SN 1999em. This is the first SN from which X-ray emission is detected *prior* to radio emission. It is anticipated that with new X-ray observations using the superior capabilities of the next generation X-ray observatories Chandra and XMM, our understanding of the physical processes producing X-ray emission in nearby spirals will be significantly expanded.

Astronomy, being one of the oldest sciences of humanity, is still one of the most vivid fields of research today. Undoubtedly, Oberth's denotion that, albeit "*Certain studies about the radiating energy are not possible from the earth because the atmosphere absorbs short-wave light rays. ... Exactly those that might easily lead ... to the most far-reaching physical-chemical discoveries*" (Oberth 1923; cf. Sec. 1.) became reality. It is anticipated that many more interesting and far-reaching discoveries will be made as mankind enters a new millennium.

APPENDIX A — SOURCE LISTS

TABLE 7.1. ROSAT HRI M31 Source List

Source	R.A. ²⁰⁰⁰ (h m s)	Dec. ²⁰⁰⁰ (° ' ")	R _{err} (")	lik.	counts	rate (10 ⁻⁴ cts s ⁻¹)	f _x (10 ⁻¹⁴ erg cm ⁻² s ⁻¹)
(1)	(2)	(3)	(4)	(5)	(6)	(7)	(8)
H1	00 41 50.06	+41 13 36.7	7.1	15.4	60.4 ± 13.2	3.5 ± 0.8	2.3 ± 0.5
H2	00 41 51.51	+41 14 38.3	5.5	27.0	73.1 ± 12.8	4.3 ± 0.7	2.8 ± 0.5
H3	00 41 52.51	+41 12 41.8	6.1	24.9	75.0 ± 13.5	4.4 ± 0.8	2.9 ± 0.5
H4	00 42 04.95	+41 18 26.1	4.0	4154.2	1658.3 ± 42.1	96.9 ± 2.5	63.7 ± 1.6
H5	00 42 05.71	+41 13 28.6	4.4	87.1	114.6 ± 13.1	6.7 ± 0.8	4.4 ± 0.5
H6	00 42 07.75	+41 18 15.2	4.1	670.7	401.3 ± 21.4	23.4 ± 1.2	15.4 ± 0.8
H7	00 42 07.78	+41 04 36.7	6.9	49.8	172.1 ± 21.2	10.1 ± 1.2	6.6 ± 0.8
H8	00 42 08.93	+41 20 49.7	4.8	44.1	81.5 ± 12.1	4.8 ± 0.7	3.1 ± 0.5
H9	00 42 09.48	+41 17 45.2	4.2	133.5	134.1 ± 13.5	7.8 ± 0.8	5.1 ± 0.5
H10	00 42 10.30	+41 15 10.7	4.7	25.9	50.6 ± 9.7	3.0 ± 0.6	1.9 ± 0.4
H11	00 42 10.72	+41 12 48.7	4.9	23.9	50.1 ± 9.8	2.9 ± 0.6	1.9 ± 0.4
H12	00 42 11.89	+41 10 49.2	5.2	22.9	56.3 ± 10.9	3.3 ± 0.6	2.2 ± 0.4
H13	00 42 12.14	+41 17 59.2	4.2	156.2	149.2 ± 14.1	8.7 ± 0.8	5.7 ± 0.5
H14	00 42 12.02	+41 16 49.2	5.1	11.2	28.0 ± 7.8	1.6 ± 0.5	1.1 ± 0.3
H15	00 42 13.12	+41 18 36.8	4.0	2637.4	1069.2 ± 33.8	62.5 ± 2.0	41.0 ± 1.3
H16	00 42 15.16	+41 12 33.8	4.1	735.3	431.0 ± 22.2	25.2 ± 1.3	16.5 ± 0.9
H17	00 42 15.50	+41 20 32.8	4.4	62.1	86.6 ± 11.6	5.1 ± 0.7	3.3 ± 0.4
H18	00 42 15.70	+41 17 21.3	4.2	144.8	137.3 ± 13.5	8.0 ± 0.8	5.3 ± 0.5
H19	00 42 15.81	+41 01 13.3	4.9	391.2	913.7 ± 38.2	53.4 ± 2.2	35.1 ± 1.5
H20	00 42 18.35	+41 12 22.3	4.0	2305.8	960.8 ± 32.1	56.1 ± 1.9	36.9 ± 1.2
H21	00 42 18.65	+41 14 01.3	4.0	1434.5	647.1 ± 26.6	37.8 ± 1.6	24.8 ± 1.0
H22	00 42 20.35	+41 26 42.9	7.4	19.9	76.0 ± 14.7	4.4 ± 0.9	2.9 ± 0.6
H23	00 42 21.47	+41 16 01.4	4.0	873.6	452.5 ± 22.5	26.4 ± 1.3	17.4 ± 0.9
H24	00 42 22.42	+41 13 33.4	4.0	566.8	326.4 ± 19.3	19.1 ± 1.1	12.5 ± 0.7
H25	00 42 22.49	+40 59 21.4	11.1	17.6	198.4 ± 28.3	11.6 ± 1.7	7.6 ± 1.1
H26	00 42 22.98	+41 15 34.9	4.0	2335.6	892.8 ± 30.8	52.2 ± 1.8	34.3 ± 1.2
H27	00 42 23.11	+41 07 37.4	5.7	21.5	63.0 ± 12.1	3.7 ± 0.7	2.4 ± 0.5
H28	00 42 23.12	+41 14 07.4	4.2	68.2	79.5 ± 10.6	4.6 ± 0.6	3.1 ± 0.4
H29	00 42 25.12	+41 13 39.9	4.1	168.7	135.1 ± 12.9	7.9 ± 0.8	5.2 ± 0.5
H30	00 42 25.29	+41 15 36.4	4.0	1775.5	811.3 ± 29.7	47.4 ± 1.7	31.1 ± 1.1
H31	00 42 26.12	+41 19 15.9	4.1	211.9	169.2 ± 14.5	9.9 ± 0.8	6.5 ± 0.6
H32	00 42 26.18	+41 25 53.9	4.7	95.5	158.6 ± 16.4	9.3 ± 1.0	6.1 ± 0.6
H33	00 42 26.44	+41 16 55.9	4.1	194.5	146.3 ± 13.4	8.5 ± 0.8	5.6 ± 0.5
H34	00 42 28.32	+41 12 21.9	4.0	2798.2	1057.7 ± 33.5	61.8 ± 2.0	40.6 ± 1.3
H35	00 42 29.05	+41 04 33.0	4.4	441.8	503.6 ± 26.8	29.4 ± 1.6	19.3 ± 1.0
H36	00 42 29.08	+41 08 15.4	4.1	609.3	440.7 ± 23.0	25.7 ± 1.3	16.9 ± 0.9
H37	00 42 29.50	+41 29 08.4	7.9	26.6	114.0 ± 18.6	6.7 ± 1.1	4.4 ± 0.7
H38	00 42 31.14	+41 16 21.5	4.0	2466.6	994.5 ± 32.6	58.1 ± 1.9	38.2 ± 1.3
H39	00 42 31.31	+41 19 40.0	4.0	950.5	468.4 ± 22.8	27.4 ± 1.3	18.0 ± 0.9
H40	00 42 32.21	+41 13 13.0	4.0	932.4	518.9 ± 24.3	30.3 ± 1.4	19.9 ± 0.9
H41	00 42 33.26	+41 03 24.5	6.3	52.9	159.9 ± 19.5	9.3 ± 1.1	6.1 ± 0.7
H42	00 42 33.36	+41 17 03.5	4.1	152.7	145.1 ± 13.8	8.5 ± 0.8	5.6 ± 0.5
H43	00 42 33.89	+41 16 19.5	4.2	205.4	218.6 ± 17.4	12.8 ± 1.0	8.4 ± 0.7
H44	00 42 35.18	+41 13 19.5	5.2	10.6	23.9 ± 6.9	1.4 ± 0.4	0.9 ± 0.3
H45	00 42 35.30	+41 20 06.5	4.3	53.2	67.7 ± 10.1	4.0 ± 0.6	2.6 ± 0.4
H46	00 42 36.69	+41 13 51.0	4.7	25.8	57.9 ± 10.5	3.4 ± 0.6	2.2 ± 0.4
H47	00 42 38.64	+41 16 03.5	4.0	14225.7	7693.2 ± 88.6	449.5 ± 5.2	295.3 ± 3.4
H48	00 42 39.57	+41 14 28.0	4.1	273.1	239.7 ± 17.5	14.0 ± 1.0	9.2 ± 0.7
H49	00 42 40.14	+41 15 46.5	4.0	1475.8	622.8 ± 25.9	36.4 ± 1.5	23.9 ± 1.0
H50	00 42 40.27	+41 18 46.5	4.5	37.9	61.8 ± 10.2	3.6 ± 0.6	2.4 ± 0.4
H51	00 42 40.72	+41 13 27.0	4.1	239.2	174.9 ± 14.6	10.2 ± 0.9	6.7 ± 0.6
H52	00 42 40.72	+41 10 30.0	5.3	10.8	28.1 ± 7.8	1.6 ± 0.5	1.1 ± 0.3
H53	00 42 40.90	+41 16 18.5	4.3	62.4	307.9 ± 22.7	18.0 ± 1.3	11.8 ± 0.9
H54	00 42 42.09	+41 15 31.0	6.3	38.2	76.9 ± 11.9	4.5 ± 0.7	3.0 ± 0.5
H55	00 42 41.83	+41 21 07.0	4.6	16.4	32.3 ± 7.6	1.9 ± 0.4	1.2 ± 0.3
H56	00 42 42.54	+41 16 59.5	4.4	96.6	218.1 ± 18.9	12.7 ± 1.1	8.4 ± 0.7
H57	00 42 42.41	+41 14 44.5	4.1	430.2	337.9 ± 20.4	19.7 ± 1.2	13.0 ± 0.8
H58	00 42 42.67	+41 15 52.0	4.1	661.0	616.4 ± 27.2	36.0 ± 1.6	23.7 ± 1.0
H59	00 42 43.07	+41 15 43.0	4.6	295.5	315.4 ± 20.8	18.4 ± 1.2	12.1 ± 0.8
H60	00 42 43.28	+41 15 11.0	4.4	66.7	232.6 ± 19.9	13.6 ± 1.2	8.9 ± 0.8
H61	00 42 43.46	+41 16 32.5	4.1	671.4	573.2 ± 26.7	33.5 ± 1.6	22.0 ± 1.0
H62	00 42 44.26	+41 28 14.0	4.4	338.7	437.8 ± 25.6	25.6 ± 1.5	16.8 ± 1.0
H63	00 42 44.48	+41 16 07.5	4.0	2676.4	1574.7 ± 41.6	92.0 ± 2.4	60.4 ± 1.6
H64	00 42 44.83	+41 11 36.5	4.0	1454.2	628.4 ± 26.1	36.7 ± 1.5	24.1 ± 1.0
H65	00 42 45.01	+41 17 38.5	4.4	92.5	186.1 ± 17.7	10.9 ± 1.0	7.1 ± 0.7

TABLE 7.1. ROSAT HRI M31 Source List (Continued)

Source	R.A. ²⁰⁰⁰ (h m s)	Dec. ²⁰⁰⁰ (° ' ")	R _{err} (")	lik.	counts	rate (10 ⁻⁴ cts s ⁻¹)	f_x (10 ⁻¹⁴ erg cm ⁻² s ⁻¹)
(1)	(2)	(3)	(4)	(5)	(6)	(7)	(8)
H66	00 42 45.01	+41 14 06.5	4.2	112.3	114.4 ± 12.5	6.7 ± 0.7	4.4 ± 0.5
H67	00 42 45.19	+41 16 21.5	4.0	1778.5	1230.7 ± 37.3	71.9 ± 2.2	47.2 ± 1.4
H68	00 42 45.06	+41 15 24.0	10.9	15.9	105.0 ± 17.5	6.1 ± 1.0	4.0 ± 0.7
H69	00 42 45.28	+41 17 22.5	4.1	227.4	215.2 ± 16.8	12.6 ± 1.0	8.3 ± 0.6
H70	00 42 46.03	+41 15 43.0	4.2	242.6	395.0 ± 23.6	23.1 ± 1.4	15.2 ± 0.9
H71	00 42 46.79	+41 16 13.0	4.1	715.6	423.8 ± 20.6	24.8 ± 1.2	16.3 ± 0.8
H72	00 42 47.05	+41 11 56.5	4.6	18.9	37.8 ± 8.3	2.2 ± 0.5	1.5 ± 0.3
H73	00 42 47.19	+41 16 28.5	4.0	4837.6	1842.8 ± 44.2	107.7 ± 2.6	70.7 ± 1.7
H74	00 42 47.76	+41 11 12.5	4.1	266.6	183.3 ± 14.7	10.7 ± 0.9	7.0 ± 0.6
H75	00 42 47.90	+41 15 33.0	4.3	674.8	490.0 ± 24.3	28.6 ± 1.4	18.8 ± 0.9
H76	00 42 48.52	+41 15 20.5	4.0	3554.1	1446.5 ± 39.3	84.5 ± 2.3	55.5 ± 1.5
H77	00 42 48.44	+41 25 24.0	4.1	860.1	576.7 ± 26.1	33.7 ± 1.5	22.1 ± 1.0
H78	00 42 48.78	+41 16 25.5	7.3	24.4	60.0 ± 11.2	3.5 ± 0.7	2.3 ± 0.4
H79	00 42 49.23	+41 18 17.0	4.2	114.7	120.8 ± 12.8	7.1 ± 0.7	4.6 ± 0.5
H80	00 42 50.47	+41 15 56.0	4.4	60.2	208.6 ± 18.9	12.2 ± 1.1	8.0 ± 0.7
H81	00 42 50.74	+41 16 14.5	4.4	48.6	218.4 ± 19.7	12.8 ± 1.1	8.4 ± 0.8
H82	00 42 51.97	+41 31 11.5	4.2	1691.6	2464.3 ± 54.9	144.0 ± 3.2	94.6 ± 2.1
H83	00 42 52.52	+41 18 55.0	4.0	3936.8	1410.2 ± 38.5	82.4 ± 2.3	54.1 ± 1.5
H84	00 42 52.55	+41 15 40.0	4.0	5347.8	1921.1 ± 45.0	112.2 ± 2.6	73.7 ± 1.7
H85	00 42 54.99	+41 16 03.0	4.0	2763.1	1119.5 ± 34.6	65.4 ± 2.0	43.0 ± 1.3
H86	00 42 55.38	+41 25 59.5	4.2	402.8	378.1 ± 22.3	22.1 ± 1.3	14.5 ± 0.9
H87	00 42 55.40	+41 18 35.5	4.2	132.7	148.5 ± 14.3	8.7 ± 0.8	5.7 ± 0.6
H88	00 42 55.98	+41 20 12.5	4.6	23.1	41.1 ± 8.5	2.4 ± 0.5	1.6 ± 0.3
H89	00 42 57.75	+41 17 19.9	4.3	42.1	55.1 ± 9.1	3.2 ± 0.5	2.1 ± 0.4
H90	00 42 57.94	+41 11 02.9	4.0	1735.5	762.5 ± 28.8	44.6 ± 1.7	29.3 ± 1.1
H91	00 42 58.36	+41 15 28.9	4.1	285.5	231.1 ± 17.0	13.5 ± 1.0	8.9 ± 0.7
H92	00 42 59.71	+41 19 19.9	4.0	1029.4	501.6 ± 23.5	29.3 ± 1.4	19.3 ± 0.9
H93	00 42 59.50	+41 12 40.9	4.9	13.7	33.1 ± 8.2	1.9 ± 0.5	1.3 ± 0.3
H94	00 42 59.91	+41 16 05.9	4.0	900.2	480.4 ± 23.2	28.1 ± 1.4	18.4 ± 0.9
H95	00 43 00.80	+41 14 39.9	5.0	18.2	46.3 ± 9.8	2.7 ± 0.6	1.8 ± 0.4
H96	00 43 01.06	+41 13 50.9	4.2	103.2	99.1 ± 11.5	5.8 ± 0.7	3.8 ± 0.4
H97	00 43 01.36	+41 30 19.4	6.3	74.1	230.6 ± 23.7	13.5 ± 1.4	8.9 ± 0.9
H98	00 43 03.15	+41 15 24.9	4.0	1779.9	915.8 ± 31.7	53.5 ± 1.9	35.2 ± 1.2
H99	00 43 03.17	+41 10 13.4	4.3	81.1	99.4 ± 12.1	5.8 ± 0.7	3.8 ± 0.5
H100	00 43 03.36	+41 21 22.9	4.1	248.5	198.0 ± 15.7	11.6 ± 0.9	7.6 ± 0.6
H101	00 43 03.09	+41 20 43.4	5.0	11.8	29.0 ± 7.7	1.7 ± 0.5	1.1 ± 0.3
H102	00 43 03.92	+41 18 04.9	4.0	1315.4	596.8 ± 25.5	34.9 ± 1.5	22.9 ± 1.0
H103	00 43 04.39	+41 16 01.4	4.3	50.1	64.2 ± 9.8	3.7 ± 0.6	2.5 ± 0.4
H104	00 43 06.59	+41 19 14.9	5.0	13.0	30.0 ± 7.8	1.8 ± 0.5	1.2 ± 0.3
H105	00 43 07.61	+41 20 19.8	4.4	34.6	54.2 ± 9.4	3.2 ± 0.5	2.1 ± 0.4
H106	00 43 08.81	+41 12 47.3	4.2	69.2	85.1 ± 11.1	5.0 ± 0.6	3.3 ± 0.4
H107	00 43 09.87	+41 19 01.3	4.0	3195.6	1156.2 ± 34.8	67.6 ± 2.0	44.4 ± 1.3
H108	00 43 10.68	+41 14 50.8	4.0	6759.2	2055.9 ± 46.0	120.1 ± 2.7	78.9 ± 1.8
H109	00 43 14.44	+41 07 18.7	4.1	711.1	569.3 ± 26.7	33.3 ± 1.6	21.9 ± 1.0
H110	00 43 15.58	+41 11 22.7	4.5	38.9	65.7 ± 10.6	3.8 ± 0.6	2.5 ± 0.4
H111	00 43 16.08	+41 18 43.7	5.3	18.1	47.8 ± 10.2	2.8 ± 0.6	1.8 ± 0.4
H112	00 43 18.78	+41 18 04.2	5.1	15.9	37.0 ± 8.7	2.2 ± 0.5	1.4 ± 0.3
H113	00 43 18.98	+41 20 17.7	4.1	332.2	273.0 ± 18.6	16.0 ± 1.1	10.5 ± 0.7
H114	00 43 20.00	+41 15 35.1	4.9	22.7	47.5 ± 9.6	2.8 ± 0.6	1.8 ± 0.4
H115	00 43 21.17	+41 17 50.6	4.1	310.8	236.3 ± 17.0	13.8 ± 1.0	9.1 ± 0.7
H116	00 43 24.99	+41 17 28.5	5.2	18.3	45.6 ± 9.8	2.7 ± 0.6	1.8 ± 0.4
H117	00 43 25.01	+41 23 28.5	6.0	19.0	65.4 ± 13.0	3.8 ± 0.8	2.5 ± 0.5
H118	00 43 28.02	+41 18 31.0	4.1	409.7	340.0 ± 20.7	19.9 ± 1.2	13.1 ± 0.8
H119	00 43 29.18	+41 07 44.4	4.6	159.3	260.7 ± 21.0	15.2 ± 1.2	10.0 ± 0.8
H120	00 43 32.49	+41 10 39.8	5.3	38.3	93.2 ± 14.0	5.4 ± 0.8	3.6 ± 0.5
H121	00 43 34.47	+41 13 22.3	4.0	2771.5	1332.9 ± 38.3	77.9 ± 2.2	51.2 ± 1.5
H122	00 43 37.46	+41 14 43.2	4.1	1233.2	788.6 ± 30.5	46.1 ± 1.8	30.3 ± 1.2
H123	00 43 39.36	+41 26 49.1	10.2	14.6	103.1 ± 20.7	6.0 ± 1.2	4.0 ± 0.8
H124	00 43 40.07	+41 20 32.1	7.2	14.6	61.7 ± 13.6	3.6 ± 0.8	2.4 ± 0.5
H125	00 43 44.21	+41 12 28.5	6.2	27.2	90.7 ± 15.3	5.3 ± 0.9	3.5 ± 0.6
H126	00 43 44.75	+41 24 12.0	5.0	174.3	348.9 ± 25.5	20.4 ± 1.5	13.4 ± 1.0
H127	00 43 53.86	+41 16 55.1	4.2	1101.6	953.4 ± 35.1	55.7 ± 2.1	36.6 ± 1.3
H128	00 43 56.30	+41 22 04.1	6.7	45.4	183.3 ± 22.4	10.7 ± 1.3	7.0 ± 0.9

TABLE 7.2. ROSAT HRI M51 Source List

Source	R.A. ²⁰⁰⁰ (h m s)	Dec. ²⁰⁰⁰ (° ' ")	R _{err} (")	lik.	counts	rate (10 ⁻⁴ cts s ⁻¹)	f_x (10 ⁻¹⁴ erg cm ⁻² s ⁻¹)
(1)	(2)	(3)	(4)	(5)	(6)	(7)	(8)
H1	13 28 32.22	+47 04 01.1	13.8	11.5	59.6 ± 14.4	9.8 ± 2.4	4.2 ± 1.0
H2	13 28 35.73	+47 16 03.4	14.5	8.8	46.3 ± 12.9	7.4 ± 2.1	3.2 ± 0.9
H3	13 28 46.02	+47 21 42.1	11.5	13.8	63.4 ± 14.2	10.3 ± 2.3	4.4 ± 1.0
H4	13 28 47.86	+47 02 43.9	11.4	11.3	50.9 ± 12.6	8.2 ± 2.0	3.5 ± 0.9
H5	13 28 48.09	+47 12 03.3	7.5	16.5	45.6 ± 10.1	7.1 ± 1.6	3.0 ± 0.7
H6	13 28 54.65	+47 08 09.1	4.6	81.0	101.3 ± 12.2	15.7 ± 1.9	6.7 ± 0.8
H7	13 29 06.58	+47 09 12.5	6.6	12.4	24.8 ± 6.8	3.8 ± 1.0	1.6 ± 0.4
H8	13 29 09.98	+47 22 13.2	8.9	11.6	42.3 ± 10.8	6.6 ± 1.7	2.9 ± 0.7
H9	13 29 20.42	+47 07 14.9	7.9	9.2	28.4 ± 8.0	4.3 ± 1.2	1.8 ± 0.5
H10	13 29 20.57	+47 18 02.3	5.7	16.1	31.9 ± 7.7	4.8 ± 1.2	2.1 ± 0.5
H11	13 29 35.53	+47 27 04.2	17.7	11.0	71.9 ± 17.3	11.7 ± 2.8	5.0 ± 1.2
H12	13 29 38.02	+47 16 14.7	4.4	14.2	18.9 ± 5.3	2.8 ± 0.8	1.2 ± 0.3
H13	13 29 38.71	+47 18 56.4	4.0	75.8	69.3 ± 9.6	10.5 ± 1.4	4.5 ± 0.6
H14	13 29 39.86	+47 12 39.4	3.8	126.9	119.0 ± 12.1	17.6 ± 1.8	7.6 ± 0.8
H15	13 29 43.36	+47 11 33.5	3.7	126.3	79.9 ± 9.6	11.8 ± 1.4	5.1 ± 0.6
H16	13 29 44.70	+47 10 21.7	5.5	9.6	21.6 ± 6.2	3.2 ± 0.9	1.4 ± 0.4
H17	13 29 46.25	+47 10 42.0	3.8	64.0	46.3 ± 7.5	6.8 ± 1.1	2.9 ± 0.5
H18	13 29 47.67	+47 09 41.0	4.2	22.7	22.7 ± 5.6	3.4 ± 0.8	1.4 ± 0.4
H19	13 29 51.41	+47 10 32.9	5.9	10.0	22.1 ± 6.4	3.3 ± 0.9	1.4 ± 0.4
H20	13 29 51.86	+47 21 16.3	7.5	9.5	24.4 ± 7.3	3.7 ± 1.1	1.6 ± 0.5
H21	13 29 52.07	+47 01 12.2	7.6	8.7	26.9 ± 8.2	4.2 ± 1.3	1.8 ± 0.5
H22	13 29 52.82	+47 11 43.9	3.5	2568.2	1408.3 ± 38.3	207.5 ± 5.6	89.2 ± 2.4
H23	13 29 53.47	+47 10 39.7	4.4	15.4	18.5 ± 5.2	2.7 ± 0.8	1.2 ± 0.3
H24	13 29 53.88	+47 14 35.8	3.7	83.9	56.4 ± 8.2	8.3 ± 1.2	3.6 ± 0.5
H25	13 29 54.44	+47 22 40.6	8.0	9.7	30.3 ± 8.7	4.7 ± 1.3	2.0 ± 0.6
H26	13 29 54.83	+47 11 01.2	4.6	11.8	17.6 ± 5.2	2.6 ± 0.8	1.1 ± 0.3
H27	13 29 57.56	+47 10 46.4	4.5	32.3	56.9 ± 9.3	8.4 ± 1.4	3.6 ± 0.6
H28	13 29 58.24	+47 16 11.4	4.5	33.3	68.8 ± 10.2	10.2 ± 1.5	4.4 ± 0.7
H29	13 29 58.90	+47 05 28.4	4.8	14.1	21.4 ± 5.9	3.2 ± 0.9	1.4 ± 0.4
H30	13 29 58.95	+47 00 06.4	7.1	18.3	48.3 ± 10.3	7.6 ± 1.6	3.2 ± 0.7
H31	13 29 59.20	+47 13 31.8	6.4	11.5	41.1 ± 9.5	6.1 ± 1.4	2.6 ± 0.6
H32	13 29 59.67	+47 15 58.9	4.0	101.9	163.8 ± 14.9	24.4 ± 2.2	10.5 ± 1.0
H33	13 29 59.82	+47 13 08.9	6.9	9.0	35.7 ± 8.9	5.3 ± 1.3	2.3 ± 0.6
H34	13 29 59.85	+47 16 17.5	5.0	24.2	75.3 ± 11.5	11.2 ± 1.7	4.8 ± 0.7
H35	13 30 00.61	+47 13 22.5	5.3	13.1	57.5 ± 10.3	8.5 ± 1.5	3.7 ± 0.7
H36	13 30 01.16	+47 13 44.0	3.6	561.7	264.3 ± 17.1	39.1 ± 2.5	16.8 ± 1.1
H37	13 30 03.18	+47 13 08.2	5.0	9.6	16.9 ± 5.3	2.5 ± 0.8	1.1 ± 0.3
H38	13 30 04.72	+47 11 36.4	4.8	8.7	13.0 ± 4.6	1.9 ± 0.7	0.8 ± 0.3
H39	13 30 05.11	+47 13 38.6	4.8	8.3	13.6 ± 4.7	2.0 ± 0.7	0.9 ± 0.3
H40	13 30 05.26	+47 05 56.4	5.4	9.9	18.4 ± 5.8	2.8 ± 0.9	1.2 ± 0.4
H41	13 30 06.26	+47 15 43.2	3.7	85.0	59.3 ± 8.4	8.8 ± 1.2	3.8 ± 0.5
H42	13 30 06.57	+47 08 34.6	4.2	22.6	24.2 ± 5.8	3.6 ± 0.9	1.5 ± 0.4
H43	13 30 07.76	+47 11 05.5	3.6	732.7	309.8 ± 18.2	45.9 ± 2.7	19.7 ± 1.2
H44	13 30 15.94	+47 15 16.1	4.5	16.6	21.5 ± 5.6	3.2 ± 0.8	1.4 ± 0.4
H45	13 30 19.40	+47 22 18.5	8.3	12.3	38.8 ± 9.9	6.0 ± 1.5	2.6 ± 0.7
H46	13 30 29.05	+47 16 06.8	4.5	32.1	41.2 ± 7.9	6.2 ± 1.2	2.7 ± 0.5
H47	13 30 32.84	+47 13 35.7	5.9	12.3	22.7 ± 6.4	3.4 ± 1.0	1.5 ± 0.4
H48	13 30 34.34	+47 09 43.8	5.6	12.2	23.3 ± 6.5	3.5 ± 1.0	1.5 ± 0.4
H49	13 30 44.78	+47 03 54.1	6.4	32.0	70.2 ± 11.7	11.0 ± 1.8	4.7 ± 0.8
H50	13 30 53.02	+47 02 27.2	5.7	69.9	134.1 ± 15.6	21.4 ± 2.5	9.2 ± 1.1
H51	13 31 04.09	+46 59 42.6	5.1	278.9	391.4 ± 24.7	64.8 ± 4.1	27.9 ± 1.8

TABLE 7.3. ROSAT HRI M83 Source List

Source	R.A. ²⁰⁰⁰ (h m s)	Dec. ²⁰⁰⁰ (° ' ")	R _{err} (")	lik.	counts	rate (10 ⁻⁴ cts s ⁻¹)	f_x (10 ⁻¹⁴ erg cm ⁻² s ⁻¹)
(1)	(2)	(3)	(4)	(5)	(6)	(7)	(8)
H1	13 36 11.17	-29 53 32.6	9.9	8.0	24.2 ± 7.6	5.3 ± 1.7	2.9 ± 0.9
H2	13 36 11.50	-29 43 30.6	8.4	21.1	58.6 ± 11.5	13.3 ± 2.6	7.3 ± 1.4
H3	13 36 13.32	-29 56 13.9	7.9	13.6	34.1 ± 8.4	7.6 ± 1.9	4.2 ± 1.0
H4	13 36 13.85	-29 58 36.9	11.3	8.6	29.8 ± 8.8	6.7 ± 2.0	3.7 ± 1.1
H5	13 36 15.15	-29 57 58.8	9.7	11.2	31.4 ± 8.5	7.0 ± 1.9	3.8 ± 1.0
H6	13 36 25.62	-29 46 21.6	7.8	9.7	25.8 ± 7.5	5.6 ± 1.6	3.1 ± 0.9
H7	13 36 38.52	-29 47 38.8	4.8	14.4	18.6 ± 5.3	4.0 ± 1.1	2.2 ± 0.6
H8	13 36 43.11	-29 51 01.5	4.6	17.0	19.6 ± 5.3	4.2 ± 1.1	2.3 ± 0.6
H9	13 36 43.15	-29 49 18.0	4.8	8.4	12.2 ± 4.3	2.6 ± 0.9	1.4 ± 0.5
H10	13 36 45.41	-29 59 11.1	4.4	52.1	53.3 ± 8.6	11.6 ± 1.9	6.4 ± 1.0
H11	13 36 45.49	-29 51 54.6	4.5	18.6	18.8 ± 5.1	4.0 ± 1.1	2.2 ± 0.6
H12	13 36 48.63	-29 52 56.5	4.1	38.4	37.5 ± 7.0	7.9 ± 1.5	4.4 ± 0.8
H13	13 36 51.10	-29 56 39.7	5.1	9.5	13.7 ± 4.7	2.9 ± 1.0	1.6 ± 0.6
H14	13 36 51.21	-29 53 31.4	4.6	13.0	15.6 ± 4.8	3.3 ± 1.0	1.8 ± 0.6
H15	13 36 55.26	-29 55 10.0	4.4	15.7	17.5 ± 5.0	3.7 ± 1.1	2.0 ± 0.6
H16	13 36 56.76	-29 53 37.1	4.7	20.3	33.0 ± 7.0	7.0 ± 1.5	3.8 ± 0.8
H17	13 36 59.09	-29 49 53.5	3.9	60.2	44.4 ± 7.4	9.4 ± 1.6	5.1 ± 0.9
H18	13 37 00.06	-29 49 05.7	5.2	8.2	14.0 ± 4.8	3.0 ± 1.0	1.6 ± 0.6
H19	13 37 00.20	-29 51 55.8	3.5	1581.8	992.4 ± 32.2	208.8 ± 6.8	114.9 ± 3.7
H20	13 37 00.95	-29 53 21.4	4.7	32.0	52.4 ± 9.0	11.0 ± 1.9	6.1 ± 1.0
H21	13 37 01.00	-29 52 42.0	4.8	9.9	12.8 ± 4.4	2.7 ± 0.9	1.5 ± 0.5
H22	13 37 01.52	-29 55 14.6	4.2	21.1	20.1 ± 5.1	4.3 ± 1.1	2.3 ± 0.6
H23	13 37 01.45	-29 51 27.4	4.4	39.0	76.1 ± 10.5	16.0 ± 2.2	8.8 ± 1.2
H24	13 37 02.18	-29 58 05.9	5.2	9.8	15.4 ± 5.1	3.3 ± 1.1	1.8 ± 0.6
H25	13 37 03.51	-29 49 24.5	5.5	10.6	21.6 ± 6.1	4.6 ± 1.3	2.5 ± 0.7
H26	13 37 03.83	-29 54 01.0	3.8	58.6	41.3 ± 7.1	8.7 ± 1.5	4.8 ± 0.8
H27	13 37 03.97	-29 51 17.2	3.8	131.5	93.6 ± 10.6	19.7 ± 2.2	10.8 ± 1.2
H28	13 37 05.05	-29 53 02.2	4.4	28.3	34.6 ± 7.0	7.3 ± 1.5	4.0 ± 0.8
H29	13 37 16.12	-29 49 34.3	5.6	8.9	17.8 ± 5.6	3.8 ± 1.2	2.1 ± 0.6
H30	13 37 19.46	-29 53 45.3	3.5	995.6	351.6 ± 19.2	74.9 ± 4.1	41.2 ± 2.3
H31	13 37 24.74	-29 58 55.2	6.2	10.6	21.8 ± 6.4	4.8 ± 1.4	2.6 ± 0.8
H32	13 37 26.88	-29 55 46.4	5.5	8.5	14.3 ± 4.9	3.1 ± 1.1	1.7 ± 0.6
H33	13 37 31.04	-29 51 52.1	5.3	17.5	23.7 ± 6.1	5.1 ± 1.3	2.8 ± 0.7
H34	13 37 36.57	-29 48 16.7	5.2	23.3	34.8 ± 7.4	7.6 ± 1.6	4.2 ± 0.9
H35	13 37 39.06	-29 43 11.5	12.5	9.3	38.7 ± 10.6	8.6 ± 2.4	4.8 ± 1.3
H36	13 38 05.32	-29 57 34.8	11.7	15.2	60.4 ± 13.2	14.0 ± 3.1	7.7 ± 1.7
H37	13 38 05.56	-29 44 33.5	20.7	13.8	94.9 ± 20.2	22.2 ± 4.7	12.2 ± 2.6

TABLE 7.4. ROSAT HRI M100 Source List

Source	R.A. ²⁰⁰⁰ (h m s)	Dec. ²⁰⁰⁰ (° ' ")	R _{err} (")	lik.	counts	rate (10 ⁻⁴ cts s ⁻¹)	f_x (10 ⁻¹⁴ erg cm ⁻² s ⁻¹)
(1)	(2)	(3)	(4)	(5)	(6)	(7)	(8)
H1	12 21 45.52	+15 49 21.8	15.3	10.8	51.9 ± 13.2	12.1 ± 3.1	5.1 ± 1.3
H2	12 22 01.45	+15 58 34.1	12.9	9.1	41.8 ± 11.5	9.8 ± 2.7	4.2 ± 1.1
H3	12 22 03.03	+15 53 43.6	10.3	8.0	28.9 ± 8.8	6.8 ± 2.1	2.9 ± 0.9
H4	12 22 14.34	+15 51 44.7	9.9	8.7	26.0 ± 7.7	6.1 ± 1.8	2.6 ± 0.8
H5	12 22 22.10	+15 39 48.8	7.6	20.1	44.9 ± 9.4	10.5 ± 2.2	4.4 ± 0.9
H6	12 22 24.62	+15 53 34.3	11.7	11.9	18.1 ± 5.5	4.2 ± 1.3	1.8 ± 0.6
H7	12 22 27.73	+15 58 14.4	8.4	12.4	26.4 ± 7.3	6.2 ± 1.7	2.6 ± 0.7
H8	12 22 30.61	+15 55 52.9	4.5	616.7	264.5 ± 16.9	61.8 ± 4.0	26.2 ± 1.8
H9	12 22 33.01	+15 37 55.4	5.7	66.3	89.6 ± 11.7	20.9 ± 2.7	8.9 ± 1.1
H10	12 22 33.33	+15 50 56.4	13.7	9.6	17.6 ± 5.5	4.1 ± 1.3	1.7 ± 0.6
H11	12 22 38.24	+15 55 52.4	8.2	21.0	23.2 ± 5.7	5.4 ± 1.3	2.3 ± 0.6
H12	12 22 42.75	+15 51 10.9	10.7	9.1	10.2 ± 3.8	2.4 ± 0.9	1.0 ± 0.4
H13	12 22 42.90	+15 44 04.4	6.0	59.4	42.5 ± 7.1	9.9 ± 1.7	4.2 ± 0.7
H14	12 22 43.72	+15 56 55.0	9.6	15.9	21.8 ± 5.8	5.1 ± 1.4	2.2 ± 0.6
H15	12 22 48.27	+15 43 08.5	7.7	30.4	28.0 ± 6.0	6.6 ± 1.4	2.8 ± 0.6
H16	12 22 50.31	+15 52 57.0	8.6	9.0	9.8 ± 3.6	2.3 ± 0.9	1.0 ± 0.4
H17	12 22 51.21	+15 49 39.0	10.2	20.3	35.9 ± 7.5	8.4 ± 1.8	3.6 ± 0.8
H18	12 22 52.21	+15 49 09.5	9.1	11.4	14.2 ± 4.6	3.3 ± 1.1	1.4 ± 0.5
H19	12 22 53.70	+15 48 46.5	9.9	8.7	12.0 ± 4.3	2.8 ± 1.0	1.2 ± 0.4
H20	12 22 53.88	+15 56 58.5	8.5	16.9	19.4 ± 5.3	4.5 ± 1.2	1.9 ± 0.5
H21	12 22 54.15	+15 49 14.5	5.2	135.8	87.5 ± 10.1	20.4 ± 2.4	8.6 ± 1.0
H22	12 22 54.40	+15 49 47.5	12.2	9.4	14.4 ± 4.8	3.4 ± 1.1	1.4 ± 0.5
H23	12 22 55.02	+15 49 22.0	5.0	241.5	187.4 ± 14.6	43.8 ± 3.4	18.6 ± 1.4
H24	12 22 58.29	+15 49 09.0	9.2	13.7	16.6 ± 4.9	3.9 ± 1.1	1.7 ± 0.5
H25	12 22 58.57	+15 47 53.5	8.1	23.2	29.5 ± 6.4	6.9 ± 1.5	2.9 ± 0.6
H26	12 23 05.09	+15 52 26.5	7.5	13.7	13.4 ± 4.2	3.1 ± 1.0	1.4 ± 0.4
H27	12 23 06.44	+15 53 28.0	10.3	8.6	11.3 ± 4.1	2.6 ± 1.0	1.1 ± 0.4
H28	12 23 10.10	+15 47 02.9	7.9	13.5	15.1 ± 4.6	3.5 ± 1.1	1.5 ± 0.5
H29	12 23 17.44	+15 44 44.9	13.2	8.9	15.7 ± 5.2	3.7 ± 1.2	1.6 ± 0.6
H30	12 23 30.92	+15 45 08.8	4.2	336.1	191.1 ± 14.7	44.7 ± 3.4	18.9 ± 1.4
H31	12 23 33.18	+15 38 29.8	5.6	109.3	147.5 ± 15.0	34.5 ± 3.5	14.6 ± 1.5
H32	12 23 36.44	+15 40 25.2	9.7	16.6	44.4 ± 10.0	10.4 ± 2.3	4.4 ± 1.0
H33	12 23 48.78	+15 59 31.6	16.0	12.5	57.8 ± 13.8	13.5 ± 3.2	5.7 ± 1.4

TABLE 7.5. ROSAT HRI M101 Source List

Source	R.A. ²⁰⁰⁰ (h m s)	Dec. ²⁰⁰⁰ (° ' ")	R _{err} (")	lik.	counts	rate (10 ⁻⁴ cts s ⁻¹)	f_x (10 ⁻¹⁴ erg cm ⁻² s ⁻¹)
(1)	(2)	(3)	(4)	(5)	(6)	(7)	(8)
H1	14 01 18.83	+54 18 39.8	4.9	270.1	983.8 ± 42.0	48.0 ± 2.0	14.4 ± 0.6
H2	14 01 23.27	+54 15 20.1	15.3	13.0	175.1 ± 29.2	8.5 ± 1.4	2.6 ± 0.4
H3	14 02 02.80	+54 18 28.1	4.5	60.5	135.9 ± 16.4	6.2 ± 0.7	1.9 ± 0.2
H4	14 02 06.07	+54 17 08.6	6.2	14.5	60.0 ± 13.4	2.7 ± 0.6	0.8 ± 0.2
H5	14 02 07.28	+54 10 29.2	7.8	31.8	164.9 ± 24.1	7.8 ± 1.1	2.3 ± 0.3
H6	14 02 09.92	+54 30 21.4	9.8	18.9	133.7 ± 24.2	6.3 ± 1.1	1.9 ± 0.3
H7	14 02 13.09	+54 21 56.8	5.2	14.9	48.1 ± 10.9	2.2 ± 0.5	0.7 ± 0.1
H8	14 02 16.72	+54 08 56.8	10.9	12.2	97.5 ± 22.0	4.6 ± 1.0	1.4 ± 0.3
H9	14 02 21.52	+54 17 56.3	3.8	108.6	141.7 ± 14.6	6.4 ± 0.7	1.9 ± 0.2
H10	14 02 27.48	+54 16 25.2	3.6	405.7	355.2 ± 21.4	16.0 ± 1.0	4.8 ± 0.3
H11	14 02 27.59	+54 12 41.8	3.8	257.4	324.0 ± 22.0	14.9 ± 1.0	4.5 ± 0.3
H12	14 02 28.06	+54 26 32.4	4.2	71.4	130.5 ± 15.2	5.9 ± 0.7	1.8 ± 0.2
H13	14 02 29.20	+54 21 18.9	3.5	1287.7	658.7 ± 27.1	29.4 ± 1.2	8.8 ± 0.4
H14	14 02 31.68	+54 20 01.2	4.5	27.3	66.2 ± 11.5	2.9 ± 0.5	0.9 ± 0.2
H15	14 02 33.88	+54 21 17.9	4.1	25.3	45.5 ± 8.9	2.0 ± 0.4	0.6 ± 0.1
H16	14 02 45.96	+54 21 51.1	4.5	17.4	43.1 ± 9.3	1.9 ± 0.4	0.6 ± 0.1
H17	14 02 46.30	+54 26 56.1	4.3	32.2	64.1 ± 10.9	2.9 ± 0.5	0.9 ± 0.1
H18	14 02 52.22	+54 21 12.6	3.7	75.4	84.4 ± 10.9	3.7 ± 0.5	1.1 ± 0.1
H19	14 03 03.46	+54 27 36.3	3.5	1084.2	607.9 ± 26.3	27.3 ± 1.2	8.2 ± 0.4
H20	14 03 03.80	+54 04 02.8	7.1	71.6	464.4 ± 35.0	22.9 ± 1.7	6.9 ± 0.5
H21	14 03 05.45	+54 07 07.7	8.0	24.3	135.4 ± 22.4	6.4 ± 1.1	1.9 ± 0.3
H22	14 03 11.86	+54 17 56.0	5.1	15.0	66.8 ± 12.7	2.9 ± 0.6	0.9 ± 0.2
H23	14 03 12.15	+54 20 54.2	3.8	110.3	174.4 ± 16.2	7.7 ± 0.7	2.3 ± 0.2
H24	14 03 12.61	+54 20 08.2	4.6	18.7	59.4 ± 11.2	2.6 ± 0.5	0.8 ± 0.1
H25	14 03 13.40	+54 18 05.2	5.2	12.5	50.6 ± 11.2	2.2 ± 0.5	0.7 ± 0.1
H26	14 03 17.33	+54 18 21.0	4.4	27.3	63.1 ± 11.1	2.8 ± 0.5	0.8 ± 0.1
H27	14 03 18.18	+54 24 31.9	4.8	11.9	31.2 ± 8.3	1.4 ± 0.4	0.4 ± 0.1
H28	14 03 18.95	+54 17 17.8	3.8	50.1	64.7 ± 9.8	2.9 ± 0.4	0.9 ± 0.1
H29	14 03 21.07	+54 19 45.5	3.8	93.8	128.7 ± 13.8	5.7 ± 0.6	1.7 ± 0.2
H30	14 03 23.63	+54 19 46.8	3.9	65.8	109.0 ± 13.1	4.8 ± 0.6	1.4 ± 0.2
H31	14 03 30.62	+54 21 58.2	5.5	9.8	40.8 ± 10.3	1.8 ± 0.5	0.5 ± 0.1
H32	14 03 32.07	+54 21 03.2	4.1	39.3	68.4 ± 10.8	3.0 ± 0.5	0.9 ± 0.1
H33	14 03 33.18	+54 18 00.6	5.0	18.6	61.2 ± 11.8	2.7 ± 0.5	0.8 ± 0.2
H34	14 03 33.62	+54 11 46.4	7.7	13.6	76.9 ± 16.5	3.5 ± 0.8	1.1 ± 0.2
H35	14 03 34.93	+54 17 08.0	4.4	21.8	52.5 ± 10.2	2.3 ± 0.5	0.7 ± 0.1
H36	14 03 35.44	+54 19 24.2	3.8	90.2	108.0 ± 12.4	4.8 ± 0.6	1.4 ± 0.2
H37	14 03 40.68	+54 19 01.5	4.9	21.7	91.4 ± 14.3	4.1 ± 0.6	1.2 ± 0.2
H38	14 03 50.20	+54 24 13.7	4.0	47.8	81.6 ± 11.8	3.7 ± 0.5	1.1 ± 0.2
H39	14 03 51.51	+54 21 47.8	4.2	11.9	53.1 ± 11.0	2.4 ± 0.6	0.8 ± 0.1
H40	14 03 53.47	+54 21 58.1	3.9	122.8	178.4 ± 16.7	8.0 ± 0.7	2.4 ± 0.2
H41	14 03 54.48	+54 21 28.7	5.5	8.0	40.0 ± 10.1	1.8 ± 0.5	0.5 ± 0.1
H42	14 03 55.65	+54 20 58.0	5.4	15.0	47.1 ± 10.7	2.1 ± 0.5	0.6 ± 0.1
H43	14 03 58.99	+54 09 10.7	8.5	22.5	126.6 ± 21.9	6.0 ± 1.0	1.8 ± 0.3
H44	14 03 59.92	+54 11 28.6	7.3	21.0	99.5 ± 18.1	4.6 ± 0.8	1.4 ± 0.3
H45	14 04 13.96	+54 26 04.6	3.6	2403.0	1528.1 ± 42.2	70.5 ± 1.9	21.2 ± 0.6
H46	14 04 14.99	+54 09 48.4	14.4	17.1	170.5 ± 31.1	8.2 ± 1.5	2.5 ± 0.4
H47	14 04 16.37	+54 16 12.3	4.5	84.0	187.8 ± 19.3	8.7 ± 0.9	2.6 ± 0.3
H48	14 04 21.43	+54 19 21.0	3.9	306.3	391.1 ± 24.1	18.0 ± 1.1	5.4 ± 0.3
H49	14 04 28.90	+54 23 53.1	4.5	129.9	281.5 ± 23.4	13.1 ± 1.1	3.9 ± 0.3
H50	14 04 39.53	+54 26 53.9	10.7	15.5	129.0 ± 23.8	6.2 ± 1.1	1.9 ± 0.3
H51	14 04 56.53	+54 24 06.6	14.0	15.6	182.7 ± 29.4	8.9 ± 1.4	2.7 ± 0.4

TABLE 7.6. ROSAT PSPC M101 Source List

Source	R.A. ²⁰⁰⁰ (h m s)	Dec. ²⁰⁰⁰ (° ' ")	<i>s/n</i>	rate (cts ks ⁻¹)	HR1	HR2	comment*
(1)	(2)	(3)	(4)	(5)	(6)	(7)	(8)
P1	14 1 19.6	54 18 41	16.9	16.2	0.34 ± 0.05	0.03 ± 0.06	H1, IPC1, star
P2	14 1 23.4	54 15 28	5.7	3.0	0.10 ± 0.14	0.27 ± 0.18	H2
P3	14 1 34.6	54 20 32	7.3	3.8	0.85 ± 0.16	0.12 ± 0.13	galaxy: <i>R</i> = 16.7, <i>B</i> = 18.7
P4	14 2 03.1	54 18 32	4.8	1.7	1.38 ± 0.42	0.16 ± 0.20	H3
P5	14 2 10.7	54 30 30	5.6	2.5	0.55 ± 0.17	0.39 ± 0.16	H6, AGN
P6	14 2 22.2	54 18 04	6.4	2.5	1.25 ± 0.23	0.45 ± 0.14	H9, XB
P7	14 2 27.9	54 12 50	6.8	2.9	0.35 ± 0.13	0.09 ± 0.15	H11, star
P8	14 2 28.2	54 16 29	12.1	7.3	1.01 ± 0.06	0.43 ± 0.08	H10, IPC2, NGC 5447
P9	14 2 29.9	54 21 21	11.9	7.0	0.33 ± 0.07	-0.17 ± 0.08	H13, star
P10	14 2 47.0	54 27 00	3.6	1.1	0.97 ± 0.40	0.33 ± 0.25	H17, galaxy
P11	14 2 52.9	54 21 15	5.5	1.8	1.23 ± 0.32	0.32 ± 0.18	H18, AGN
P12	14 3 00.8	54 14 28	4.5	1.3	1.73 ± 0.87	-0.23 ± 0.24	NGC 5455
P13	14 3 03.9	54 27 36	11.1	6.1	0.96 ± 0.07	0.28 ± 0.09	H19, IPC5, SNR MF37
P14	14 3 05.2	54 07 25	4.5	1.7	0.66 ± 0.26	0.15 ± 0.20	H21
P15	14 3 06.0	54 03 59	6.9	3.8	0.12 ± 0.12	-0.32 ± 0.14	H20, star
P16	14 3 12.6	54 21 04	5.9	2.0	-0.07 ± 0.12	0.14 ± 0.17	H23, nucleus of M101+DX
P17	14 3 15.2	54 17 56	4.2	1.3	-0.10 ± 0.20	0.17 ± 0.28	H22/H25, DX
P18	14 3 19.6	54 17 20	7.4	3.0	0.72 ± 0.13	0.30 ± 0.12	H28, XB or AGN
P19	14 3 22.2	54 19 52	8.1	3.5	0.58 ± 0.13	0.74 ± 0.11	H29/H30, SNRs
P20	14 3 28.5	54 21 24	3.8	1.1	0.07 ± 0.20	-0.47 ± 0.22	DX
P21	14 3 36.0	54 19 30	4.7	1.5	0.49 ± 0.27	0.79 ± 0.22	H36, SNR
P22	14 3 40.7	54 19 02	6.4	2.4	0.78 ± 0.20	0.04 ± 0.16	H37, NGC 5461
P23	14 3 41.8	54 31 40	5.2	2.0	0.53 ± 0.19	-0.21 ± 0.18	star: <i>B</i> = 20.7, <i>R</i> = 18.8
P24	14 3 49.7	54 24 14	3.9	1.2	0.90 ± 0.39	0.39 ± 0.24	H38, AGN
P25	14 3 53.7	54 21 57	8.0	3.3	0.53 ± 0.13	0.23 ± 0.13	H39/H40/H41, NGC 5462
P26	14 4 00.1	54 09 00	6.3	2.8	0.48 ± 0.16	0.47 ± 0.15	H43, AGN
P27	14 4 00.1	54 11 40	5.0	1.8	1.06 ± 0.33	0.09 ± 0.21	H44, IPC7, AGN
P28	14 4 14.0	54 26 06	18.6	16.7	0.88 ± 0.04	0.18 ± 0.05	H45, IPC8, XB
P29	14 4 15.4	54 09 58	6.0	2.6	0.53 ± 0.18	0.21 ± 0.18	H46, AGN or star
P30	14 4 16.2	54 16 16	6.7	2.8	0.66 ± 0.16	0.27 ± 0.14	H47
P31	14 4 21.8	54 19 18	8.5	4.2	0.37 ± 0.10	-0.17 ± 0.11	H48, star
P32	14 4 28.9	54 23 48	6.8	3.0	0.52 ± 0.14	-0.29 ± 0.13	H49, SNR, NGC 5471B
P33	14 4 55.8	54 23 54	5.3	2.4	1.27 ± 0.49	-0.28 ± 0.21	H51, galaxy

(4): signal-to-noise ratio

(5): count rates in the PSPC 0.5–2 keV hard band.

(6), (7): hardness ratios, defined as $HR1 = (\text{hard} - \text{soft})/(\text{hard} + \text{soft})$ and $HR2 = (\text{hard2} - \text{hard1})/(\text{hard2} + \text{hard1})$, where 'soft' and 'hard' stand for the net source count rates in the soft (0.11–0.41 keV) and hard (0.52–2.01 keV) bands, while 'hard1' and 'hard2' are the split of a hard-band rate into two: 0.52–0.90 keV for hard1 and 0.91–2.01 keV for hard2. The unphysical values of $HR1 > 1$ for several sources are a result of statistical uncertainties in the data, most serious in the soft band. $HR1$ is particularly sensitive to X-ray absorption, whereas $HR2$ to the intrinsic X-ray spectral shape of a source.

(8): identifications with other source catalogues and comments.

XB: X-ray binary in M101; DX: diffuse X-ray emission region in M101.

'HRI': ROSAT HRI sources (cf. Tab. 7.12); 'IPC': EINSTEIN IPC sources (Trinchieri, Fabbiano & Romaine 1990);

'AGN', 'star': classifications based on optical APM identifications, with positional offsets less than the ROSAT PSPC positional errors; 'MF': optical identifications of SNRs (Matonick & Fesen 1997)

APPENDIX B — SOURCE IDENTIFICATIONS

TABLE 7.7. Identification of ROSAT HRI Sources in M31

Source		identification				comment
ROSAT HRI 171 ks (1)	L_x (10^{36} erg s $^{-1}$) (2)	ROSAT HRI 31 ks (3)	ROSAT PSPC (4)	EINSTEIN HRI (5)	ROSAT diff (6)	
H1	1.1 ± 0.2	—	P130	—	—	
H2	1.4 ± 0.2	—	P132	—	—	
H3	1.4 ± 0.2	—	—	—	—	
H4	31.0 ± 0.8	—	—	—	—	
H5	2.1 ± 0.2	#3	—	—	—	
H6	7.5 ± 0.4	#4	—	E12	—	
H7	3.2 ± 0.4	—	P140	—	—	
H8	1.5 ± 0.2	—	P142	—	—	
H9	2.5 ± 0.3	#5	—	—	—	
H10	0.9 ± 0.2	#6	—	—	—	
H11	0.9 ± 0.2	—	—	—	—	
H12	—	#7	P144	—	—	star EQ 003926+40544
H13	2.8 ± 0.3	—	—	—	—	
H14	0.5 ± 0.1	#8	—	—	—	GC
H15	—	#9	—	E14	—	star
H16	8.1 ± 0.4	#10	—	—	—	
H17	1.6 ± 0.2	#11	P152	—	—	
H18	2.6 ± 0.3	#12	P151	E17	—	
H19	17.1 ± 0.7	#13	P150	E16	—	GC
H20	18.0 ± 0.6	#14	—	E19	—	
H21	12.1 ± 0.5	#15	P158	E20	—	GC
H22	1.4 ± 0.3	#16	—	—	—	
H23	8.5 ± 0.4	#17	—	E21	—	
H24	6.1 ± 0.4	#18	—	E22	—	
H25	3.7 ± 0.5	#19	P162	—	—	
H26	16.7 ± 0.6	#20	P163	E23	—	
H27	1.2 ± 0.2	—	P164	—	—	
H28	1.5 ± 0.2	—	—	—	—	
H29	2.5 ± 0.2	#22	—	E25	—	
H30	15.1 ± 0.6	—	—	—	—	
H31	3.2 ± 0.3	#23	—	E26	—	GC
H32	3.0 ± 0.3	#24	P167	—	—	
H33	2.0 ± 0.3	—	—	—	—	
H34	19.8 ± 0.6	#25	—	E27	—	
H35	9.4 ± 0.5	#26	P173	E28	—	
H36	8.2 ± 0.4	—	—	—	—	
H37	—	—	P174	—	—	star
H38	18.6 ± 0.6	#27	P176	E32	D1	
H39	8.8 ± 0.4	#28	P175	E33	—	GC
H40	9.7 ± 0.5	#29	P177	E34	—	
H41	3.0 ± 0.4	#30	P178	—	—	GC
H42	2.7 ± 0.3	#31	—	—	D2	
H43	4.1 ± 0.3	#32	—	E36	D3	
H44	0.4 ± 0.1	#33	—	—	—	
H45	1.3 ± 0.2	#34	—	—	—	
H46	1.1 ± 0.2	—	P181	—	D4	
H47	143.8 ± 1.7	#35	P184	E41	D6/D7/D8	GC
H48	4.5 ± 0.3	#36	—	—	D10	
H49	11.6 ± 0.5	#37	—	E44	D11	
H50	1.1 ± 0.2	—	—	—	—	
H51	3.2 ± 0.3	#38?	P187	—	—	
H52	0.5 ± 0.1	—	P186	—	—	
H53	1.1 ± 0.2	—	—	—	D14	
H54	1.4 ± 0.2	—	—	—	—	
H55	0.6 ± 0.1	—	—	—	D18	
H56	4.1 ± 0.4	#39	P189	E48	D19	
H57	6.3 ± 0.4	#40	—	E50	D20	
H58	11.5 ± 0.5	#41	—	E49	D21	
H59	5.9 ± 0.4	#42	—	E52	D22	
H60	4.3 ± 0.4	—	—	—	D22	

TABLE 7.8. Identification of ROSAT HRI Sources in M31 — Continued

Source		identification				comment
ROSAT HRI 171 ks (1)	L_x (10^{36} erg s $^{-1}$) (2)	ROSAT HRI 31 ks (3)	ROSAT PSPC (4)	EINSTEIN HRI (5)	ROSAT diff (6)	(7)
H61	10.7 ± 0.5	#43	—	E55	D26	
H62	8.2 ± 0.5	—	P194	—	—	
H63	29.4 ± 0.8	#44	—	E56	D27	nucleus
H64	11.8 ± 0.5	#45	P195	E58	—	
H65	3.5 ± 0.3	#46	P197	—	D28	
H66	2.1 ± 0.2	—	—	—	D29	
H67	23.0 ± 0.7	—	—	—	D32	
H68	2.0 ± 0.3	#47	—	E57	D29	
H69	4.0 ± 0.3	—	—	—	D31	
H70	7.4 ± 0.4	#48	—	—	D36	
H71	7.9 ± 0.4	#40	—	E59	D39	
H72	0.7 ± 0.2	—	—	—	—	
H73	34.4 ± 0.8	#50	—	E60	D40	
H74	3.4 ± 0.3	#51	—	—	—	GC
H75	9.2 ± 0.5	#52	—	E61	D41	
H76	27.0 ± 0.7	#53	P201	E62	—	
H77	10.8 ± 0.5	#54	—	E63	D44/D46	
H78	1.2 ± 0.2	—	—	—	—	
H79	2.3 ± 0.2	#55	—	E64	D45/D47	
H80	3.9 ± 0.4	—	—	—	D49	
H81	1.1 ± 0.2	—	—	—	D50	
H82	47.1 ± 1.0	#56	P205	E67	—	GC
H83	26.4 ± 0.7	#57	P206	E68	—	
H84	35.9 ± 0.7	#58	P208	E69	D51	
H85	20.9 ± 0.6	#60	—	E71	D52	
H86	7.1 ± 0.4	#59/#61	P211	—	—	SNR
H87	2.8 ± 0.3	#62	—	—	—	GC
H88	0.8 ± 0.2	#63	—	—	—	
H89	1.0 ± 0.2	—	—	—	—	
H90	14.2 ± 0.5	#64	P213	E73	—	
H91	4.3 ± 0.3	#65	—	E74	—	
H92	9.4 ± 0.4	—	—	—	—	
H93	0.6 ± 0.2	#66	P217	E76	—	GC
H94	9.0 ± 0.4	#67	—	E77	—	GC
H95	0.8 ± 0.2	—	—	—	—	
H96	1.9 ± 0.2	#68	—	—	—	
H97	4.3 ± 0.4	#69	P218	—	—	GC
H98	17.1 ± 0.6	—	—	—	—	
H99	1.9 ± 0.2	#70	P220	E79	—	GC
H100	—	#71	P221	—	—	star
H101	0.5 ± 0.1	#72	P222	—	—	GC
H102	11.1 ± 0.5	#73	P223	E80	—	GC
H103	1.2 ± 0.2	—	—	—	—	
H104	0.6 ± 0.1	—	—	—	—	
H105	1.0 ± 0.2	—	—	—	—	
H106	1.6 ± 0.2	#74	P225	—	—	
H107	21.6 ± 0.7	#75	P226	E82	—	
H108	38.4 ± 0.9	#76	P228	E83	—	GC
H109	10.6 ± 0.5	#77	P229	E85	—	GC
H110	1.2 ± 0.2	#78	—	—	—	GC
H111	0.9 ± 0.2	—	P234	—	—	
H112	1.7 ± 0.2	—	—	—	—	
H113	5.1 ± 0.3	—	P235	—	—	
H114	0.9 ± 0.2	—	—	—	—	
H115	4.4 ± 0.3	#79	—	—	—	
H116	0.8 ± 0.2	—	—	—	—	
H117	1.2 ± 0.2	—	—	—	—	
H118	6.3 ± 0.4	#80	P240	E89	—	SNR
H119	4.9 ± 0.4	#81	P241	—	—	
H120	1.7 ± 0.3	—	P243	—	—	

TABLE 7.8. Identification of ROSAT HRI Sources in M31 — Continued

Source		identification				comment
ROSAT HRI 171 ks (1)	L_x (10^{36} erg s $^{-1}$) (2)	ROSAT HRI 31 ks (3)	ROSAT PSPC (4)	EINSTEIN HRI (5)	ROSAT diff (6)	(7)
H121	—	#82	P244	E91	—	star
H122	14.7 ± 0.6	#83	P247	E92	—	GC
H123	1.9 ± 0.4	—	P249	—	—	SNR
H124	1.2 ± 0.3	—	—	—	—	
H125	1.7 ± 0.3	#84	P251	—	—	
H126	6.5 ± 0.5	#85	—	E93	—	
H127	17.8 ± 0.7	#86	P256	E94	—	
H128	3.4 ± 0.4	—	P261	—	—	GC

(1): ROSAT HRI sources detected in the 171 ks observation of M31. ‘|’denotes bulge sources within < 1 kpc radius from the nucleus

(2): ROSAT HRI (0.1–2.4 keV band) luminosities, assuming a thermal bremsstrahlung spectrum with $kT = 5$ keV, a Galactic column density of $N_H = 7.0 \times 10^{20}$ cm $^{-2}$ and a distance of 690 pc

(3): ROSAT HRI sources from Primini, Forman & Jones (1993), based on a 31 ks ROSAT HRI observations of the M31 bulge region

(4): ROSAT PSPC sources from Supper et al. (1997)

(5): EINSTEIN HRI sources from Fabbiano, Trinchieri & van Speybroeck (1987)

(6): variable X-ray sources detected with the ‘image subtraction technique’ applied to the 171 ks ROSAT HRI observation

TABLE 7.9. ROSAT HRI Sources inside the D_{25} Ellipse of M51

Source	L_x (10^{38} erg s $^{-1}$)	comment
(1)	(2)	(3)
H12	0.8 ± 0.2	
H14	5.1 ± 0.5	P: R7 (5.1×10^{38} erg s $^{-1}$) E: source C (6.2×10^{38} erg s $^{-1}$) HII region S318, H I hole variable
H15	3.4 ± 0.4	P: R6 (7.5×10^{38} erg s $^{-1}$) HII region CCM77, H I hole variable
H16	0.9 ± 0.3	HII region CCM72
H17	2.0 ± 0.3	P: R5 (4.2×10^{38} erg s $^{-1}$)
H18	1.0 ± 0.3	P: R4 (9.2×10^{38} erg s $^{-1}$) HII region CCM68, S98, H I hole
H19	1.0 ± 0.3	HII region S98, H I hole
H22	60.2 ± 1.6	nucleus of M51 (NGC 5194) (P: 5.0×10^{39} erg s $^{-1}$) (E: 5.4×10^{39} erg s $^{-1}$)
H23	0.8 ± 0.2	HII region CCM60
H24	2.4 ± 0.3	P: R8 (4.0×10^{38} erg s $^{-1}$) HII region S454
H26	0.8 ± 0.2	HII region CCM58
H27	2.4 ± 0.4	HII region CCM56
H28	3.0 ± 0.4	
H31	1.8 ± 0.4	
H32	7.1 ± 0.6	nucleus of NGC 5195
H33	1.5 ± 0.4	
H35	2.5 ± 0.4	HII region CCM19
H36	11.3 ± 4.9	E: source A (7.7×10^{38} erg s $^{-1}$) HII region CCM11 variable
H37	0.7 ± 0.2	HII region
H38	0.6 ± 0.2	
H39	0.6 ± 0.2	
H41	2.6 ± 0.3	
H42	1.0 ± 0.3	
H43	13.3 ± 0.8	P: R3 (2.0×10^{39} erg s $^{-1}$) E: source B (9.0×10^{38} erg s $^{-1}$) HII region S184 variable
H44	0.9 ± 0.2	
D1	4.6 ± 2.1	variable 19'' north-west of nucleus
D2	8.9 ± 3.0	variable 6'' north-west of nucleus
D3	7.1 ± 2.6	variable 7'' south-west of nucleus
D4	10.0 ± 3.1	variable 12'' north-east of nucleus
D5	12.0 ± 3.4	variable nucleus of M51, H22
D6	10.0 ± 3.1	variable 6'' north-east of nucleus

(1): 'H' denotes ROSAT HRI sources, 'D' denotes variable sources detected with the 'image subtraction technique' within the < 1 kpc radius bulge region of M51

(2): ROSAT HRI (0.1–2.4 keV band) luminosities, assuming a thermal bremsstrahlung spectrum with $kT = 5$ keV, a Galactic column density of $N_H = 1.3 \times 10^{20}$ cm $^{-2}$ and a distance of 7.7 Mpc

(3): 'P:' denotes ROSAT PSPC sources (R1–R8; Marston et al. 1995), 'E:' Einstein HRI sources (Palumbo et al. 1985). Luminosities are corrected for a distance of 7.7 Mpc and an assumed 5 keV thermal bremsstrahlung spectrum. HII regions are denoted 'S' for sources listed in Scowen 1992 and 'CCM' for Carranza, Crillon & Monnet 1969

TABLE 7.10. ROSAT HRI Sources inside the D_{25} Ellipse of M83

Source	L_x (10^{38} erg s $^{-1}$)	comment
(1)	(2)	(3)
H8	2.1 ± 0.6	P1 (2.5×10^{38} erg s $^{-1}$)
H9	1.3 ± 0.5	—
H11	2.0 ± 0.6	P2 (5.0×10^{38} erg s $^{-1}$)
H12	4.0 ± 0.8	P3 (3.5×10^{38} erg s $^{-1}$)
H13	1.5 ± 0.5	—
H14	1.7 ± 0.5	—
H15	1.9 ± 0.5	—
H16	3.5 ± 0.8	—
H17	4.8 ± 0.8	P4 (5.0×10^{38} erg s $^{-1}$)
H18	1.5 ± 0.5	—
H19	106.0 ± 3.4	nucleus of M83, variable P6 (66.6×10^{38} erg s $^{-1}$) E: H1 (113×10^{38} erg s $^{-1}$)
H20	5.6 ± 1.0	P7 (4.2×10^{38} erg s $^{-1}$)
H21	1.4 ± 0.5	HII region
H22	2.2 ± 0.6	—
H23	8.1 ± 1.1	HII region 6 cm + 20 cm radio source
H25	2.3 ± 0.7	—
H26	4.4 ± 0.8	HII region 6 cm + 20 cm radio source CRB 8
H27	10.0 ± 1.1	P9 (7.5×10^{38} erg s $^{-1}$) P8 (6.6×10^{38} erg s $^{-1}$) E: H4 (13×10^{38} erg s $^{-1}$)
H28	3.7 ± 0.8	P10 (3.3×10^{38} erg s $^{-1}$)
H29	1.9 ± 0.6	P12 (4.3×10^{38} erg s $^{-1}$)
H30	38.0 ± 2.1	BHC, variable P13 (36.4×10^{38} erg s $^{-1}$) E: I2 (39×10^{38} erg s $^{-1}$) E: H2 (24×10^{38} erg s $^{-1}$) faint extended optical object
D1	10.0 ± 3.1	variable nucleus of M83, H19
D2	6.2 ± 2.5	variable 12'' south of nucleus
D3	3.7 ± 1.9	variable 6'' east of nucleus
D4	3.5 ± 1.8	variable 11'' east of nucleus

(1): ‘H’ denotes ROSAT HRI sources, ‘D’ denotes variable sources detected with the ‘image subtraction technique’ within the < 1 kpc radius bulge region of M83

(2): ROSAT HRI (0.1–2.4 keV band) luminosities, assuming a thermal bremsstrahlung spectrum with $kT = 5$ keV, a Galactic column density of $N_H = 4.0 \times 10^{20}$ cm $^{-2}$ and a distance of 8.9 Mpc

(3): ‘P’ denotes ROSAT PSPC sources (Ehle et al. 1998), ‘E: I’ Einstein IPC and ‘E: H’ Einstein HRI sources (Trinchieri, Fabbiano & Palumbo 1985). Luminosities are corrected for a distance of 8.9 Mpc and an assumed 5 keV thermal bremsstrahlung spectrum. ‘CRB’ denotes a VLA radio source (Cowan, Robert & Branch 1994)

TABLE 7.11. ROSAT HRI Sources inside the D_{25} Ellipse of M100

Source	L_x (10^{38} erg s $^{-1}$)	comment
(1)	(2)	(3)
H17	13.4 ± 2.8	
H18	4.5 ± 1.7	
H19	4.5 ± 1.7	E5 (1.9×10^{39} erg s $^{-1}$)
H21	32.6 ± 3.8	15'' offset from nucleus E4 (4.2×10^{39} erg s $^{-1}$)
H22	4.9 ± 1.8	
H23	65.0 ± 5.4	nucleus of M100 E7 (5.1×10^{39} erg s $^{-1}$)
H24	6.2 ± 1.8	HII region CB 336
H25	11.0 ± 2.4	SN 1979C

(1): 'H' denotes ROSAT HRI sources

(2): ROSAT HRI (0.1–2.4 keV band) luminosities, assuming a thermal bremsstrahlung spectrum with $kT = 5$ keV, a Galactic column density of $N_H = 2.3 \times 10^{20}$ cm $^{-2}$ and a distance of 17.1 Mpc

(3): 'E' denotes Einstein HRI sources (Palumbo et al. 1981). Luminosities are corrected for a distance of 17.1 Mpc and an assumed 5 keV thermal bremsstrahlung spectrum. 'CB' refers to an HII region (Cepa & Beckmann 1990)

TABLE 7.12. ROSAT HRI Sources inside the D_{25} Ellipse of M101

Source	L_x (10^{38} erg s $^{-1}$)	comment
(1)	(2)	(3)
H3	1.7 ± 0.2	P4 (HR1 = 1.38 ± 0.42 , HR2 = 0.16 ± 0.20)
H4	0.7 ± 0.2	non-stellar object ($B = 21.23$ mag)
H6	—	AGN ($R = 18.57$ mag, $B = 19.28$ mag)
		P5 (HR1 = 0.55 ± 0.17 , HR2 = 0.39 ± 0.16)
H7	0.6 ± 0.1	
H9	1.7 ± 0.2	P6 (HR1 = 1.25 ± 0.23 , HR2 = 0.45 ± 0.14)
H10	4.3 ± 0.3	IPC2
H11	—	star ($R = 14.89$ mag, $B = 17.31$ mag)
		P7 (HR1 = 0.35 ± 0.13 , HR2 = 0.09 ± 0.15), variable
H12	1.6 ± 0.2	non-stellar object ($B = 21.58$ mag)
H13	—	star GSC 1275 ($R = 14.83$ mag)
		P9 (HR1 = 0.33 ± 0.07 , HR2 = -0.17 ± 0.08), variable
H14	0.8 ± 0.1	
H15	—	star ($R = 18.08$ mag, $B - R \geq 2.92$ mag)
H16	0.5 ± 0.1	
H17	—	galaxy ($R = 21.08$ mag, $B - R = 1.78$ mag)
		P10 (HR1 = 0.97 ± 0.40 , HR2 = 0.33 ± 0.25)
H18	—	AGN ($R = 20.39$ mag, $B - R \leq 0.39$ mag)
		P11 (HR1 = 1.23 ± 0.32 , HR2 = 0.32 ± 0.18)
H19	7.3 ± 0.3	SNR MF37, IPC5, variable
		P13 (HR1 = 0.96 ± 0.07 , HR2 = 0.28 ± 0.09)
H22	0.8 ± 0.2	P17 (HR1 = -0.10 ± 0.20 , HR2 = 0.17 ± 0.28)
H23	2.1 ± 0.2	nucleus of M101
		P16 (HR1 = -0.07 ± 0.12 , HR2 = 0.14 ± 0.17)
H24	0.7 ± 0.1	two sources
H25	0.6 ± 0.1	P17 (HR1 = -0.10 ± 0.20 , HR2 = 0.17 ± 0.28)
H26	0.8 ± 0.1	
H27	0.4 ± 0.1	
H28	0.8 ± 0.1	P18 (HR1 = 0.72 ± 0.13 , HR2 = 0.30 ± 0.12), variable
H29	1.5 ± 0.2	SNR MF54
		P19 (HR1 = 0.58 ± 0.13 , HR2 = 0.74 ± 0.11)
H30	1.3 ± 0.2	SNR MF57
		P19 (HR1 = 0.58 ± 0.13 , HR2 = 0.74 ± 0.11)
H31	0.5 ± 0.1	variable
H32	—	AGN ($B = 21.13$ mag, $B - R \leq 1.13$ mag), variable
H33	0.7 ± 0.1	non-stellar object ($R = 18.23$ mag, $B = 20.26$ mag, $B - R = 2.03$ mag)
H34	0.9 ± 0.2	
H35	—	AGN ($B = 21.10$ mag, $B - R \leq 1.10$ mag)
H36	1.3 ± 0.2	SNR MF83
		P21 (HR1 = 0.49 ± 0.27 , HR2 = 0.79 ± 0.22)
H37	1.1 ± 0.2	HII region NGC 5461
		P22 (HR1 = 0.78 ± 0.20 , HR2 = 0.04 ± 0.16)
H38	—	AGN ($R = 19.98$ mag, $B = 20.39$ mag, $B - R = 0.95$ mag)
		P24 (HR1 = 0.90 ± 0.29 , HR2 = 0.39 ± 0.24)
H39	0.6 ± 0.1	P25 (HR1 = 0.53 ± 0.13 , HR2 = 0.23 ± 0.13)
H40	2.2 ± 0.2	HII region NGC 5462, SN 1951H
		P25 (HR1 = 0.53 ± 0.13 , HR2 = 0.23 ± 0.13)
H41	0.5 ± 0.1	
H42	—	star ($R = 15.46$ mag, $B = 18.39$ mag, $B - R = 2.93$ mag)
H44	—	AGN ($R = 19.21$ mag, $B = 19.80$ mag, $B - R = 0.59$ mag)
		P27 (HR1 = 1.06 ± 0.33 , HR2 = 0.09 ± 0.21), IPC7
H45	19.0 ± 0.5	P28 (HR1 = 0.88 ± 0.04 , HR2 = 0.18 ± 0.05), IPC8, variable
H48	—	star GSC 1062, AG 10 ($R = 10.91$ mag, $B = 12.68$ mag, $B - R = 1.77$ mag)
		P31 (HR1 = 0.37 ± 0.10 , HR2 = -0.17 ± 0.11)
H49	3.5 ± 0.3	HII region NGC 5471
		P32 (HR1 = 0.52 ± 0.14 , HR2 = $-0.29 \pm 0.0.13$)

(1): ‘H’ denotes ROSAT HRI sources

(2): ROSAT HRI (0.1–2.4 keV band) luminosities, assuming a thermal bremsstrahlung spectrum with $kT = 5$ keV, a Galactic column density of $N_H = 1.1 \times 10^{20}$ cm $^{-2}$ and a distance of 7.5 Mpc

(3): ‘P’: ROSAT PSPC sources (cf. Tab. 7.6); hardness ratios HR1 and HR2 are given (Wang, Immler & Pietsch 1999); ‘IPC’: EINSTEIN IPC sources (Trinchieri, Fabbiano & Romaine 1990); ‘AGN’, ‘star’, ‘stellar object’ and ‘non-stellar object’: classifications based on optical APM identifications, with positional offsets less than the ROSAT HRI positional errors; red (R) and blue (B) magnitudes are given; ‘MF’: optical identifications of SNRs (Matonick & Fesen 1997); ‘GSC’: HST Guide Star Catalogue; ‘AG’: Allen & Goss (1979) catalogue of stars

APPENDIX C — LIGHTCURVES

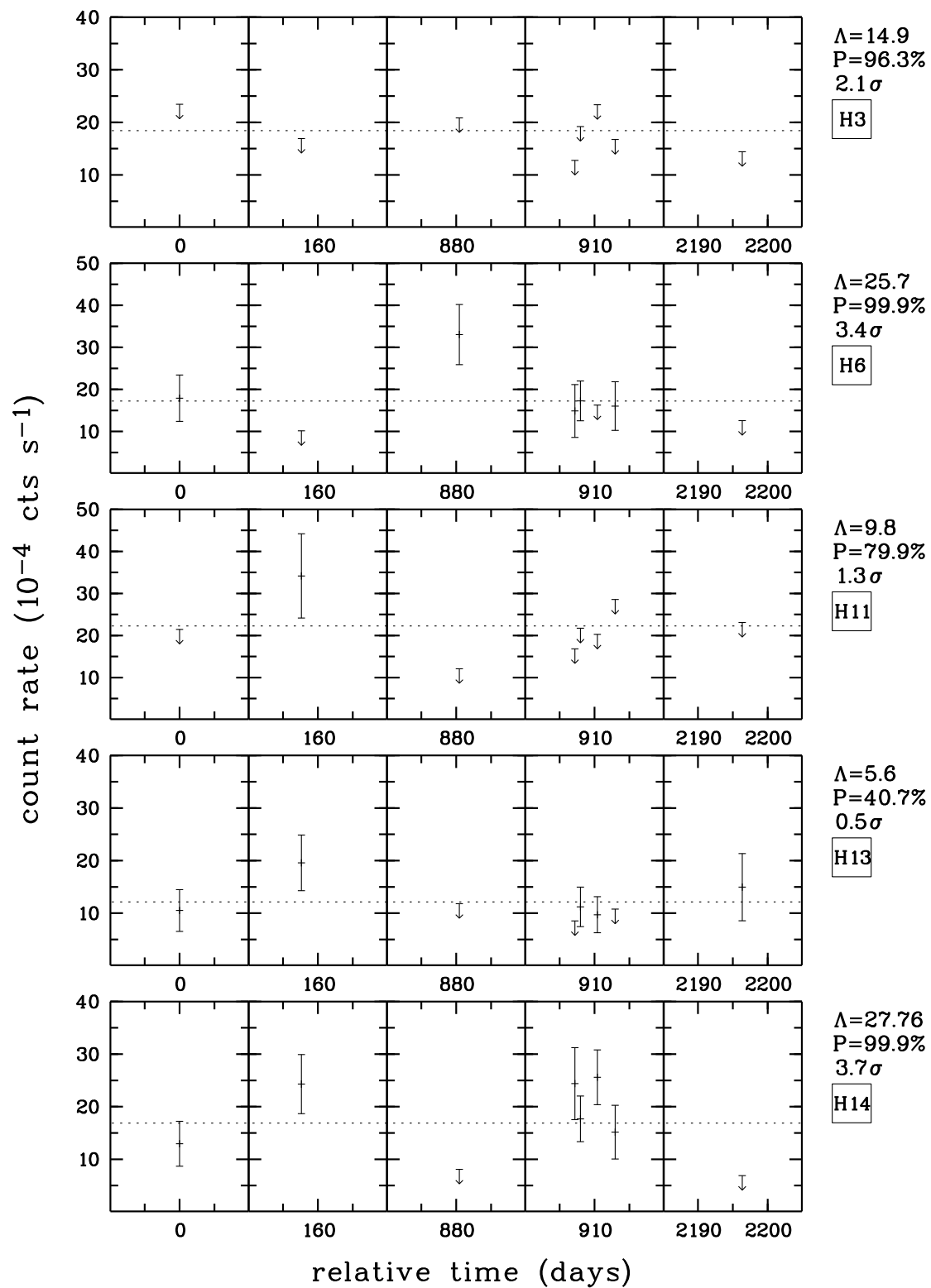


FIGURE 7.1. Lightcurves of the brightest ROSAT HRI X-ray sources in M51.

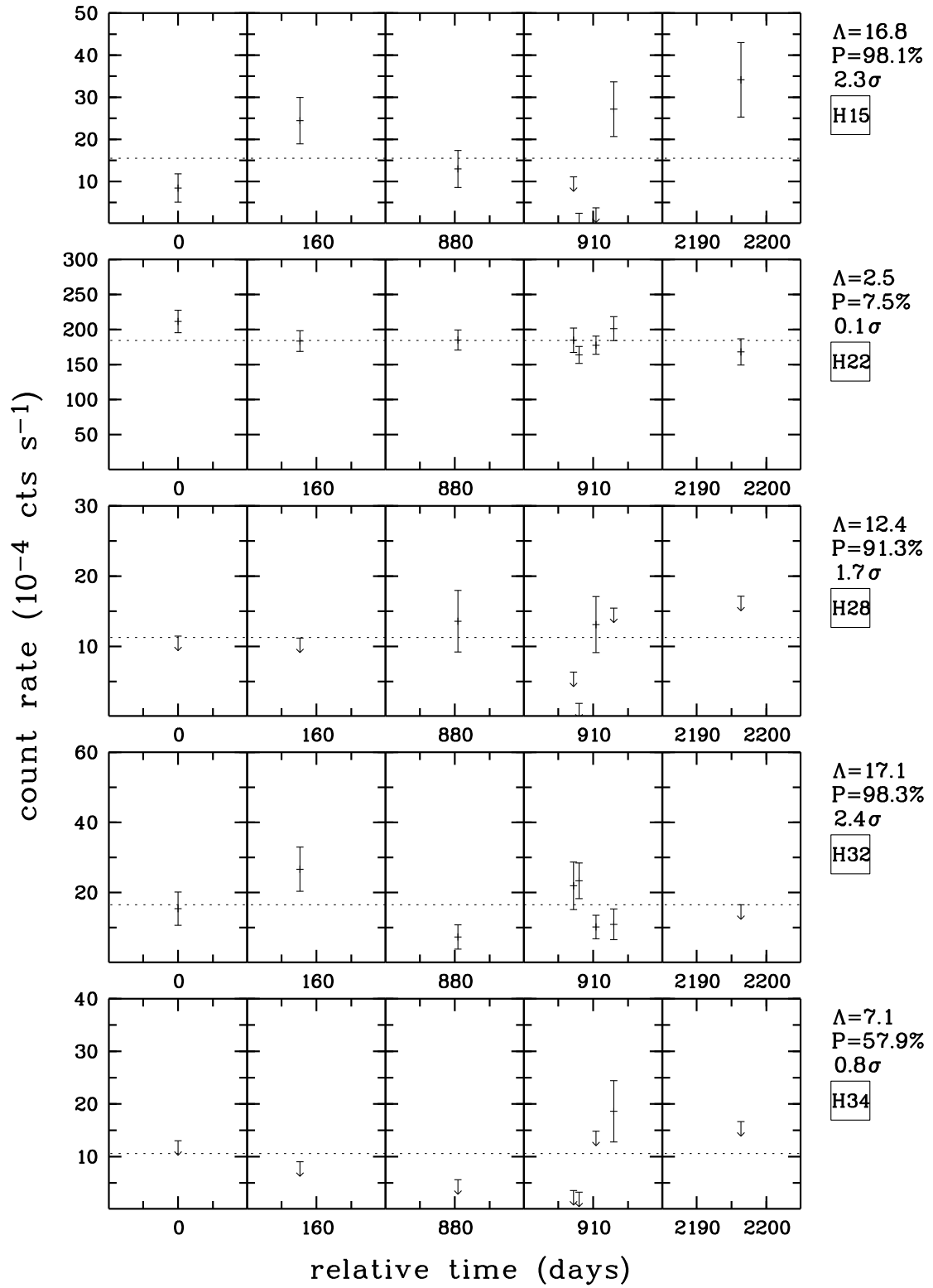


FIGURE 7.2. Lightcurves of the brightest ROSAT HRI X-ray sources in M51.

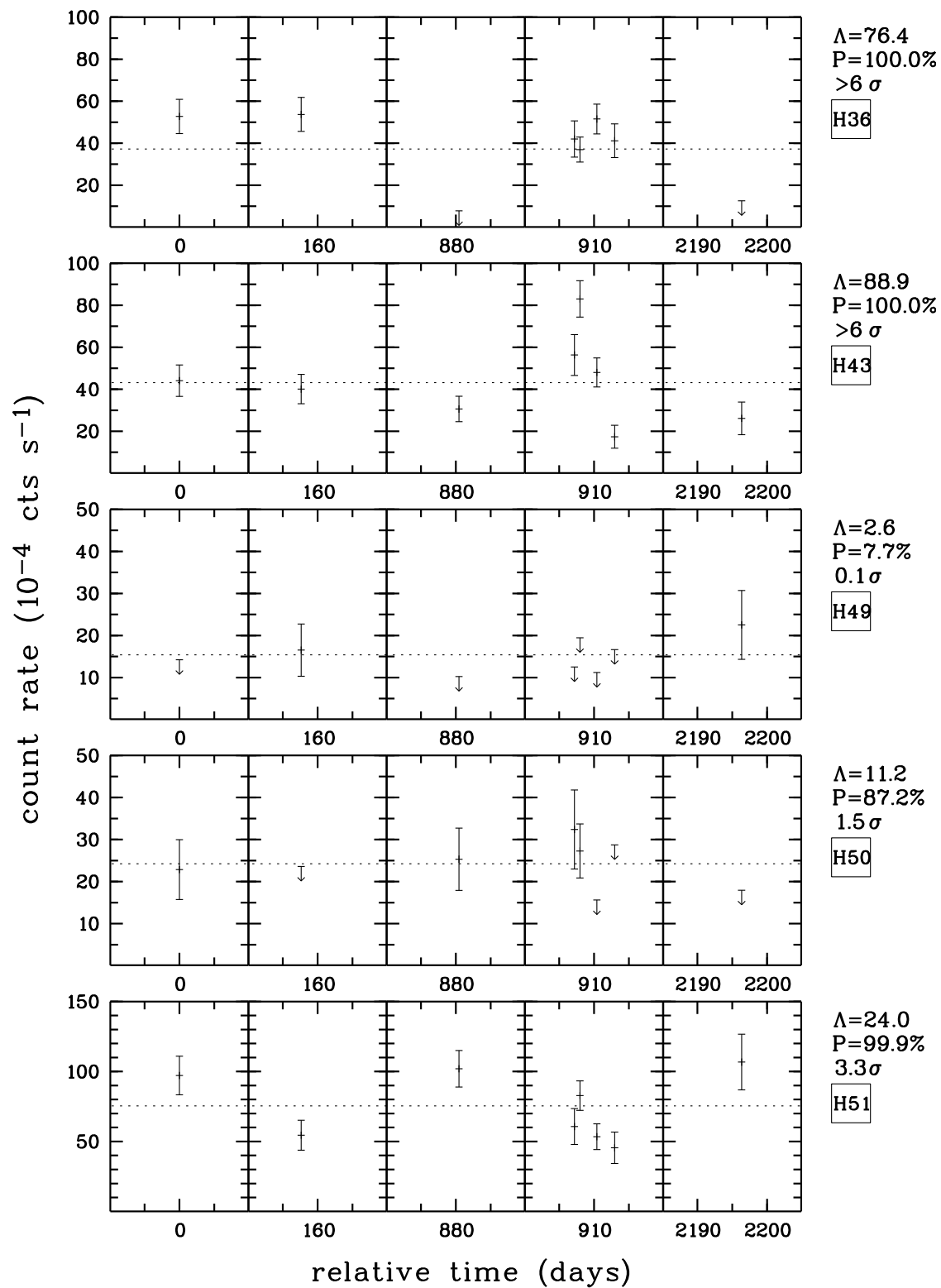


FIGURE 7.3. Lightcurves of the brightest ROSAT HRI X-ray sources in M51.

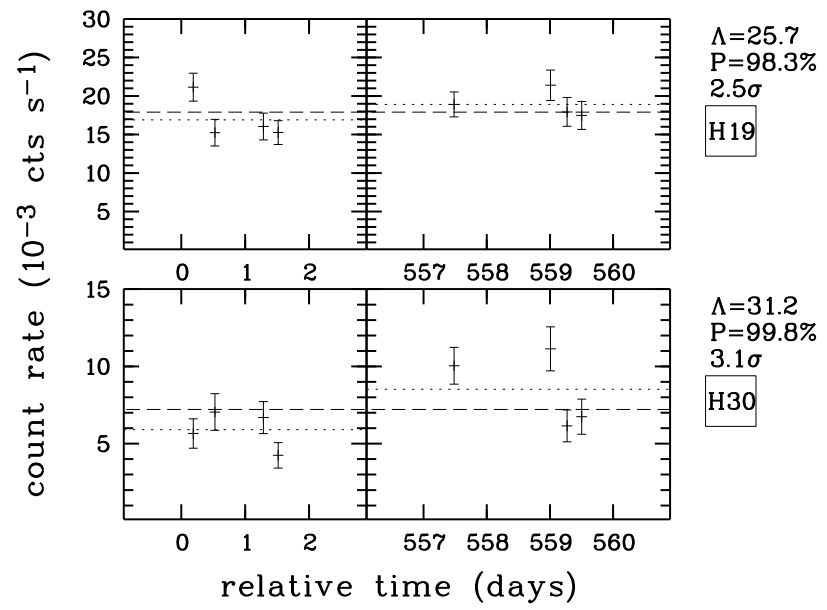


FIGURE 7.4. Lightcurves of the nuclear X-ray source (H19) and the superluminous X-ray source H30 in M83. The likelihood ratio value Λ , as well as the variability probability P and significance are given on the right-hand side. The vertical error bars represent $\pm 1\sigma$ statistical errors. The dotted lines give the mean count rates over the two observation blocks, the dashed line indicates the mean count rates over the complete observation

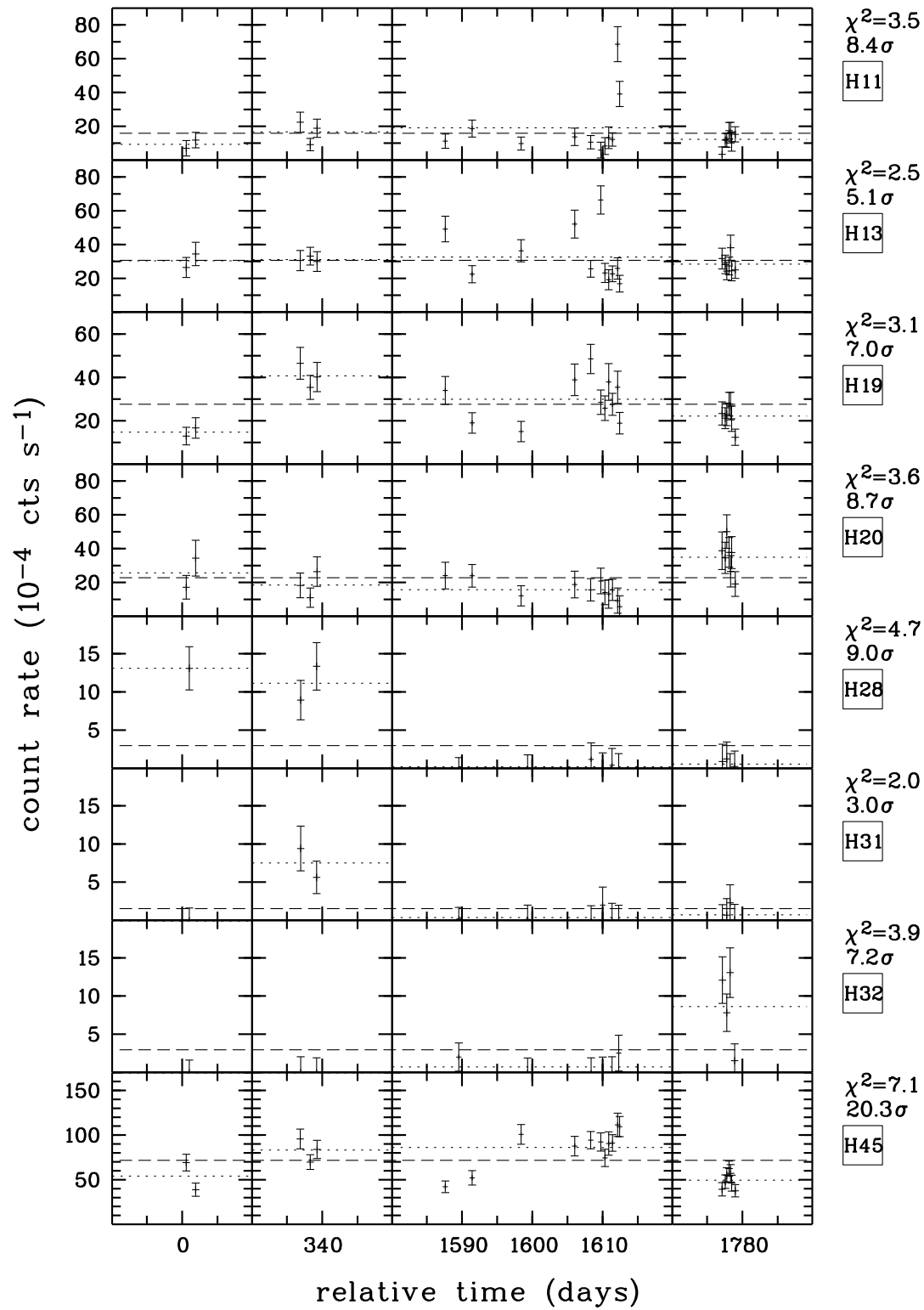


FIGURE 7.5. Lightcurves of the brightest ROSAT HRI X-ray sources in M101.

APPENDIX D — COLOUR PLATES

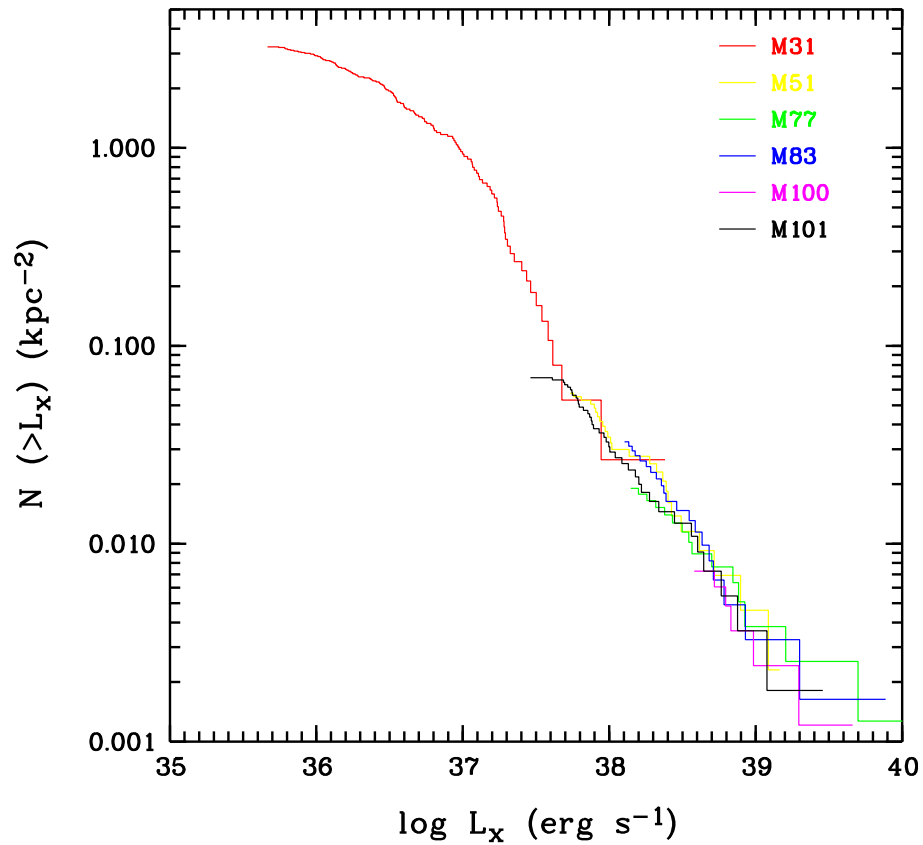


FIGURE 7.6. Luminosity distribution of ROSAT HRI X-ray sources inside the galaxies M31, M51, M83, M100 and M100 (colour representation of Fig. 4.23).

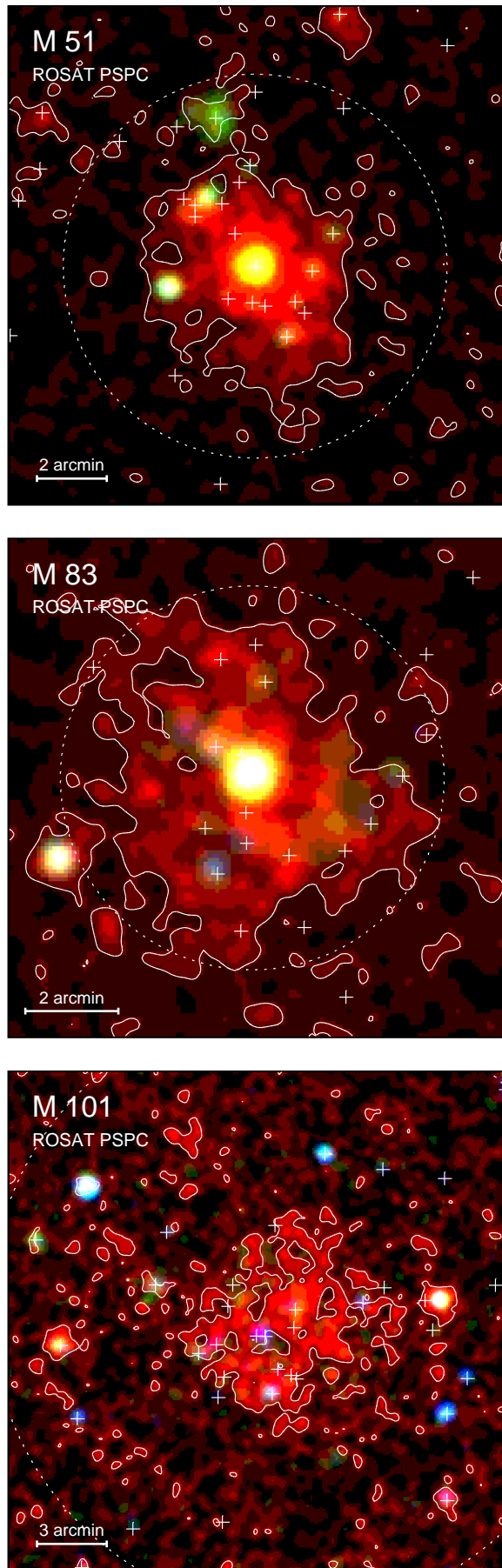


Figure 7.7. ‘Real colour’ ROSAT PSPC images of M51, M83 and M101. The colour plates are composites of red, green and blue images from the PSPC soft (0.11–0.41 keV), hard1 (0.52–0.90 keV) and hard2 (0.91–2.01 keV) bands, respectively. HRI sources are marked with crosses, the optical sizes of the galaxies are indicated by dashed D_{25} ellipses. 3σ contour lines for the emission in the soft band are drawn in order to illustrate the extent of diffuse X-ray emission in each galaxy.

APPENDIX E — ADVANCE PUBLICATIONS

Selected results of the thesis are published in:

- Immler, S., Pietsch, W.:
“X-ray Emission from Supernovae”
2000, Astrophysical Letters and Communications, in press
- Immler, S., Vogler, A., Ehle, M., Pietsch, W.:
“Detection of Supernova Remnant and Black Hole Candidates in M83 with ROSAT”
2000, Astrophysical Letters and Communications, in press
- Immler, S., Vogler, A., Ehle, M., Pietsch, W.:
“ROSAT high-resolution X-ray observations of M83:
Detection of supernova remnant and black hole candidates”
1999, Astronomy & Astrophysics 352, 415
- Wang, Q.D., Immler, S., Pietsch, W.:
“An Ultradeep High Resolution X-ray Image of M101:
The X-ray Source Population in a Late-type Spiral”
1999, Astrophysical Journal 523, 121
- Immler, S., Pietsch, W., Aschenbach, B.:
“X-ray emission from NGC 4321 (M100): detection of supernova 1979C”
1998, Astronomy & Astrophysics 331, 601
- Immler, S., Pietsch, W., Aschenbach, B.:
“Evidence for X-ray emission from the type Ic supernova 1994I”
1998, Astronomy & Astrophysics 336, L1
- Immler, S., Pietsch, W.:
“X-ray emission from NGC 4321 (M 100): detection of supernova 1979C”
1998, Astronomische Nachrichten 319, 27

List of Figures

1.1	Transmission of electromagnetic radiation by the Earth's atmosphere	4
1.2	Schematic representation of a Wolter I X-ray telescope	6
1.3	Schematic representation of the ROSAT X-ray telescope and the detector unit	7
1.4	Illustration of the ROSAT flight configuration	8
2.1	Optical image of the 'Andromeda galaxy' M31	11
2.2	ROSAT HRI image of the 'Andromeda galaxy' M31	12
2.3	Characteristic spectral forms	20
2.4	Raymond & Smith spectrum	20
2.5	Luminosity distribution of EINSTEIN HRI sources in M31	25
3.1	ROSAT HRI X-ray image of eight co-added point sources in M51	28
3.2	Radial surface brightness profile of the eight co-added HRI point sources in M51 . . .	28
4.1	The 'Hubble sequence' of galaxies	34
4.2	Schematic representation of a spiral galaxy, seen edge-on (a) and face-on (b)	35
4.3	Adaptively filtered ROSAT HRI maps of M51, M83 and M100	37
4.4	ROSAT HRI X-ray contours of X-ray emission from M31	42
4.5	Luminosity distribution of bulge and disk sources in M31	43
4.6	Luminosity distribution of bulge X-ray sources in M31	43
4.7	X-ray contours from the bulge region of M31	45
4.8	X-ray contours from the bulge region of M31 ('image subtraction technique')	46
4.9	Luminosity distribution of X-ray sources in M31 at a virtual distance of M51	48
4.10	Overlay of M31 X-ray sources at a distance of M51 onto a 12'' (FWHM) image	49
4.11	<i>Variable</i> X-ray emission from the M31 bulge region at a virtual distance of M51	49
4.12	ROSAT HRI X-ray contours from M31 at a virtual distance of M51	50
4.13	ROSAT HRI contours of X-ray emission from M51	52
4.14	ROSAT HRI contours of X-ray emission from M83	53
4.15	X-ray contour map of M100, superposed on an optical plate	54
4.16	ROSAT HRI contours of X-ray emission from M101	55
4.17	Overlay of HRI contours (12'' FWHM) on an deep H α map of M83	57
4.18	Overlay of HRI contours (12'' FWHM) on a 6 cm radio continuum map of M83	57
4.19	Overlay of HRI contours (12'' FWHM) on an H α map of M51	57
4.20	Overlay of HRI contours (12'' FWHM) on a 6 cm radio continuum map of M51	57
4.21	Overlay of HRI contours of source H30 in M83 onto a deep optical image	63
4.22	ROSAT PSPC spectrum of H30 in M83	65
4.23	Luminosity distribution of X-ray sources in galaxies	66
4.24	Comparison of X-ray source luminosity distribution of nearby spirals	67
4.25	Number of superluminous sources vs. ratio between X-ray and blue luminosities	69
5.1	X-ray emission from SN 1970G/NGC 5455, superposed on an H α image	75
5.2	X-ray emission from SN 1951H/NGC 5462, superposed on an H α image	76
5.3	Overlay of X-ray contours onto an H α map of NGC 5462	76
5.4	ROSAT PSPC spectrum of H22 in M101 in the (0.1–2.4 keV) band	78
5.5	HRI raw spectrum of SN 1994I, the M51 nucleus and a large background region	80
5.6	Radial surface brightness profile of the X-ray emission from the M51 nucleus	81

5.7	X-ray lightcurve of SN 1994I	82
5.8	X-ray contour maps of M100 and SN 1979C, superposed on an optical plate	84
5.9	PSPC pulse height spectrum of photons recorded from SN 1979C	86
5.10	Radio lightcurve of SN 1979C	88
5.11	X-ray lightcurve of SN 1979C	89
6.1	X-ray emission (HRI) from the inner region of M83	92
6.2	Radial surface brightness profile of the X-ray emission from the M83 bulge region	93
6.3	Radial surface brightness profile of the X-ray emission from the M51 bulge region	93
6.4	ROSAT HRI contours of the inner $4'.3 \times 4'.3$ region of M101	94
6.5	Radial surface brightness profile of the X-ray emission from the M101 bulge region	94
6.6	Combined ROSAT PSPC and ASCA GIS spectrum of the M101 bulge region	95
6.7	ROSAT HRI X-ray emission from the bulge region of M51	97
6.8	6 cm radio band and NII emission from the bulge region of M51	98
6.9	ROSAT HRI contour map, superposed on a 6 cm radio and NII emission of M51	98
6.10	Variable X-ray emission, superposed on 6 cm radio and NII emission of M51	99
6.11	ROSAT HRI X-ray contours minus a modelled point-sources of the M51 bulge region	99
6.12	Variable X-ray emission, superposed on HCN und 6 cm radio emission of M51	101
7.1	Lightcurves of the brightest ROSAT HRI X-ray sources in M51	124
7.2	Lightcurves of the brightest ROSAT HRI X-ray sources in M51	125
7.3	Lightcurves of the brightest ROSAT HRI X-ray sources in M51	126
7.4	Lightcurves of the nuclear X-ray source and the superluminous X-ray source in M83	127
7.5	Lightcurves of the brightest ROSAT HRI X-ray sources in M101	128
7.6	Luminosity distribution of X-ray sources inside the galaxies (colour plate)	129
7.7	'Real colour' ROSAT PSPC images of M51, M83 and M101	131

List of Tables

3.1	ROSAT HRI Energy Conversion Factors	30
4.1	General Parameters of the Galaxies	35
4.2	ROSAT Observations of Nearby Galaxies	39
4.3	Emission Components in the Galaxies	40
4.4	ROSAT HRI Luminosity Function of X-Ray Sources in M31	41
4.5	ROSAT HRI Luminosity Function of X-Ray Sources in a virtual M31 observation	48
4.6	X-Ray Emitting HII Regions	56
4.7	X-Ray Emitting SNR Candidates	58
4.8	Superluminous X-Ray Sources	61
4.9	ROSAT HRI Luminosity Function of X-Ray Sources inside Galaxies	68
4.10	Selected Multiwavelength Properties of the Galaxies	68
5.1	Complete List of X-Ray Supernovae	72
5.2	X-Ray Emission from the Positions of Supernovae in M83	73
5.3	X-Ray Emission from the Positions of Supernovae in M100	73
5.4	X-Ray Emission from the Positions of Supernovae in M101	77
5.5	ROSAT HRI Observation Intervals of SN 1994I	79
5.6	X-Ray Emission from the Position of SN 1994I	80
5.7	X-Ray Emission from SN 1979C	87
7.1	ROSAT HRI M31 Source List	108
7.1	ROSAT HRI M31 Source List — Continued	109
7.2	ROSAT HRI M51 Source List	110
7.3	ROSAT HRI M83 Source List	111
7.4	ROSAT HRI M100 Source List	112
7.5	ROSAT HRI M101 Source List	113
7.6	ROSAT PSPC M101 Source List	114
7.7	Identification of ROSAT HRI Sources in M31	116
7.8	Identification of ROSAT HRI Sources in M31 — Continued	117
7.8	Identification of ROSAT HRI Sources in M31 — Continued	118
7.9	ROSAT HRI Sources inside the D_{25} Ellipse of M51	119
7.10	ROSAT HRI Sources inside the D_{25} Ellipse of M83	120
7.11	ROSAT HRI Sources inside the D_{25} Ellipse of M100	121
7.12	ROSAT HRI Sources inside the D_{25} Ellipse of M101	122

LIST OF BOXES

1. X-Ray Emission from Accretion	14
2. The Eddington Limit	16
3. X-Ray Emission Mechanism	21
4. The Circumstellar Interaction Model for SNe	74

GLOSSARY

Å	Ångström (10^{-10} m)
A&A	Astronomy and Astrophysics Journal
A&AS	Astronomy and Astrophysics Supplement Journal
AAO	Anglo Australian Observatory
ADIL	Astronomy Digital Image Library
ADS	Astronomical Data Service
AGN	Active Galactic Nucleus
AJ	Astronomical Journal
AN	Astronomische Nachrichten
ANS	Astronomische Nederlandse Satelliet
ApJ	Astrophysical Journal
ApJS	Astrophysical Journal Supplement
APM	Automated Plate Measuring
ARA&A	Annual Review of Astronomy and Astrophysics
ASCA	Advanced Satellite for Cosmology and Astrophysics
astro-ph	Astrophysics 'arXiv' e-Print Archive
BAAS	Bulletin of the American Astronomical Society
BH	Black Hole
BHC	Black Hole Candidate
BL Lac	Broad-Line Emission Galaxy
BLRG	Broad-Line Radio Galaxy
BMBF	Bundesministerium für Bildung und Forschung, Berlin/Germany
CEA	Commissariat à l'Energie Atomique, Paris/France
CfA	Center for Astrophysics, Cambridge/USA
Chandra	Chandra X-Ray Observatory (NASA)
Col	Co-Investigator
CSM	Circumstellar Matter
Dec.	Declination
DLR	Deutsche Anstalt für Luft und Raumfahrt, Weilheim/Germany
d.o.f.	degree of freedom
DSS	Digitized Sky Survey
ECF	Energy Conversion Factor
EINSTEIN	Einstein Observatory, NASA's second High Energy Astrophysical Observatory (HEAO-2)
ESA	European Space Agency
ESO	European Southern Observatory
ESO-MIDAS	Munich Information and Data Analysis System
eV	electron Volt
EXOSAT	European X-Ray Observatory Satellite
EXSAS	Extended Scientific Analysis System
FITS	Flexible Image Transport System
FR I/II	Fanaroff-Riley Galaxy

FWHM	Full Width at Half Maximum
GINGA	Japanese X-ray astronomy mission (Japanese for 'galaxy')
GRB	γ -Ray Bursts
GSF	NASA Goddard Space Flight Center, Greenbelt/USA
GSC	Guide Star Catalogue
GSOC	German Space Operation Center, Weilheim/Germany
HEAO	High Energy Astronomical Observatory
HEASARC	High Energy Astrophysics Science Archive Research Center
HMXB	High Mass X-ray Binary
HRI	High Resolution Imager onboard EINSTEIN and ROSAT
HST	Hubble Space Telescope
IAUC	International Astronomical Union Circular
IPC	Imaging Proportional Counter
ISM	Interstellar Medium
JAC	Joint Astronomy Center, Hawaii/USA
LINER	Low Ionization Nuclear Emission Region
LMC	Large Magellanic Cloud
LMXB	Low Mass X-ray Binary
Mxxx	Object xxx from the Messier Catalog (1784)
MCP	Micro Channel Plate
MIDAS	Munich Data Analysis System
MIT	Massachusetts Institute of Technology, Cambridge/USA
MPE	Max-Planck-Institut für extraterrestrische Physik, Garching/Germany
MPG	Max-Planck-Gesellschaft, Munich/Germany
MPIfR	Max-Planck-Institut für Radioastronomie, Bonn/Germany
NASA	National Aeronautics and Space Administration, Washington/USA
NED	NASA Extragalactic Database
NGC xxx	Object xxx from the New General Catalogue (1888)
NRL	Naval Radio Laboratory, Washington/USA
NLRG	Narrow-Line Radio Galaxy
NS	Neutron Star
OAO	Orbiting Astronomical Observatory
OBI	Observation Interval
OSO	Orbiting Solar Observatory
P.A.	Position Angle
PASJ	Publication of the Astronomical Society of Japan
PASP	Publication of the Astronomical Society of the Pacific
pc	parsec (3.085×10^{18} cm or 3.26 light years)
PI	Principal Investigator
PIMMS	Portable Interactive Multi-Mission Simulator
POSS	Palomar Observatory Sky Survey
POWL	Power-Law
PSF	Point Spread Function
PSPC	Position Sensitive Proportional Counter onboard ROSAT
QSO	Quasi-Stellar Object
R.A.	Right Ascension
RASM	Raymond & Smith
ROE	Royal Observatory of Edinburgh, UK
ROSAT	Röntgensatellit
SAO	Smithsonian Astrophysical Observatory, Harvard/USA

SAS	Small Astronomical Satellite
SASS	Standard Analysis Software System
SIMBAD	Set of Identifications, Measurements, and Bibliography for Astronomical Data, Strassburg/France
SMC	Small Magellanic Cloud
SN	Supernova (plural: supernovae, SNe)
SNR	Supernova Remnant
SSS	Supersoft X-Ray Sources
STScI	Space Telescope Science Institute, Baltimore/USA
Sy	Seyfert galaxy
THBR	Thermal Bremsstrahlung
TOO	Target of Opportunity
UMass	University of Massachusetts, Amherst/USA
UV	Ultraviolet
W3PIMMS	Web version of the PIMMS
WD	White Dwarf
WSRT	Westerbork Synthesis Radio Telescope, NL
XMM	X-Ray Multi-Mirror Mission (ESA)
XRT	X-Ray Telescope

BIBLIOGRAPHY

"Quote me as saying I was mis-quoted."

Groucho Marx

- Allen, R.J., Goss, W.M., 1979, A&AS 36, 182
- Aschenbach, B., 1988, Appl. Optics 27, 1404
- Aschenbach, B., Egger, R., Trümper, J., 1995, Nature 373, 587
- Aschenbach, B., 1996, in Conf. Proc. "Röntgenstrahlung from the Universe", MPE Report 263
- Barth, H., 1991, "Hermann Oberth: Vater der Raumfahrt", Bechte Verlag, München
- Beuermann, K., Brandt, S., Pietsch, W., 1994, A&A 281, L45
- Bregman, J.N., Pildis, R.A., 1992, ApJ 398, L107
- Bregman, J.N., Pildis, R.A., 1994, ApJ 420, 570
- Brinkmann, W., Siebert, J., Feigelson, E.D., et al., 1997, A&A 323, 739
- Bomans, D.J., Dennerl, K., Kürster, M., 1994, A&A 283, L21
- Canizares, C., Kriss, G.A., Feigelson, E.D., 1982, ApJ 253, L17
- Carranza, G., Crillon, R., Monnet, G., 1969, A&A 1, 479
- Cecil, G., 1988, ApJ 329, 38
- Cecil, G., Watson, A.S., dePree, C., 1995, ApJ 440, 181
- Cepa, J., Beckman, J.E., 1990, A&AS 83, 211
- Charles, P.A., Seward, F.D., 1995, "Exploring the X-ray Universe",
University Press, Cambridge, New York
- Chevalier, R.A., 1982a, ApJ 258, 790
- Chevalier, R.A., 1982b, ApJ 259, 302
- Chevalier, R.A., 1984a, ApJ 285, L63
- Chevalier, R.A., 1984b, Ann. NY Acad. Sci. 422, 215
- Chevalier, R.A., 1998, ApJ 499, 810
- Chevalier, R.A., Fransson, C., 1994, ApJ 420, 268
- Chu, Y.-H., Mac Low, M.-M., 1990, ApJ 365, 510
- Chu, Y.-H., Mac Low, M.-M., Garcia-Segura, G., et al., 1993, ApJ 414, 213
- Chu, Y.-H., Chang, H.-W., Su, Y.-L., et al., 1995a, ApJ 450, 157
- Chu, Y.-H., Dickel, J.R., Staveley-Smith, L., et al., 1995b, AJ 109, 1729
- Chugai, N.N., 1993, ApJ 414, L101

- Cowan, J.J., Branch, D., 1985, ApJ 293, 400
- Cowan, J.J., Robert, D.A., Branch, D., 1994, ApJ 434, 128
- Crane, P.C., van der Hulst, J.M., 1992, AJ 103, 1146
- Dahlem, M., Weaver, K.A., Heckman, T.M., 1998, ApJS 118, 401
- David, L.P., Harnden, F.R., Kearns, K.E., et al., 1997, "The ROSAT High Resolution Imager Calibration Report", US ROSAT Science Data Center/SAO
- Devereux, N.A., Eales, S.A., 1989, ApJ 340, 708
- Deutsch, E.W., Allen, R.J., 1993, AJ 106, 1812
- Dickey, J.M., Lockman, F.J., 1990, ARA&A 28, 215
- Dufour, R.J., Talbot, R.J. Jr., Jensen, E.B., et al., 1980, ApJ 236, 119
- Dunne, B.S., Gruendl, R.A., Chu, Y.-H., 2000, AJ in press (astro-ph/9912003)
- van Dyk, S.D., Weiler, K.W., Sramek, R.A., et al., 1993, ApJ 419, L69
- Ehle, M., Pietsch, W., Beck, R., 1995, A&A 295, 289
- Ehle, M., Beck, R., Heynes, R.F., et al., 1996, A&A 306, 73
- Ehle, M., Pietsch, W., Beck, R., Klein, U., 1998, A&A 329, 39
- Fabbiano, G., 1988a, ApJ 325, 544
- Fabbiano, G., 1988b, ApJ 330, 672
- Fabbiano, G., 1989, ARA&A 27, 138
- Fabbiano, G. 1990, "X-Rays from Spirals and Starburst Galaxies", in: Elvis, M., (ed.), "Imaging X-Ray Astronomy", Cambridge University Press
- Fabbiano, G., Trinchieri, G., van Speybroeck, L.S., 1987, ApJ 316, 127
- Fabbiano, G., Kim, D.-W., Trinchieri, G., 1992, ApJS 80, 531
- Fabian, A.C., Terlevich, R., 1996, MNRAS 280, L5
- Fabian, A.C., et al., 1999a, private communication
- Fabian, A.C., et al., 1999b, private communication
- Filippenko, A.V., 1997, ARA&A 35, 309
- Filippenko, A.V., Barth, A.J., Mathewson, T., et al., 1995, ApJ 450, L11
- Ford, H.C., Crane, P.C., Jacoby, G.H., et al., 1985, ApJ 293, 132
- Fox, D.W., Lewin, W., et al., 1999, IAUC # 7318
- Fransson, C., Lundqvist, P., Chevalier, R. A., 1996, ApJ 461, 993
- Freeman, M., 1993, "How we got to the Moon: the Story of the German Space Pioneers", 21st Century Science Associates, Washington D.C.
- German edition: 1995, "Hin zu neuen Welten – Die Geschichte der Deutschen Raumfahrtspioniere", Dr. Böttiger Verlags-GmbH, Wiesbaden
- Fryer, C., Woosley, S., 1998, ApJ 502, L9
- Galama, T.J., Vreeswijk, P.M., van Paradijs, J., et al., Nature 395, 670
- Giacconi, R., Gursky, H., Paolini, F.R., Rossi, B., 1962, Phys. Review Letters 9, 11
- Gotthelf, E.V., Petre, R., Vasisht, G., 1999, ApJ 514, L107

- Gorenstein, P., Hughes, J.P., Tucker, P., 1994, ApJ 420, L25
- Greiner, J., Hasinger, G., Kahabka, P., 1991, A&A 246, L17
- Grillmair, C.J., Faber, S.M., Lauer, T.R., et al., 1997, AJ 113, 225
- Harris, D.E., 1984, EINSTEIN Observatory Revised User's Manual, CfA Cambridge/USA
- Hasinger, G., Schmidt, M., Trümper, J., 1991, A&A 246, L2
- Hasinger, G., Aschenbach, B., Trümper, J., 1996, A&A 312, L9
- Helfand, D.J., 1984, PASP 96, 913
- Houck, J.C., Bregman, J.N., Chevalier, R.A., Tomisaka, K., 1998, ApJ 493, 431
- Hulst, van der, J.M., Kennicutt, R.C., Crane, P.C., Rots, A.H., 1988, A&A 195, 38
- Immler, S., Pietsch, W., Aschenbach, B., 1998a, A&A 331, 601
- Immler, S., Pietsch, W., Aschenbach, B., 1998b, A&A 336, L1
- Immler, S., Pietsch, W., Aschenbach, B., 1998c, AN 319, 27
- Immler, S., Vogler, A., Ehle, M., Pietsch, W., 1999, A&A 352, 415
- Immler, S., Pietsch, W., 2000, Astrophysical Letters and Communications in press
- Immler, S., Vogler, A., Ehle, M., Pietsch, W., 2000, Astrophysical Letters and Communications in press
- Irwin, M., Maddox, S., McMahon, R., 1994, Spectrum 2, 14
- Iwamoto, K., Mazzali, P.A., Nomoto, K., et al., 1998, Nature 395, 672
- Kamphuis, J., Sancisi, R., van der Hulst, T., 1991, A&A 244, L29
- Karttunen, H., Kröger, O., Oja, H., et al., (eds.), 1993, "Fundamental Astronomy", Springer Verlag, Berlin
- Kim, D.-W., Fabbiano, G., Trinchieri, G., 1992, ApJS 80, 645
- Kitchin, C.R., (edt.), 1998, "Astrophysical Techniques", Institute of Physics Publishing, London
- Kohmura, Y., Inoue, H., Aoki, T., et al., 1994, PASJ 46, L157
- Kohno, K., Kawebe, R., Tosaki, T., et al., 1996, ApJ 461, L29
- Komossa, S., Bade, N., 1999, A&A 343, 775
- Kulkarni, S.R., Frail, D.A., Wieringa, M.H., et al., 1998, Nature 395, 663
- Kulkarni, S.R., Frail, D.A., Wieringa, M.H., et al., 1999, Nature 398, 389
- Lacey, C.K., van Dyk, S.D., Weiler, K., et al., 1999, private communication
- Lewin, W., Zimmermann, H.-U., Pietsch, W., et al., 1994, IAUC # 6019
- Lewin, W., Zimmermann, H.U., Aschenbach, B., 1995, IAUC # 6445
- Lewin, W., van Paradijs, J, van der Heuvel, E., 1995, "X-Ray Binaries", Cambridge University Press
- Lewin, W., Zimmermann, H.-U., Aschenbach, B., 1996, IAUC # 6445
- Lewin, W., Zimmermann, H.-U., Aschenbach, B., 1997, private communication
- Lewin, W., et al., 1999, private communication
- Long, K.S., Charles, P.A., Blair, W.P., Gordon, S.M., 1996, ApJ 466, 750
- Lucke, R., Yentis, D., Friedman, H., et al., 1976, ApJ 206, L25
- Lundqvist, P., Fransson, C., 1988, A&A 192, 221
- Maccacaro, T., Gioia, I.M., Wolter, A., et al., 1996, ApJ 464, 829

- Magnier, E.A., Chu, Y.-H., Points, S.D., et al., 1996, ApJ 464, 829
- Makishima, K., et al., 1989, PASP 41, 697
- Marston, A.P., Elmgreen, D., Elmgreen, B., et al., 1995, ApJ 438, 663
- Matonick, D.M., Fesen, R.A., 1997, ApJS 112, 49
- McKee, C.F., Ostriker, J.P., 1977, ApJ 287, 16
- Montes, M.J., Weiler, K.W., van Dyk, S.D., et al., 2000, ApJ in press (astro-ph/9911399)
- Morrison, L.V., Argyle, R.W., 1994, IAUC # 5989
- Nomoto, K., Yamaoka, H., Pols, O.R., et al., 1994, Nature 371, 227
- Norman, C.A., Ikeuchi, S., 1989, ApJ 345, 372
- Oberth, H., 1923, "Die Rakete zu den Planetenräumen", Oldenbourg Verlag
- Paczýński, B., 1998, ApJ 494, L45
- Palumbo, G.G.C., Maccacaro, T., Zamorani, G., et al., 1981, ApJ 247, 484
- Palumbo, G.G.C., Fabbiano, G., Fransson, C., Trinchieri, G., 1985, ApJ 298, 259
- Pfeffermann, E., Briel, U.G., Hippmann, H., et al., 1988, Proc. SPIE 733, 519
- Pian, E., Amati, L., Antonelli, L.A., et al., 1999, A&AS 138, 463
- Pietsch, W., Vogler, A., Kahabka, P., et al., 1994, A&A 284, 386
- Pietsch, W., Trinchieri, G., Vogler, A., 1998, A&A 340, 351
- Primini, F.A., Forman, W., Jones, C., 1993, ApJ 410, 615
- Rand, R.J., Steven, D.L., Higdon, J.L., 1999, ApJ 513, 720
- Rauschenbach, B., 1994, "Hermann Oberth: The Father of Space Flight", West-Art, New York
German edition: 1995, "Hermann Oberth: Über die Erde hinaus – eine Biographie",
Dr. Böttiger Verlags-GmbH, Wiesbaden
- Raymond, J.C., Cox, D.P., Smith, B.W., 1976, ApJ 204, 290
- Raymond, J.C., Smith, B.W., 1977, ApJS 35, 419
- Read, A., Ponman, T.J., Strickland, D.K., 1997, MNRAS 286, 626
- Rice, W., Lonsdale, C.J., Soifer, B.T., et al., 1988, ApJS 68, 91
- Rumstay, K.S., Kaufman, M., 1983, ApJ 274, 611
- Ryder, S.D., Dopita, M.A., Stavley-Smith, L., et al., 1992, IAUC # 5615
- Ryder, S.D., Stavley-Smith, L., Dopita, M.A., et al., 1993, ApJ 416, 167
- Sakamoto, K., Okumura, S., Minezaki, T., et al., 1995, AJ 110, 2075
- Sandage, A., Tammann, G.A., 1975, ApJ 194, 559
- Schlegel, E.M., 1994, ApJ 424, L99
- Schlegel, E.M., 1995, Rep. Prog. Phys. 58, 1375
- Schlegel, E.M., Petre, R., 1993, ApJ 412, L29
- Schlegel, E.M., 1999, ApJ 527, L85
- Schulman, E., Bregman, J.N., 1995, ApJ 441, 568
- Scoville, N.Z., Yun, M.S., Armus, L., Ford, H., 1998, ApJ 493, L63
- Scowen, P.A., 1992, Ph.D. thesis, Rice University, Houston, Texas

- Shapiro, P.R., Field, G., 1976, A&A 205, 762
- Snowden, S.L., Petre, R., 1994, ApJ 436, L123
- Snowden, S.L., Pietsch, W., 1995, ApJ 452, 627
- Soifer, B.T., Boehmler, L., Neugebauer, G., 1989, AJ 98, 766
- Spitzer, L., 1956, ApJ 124, 20
- Sramek, R.A., Panagia, N., Weiler, K., 1984, ApJ 285, L62
- Stocke, J.T., Morris, S.L., Gioia, I.M., et al., 1991, ApJS 76, 813
- Sukumar, S., Allen, R.J., Beck, R., et al., 2000, in prep.
- Supper, R., Hasinger, G., Pietsch, W., et al., 1997, A&A 317, 328
- Tananbaum, H., et al., 1972, ApJ 174, L143
- Tananbaum, H., Avni, Y., Branduardi, G., et al., 1979, ApJ 234, L9
- Terashima, Y., Ptak, A., Fujimoto, R., et al., 1998, ApJ 496, 210
- Tilanus, R.P.J., Allen, R.J., 1993, A&A 274, 707
- Trinchieri, G., Fabbiano, G., Palumbo, G.C.C., 1985, ApJ 290, 96
- Trinchieri, G., Fabbiano, G., Romaine, S., 1990, ApJ 356, 110
- Trinchieri, G., Fabbiano, G., 1991, ApJ 382, 82
- Trümper, J., 1983, Adv. Space Res. 2, 241
- Trümper, J., Hasinger, G., Aschenbach, B., et al., 1991, Nature 349, 583
- Tully, R.B., 1988, "Nearby Galaxies Catalog", Cambridge University Press
- Urry, C.M., Padovani, O., 1995, PASP 107, 803
- de Vaucouleurs, G., 1979, AJ 84, 1270
- de Vaucouleurs, G., et al., 1991, "Third Reference Catalogue of Bright Galaxies",
Springer Verlag, New York
- Voges, W., et al., 1992, in: Guyenne, T.D., Hunt, J.J. (eds.),
Proc. European ISY Conf., ESA ISY-3, 223
- Vogler, A., Pietsch, W., 1996, A&A 311, 35
- Vogler, A., Pietsch, W., Kahabka, P., 1996, A&A 305, 74
- Vogler, A., Pietsch, W., 1997, A&A 319, 459
- Vogler, A., Pietsch, W., Bertoldi, F., 1997, A&A 318, 768
- Wang, Q.D., 1999, ApJ 517, L30
- Wang, Q.D., Helfand, D.J., 1991, ApJ 279, 327
- Wang, Q.D., Hamilton, T.T., Helfand, D.J., Wu, X., 1991, ApJ 374, 475
- Wang, Q.D., Walterbos, R., Steakley, M., et al., 1995, ApJ 439, 176
- Wang, Q.D., Immler, S., Pietsch, W., 1999, ApJ 523, 121
- Watson, M.G., 1990, in: Fabbiano, G., Gallagher, J.S., Renzini, A., (eds.),
"Windows on Galaxies", Kluwer, Dordrecht
- Watson, M.G., Stanger, V., Griffiths, 1984, ApJ 286, 144
- Weaver, R., McCray, R., Castor, J., et al., 1977, ApJ 218, 337

- Weiler, K.W., Sramek, R.A., Panagia, N., et al., 1986, ApJ 301, 790
- Weiler, K.W., van Dyk, S.D., Panagia, N., et al., 1991, ApJ 380, 161
- Weiler, K.W., van Dyk, S.D., Panagia, N., et al., 1993, "Radio Supernovae & Massive Stellar Winds",
in: "Massive Stars: Their Lives in the Interstellar Medium", ASP Conf. Series, vol. 35, 436
- Weiler, K.W., Montes, M.M., van Dyk, S.D., et al., 1997, "Type II Radio Supernovae and SN 1987A",
in: "SN 1987A: Ten Years after", Workshop. Proc., La Serena/Chile
- Wiklund, T., Rydbeck, G., Hjalmarsen, Å., et al., 1990, A&A 232, L11
- Williams, R., Chu, Y.-H., 1995, ApJ 439, 132
- Williams, R., Chu, Y.-H., Dickel, J.R., et al., 1997, ApJ 480, 618
- Williams, R., Chu, Y.-H., Dickel, J.R., et al., 1999a, ApJ 439, 132
- Williams, R., Chu, Y.-H., Dickel, J.R., et al., 1999b, ApJ 514, 798
- Williams, R., Chu, Y.-H., Dickel, J.R., et al., 1999c, ApJS 123, 467
- Wolter, H., 1952, Annalen der Physik, 10, 94
- Woosley, S.E., Langer, N., Weaver, T.A., 1995, ApJ 448, 315
- Zimmermann, H.-U., Lewin, W., Predehl, P., et al., 1994a, Nature 367, 621
- Zimmermann, H.-U., Becker, W., Belloni, T., et al., 1994b, EXSAS User's Guide, MPE Report 257
- Zimmermann, H.-U., Lewin, W., Aschenbach, B., 1996a, IAUC # 6339
- Zimmermann, H.-U., Lewin, W., Aschenbach, B., 1996b, in Conf. Proc.
"Röntgenstrahlung from the Universe", MPE Report 263
- Zimmermann, H.-U., et al., 1999, private communication

ACKNOWLEDGEMENTS

*“Doubt thou the stars are fire;
Doubt that the sun doth move;
Doubt truth to be a liar;
But never doubt I love.”*

William Shakespeare

In an effort to express that a successful Ph.D. thesis can only grow out of an inspiring environment, including both helpful colleagues, supporting agencies and, most important, good friends, it is a pleasure for me to express my gratitude to:

- Dr. Wolfgang Pietsch, my thesis supervisor, for dedicating an enormous amount of his time to discussions related to my work. With his father-like attitude of supervising and carefully guiding me, he eventually made me an X-ray astronomer that learned and loved to do science in an exact way while still being able to enjoy the sometimes tedious task of evaluating and interpreting data from space-born observatories,
- Prof. Dr. Joachim Trümper, both the ‘father’ of the ROSAT mission and my humble Ph.D. thesis, for giving me the opportunity to conduct my studies in the ROSAT group at the Max-Planck-Institut für extraterrestrische Physik and for his very warm-hearted manner to letting an unexperienced and sometimes naïve scientist grow-up in the world of science,
- Dr. ‘Sir’ Andy Read, for his outstanding commitment – almost as massive as his beard – to regarding socializing an indispensable part of being a successful scientist and a pleasant ‘earthling’. I wish to thank him for his help in numerous ‘affairs’ regarding the publication of results in English, his wonderful friendship, far exceeding what one generally experiences from office colleagues, and for the many pints of beer I had the pleasure to drink with him, occasionally culminating in rather absurd discussions like how a single decaying atom destines our fate. May the power be with this gifted young musician!
- The data and the EXSAS groups at the MPE for their excellent computing support, in particular Harald Baumgartner, Achim Bohnet, Berndt Christandl, Dr. Stephan Döbereiner, Dr. Carlo Izzo and Jochen Paul.

Also, I wish to thank all persons within the scientific community that helped and supported me by either sharing unpublished data and discussing results with me or giving me first-hand knowledge of their experience. Of many others, I wish to mention in person Drs. Ron Allen (STScI), Bernd Aschenbach (MPE), Rainer Beck (MPIfR), You-Hua Chu (U. Oregon), Matthias Ehle (MPE), Stefanie Komossa (MPE; always being the first in citing my publications, giving me confidence that some people have trust in what I am doing), Walter Lewin (MIT), David Malin (AAO), Sidney Ryder (JAC), Daniel Wang (UMass), Kurt Weiler (NRL), and — in particular — Andreas Vogler (MPE/CEA), who all shared my enthusiasm about X-ray emission from galaxies and supernovae. My gratitude also goes to Dr. Erna Roth-Oberth for sending me a signed reprint of her father’s book “Die Rakete zu den Planetenräumen” (Oberth 1923).

This research made also use of various online services and databases (e.g. ADIL, ADS, APM, Asiago, astro-ph, DSS, HEASARC, NED, ROE and SIMBAD). The ROSAT project is supported by the German Bundesministerium für Bildung, Wissenschaft, Forschung und Technologie (BMBF/DLR) and the Max-Planck-Gesellschaft (MPG), who I wish to thank for financial and administrative support.

As from a personal and friendship perspective, I'd like to thank:

- Dr. Jannis 'Mr 6.5 on the Richter scale' Fassomytakís for his appealing taste in Whiskey and his imperturbable efforts in dragging me into sleazy bars (inevitably leading to some glasses of smooth single malts with a loooong finish), and for his passionate quest for the beauty in life (no – not just women!). Thank you for your wonderful friendship Jannis!
- Robert 'the gig' Erb for his enviable solid-rock attitude of not taking things too serious in life and for letting me wonder how lousy copper cables connecting computers can change the world and people's life therein. May many generations of digicams capture a glimpse of our friendship!
- Sabine 'Rübe' Rube for her seemingly endless stock of good mood, cool phrases, wines and prosecco.
- Ulrike Rügemer for her encouragement and for helping me through numerous 'I'm so sick of science – I just want to be a truck driver!'-phases and for the wonderful years of living together.
- Dr. Thomas Schwägerl for his escorting friendship over many years and the numerous entertaining evenings in the cafes of Munich and Regensburg and during diverting tennis tournaments.
- Sandra Reich for her affectionate and selfless support during the rather hectic last months.

However, despite my love to all persons mentioned above, my deepest gratitude goes to my beloved family: my mother Katharina Immler and father Horst Immler, my sister Gerda-Katharina Stuth, my brother-in-law Dr. Ronaldo Stuth, my nephews Enrico and Dario Stuth and my lovely and generous aunt Theresia Forster. I wish to thank them for their support, encouragement and love, not only during my studies but throughout the whole of my life!

CURRICULUM VITÆ

Stefan Immler

Date of Birth: February 23, 1968

Place of Birth: Nabburg, Germany

Citizenship: German

Sep 1978 – Jul 1987	School-leaving examination (Abitur) at the Johann-Andreas-Schmeller Gymnasium Nabburg/Germany
Sep 1987 – Oct 1989	Compulsory military service
Nov 1989 – Oct 1996	Course of study 'Physics' (Diplom), minor 'Astronomy', at the Ludwig-Maximilians-Universität München/Germany
Sep 1991 – Jun 1992	Course of study 'Physics and Astronomy' (B.Sc. and M.Sc.) at the Imperial College of Science, Technology & Medicine, London/UK
Jun – Sep 1992	Research student in the astrophysics group at the Imperial College of Science, Technology & Medicine, London/UK
Sep – Nov 1993	Research assistant in space sciences at the Space Science Center, Institute for the Study of Earth, Oceans and Space, University of New Hampshire, Durham/USA
Sep 1995 – Sep 1996	Diploma thesis in physics and astronomy at the Max-Planck-Institut für extraterrestrische Physik, Garching/Germany
Oct 1996	Diploma exam in physics and astronomy at the Ludwig-Maximilians-Universität München/Germany Academic title 'Diplom-Physiker (Univ.)'
Dec 1996 – Dec 1999	Ph.D. thesis in astrophysics at the Max-Planck-Institut für extraterrestrische Physik, Garching/Germany
Dec 1999 – Mar 2000	Research fellow at the Max-Planck-Institut für extraterrestrische Physik, Garching/Germany
from Apr 2000	Research associate in the Astronomy Department at the University of Massachusetts, Amherst/USA